applied sciences

MDPI

Perspective

A Perspective on Software-in-the-Loop and Hardware-in-the-Loop Within Digital Twin Frameworks for Automotive Lighting Systems

George Balan [1,*], Philipp Neninger [2], Enrique Ruiz Zúñiga [3], Elena Serea [1], Dorin-Dumitru Lucache [1] and Alexandru Sălceanu [1]

[1] Faculty of Electrical Engineering, Technical University of "Gheorghe Asachi" Iasi, 700050 Iași, Romania; edanila@tuiasi.ro (E.S.); dumitru-dorin.lucache@academic.tuiasi.ro (D.-D.L.); alexandru.salceanu@academic.tuiasi.ro (A.S.)
[2] Institute of Energy Efficient Mobility, University of Applied Sciences Karlsruhe, 76133 Karlsruhe, Germany; philipp.nenninger@h-ka.de
[3] School of Engineering Science, University of Skövde, 541 28 Skövde, Sweden; enrique.ruiz.zuniga@his.se
* Correspondence: george.balan@student.tuiasi.ro; Tel.: +40-787-269-199

Abstract

The increasing complexity of modern automotive lighting systems requires advanced validation strategies that ensure both functional performance and regulatory compliance. This study presents a structured integration of Software-in-the-Loop (SiL) and Hardware-in-the-Loop (HiL) testing within a digital twin (DT) framework for validating headlamp systems. A gated validation process (G10–G120) is proposed, aligning each development phase with corresponding simulation stages from early requirements and concept validation to real-world scenario testing and continuous integration. A key principle of this approach is the adoption of a framework built upon the V-Cycle, adapted to integrate DT technology with SiL and HiL workflows. This architectural configuration ensures a continuous data flow between the physical system, the digital twin, and embedded software components, enabling real-time feedback, iterative model refinement, and traceable system verification throughout the development lifecycle. The paper also explores strategies for effective DT integration, such as digital twin-as-a-service, which combines virtual testing with physical validation to support earlier fault detection, streamlined simulation workflows, and reduced dependency on physical prototypes during lighting system development. Unlike the existing literature, which often treats SiL, HiL, and DTs in isolation, this work proposes a unified, domain-specific validation framework. The methodology addresses a critical gap by aligning simulation-based testing with development milestones and regulatory standards, offering a foundation for industrial adoption.

Keywords: digital twin; software-in-the-loop; hardware-in-the-loop; automotive; headlamps

check for updates

Academic Editor: Douglas O'Shaughnessy

Received: 4 July 2025
Revised: 24 July 2025
Accepted: 27 July 2025
Published: 30 July 2025

Citation: Balan, G.; Neninger, P.; Ruiz Zúñiga, E.; Serea, E.; Lucache, D.-D.; Sălceanu, A. A Perspective on Software-in-the-Loop and Hardware-in-the-Loop Within Digital Twin Frameworks for Automotive Lighting Systems. *Appl. Sci.* **2025**, *15*, 8445. https://doi.org/10.3390/app15158445

1. Introduction

Modern automotive development increasingly relies on virtual validation technologies to manage system complexity, ensure functional safety, and accelerate development cycles. Among these, Software-in-the-Loop (SiL), Hardware-in-the-Loop (HiL), and digital twin (DT) techniques have emerged as critical enablers for model-based verification. However, the existing literature tends to treat these approaches in isolation or apply them generically across various domains, without tailoring to domain-specific challenges, such as those present in adaptive lighting systems.

This paper addresses a significant gap in the current State of the Art: the lack of an integrated, traceable framework that combines SiL, HiL, and DT technologies into a single development and validation pipeline for automotive headlamp systems. The structure of this paper is as follows:

- After the introduction in Section 1, Section 2 presents the background on virtual validation technologies and outlines key standards such as AUTOSAR, ISO 26262 [1], and ASPICE while framing the need to adapt the well-established V-Cycle model to support DT–SiL–HiL integration in lighting validation contexts;
- Section 3 introduces the proposed multi-layered architecture, detailing the system, software, and digital twin layers, and defines abstraction levels (L0–L4) used in validation;
- Section 4 applies the framework to lighting-specific validation requirements, supported by case-based examples and lifecycle traceability;
- Sections 5–8 address implementation aspects, including development gates, test environment integration, risk analysis, and system traceability;
- Section 9 provides a strategic outlook on the evolution of DT validation systems and future research directions;
- Section 10 concludes the study and highlights future applied research opportunities.

Software-in-the-Loop (SiL) involves testing software components in a simulated environment, where the software is executed on a virtual platform instead of physical hardware [2,3]. Hardware-in-the-Loop (HiL) complements this by integrating real hardware components into a simulated environment, allowing for real-time interaction and behavior assessment [4–6]. When combined with a digital twin (DT)—a virtual representation of the physical system—these methods provide a comprehensive validation approach: SiL verifies software logic early, HiL ensures real-time response, and the DT enables traceability, continuous monitoring, and predictive diagnostics throughout the system lifecycle [7–9].

While the integration of DT, SiL, and HiL technologies offers a promising path toward comprehensive validation, it also introduces a complex set of challenges that must be addressed for successful implementation. These challenges extend to multiple dimensions, including technical interoperability, real-time system requirements, data infrastructure, and organizational readiness [4,6,8].

From a technical standpoint, integrating virtual models with physical testing environments involves synchronizing systems that operate at different abstraction levels. Achieving seamless interoperability between digital twin (DT), Software-in-the-Loop (SiL), and Hardware-in-the-Loop (HiL) components requires the adoption of standardized communication protocols, precise time synchronization mechanisms, and model compatibility across heterogeneous toolchains and execution platforms [4,7,9]. Moreover, real-time processing constraints—particularly within HiL and SiL environments—demand high-fidelity simulation engines and deterministic communication interfaces, which are not always readily available or scalable [10–13].

Beyond the technical hurdles, operational challenges such as data accessibility, quality assurance, and scalability significantly affect system performance and reliability. Digital twins rely heavily on live, high-quality data streams to provide predictive insight and maintain model fidelity. However, many organizations face data silos, inconsistent formats, or proprietary systems that limit cross-domain integration and slow down development cycles [14–16].

Digital twin frameworks are rapidly becoming foundational in modern engineering, offering scalable, secure, and standardized ways to replicate physical systems virtually. The strategic importance of architectural and security guidelines for ensuring the robust deployment of DTs across cyber–physical networks has been emphasized in recent surveys [17]. In alignment with the goals of Industry 4.0 and sustainable European manufacturing, dedicated projects have shown how DTs can enhance intelligent lighting systems through real-time monitoring and AI integration [18]. This is particularly relevant for automotive applications, where DTs are increasingly used to support diagnostic processes and predictive maintenance. One approach demonstrates the use of a 3D-simulated environment with camera-integrated virtual lighting systems for classifying headlamp states using neural networks, with an accuracy of 80% under real-world conditions [19]. Another method combines digital signal analysis and machine learning to detect short-circuit LED failures, with precision exceeding 99% [20]. These targeted implementations complement broader efforts to model vehicle environments and behaviors for safer, more efficient road operation through DT-enabled visual recognition and simulation techniques [19].

In addition, organizational resistance to technological change, combined with skill shortages in simulation-based validation, can hinder adoption. The implementation of a DT–SiL–HiL framework requires not only advanced tooling and infrastructure but also a workforce trained in systems modeling, real-time simulation, and cyber–physical system design. Bridging these gaps demands investment in upskilling, as well as cultural alignment within engineering and quality assurance teams to embrace model-based verification methodologies [21,22].

This paper addresses these multi-dimensional challenges by proposing a process-oriented framework that strategically integrates SiL, HiL, and DT technologies into a cohesive validation environment for automotive headlamp systems. The aim is to define a unified and traceable methodology that aligns simulation-based testing with system requirements and industry standards.

2. Fundamentals and Terminology

This chapter provides a conceptual foundation for the validation and simulation approaches used in automotive lighting system development. It first introduces the core technologies of HiL, SiL, and DTs, outlining how each supports the virtual testing and integration of embedded systems. These techniques are essential for creating a safe and iterative development environment before physical prototypes are available.

The structure of this chapter also aligns with a V-Cycle testing model, which is widely adopted in automotive system engineering. The V-Cycle reflects the parallel relationship between system specification and verification stages, ensuring that each development phase is validated through a corresponding testing activity. Within this adapted V-Cycle, SiL and HiL simulations, as well as DT-based approaches, are strategically placed to cover both early software verification and late-stage system validation. Section 2.2 presents how this model applies to the stepwise development of automotive lighting systems, mapping typical industry gates (e.g., G10 to G120) to validation levels from concept to integration.

2.1. Hardware-in-the-Loop (HiL), Software-in-the-Loop (SiL), and Digital Twin (DT)

The concepts of HiL and SiL are integral parts of the V-Cycle development process, which is commonly used in the automotive industry.

HiL is a standard method for testing Electronic Control Unit (ECU) software in automotive development [23]. SiL testing involves generating code from Simulink models and deploying it on hardware devices [2].

DTs are used to create virtual representations of physical systems, allowing for comprehensive testing and validation in a controlled environment. This approach is particularly useful for testing complex systems like automotive lighting under various simulated conditions [24].

In the context of this review, we define a digital twin (DT) in alignment with the Basyx Asset Administration Shell (AAS) type 2 classification. This definition characterizes the DT as more than a static data container (type 1, i.e., a serialized AAS); rather, it is an active software entity deployed on a server. It exposes an interface—referred to as the front end in the Basyx framework—that allows interaction with other parts of the system, in our case, the operational environment. This interface provides access to both properties and operations, enabling runtime interaction. While a metamodel may also be included in accordance with the AAS type 2 specification, it is not essential for the discussion presented in this paper. Importantly, unlike a type 3 AAS, the DT defined here is not autonomous in initiating negotiations with other components. This distinction is critical because autonomous behavior in safety-critical systems—such as vehicle subsystems governed by ISO 26262—requires extensive validation and formal guarantees of functional safety. Limiting the DT to type 2 ensures that it remains predictable and verifiable, avoiding the introduction of runtime uncertainties that could compromise system integrity [25].

Figure 1 presents a V-Cycle representation adapted for automotive systems engineering with integrated DT functionality. The left branch of the V reflects the development workflow, beginning with system requirements and progressing through system-level design, component specification, and software implementation. Each layer incrementally refines the system architecture in preparation for integration and testing. The right branch represents the validation process, starting with HiL and SiL evaluations, advancing to integrated HiL/ViL (Vehicle-in-the-Loop) scenarios, and culminating in complete vehicle testing to ensure regulatory compliance and real-world performance. At the center, the DT serves as a cross-domain enabler, synchronizing data between virtual models and physical systems throughout the development lifecycle. This integration supports continuous monitoring, traceability, and predictive analytics, enhancing both early design validation and post-deployment feedback. The figure also emphasizes the shift toward a data-driven, simulation-supported validation strategy that aligns with current trends in automotive system digitization.

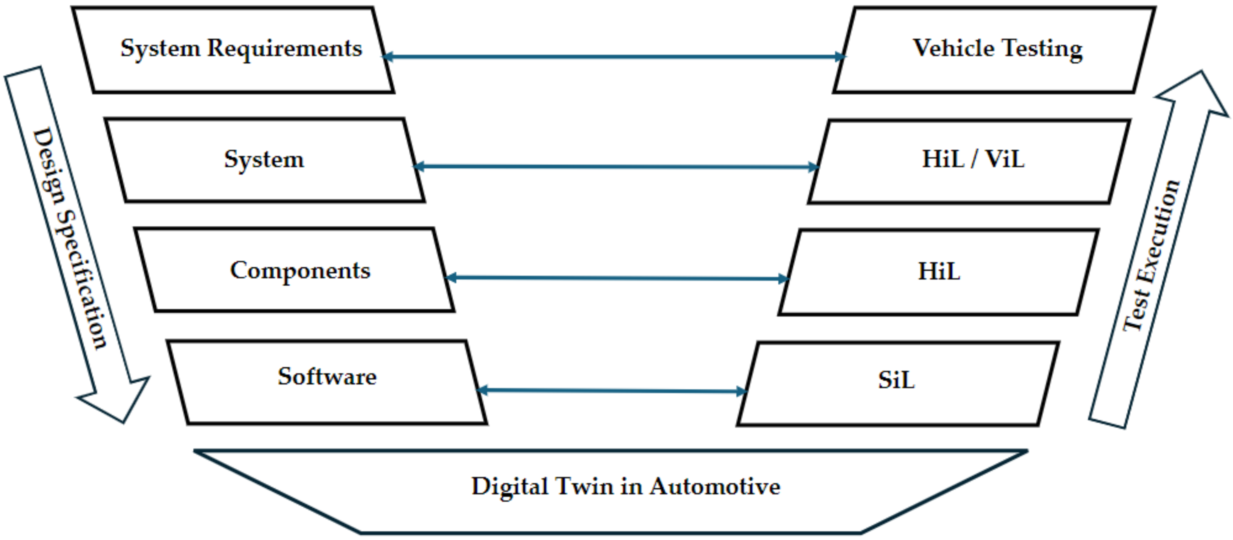

Figure 1. V-Cycle development process for digital twin in automotives.

2.2. Automotive Lighting System Development Stages

Gantt charts are a popular tool for visualizing temporal discrete event sequences with dependencies, commonly used in manufacturing and computing [26].

Figure 2 illustrates a structured integration of DT technology into the development lifecycle of automotive headlamp systems. Each gate represents a critical validation point, ensuring continuous alignment between the DT framework and system engineering processes. The key gate activities are outlined as follows:

- G10—Initial DT Requirements: The system requirements—both functional and non-functional—are defined and analyzed from the perspective of the DT, ensuring that the DT-related needs are identified and aligned with the overall system objectives;
- G20—System DT Architecture: General system aspects are defined through the DT view, establishing a high-level structure that guides DT integration within the overall system architecture;
- G30—Concept DT Validation: This gate evaluates the feasibility of the conceptual DT representation. Verification activities include preliminary simulations and use–case alignment to confirm that the DT can represent essential system behaviors accurately at an abstract level;
- G40—SiL Integration with DT: The DT logic is integrated into the simulation environment to enable virtual testing and validation of system behavior during early development stages;
- G50—HiL Integration with DT: The DT components are connected to physical subsystems, enabling real-time validation of the system interactions;
- G60—Requirements Traceability via DT: This stage focuses on the behavior of test cases against the requirements, which are integrated with the DT concept to ensure complete traceability;
- G70—DT Calibration: This process aligns the DT with real-world data through calibration;
- G80—Scenario-Based Testing: This gate allows the DT to be tested across a wide range of real-world and edge-case scenarios, helping to assess system robustness, safety performance, and behavior under uncommon or critical conditions;
- G90—Analytics for DT-Based Diagnostics: Diagnostic analytics are integrated with the DT to enable fault detection, root cause analysis, and prognostics;
- G100—Standards Compliance Validation (via DT Simulations): DT-based simulations are used to verify compliance with industry standards and certification requirements;
- G110—Continuous Integration and Testing (CI/CT) with DT: The DT is incorporated into automated CI/CT workflows, supporting regression testing and continuous verification;
- G120—Final Deployment Readiness and Field Monitoring with DT: The final gate assesses deployment readiness, with the DT prepared for post-deployment monitoring.

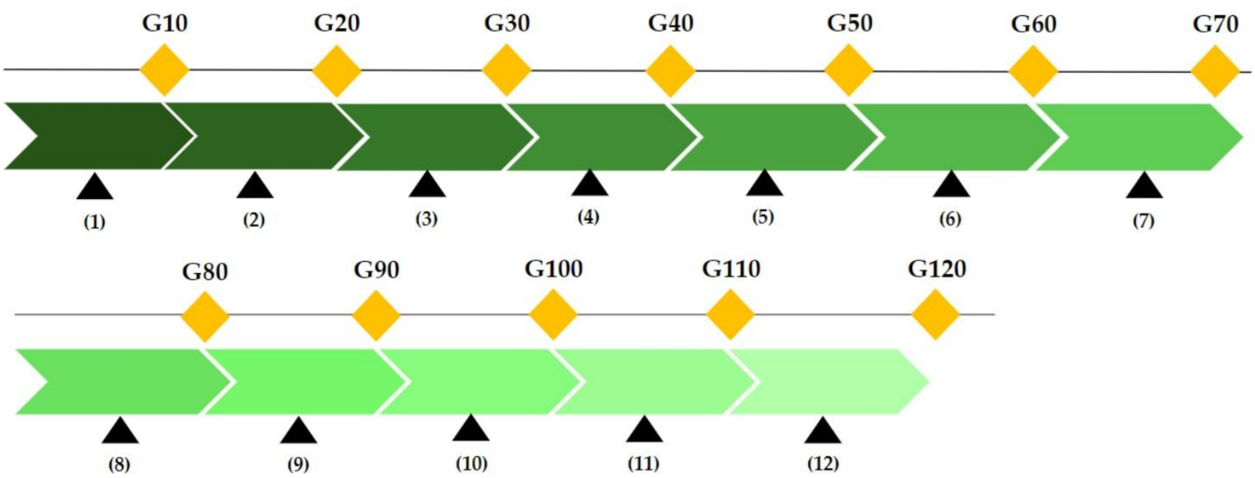

Figure 2. Development gates for digital twin in automotives. (1) Initial DT requirements; (2) system DT architecture; (3) concept DT validation; (4) SiL–DT; (5) HiL–DT; (6) REQ traceability–DT; (7) DT calibration; (8) scenario-based testing; (9) analytics for DT-based diagnostics; (10) standards compliance validation (via DT simulations); (11) continuous integration/testing (CI/CT) with DT; (12) final deployment readiness + DT for field monitoring.

To further demonstrate the systematic role of the DT in the development and validation of automotive lighting systems, we analyzed the implementation of functional and non-functional technical requirements across all 12 validation gates (G10–G120), as shown in Table 1. This approach highlights not only the relevance of the DT at each phase but also the coherence and traceability it enables throughout the entire lifecycle from early design to field operation.

Table 1. Lifecycle validation of a lighting system requirement across DT development gates.

Gate	REQ_01_Lighting_Behavior	REQ_02_Fault_Response	REQ_03_Response_Time
G10	Define DT validation objectives for lighting: response time, beam compliance, system interaction	Identify fault detection timing and CAN signaling as critical diagnostic objectives	Define maximum acceptable ECU lighting response delay (200 ms)
G20	Structure the DT to modularly include lighting elements, sensor emulation, and ECU logic	Include diagnostic logic for LED/sensor fault injection in the DT model	Include timing paths and latency estimators in the DT
G30	Test early DT behaviors like auto-on under concept scenarios (e.g., entering a tunnel)	Evaluate error response through simulated fault injection scenarios	Evaluate logic-to-actuator delay through timing simulation in the DT
G40	Verify lighting control software in virtual conditions through DT-CAN message simulation	Simulate fault detection logic for various LED/sensor failure cases	Verify latency in signal propagation using SiL
G50	Assess real-time lighting system response with DT connected to hardware	Inject real-time faults and confirm ECU detection via HiL interface	Measure actual sensor-to-actuator delay on the HiL bench
G60	Link lighting requirements to test cases validated in the DT simulation framework	Trace fault detection events against expected fault model behavior	Document timing conformance with the requirement across configurations
G70	Use real measurements to adjust lighting model for beam intensity and distribution	Adjust DT to simulate varying fault severities (LED, power)	Calibrate model delays using real timing logs
G80	Simulate real-world events (fog, night driving) to test lighting safety and robustness	Create composite scenarios: LED fault + communication error during fog driving	Inject environmental load (fog, temperature) and measure response time
G90	Enable detection of lighting faults (LED failure, delay) via integrated analytics	Enable predictive analytics for fault detection and failure prediction	Predict delay risks using historical timing anomalies
G100	Verify DT behavior against lighting compliance regulations (e.g., UNECE)	Confirm diagnostic flow meets regulatory and OEM safety requirements	Validate conformance to latency standards (e.g., ISO), if applicable
G110	Automate lighting validation through DT in CI pipeline post-software updates	Run fault regression tests using CI-integrated DT model	Integrate timing benchmarks into nightly CI validation
G120	Monitor headlamp performance live using DT telemetry and support OTA updates	Enable real-time fault status tracking and analytics via cloud telemetry	Enable real-time latency tracking during fleet testing

The analysis shows that a well-defined DT can be aligned with each development milestone, acting as a central validation mechanism. In the early phases (G10–G30), the DT helps capture functional requirements and simulate key lighting behaviors in conceptual form. During integration phases (G40–G50), it enables both virtual (SiL) and real-time (HiL) testing, ensuring that software logic and physical subsystems respond appropriately to various input conditions.

From G60 onward, the DT becomes essential for maintaining traceability and realism. It links specifications to concrete test cases, incorporates real-world calibration data, and is capable of executing complex scenario-based tests (e.g., fog, curves, night driving). Advanced features such as predictive diagnostics (G90) and standards compliance simulations (G100) further extend its value. Finally, its integration into CI workflows (G110) and deployment environments (G120) ensures that lighting system behavior is continuously verified, even after release, enabling a feedback loop for over-the-air improvements.

3. Architectural Layers and Digital Twin Integration for Headlamp Systems

Modern headlamp systems have evolved beyond traditional electromechanical design and now function as complex, software-driven subsystems. Their performance relies on real-time integration with vehicle dynamics, environmental inputs, and adaptive control algorithms. To manage this complexity, contemporary development approaches employ a layered system architecture and leverage DT technology for early validation, logic testing, and continuous integration. This section presents a layered view of headlamp system architecture and discusses abstraction levels critical to simulation and testing.

3.1. Architectural Layers

To further clarify the functional content of the system and software architecture layers depicted in Figure 3, the system layer includes physical subsystems, such as ambient light sensors, camera-based perception units, LED arrays, stepper motors for beam adjustment, and the headlamp management ECU. These components interact via CAN FD communication and are powered through monitored supply lines.

Figure 3 presents an integrated view of the system and software architecture for an automotive headlamp system, illustrating the interaction between physical components, embedded logic, and their virtualization via the digital twin.

A practical example of how this layered architecture operates can be seen when a vehicle enters a short, unlit tunnel. In this scenario, the system layer detects the ambient light drop via onboard sensors and relays the signal to the lighting control ECU. The software layer evaluates this input and activates the headlamps through CAN FD-based control logic. The DT replicates the sensor signal and software response in a virtual environment, allowing engineers to verify system behavior, switching time, and compliance without physical testing.

3.1.1. System Architecture Layer

This includes the physical components such as lighting elements (e.g., LED matrices), actuators (e.g., stepper motors for beam adjustment), sensors (e.g., ambient light, rain, camera), and control ECUs (drivers). It defines how the headlamp unit interacts with the vehicle and the external environment.

3.1.2. Digital Twin Layer

The DT mirrors the behavior of the real-world headlamp system in a virtual environment. It simulates sensor input, hardware response, and environmental conditions to enable

- Early validation of software logic and control strategies;
- Scenario-based testing (e.g., glare detection, city/highway adaptation);

- Continuous verification of software changes without requiring physical hardware.

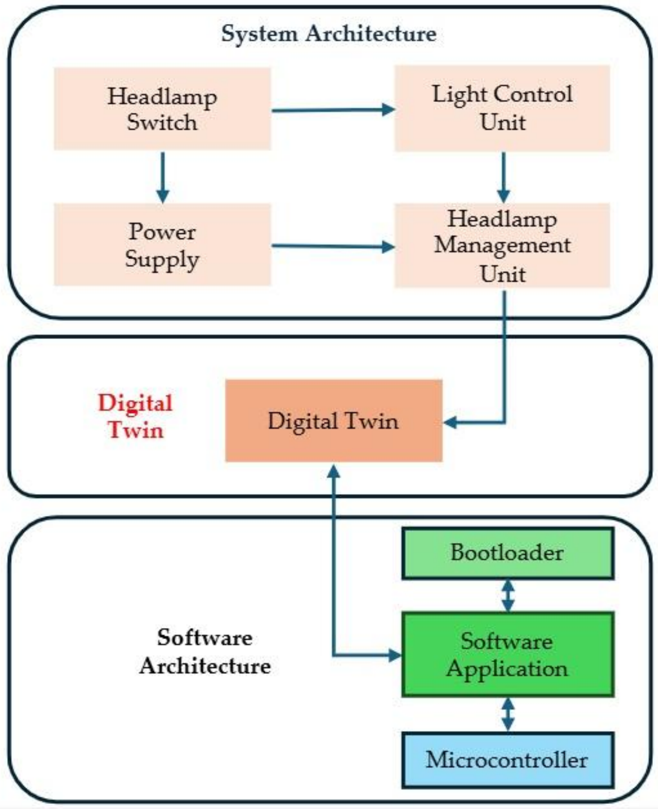

Figure 3. System-software architecture with digital twin integration for headlamp management.

3.1.3. Software Architecture Layer

This layer encompasses the embedded control software, including functional algorithms (e.g., Adaptive Driving Beam control), middleware (communication stacks, diagnostic services), and safety components. Model-based design (e.g., Simulink, AUTOSAR) is commonly used here to support reusability and formal verification.

3.2. Abstraction Levels: L0, L1, L2, L3, and L4

To enable systematic virtual validation and efficient integration of DT technology into automotive headlamp systems, we define a multi-level abstraction model that structures the gradual evolution of the system from conceptual design to real-world deployment.

This layered approach provides a framework for organizing validation strategies according to system maturity and complexity. These levels reflect the increasing degree of system realism, from early behavioral modeling to full-scale DT deployment, and their ability to represent the real ECU and its physical environment. Figure 4 illustrates this progression, showing how DT involvement expands as the system moves from concept to test drives and finally to a fully integrated digital replica:

- L0 (conceptual validation) uses abstract behavioral models with minimal realism, focused on early functional exploration. DT involvement is limited, serving only basic traceability.
- L1 (Software-in-the-Loop) introduces executable code within a virtualized ECU, allowing early logic validation. The DT begins supporting behavioral tracking and input simulation.
- L2 (Hardware-in-the-Loop) blends virtual and real components, enabling validation of real-time behavior on physical hardware. The DT support increases, contributing to environmental modeling and prediction.

- L3 (test drive) integrates the DT with real-world driving tests, enabling parallel monitoring and scenario-based diagnostics.
- L4 (full DT integration) represents a fully bidirectional connection between virtual and physical domains, supporting high-fidelity simulations, predictive maintenance, and scalable validation of advanced lighting features.

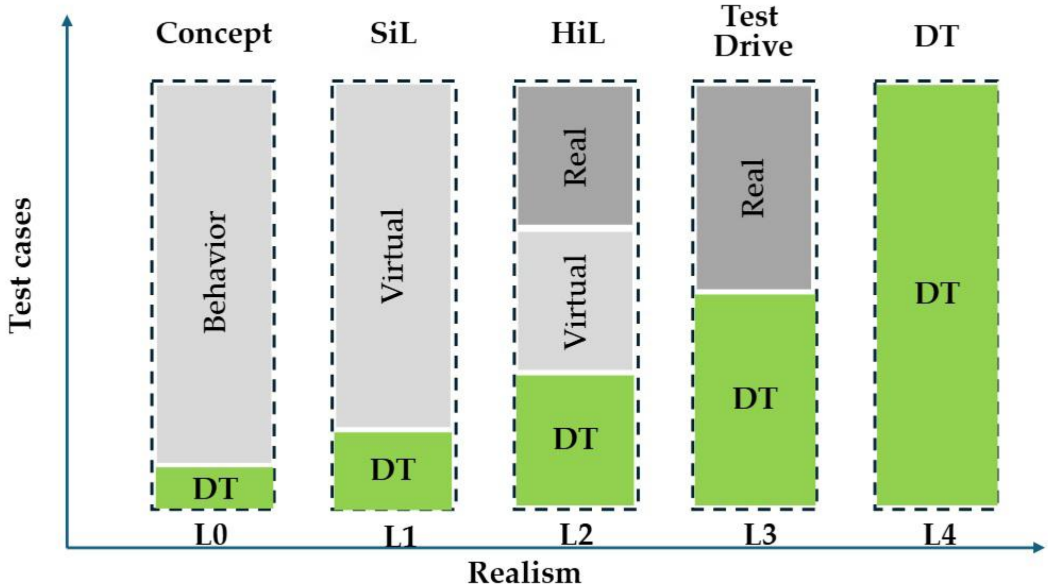

Figure 4. Architecture of digital twin in concept, SiL, and HiL—a schematic showing how the DT wraps around the test ecosystem (software + systems).

3.3. Role of DT in Virtual Validation

Building upon the abstraction model introduced in the previous section, this part outlines the practical validation capabilities enabled by DT integration across the L0–L4 levels. The digital twin enables early-stage software verification, real-time interaction testing, and predictive analysis in both simulated and physical environments. In headlamp system development, these capabilities facilitate a shift from hardware-dependent validation toward proactive, model-based strategies aligned with AUTOSAR-compliant ECU architectures.

In practical terms, the proposed abstraction levels allow engineers to progressively develop and reuse models, test scenarios, configuration data, and validation results throughout the V-Cycle. For example, consider the case of an automatic headlamp function that activates an LED string. At the conceptual level (L0), the requirement is defined as a basic lighting behavior specification, described through logical flowcharts or functional diagrams without implementation. At the SiL stage (L1), the logic is implemented and tested in a virtual environment using simulated light sensor input. At L2 (HiL), the same logic is integrated with real hardware components—such as the ECU and lighting control unit—allowing engineers to verify switching behavior under real-time conditions and actual CAN messages. During L3 (test drive), the system is validated in a real vehicle under dynamic conditions, confirming performance under real-world scenarios. Finally, in L4 (DT), data from physical tests is reused to refine the digital representation of the system, enabling engineers to simulate similar lighting events without requiring physical testing setups. This structured flow ensures continuity across development levels and supports traceability, reusability, and increasing system realism.

4. Requirement Validation and Compatibility Analysis

4.1. Overview of Standards

AUTOSAR, an open and standardized automotive software architecture, separates application software from associated hardware to improve cost-efficiency and reusability [27,28]. Another key aspect of this concept is the modularity of the architecture, which enables the development of software components independently of specific hardware platforms or operating systems. This abstraction allows application developers to concentrate on software functionality without being constrained by ECU hardware variants or underlying operating environments [29].

Table 2 illustrates the relationship between the key aspects and implementation details of automotive validation within an AUTOSAR-compliant distributed test framework. The integration of AUTOSAR standards with DT technology creates a traceable pathway from simulation to real-world deployment that is particularly valuable for complex systems like adaptive headlight controls or predictive maintenance architectures.

Table 2. AUTOSAR-compliant digital twin framework for automotive validation.

Aspect	Details
Standard Overview	Leading architecture, global cooperation, separation of software and hardware, layered design
Digital Twin Integration	Service-oriented architecture, modular design, configuration, and automation
Testing and Validation	Dependability assessment, automated testing tools, model-based testing, virtual testing, and interface checks

ISO 26262 is a critical standard for the development of automotive safety-related systems. It explicitly mentions HiL as a suitable test environment for software unit tests, integration tests, and verification of safety requirements at the component level [23]. This standard is mandatory for passenger car development worldwide and provides guidelines on the development and testing of automotive electronics, including lighting systems.

ASPICE is a process assessment model that provides a framework for evaluating the performance of automotive software development processes. It is often used in conjunction with ISO 26262 to ensure comprehensive compliance and quality assurance [30]. These standards facilitate the interoperability and efficiency of testing platforms, which is crucial for the effective use of digital twins in automotive lighting testing.

ASAM (Association for Standardization of Automation and Measuring Systems) standards, such as ASAM XIL, provide guidelines for the integration and automation of test systems, including HiL and SiL environments [31]. These standards facilitate the interoperability and efficiency of testing platforms, which is crucial for the effective use of digital twins in automotive lighting testing.

4.2. Case-Based Requirement Analysis

The DT process plays a significant role in the automotive industry, especially in the development of complex lighting systems. Validation of this process happens across several levels, each with a specific purpose. Initially, theoretical requirements are established through sketches, preliminary calculations, and risk analyses at the conceptual stage. This helps define general specifications and identify potential issues before starting development. Software algorithms are tested in a virtual environment, eliminating the need for physical components, verifying logic and performance, thereby reducing the requirement for early physical prototypes (SiL). Hardware components, such as ECUs or sensors, are tested by connecting them to a real-time simulator to validate system behavior under conditions close to reality (HiL). Finally, a complete virtual replica of the system is created, which is used for complex simulations and predictive analyses (DT). This allows real-time monitoring, performance optimization, and problem detection before physical implementation. This process strengthens development and reduces associated risks.

Table 3 summarizes different validation requirements (REQs). Requirement 1 is validated primarily at the SiL and DT stages, reflecting the focus on software logic testing and advanced virtual simulation. Requirement 2 is covered at all stages—conceptual, SiL, HiL, and DT—indicating it is a fundamental aspect addressed throughout the entire development process, from early theoretical definition to real-time monitoring. Requirement 3 appears only at the HiL and DT stages, highlighting the need for physical hardware testing and comprehensive virtual replication to validate system behavior under realistic conditions.

Table 3. Distribution of validation requirements across concept, SiL, HiL, and digital twin.

REQ	Concept	SiL	HiL	DT
1	—	✓	—	✓
2	✓	✓	✓	✓
3	—	—	✓	✓

✓: Requirement is validated/covered in this stage. —: Requirement is not validated/not applicable in this stage.

Table 4, analyzing the conceptual, SiL, HiL, and DT perspectives on each requirement, highlights the progressive validation approach embedded in the development process. At the conceptual stage, the focus is on theoretical validation. Beam adjustment sketches or redundancy block diagrams are used to define functional expectations early on, enabling risk identification before any implementation begins. In the SiL phase, simulated environments and software models validate control logic under virtual conditions, such as testing response times or handling signal loss, without requiring physical hardware. This allows fast iterations and early detection of logic or integration issues.

Table 4. Progressive validation approach across Conceptual, SiL, HiL, and DT stages.

Requirement	Test Type	Input	Output
REQ_01_AdaptiveLight	Conceptual	Beam adjustment sketches	Theoretically validated concept
	SiL	Simulated data: car in the opposite direction	Beam was adjusted without glare
	HiL	CAN signal from real camera	Response < 50 ms
	DT	Three-dimensional environment with rain + traffic	Correct beam adjustment
REQ_02_ElectricalFault	Conceptual	Redundancy block diagram	Safety feature requirements
	SiL	CAN signal loss test	The system passes safely
	HiL	Short circuit injection	The headlight deactivates in controlled mode
	DT	Cascade defect simulation	System impact analysis

Moving into HiL, real components are integrated to test how the system responds to physical signals and disturbances, such as real camera inputs or fault injections. This stage brings virtual validation closer to reality by introducing tangible behaviors and interactions. Finally, the DT level provides a comprehensive, real-time simulation of the entire system within realistic scenarios—weather, traffic, and cascading faults—capturing complex interdependencies and verifying the system-wide impact. This layer closes the loop by enabling predictive analysis and performance optimization before physical deployment.

It is important to note that Tables 3 and 4 present illustrative validation scenarios designed to demonstrate the structure and logic of the proposed framework. Although the data itself is fictional, the validation sequences and requirements reflect realistic engineering processes observed in current automotive development. The framework is, therefore, technically applicable in industrial contexts. Future work will focus on applying the method to empirical data obtained from actual headlamp system projects to further evaluate its robustness and integration potential.

While this paper does not report experimental prototyping or implementation of a full case study, its primary objective is to define a reusable and transferable validation structure that integrates SiL, HiL, and DT methods. The validation logic—though presented in abstract form—is grounded in common industry practices, and a pilot application is planned in future work to strengthen the framework's empirical foundation.

5. Stage-Wise Role of SiL and HiL Across Development Phases

5.1. Applicability of SiL and HiL Testing

In the development of automotive lighting systems, selecting between SiL and HiL testing is not a matter of preference but rather a strategic alignment with system maturity and the complexity of requirements.

Software-in-the-Loop testing proves most effective in early development phases, where control logic and software algorithms must be verified quickly and without hardware dependencies. Simulated environments allow iterative testing under various scenarios, contributing to early fault detection and reduced development costs.

Hardware-in-the-Loop testing, by contrast, becomes essential when validating real-time interactions between software and physical components. For requirements involving precise response timing, safety-critical behavior, or physical signal processing, HiL is the only viable option. It enables the injection of realistic disturbances and ensures compliance with functional safety standards.

5.2. Strengths and Benefits of Each Approach

Software-in-the-Loop procedures offer speed, flexibility, and cost-efficiency. They allow high-frequency regression testing, support automated verification workflows, and facilitate the rapid prototyping of control strategies. SiL is well-suited for algorithm validation, internal communication, fault injection (e.g., signal loss), and early behavioral tuning.

Hardware-in-the-Loop procedures, on the other hand, provide critical realism. They validate signal integrity, actuator response, and the real-time performance of embedded systems under physical conditions. This is particularly important for tests where software behavior must react to sensor inputs or disturbances such as voltage spikes or CAN bus errors.

Together, SiL and HiL create a complementary validation chain: SiL accelerates early design loops, while HiL ensures that physical integration meets safety, timing, and hardware constraints.

5.3. Operational and Methodological Limitations

Software-in-the-Loop's primary limitation is its lack of physical realism. Although high-fidelity models can simulate inputs, they cannot fully replicate the nuances of hardware timing, signal delays, or environmental noise. Moreover, performance on virtual ECUs may diverge from behavior on physical platforms due to timing discrepancies or resource contention. These limitations may be acceptable in many cases, especially when the development process favors early (unit) testing. Nonetheless, developers must remain aware of the reduced level of realism when interpreting results.

Hardware-in-the-Loop introduces realism but at the expense of scalability and cost. Setting up and maintaining a HiL bench requires specialized equipment, calibration time, and manual oversight. The iterative process slows down considerably compared to SiL, and hardware availability often becomes a bottleneck.

Both methods require careful planning to balance depth of coverage against cost, repeatability, and system maturity.

5.4. Test Coverage Across Development Stages

Digital twin technology involves creating a virtual replica of a physical system to simulate, predict, and optimize its performance. Both SiL and HiL testing play significant roles in the development and validation of DTs [32,33].

In a modern development pipeline, SiL and HiL are not mutually exclusive but are sequentially and iteratively integrated. A DT framework bridges both layers, enabling models and real hardware to synchronize through shared scenarios and data sets.

The Gantt-based development timeline introduced in Section 2.2 outlines a gated process (G10–G120) for integrating SiL, HiL, and DT technologies across the product lifecycle. This framework, presented in Table 5, aligns validation methods with engineering milestones.

Table 5. Test method distribution across development gates.

Gate	Activity Focus	Dominant Test Level	SiL Role	HiL Role	Digital Twin Role
G10–G30	System definition, design	L0	—	—	Initial requirement mapping
G40–G50	Logic and software validation	L1	✓	—	Simulation support
G60	Traceability and requirements	L1	✓	—	Documentation and linkage
G70	DT calibration	L2	✓	✓	Digital modeling foundation
G80–G90	Real-time validation	L2	✓	✓	Environment integration
G100	Integration pipeline	L3	✓	✓	Scenario orchestration
G110–120	Launch and operation	L4	—	—	Monitoring and analytics

✓: Method applicable/used at this development gate. —: Method not applicable/not used at this development gate.

5.4.1. Phase I—Definition and Design (G10–G70)

G10–G30 focused on system requirements and early functional discovery. At this stage, conceptual validation (L0) is the dominant approach. In G40–G50, SiL is introduced to test control logic and virtual ECU behavior, independent of hardware. This phase enables the rapid iteration of software functions. G60 supports requirement traceability, connecting SiL outcomes to functional and safety requirements in preparation for physical validation.

5.4.2. Phase II—Validation and Integration (G70–G110)

The second phase begins with DT calibration within G70. Simulation environments are refined using data from prior SiL tests and physical system constraints. From G80 to G90, HiL testing enables real-time performance validation under realistic electrical and sensor conditions. Fault injection, timing analysis, and ISO 26262 compliance are key activities during this phase. At G100, a continuous integration and testing pipeline emerges, synchronizing SiL and HiL outputs within a centralized DT platform. Testing becomes iterative, coordinated, and traceable. Ultimately, G110 pre-deployment activities encompass scenario-based simulation, diagnostics, and operational readiness verification through hybrid test environments.

5.4.3. Phase III—Post-Deployment (G120)

In G120, the DT plays a monitoring role, tracking live system performance, detecting anomalies, and enabling predictive maintenance, eliminating the need for redundant physical revalidation.

6. Assessment of Integration Within Digital Twin

6.1. Deployment Readiness and Validation Depth

The simulation of real-world conditions within a DT framework depends heavily on the quality of the simulated environment, which must cover various driving scenarios, including diverse lighting and weather conditions. This allows for a comprehensive evaluation of the headlamp system's behavior and performance [19,34]. By continuously monitoring the virtual model, potential failures can be identified and addressed early, thereby avoiding disruptions in the physical system. This predictive capability contributes to reducing both downtime and maintenance costs [35,36].

Digital twins also play a key role in developing and validating advanced safety functionalities such as Adaptive Front-lighting Systems (AFSs), which dynamically adjust the headlamp direction based on steering input to enhance driver visibility on curves [37].

An example of a real-world scenario simulation is illustrated in Figure 5, which shows the static driving simulator developed at Hochschule Karlsruhe (HKA). This system enables the immersive reproduction of complex road environments. Curves, varying illumination, and environmental stimuli can be reproduced consistently, making it a valuable platform for testing adaptive lighting systems in a repeatable manner. It is also conceivable that this setup lets test engineers include cases that are hard to encounter in test drives, like heavy fog, and vary the position of external illumination, like street lighting.

(**a**) (**b**)

Figure 5. Driving simulator environment for digital twin-based headlamp validation. (**a**) shows a physical driving simulator setup with a car mock-up; (**b**) shows the driver's view inside the simulator, displaying a virtual urban scene projected in front of the car for immersive testing.

Moreover, such environments support proactive system monitoring. Using embedded sensors, including cameras, the simulator can collect behavioral data and establish feedback loops between the physical and virtual models. This supports predictive diagnostics by identifying anomalies, misalignments, or delayed responses in the lighting system.

Since the system is purely virtual, it also offers evaluation methods not available in physical test drives. As an example, it allows for the placement of virtual cameras freely in space, either static or relative to the movement of vehicles. This feature can be used to evaluate the effects of the lighting system on oncoming vehicles. By using virtual cameras, the test can be run for trucks, cars, and bicycles simultaneously by placing three different virtual cameras in the respective positions.

The functional behavior of the headlamp system is modeled using Simulink, allowing for modular representation and early verification of control logic. This model is intended to represent the lighting subsystem independently of vehicle-level interactions. To simulate and validate the broader vehicle context, including sensor signals, traffic, and interaction timing, the environment was emulated in CANoe. Within CANoe, system logic is expressed using CAPL (Communication Access Programming Language), which enables flexible simulation of driving conditions, lighting commands, and error handling. This separation allows the headlamp model to be tested both in isolation (SiL) and as part of an integrated virtual vehicle environment (HiL or DT) while maintaining a clear boundary between subsystem development and system-level validation.

6.2. Compatibility Between Test Levels and Requirement Types

The integration of SiL and HiL within a DT framework allows for a structured and scalable validation architecture, where each test level corresponds to specific requirement types. Functional and algorithmic requirements—often related to logic flow, data handling, or embedded algorithms—are most efficiently addressed through system-level (SiL) design during early development phases. In contrast, hardware-dependent or safety-critical requirements demand HiL validation, where real-time electrical signals and physical sensor feedback must be processed under realistic operating constraints.

Digital twin technology serves as a unifying layer that ensures traceability between requirements, simulation of artefacts, and real-world outcomes. It provides a bidirectional link that helps propagate insights and faults across all development levels. Rather than replacing SiL or HiL, the DT strengthens its impact by enabling continuous validation, synchronizing cross-domain data, and supporting test coverage extension with minimal physical effort.

6.3. Non-DT-Testable Requirements and Subjectivity

Digital twin technology does not yet fully address all categories of requirements. Certain specifications remain difficult or impossible to validate in an entirely virtual space due to their reliance on subjective interpretation, physical interaction, or unpredictable context sensitivity.

For instance, luminance-related requirements—such as achieving a minimum 1000 lx at a specified distance—can be evaluated through photometric simulation. However, real-world perception of glare, beam uniformity, and visual comfort depends heavily on individual user feedback and environmental influences, which are beyond the scope of current digital models.

Other examples of non-DT-testable requirements include cybersecurity robustness, where network-based threats and penetration vulnerabilities require real-world testing environments; aerodynamic behavior, which, while partially simulated, still relies on wind tunnel validation for certification; and mechanical tolerances in mounting structures, where fundamental assembly dynamics can introduce deviations difficult to replicate virtually. Additionally, subjective evaluations—such as visual quality, light tone appeal, or perceived system responsiveness—are inherently subjective and cannot be fully validated through DT simulation; therefore, they must be assessed through physical trials or user-based testing protocols.

These limitations highlight the need for hybrid validation strategies. Digital twins should be complemented with physical prototypes and field trials to fully capture user perception, aesthetic integration, and compliance with regulatory nuances. In such cases, the DT remains an indispensable tool, but one that must be integrated wisely within a broader test ecosystem.

7. Discussion and Open Questions

Despite the increasing adoption of DT frameworks coupled with SiL and HiL testing for automotive headlamp systems, several architectural and methodological gaps remain. Key challenges include insufficient traceability between system requirements and validation artifacts, limited scenario coverage—particularly for edge cases—and fragmented feedback loops across abstraction levels (L0–L4). Gate-based development flows often lack enforcement in hybrid test environments, leading to misaligned verification stages and latent functional risks. This section outlines these critical issues, examines infrastructure and tooling limitations, and integrates recent findings from the literature to define open questions for future standardization and implementation.

7.1. Identified Gaps in Current DT-Based Validation Approaches

Although the integration of SiL, HiL, and DT technologies offers a promising validation architecture for automotive lighting systems, several critical gaps remain. A key concern is the disconnect between theoretical requirements and their practical testability. Many requirements are defined at a conceptual level without being fully traceable by virtual or hybrid validation stages. This lack of end-to-end alignment creates ambiguity about what is being tested, how it is being validated, and with what level of confidence.

Additionally, there are integration gaps between abstraction levels, particularly between L3 (test drives with DT) and L4 (full DT integration). In many cases, feedback loops are fragmented or manual, preventing real-time synchronization between the physical system and its digital counterpart. Without a continuous, bidirectional data exchange pipeline, predictive validation remains narrow in scope. Finally, validation often emphasizes functional coverage under standard operating conditions while neglecting edge-case scenarios or rare environmental conditions that are crucial for safety and robustness.

Gate-based development processes (G10–G120) assume a sequential and coherent flow between design, integration, and validation phases. However, in real-world implementations, certain gates may be handled superficially or skipped entirely. For instance, if G60 (requirements traceability) is not thoroughly addressed before G80 (scenario-based testing), validation activities may be performed based on incomplete or unverified specifications. This misalignment between gates compromises the integrity of the testing process and risks passing systems that have not been fully evaluated.

Most validation workflows focus on common operational conditions. Yet, lighting systems must also function reliably under rare or extreme conditions, such as

- Reflective glare from wet roads;
- Dense fog that diffuses headlamp output;
- Snow occlusion on sensors;
- Interactions with vehicles having non-standard light signatures.

Neglecting these conditions leaves the system vulnerable to failure in critical real-world situations. Digital twins offer an opportunity to simulate these edge cases with high fidelity. However, this requires a rich library of scenario models and advanced simulation capabilities that are often missing or underdeveloped.

7.2. Infrastructure Requirements for Effective DT Feedback Integration

One of the key promises of DTs is the establishment of a constant feedback loop between the physical system and its digital representation. In practice, this feedback is often fragmented due to

- A lack of standardized protocols for real-time data exchange;
- Limited capabilities for collecting and synchronizing field data;
- Insufficient edge or cloud-based computing resources to process telemetry efficiently.

Without a robust and scalable digital infrastructure, the DT remains largely a static simulation model rather than a dynamic, real-time diagnostic and optimization platform. This limits its role in predictive maintenance, auto-calibration, and lifecycle performance management.

7.3. Underutilized Potential of Abstraction Layers (L0–L4)

The L0–L4 abstraction model provides a structured framework for progressive system validation, from conceptual modeling to complete system integration in real-world environments. However, its practical implementation is often inconsistent:

- L0 models are disconnected from downstream validation efforts and rarely reused.
- L1 (SiL) environments are limited to isolated logic testing, without direct traceability to requirements or outcomes at later levels.
- L3 and L4 stages are rarely implemented due to a lack of tools, data collection capabilities, or test infrastructure.

Recent studies further substantiate these findings and expand the contextual relevance of DT-based automotive validation. Eddy et al. [38] implement a digital twin for ground-vehicle predictive maintenance, integrating real telemetry, closely matching our assertion of necessary bi-directional data loops at abstraction levels L3–L4. A review in Advanced Engineering Informatics [39] emphasizes methodological requirement traceability in DT predictive maintenance systems, reaffirming our concerns regarding gaps in gate-based processes and edge-case coverage. In the area of cybersecurity, a survey in [40] outlines layered DT security challenges, offering systematic threat categorizations that align with and expand our discussion in Section 8.3. The issue that increasing connectivity of DT platforms exposes the validation environment to cybersecurity threats, such as unauthorized access and data falsification, has been notably addressed in another recent systematic review by El-Hajj et al. [41]. They analyzed 67 studies and highlighted common attack vectors, intrusion detection, spoofed telemetry, and vulnerabilities in IIoT-to-DT communication, as well as methods for ensuring data confidentiality and authentication. These findings substantiate our calls for proactive security measures, including lightweight secure communication, integrated intrusion detection, and robust encryption, even in resource-constrained validation setups.

7.4. Risk Analysis in Digital Twin-Based Validation Frameworks

The integration of DT, SiL, and HiL technologies in automotive lighting system validation introduces numerous benefits, such as accelerated development cycles, enhanced test coverage, and early defect detection. However, these advances also introduce a variety of risks that can undermine system safety, reliability, and regulatory compliance if not adequately managed. Timely identification and mitigation of these risks are critical to leverage the full potential of virtual and hybrid validation frameworks while maintaining trust in their outcomes.

There are five identified risks regarding requirement management and operational safeguards [42].

7.4.1. Risks Associated with Model Fidelity and Validation Gaps

A primary risk arises from discrepancies between digital models and their physical counterparts. Inaccurate or incomplete simulation models can lead to false confidence in system behavior, particularly for safety-critical functions such as adaptive headlamp control. These modeling errors may result from simplified or outdated environmental representations (e.g., lighting conditions, weather effects), insufficient coverage of edge cases and rare operating scenarios, and limited representation of sensor inaccuracies or hardware variability [43].

Examples are as follows:

- An adaptive headlamp system model used in a DT may simplify environmental factors such as fog density or wet road reflectivity. In a real-world scenario, the system might fail to correctly adjust beam patterns under heavy fog, causing glare to oncoming drivers. If this edge case is absent or poorly represented in the simulation, the false sense of system reliability could lead to hazardous conditions post-deployment;
- Simulation of sensor noise: If a camera sensor model does not accurately represent the noise characteristics caused by low light or dirty lenses, the system's object detection reliability may be overestimated in the virtual tests;
- Failure to model hardware aging: An LED light's luminance may degrade over time, but if the model only represents ideal initial conditions, maintenance schedules based on DT predictions may be inaccurate.

Failure to identify these gaps can cause undetected system faults, impacting vehicle safety and regulatory compliance. Rigorous model validation against empirical data and continuous model updates are necessary to minimize these risks [44].

Although it is possible to include all of these effects in high-fidelity models within the DT framework, organizations must ultimately determine an appropriate balance between the development effort and the anticipated return on investment. Beyond a certain level of complexity, further model refinement may no longer be economically justifiable.

7.4.2. Traceability and Requirement Coverage Risks

The complexity of requirements mapping across SiL, HiL, and DT environments poses risks related to incomplete or ambiguous test coverage. Insufficient traceability may lead to omission of critical functional or safety requirements during simulation, validation activities performed on outdated or unverified specifications, and misalignment between virtual test results and physical system behavior [45].

Examples include the following:

- Suppose a safety requirement mandates automatic dimming of high beams when oncoming traffic is detected at night. If this requirement is not properly linked to test cases in the HiL validation phase, the software controlling this function might be insufficiently tested, leading to failures not caught before vehicle release;
- If regulatory requirements for glare limits change late in the project, and the updated requirements are not propagated to all simulation environments, the test results may reflect outdated compliance criteria, risking certification delays or recalls.

This risk emphasizes the need for robust requirements management frameworks that maintain end-to-end traceability [46], ensuring that all requirements are systematically addressed through corresponding test cases at appropriate abstraction levels.

7.4.3. Cybersecurity Risks in Connected Digital Twins

The increasing connectivity of DT platforms exposes the validation environment to cybersecurity threats, as extensively presented in Section 8.3. Given the safety-critical nature of automotive lighting systems, such breaches could compromise validation integrity and vehicle operation; thus, embedding cybersecurity measures, such as encrypted communications, access control, and intrusion detection, is imperative [47].

Examples include the following:

- In 2023, a reported cybersecurity incident involved unauthorized access to a cloud-hosted DT environment used for vehicle software validation. Attackers manipulated

test parameters, causing false positives in safety tests that could have masked latent system defects [48];
- Injection of false telemetry data into a digital twin during operational monitoring may lead to incorrect maintenance decisions;
- Denial-of-service attacks may occur that disable remote simulation capabilities during critical validation phases.

7.4.4. Operational and Deployment Risks

Post-deployment, the DT is leveraged for continuous monitoring and predictive maintenance. However, this phase involves risks related to reliance on telemetry data quality, which may be affected by sensor failures or communication losses, model drift over time as physical system behavior deviates due to aging or environmental factors, and inadequate responsiveness of the DT to emerging fault conditions, leading to missed or late anomaly detection [49].

Examples are as follows:

- A fleet of vehicles equipped with headlamp DTs experienced a sudden drop in anomaly detection accuracy after a firmware update altered sensor calibration characteristics. The DT models, based on prior calibration data, failed to adapt promptly, delaying fault detection and potentially risking driver safety;
- Telemetry loss may occur due to poor cellular coverage during vehicle operation, resulting in gaps in DT data streams;
- Model drift caused by environmental factors such as extreme temperature variations not accounted for in the initial DT calibration may occur.

Operational risk management must include validation of telemetry integrity, adaptive model updating mechanisms, and fail-safe procedures to handle detected anomalies.

7.4.5. Risk Mitigation Strategies

Effective risk management requires a balanced combination of technical solutions and organizational practices. A multifaceted approach is necessary to ensure the safety, reliability, and compliance of automotive lighting systems across all stages of validation and deployment.

First, comprehensive validation practices must be adopted by leveraging multi-level testing. This includes a systematic combination of SiL, HiL, and physical testing methods to cross-verify results and identify discrepancies or gaps in system behavior that might not be evident in any single validation environment. This layered approach helps ensure robust coverage of both functional and safety-critical requirements.

Second, the use of advanced traceability tools is essential. Requirement management systems that are integrated with simulation and testing platforms can facilitate consistent coverage, transparent traceability, and full auditability of validation activities. Such tools support alignment between requirements, test cases, and simulation results, reducing the risk of overlooked functionalities or misaligned specifications.

Third, a cybersecurity-by-design philosophy should be embedded from the early stages of DT development. This involves integrating cybersecurity measures such as encrypted communication protocols, access control mechanisms, and intrusion detection systems in accordance with established standards like ISO/SAE 21434 and UNECE WP.29. Early incorporation of these safeguards helps protect the integrity of both virtual validation environments and deployed systems [50].

Fourth, continuous monitoring and feedback loops between the physical system and its digital twin should be established. This bi-directional data flow enables real-time tracking of system performance, early detection of deviations, and adaptive model updates. Such mechanisms are particularly important in the post-deployment phase, where operational risks due to model drift or sensor degradation must be proactively managed.

Finally, hybrid validation strategies should be implemented by balancing the efficiency of virtual testing with the realism of physical trials. While simulation offers speed and flexibility, targeted physical tests remain indispensable for validating mechanical interactions and subjective performance aspects, such as optical quality and user perception of adaptive lighting.

Examples include the following:

- A leading automotive supplier implemented a hybrid validation approach combining extensive SiL and HiL testing with periodic physical validation runs in climatic chambers simulating diverse weather conditions. This approach uncovered discrepancies in sensor response under heavy rain, which were corrected before production;
- Automated traceability tools should be deployed that alert engineers to missing test cases when requirements change;
- ISO/SAE 21434-compliant cybersecurity frameworks should be implemented to protect DT environments using multi-factor authentication and encrypted communications [51];
- Machine learning algorithms should be used to monitor telemetry data quality in real time and trigger model recalibration when deviations are detected [52].

In Table 6, a semi-quantitative assessment of key risks associated with the integration of a DT, SiL, and HiL in automotive lighting system validation is presented, which is widely used in systems engineering and model-based development for emerging validation technologies. Each risk category is evaluated based on two critical dimensions: likelihood (the probability of the risk occurring) and impact (the severity of consequences if the risk materializes). Both dimensions are scored on a numeric scale from 1 (lowest) to 5 (highest), based on a hypothetical evaluation intended to illustrate the risk management approach. The risk score, the product of likelihood and impact scores, provides an effective metric for prioritizing mitigation actions when historical failure data or quantitative probabilistic models are not available. This approach is particularly suited for hybrid SiL/HiL/DT validation environments, where conventional Failure Mode and Effects Analysis (FMEA) may be either premature or computationally impractical due to dynamic model granularity, variable abstraction layers, and evolving requirement sets. The 1–5 scale corresponds to defined bins of probability and consequence thresholds adopted from ISO 31010 [53]-aligned risk matrices. As the DT validation process matures, this framework can be extended to integrate more formalized risk estimation models. Mitigation strategies outline targeted technical and organizational measures designed to reduce the occurrence or consequences of each risk. These mitigations represent best practices and industry standards tailored to the unique challenges posed by virtual and hybrid validation environments.

High-risk areas such as model fidelity and cybersecurity require proactive management strategies, including rigorous model validation, continuous synchronization, and robust security protocols. Medium-risk categories underscore the need for integrated requirements management and operational safeguards. By quantitatively prioritizing risks, this approach supports the development of targeted mitigation plans, enhancing the safety, reliability, and regulatory compliance of automotive lighting systems validated via DT, SiL, and HiL technologies.

Table 6. Categorization and management of risks in digital twin implementation.

Risk Category	Likelihood (1–5)	Impact (1–5)	Risk Score (L × I)	Risk Level	Mitigation Strategies
Model fidelity and validation gaps	3	5	15	High	Rigorous model validation with empirical data; continuous model updates; extensive coverage of edge cases and scenarios
Traceability and requirement coverage	3	3	9	Medium	Robust requirements management systems; maintain end-to-end traceability; automated test mapping
Cybersecurity in connected DTs	3	5	15	high	Cybersecurity-by-design; encrypted communications; access control; intrusion detection aligned with ISO/SAE 21434
Operational and deployment risks	4	3	12	Medium-high	Validate telemetry data integrity; adaptive model updating; fail-safe procedures for anomaly detection
Risk mitigation strategy effectiveness	2	4	8	Medium	Continuous process improvement; regular audits; integration of cross-functional teams to enforce mitigation adherence

8. Application Challenges and Strategic Directions for Digital Twin Integration

The increasing complexity of automotive systems and the transition toward model-based development paradigms have catalyzed the use of DT technology across engineering workflows [54,55]. In the context of headlamp system validation, DTs offer simulation-based platforms that complement SiL and HiL testing [19] by enabling continuous integration, scenario-driven validation, and early design verification. However, the general adoption of DTs in industrial settings is limited by a combination of technical, organizational, and regulatory barriers [51,56].

This section explores the current limitations of DT integration. It outlines strategic directions that aim to address these barriers, thereby facilitating the scalable deployment of DT frameworks across the automotive lifecycle.

8.1. Practical Scope of Digital Twin Utilization in Automotive Development

Digital twin technology has the potential to support multiple functions across the design–validation–deployment continuum:

- In early development, DTs can be used for virtual prototyping and functional modeling, enabling engineers to explore design alternatives without physical prototypes;
- During the SiL and HiL stages, DTs support real-time simulation of hardware–software interactions, augmenting traditional test platforms through model-driven fault injection, scenario orchestration, and predictive behavior analysis;
- In the post-deployment phase, DTs allow for continuous monitoring, performance analytics, and remote diagnostic capabilities. By leveraging vehicle telemetry, they support condition-based maintenance, dynamic calibration, and long-term operational optimization.

Beyond these stages, DTs may also be used in

- Manufacturing process validation by modeling assembly line behavior and tolerances;
- Fleet-level analysis by aggregating DT data across vehicle populations to identify systemic reliability trends;
- Human-in-the-loop simulation by reproducing user inputs and their impact on vehicle systems.

While these use cases are technically feasible, integration across the entire lifecycle remains uncommon, primarily due to ecosystem fragmentation and resource constraints.

8.2. Barriers to Deployment: Organizational, Technical, and Cultural Factors

8.2.1. Skills Gap and Organizational Resistance

A significant obstacle to the deployment of DTs is the shortage of interdisciplinary expertise. Effective DT integration requires the convergence of systems engineering, embedded software, real-time simulation, and cybersecurity—disciplines that are often separated within traditional automotive organizations.

Moreover, development teams often show inertia toward replacing well-established test procedures with simulation-driven workflows, especially for safety-critical systems. This highlights the need to establish dedicated DT specialists with cross-domain proficiency in model integration, physical-to-virtual synchronization, and secure data handling.

Organizational resistance may also stem from perceived risks related to the reliance on virtual models over physical validation. Overcoming this challenge requires the establishment of robust test traceability, quantitative validation metrics, and continuous alignment between DT predictions and empirical outcomes.

8.2.2. Tool Fragmentation and Lack of Standardization

Digital twin integration is further complicated by the heterogeneity of simulation tools and the lack of standardized modeling formats [8]. Inconsistent model exchange formats, time synchronization mechanisms, and interface semantics impede interoperability between tools used in SiL, HiL, and DT workflows.

Despite efforts by standardization bodies, such as AUTOSAR, ASAM, and the Modelica Association [57,58], practical interoperability remains limited. Test artifacts developed in SiL environments often cannot be reused seamlessly in HiL or DT settings, which leads to redundant engineering effort and reduced efficiency in regression testing and requirement verification.

8.3. Cybersecurity Considerations for Connected Digital Twins

As DTs increasingly operate in connected environments—integrated with in-vehicle networks, cloud-based analytics platforms, and over-the-air (OTA) update systems—they introduce a new class of cybersecurity risks. These include

- Data spoofing attacks, where manipulated sensor inputs are injected into the DT, leading to invalid conclusions or inappropriate responses;
- Model leakage and IP theft, as adversaries could reverse-engineer simulation models or extract system parameters through observation of DT outputs;
- Attacker training, as attackers could practice and evaluate attacks virtually with little risk of detection;
- Unauthorized access to test interfaces, which potentially compromises the integrity of the test environment or allowing command injection into safety-critical systems.

These risks necessitate a cybersecurity-first approach to digital transformation (DT) architecture. To mitigate vulnerabilities, future DT platforms should implement

- Encrypted communication protocols to safeguard data exchange between components and external systems;
- Isolated model execution sandboxes to prevent cross-domain interference;
- Secure and restricted interface layers to limit access strictly to authenticated and validated simulation APIs.

These risks underscore the importance of embedded emerging automotive cybersecurity regulations, such as ISO/SAE 21434 [51], into DT lifecycle management and test documentation practices. Aligning DT architectural practices with these standards ensures compliance with both industry expectations and related regulations, such as UNECE R.155 [52], which mandates certification of cybersecurity management systems for type approval.

8.4. Strategic Directions for Scalable DT Integration

8.4.1. Role Specialization and Workflow Integration

To achieve scalable DT deployment, responsibilities across the development team must be clearly defined:

- System architects must design DT specifications aligned with functional and non-functional system requirements;
- Simulation engineers must be tasked with building high-fidelity models and managing physical–virtual synchronization;
- Cybersecurity engineers must evaluate threat surfaces and embed protections at both interface and model levels;
- Validation experts must translate real-world scenarios into reproducible simulation-based test cases and verify requirement coverage.

Such role-based structuring allows for modular development and efficient lifecycle management of the DT environment [59].

8.4.2. DT-Driven Certification and Homologation

One of the most transformative directions for DT is its potential use in regulatory compliance. By digitally signing simulation results and ensuring a version-controlled traceability of test cases, DTs could become part of certification dossiers [54]. This would reduce the physical testing burden while improving repeatability and auditability of functional safety evaluations.

Simulation-based certification is particularly promising for

- Adaptive headlight performance under variable weather conditions;
- Failure mode validation in redundant lighting architectures;
- System behavior in pre-defined regulatory scenarios.

8.4.3. Cloud-Based Digital Twin-as-a-Service (DTaaS)

The advancement of cloud-native automotive architectures has paved the way for digital twin-as-a-service (DTaaS) solutions that align with modern vehicle development workflows. Within these frameworks, digital twin instances can be deployed dynamically in secure cloud containers to support scalable simulation and validation tasks. Simulation workloads are distributed across OEMs, enabling seamless collaboration throughout the supply chain. Centralized repositories ensure version control and traceability of test results, promoting consistency across development stages and supporting compliance with functional safety and cybersecurity standards [60–62].

This DTaaS model fosters collaboration, promotes traceable development practices, and aligns with agile methodologies, including continuous integration and deployment (CI/CD) pipelines. Its advantages have translated into significant real-world benefits. Automotive manufacturers have integrated DTaaS into R&D and supply chain operations, leveraging virtual prototyping to reduce vehicle development cycles by 30%. A major Swedish electric vehicle OEM reported a 40% reduction in battery testing costs through DTaaS-based thermal behavior simulations under extreme conditions [63]. Over 60% of automotive companies now prefer per-use pricing for DTaaS in production line optimization, avoiding fixed costs amid seasonal demand fluctuations. However, this shift to flexible pricing and scalable deployment does not eliminate barriers, especially for smaller enterprises. Small and Medium Enterprises (SMEs) continue to face prohibitive upfront costs. For instance, a German automotive parts supplier terminated its DTaaS pilot upon discovering a USD 120,000 platform setup cost—nearly 15% of its annual IT budget—making it economically unjustifiable [64].

8.4.4. Toward a Hybrid Validation Strategy: Blending Virtual and Physical Testing

Although DTs substantially reduce the need for physical prototyping, some validation tasks remain inherently physical [29]. These include

- Visual comfort assessments, such as perceived glare or light tone consistency;
- Mechanical durability and mounting stress validation;
- Electromagnetic compatibility (EMC) and cross-interference testing;
- Subjective user acceptance testing under real driving conditions.

Rather than viewing physical and virtual validation as competing paradigms, the future of automotive testing lies in a hybrid strategy that integrates

- The use of DTs to reduce prototype cycles and optimize test parameters;
- Selective validation of edge-case findings through physical test rigs;

- The establishment of bi-directional feedback loops from real-world usage into DT updates.

A hybrid validation strategy, integrating both DTs and physical testing, is pivotal in advancing automotive development. This approach leverages the scalability and efficiency of virtual simulations alongside the fidelity and assurance provided by real-world testing, ensuring comprehensive validation across the vehicle lifecycle. Digital twins facilitate early-stage validation by enabling high-fidelity simulations of vehicle systems, allowing engineers to test a multitude of scenarios in a controlled virtual environment. Given the example of a major Nordic OEM [65], its autonomous solution employs a closed-loop simulation setup where control signals are directed to both real trucks and their digital twins. This method, encompassing SiL and HiL testing, allows for the detection of software and hardware integration issues, latency effects, and timing bugs before physical deployment. However, certain aspects of vehicle performance, such as visual comfort, mechanical durability, and electromagnetic compatibility, necessitate physical validation. These real-world tests ensure that the vehicle meets safety standards and user expectations. By focusing physical testing on these critical areas, manufacturers can optimize resource allocation and reduce costs. The integration of virtual and physical testing also supports regulatory compliance. Combined documentation from both approaches provides a comprehensive audit trail, facilitating traceability and reproducibility, which are important in meeting stringent safety and environmental standards. Moreover, the continuous feedback loop between virtual simulations and physical tests allows for the refinement of digital models. Incorporating real-world data into digital twins enhances their accuracy, leading to more reliable predictions and improved vehicle performance over time.

In summary, this section presents key strategic avenues for scaling DT integration in automotive development. These include clear role specialization across interdisciplinary teams, simulation-based certification workflows aligned with evolving safety regulations, the adoption of cloud-based DTaaS models for scalable collaboration, and hybrid validation strategies that blend virtual and physical testing. Addressing current barriers—such as cybersecurity risks, toolchain fragmentation, and organizational resistance—will be critical to realizing the full potential of DTs across all development stages.

Ultimately, a hybrid validation strategy that combines the scalability and speed of digital twins with the assurance and realism of physical testing offers a balanced path forward. This dual approach enhances the efficiency, adaptability, and overall quality of modern automotive systems.

9. Strategic Outlook for Next Generation Validation Systems and Research Direction

The integration of DT, SiL, and HiL technologies marks a pivotal shift in the evolution of automotive system validation. As embedded systems become more complex and regulatory demands increase in terms of traceability and functional safety, traditional validation workflows—based on sequential prototyping and isolated test benches—are rapidly reaching their limits.

Next-generation validation environments must support distributed, parallel, and multidisciplinary development processes. SiL and HiL components, together with DT services, must operate as orchestrated subsystems within a unified architecture. There is a growing need for scalable simulation platforms that are capable of real-time synchronization, modular deployment, and remote co-simulation, enabling OEMs and suppliers to collaborate effectively without relying on localized physical setups.

To unlock the full potential of DTs in industrial and regulatory contexts, validation artifacts must evolve into certifiable assets. Simulation outputs, test cases, and model configurations should be version-controlled, digitally signed, and aligned with safety standards such as ISO 26262 and ISO/SAE 21434. This transition requires the implementation of formal model verification workflows, traceability tools, and simulation-driven homologation processes. Certification bodies must also adapt to simulation-first validation pipelines, particularly for systems that undergo frequent updates.

Looking beyond development environments, digital twins are expected to function as real-time operational mirrors, continuously fed with vehicle telemetry. This capability would enable predictive maintenance, adaptive headlamp calibration, and in-service anomaly detection. Such feedback mechanisms demand secure cloud infrastructure, high-fidelity sensor emulation, and real-time data pipelines that minimize divergence between virtual and physical system states.

Despite strong progress in technical validation, current DT frameworks still struggle to address subjective and perceptual performance criteria, such as visual comfort, glare perception, and driver behavior under dynamic lighting conditions. These aspects are naturally difficult to simulate and often require human-in-the-loop feedback, experimental studies, or VR/AR-based testbeds. Future research should explore how these perceptual and behavioral dimensions can be embedded into simulation workflows to extend validation coverage beyond purely functional metrics.

Several cross-cutting priorities also emerge: the adoption of open modeling standards (e.g., ASAM XIL, Modelica, FMI) to ensure toolchain interoperability; the use of AI-augmented testing to generate edge-case scenarios and uncover non-obvious failure modes; and the integration of cybersecurity validation, embedding threat simulations, anomaly detection, and secure interface testing into the DT framework.

By consolidating these directions into a coherent and forward-looking approach, validation shifts from being a final quality gate to becoming a continuous, intelligent, and predictive process embedded throughout the product lifecycle. This paradigm lays the groundwork for a new era in automotive engineering, where systems are not only tested for compliance but designed for resilience, adaptability, and long-term performance.

10. Conclusions and Future Work

This paper proposes an integrated validation framework that combines digital twin, Software-in-the-Loop, and Hardware-in-the-Loop technologies, specifically tailored for automotive headlamp systems. The study contributes a layered architecture model, a structured requirement-to-validation traceability approach, and scenario-based validation examples that align with industry practices and standards.

The framework emphasizes the transition from fragmented test stages to a unified validation pipeline that supports predictive, modular, and simulation-driven engineering. The use of conceptual validation chains and synthetic examples illustrates the practical relevance of the approach, even in the absence of physical prototyping.

However, the study has several limitations. First, it does not include empirical implementation results or a full pilot case study. The validation scenarios are demonstrative, although grounded in realistic automotive challenges. Furthermore, the evaluation does not yet cover subjective metrics, such as visual comfort or real-time driver feedback, which are increasingly important in lighting system performance.

Future research should focus on implementing the proposed framework within an industrial development project, allowing for quantitative performance assessment and real-world system integration. Additionally, research should explore the inclusion of human-in-the-loop simulations, cognitive feedback, and AI-assisted edge case generation. These extensions will help refine digital twin-based validation workflows into operationally relevant tools for both OEMs and regulatory stakeholders.

Author Contributions: Conceptualization, G.B., P.N. and E.S.; methodology, G.B., P.N. and E.S.; software, G.B. and E.S.; validation, E.R.Z. and A.S.; formal analysis, G.B.; investigation, G.B., P.N. and E.S.; resources, G.B., P.N. and E.R.Z.; data curation, E.S.; writing—original draft preparation, G.B. and E.S.; writing—review and editing, G.B., P.N., E.R.Z., E.S., D.-D.L. and A.S.; visualization, D.-D.L.; supervision, D.-D.L.; project administration, A.S.; funding acquisition, A.S. All authors have read and agreed to the published version of the manuscript.

Funding: This research paper was supported by the "Boosting Ingenium for Excellence" (BI4E) project, funded by the European Union's HORIZON–WIDERA–2021–ACCESS–05–01–European Excellence Initiative under the Grant Agreement No. 101071321.

Data Availability Statement: Not applicable.

Conflicts of Interest: The authors declare no conflicts of interest.

References

1. *ISO 26262-1:2018*; Road Vehicles—Functional Safety—Part 1: Vocabulary. ISO: Geneva, Switzerland, 2018.
2. Zhao, W.; Gong, S.; Zhao, D.; Liu, F.; Sze, N.N.; Quddus, M.; Huang, H. Developing a New Integrated Advanced Driver Assistance System in a Connected Vehicle Environment. *Expert Syst. Appl.* **2024**, *238*, 121733. [CrossRef]
3. Matinnejad, R.; Nejati, S.; Briand, L.; Bruckmann, T.; Poull, C. Search-Based Automated Testing of Continuous Controllers: Framework, Tool Support, and Case Studies. *Inf. Softw. Technol.* **2015**, *57*, 705–722. [CrossRef]
4. Patnaik, P.D.R.; Gengaje, S.R. A Systematic Review of Hardware-in-The-Loop (HiL) Frameworks for Internet of Things Applications. *Grenze Int. J. Eng. Technol.* **2024**, *1*, 1120–1127.
5. King, P.J.; Copp, D.G. Hardware in the Loop for Automotive Vehicle Control Systems Development and Testing. *Meas. Control* **2006**, *39*, 19–23. [CrossRef]
6. Joshi, A. An SAE deep dive. In *Automotive Applications of Hardware-in-the-Loop (HIL) Simulation*; SAE International: Warrendale, PA, USA, 2020; ISBN 978-1-4686-0003-2.
7. Zahediyami, M.; Gorecki, S.; Traoré, M.K. Software Testing Approach for Digital Twin Verification and Validation. In *IFIP Advances in Information and Communication Technology*; Springer Nature Switzerland: Cham, Switzerland, 2024; pp. 115–129, ISBN 978-3-031-71742-0.
8. Zhuang, C.; Liu, J.; Xiong, H. Digital Twin-Based Smart Production Management and Control Framework for the Complex Product Assembly Shop-Floor. *Int. J. Adv. Manuf. Technol.* **2018**, *96*, 1149–1163. [CrossRef]
9. Abboush, M.; Knieke, C.; Rausch, A. A Virtual Testing Framework for Real-Time Validation of Automotive Software Systems Based on Hardware in the Loop and Fault Injection. *Sensors* **2024**, *24*, 3733. [CrossRef]
10. Rosa, L.H.L.; Meschini Almeida, C.F.; De Souza Pereira, D.; Kagan, N. A Systemic Approach for Assessment of Advanced Distribution Automation Functionalities. *IEEE Trans. Power Deliv.* **2019**, *34*, 2008–2017. [CrossRef]
11. Qamsane, Y.; Phillips, J.R.; Savaglio, C.; Warner, D.; James, S.C.; Barton, K. Open Process Automation- and Digital Twin-Based Performance Monitoring of a Process Manufacturing System. *IEEE Access* **2022**, *10*, 60823–60835. [CrossRef]
12. Villegas, L.F.; Macchi, M.; Polenghi, A. Conceptualization of a Platform Architecture for the Rapid Development of Digital Twins in Manufacturing. In Proceedings of the XXIX SUMMER SCHOOL "Francesco Turco"—Industrial Systems Engineering, Lecce, Italy, 10–12 September 2025; Politecnico di Milano: Milan, Italy, 2024.
13. Bowman, D.; Dwyer, L.; Levers, A.; Patterson, E.A.; Purdie, S.; Vikhorev, K. A Unified Approach to Digital Twin Architecture-Proof-of-Concept Activity in the Nuclear Sector. *IEEE Access* **2022**, *10*, 44691–44709. [CrossRef]
14. Stetter, R.; Grüble, T.; Till, M. Geometric and Kinetic Digital Twin of a Body-in-White Assembly System for Virtual Commissioning. *Procedia CIRP* **2023**, *119*, 109–114. [CrossRef]
15. Guo, Y.; Klink, A.; Bartolo, P.; Guo, W.G. Digital Twins for Electro-Physical, Chemical, and Photonic Processes. *CIRP Ann.* **2023**, *72*, 593–619. [CrossRef]
16. Mazza, A.; Benedetto, G.; Pons, E.; Bompard, E.; Paola, A.D.; Thomas, D.; Kotsakis, E.; Fulli, G.; Vogel, S.; Gil, A.A.; et al. On the Model Flexibility of the Geographical Distributed Real-Time Co-Simulation: The Example of ENET-RT Lab. *Sustain. Energy Grids Netw.* **2024**, *40*, 101501. [CrossRef]
17. Sai, A.M.V.V.; Wang, C.; Cai, Z.; Li, Y. Navigating the Digital Twin Network Landscape: A Survey on Architecture, Applications, Privacy and Security. *High-Confid. Comput.* **2024**, *4*, 100269. [CrossRef]
18. Martin, G.; Poppe, A.; Schöps, S.; Kraker, E.; Marty, C.; Soer, W.; Yu, J. AI-TWILIGHT: AI-Digital TWIn for LIGHTing—A New European Project. In Proceedings of the 2021 27th International Workshop on Thermal Investigations of ICs and Systems (THERMINIC), Berlin, Germany, 23 September 2021; pp. 1–6.

19. Dawid, A.; Buchwald, P. The System of Headlights Operation Recognition Using the Digital Twin Method. *Int. J. Electron. Telecommun.* **2024**, *70*, 51–58. [CrossRef]
20. Martínez-Pérez, J.R.; Carvajal, M.A.; Santaella, J.J.; López-Ruiz, N.; Escobedo, P.; Martínez-Olmos, A. Advanced Detection of Failed LEDs in a Short Circuit for Automotive Lighting Applications. *Sensors* **2024**, *24*, 2802. [CrossRef] [PubMed]
21. Barbie, A.; Hasselbring, W. Embedded Software Development with Digital Twins: Specific Requirements for Small and Medium-Sized Enterprises. In Proceedings of the 2023 IEEE Smart World Congress (SWC), Portsmouth, UK, 28–31 August 2023; IEEE: Portsmouth, UK, 2023; pp. 1–6.
22. Singh, S.; Shehab, E.; Higgins, N.; Fowler, K.; Tomiyama, T.; Fowler, C. Challenges of Digital Twin in High Value Manufacturing. In Proceedings of the SAE International—Aerospace Systems and Technology Conference 2018, London, UK, 30 October 2018.
23. Himmler, A.; Lamberg, K.; Beine, M. Hardware-in-the-Loop Testing in the Context of ISO 26262. In Proceedings of the SAE 2012 World Congress & Exhibition, Detroit, MI, USA, 24–26 April 2012; SAE International: Warrendale, PA, USA, 2012.
24. Katzorke, N.; Vinçon, C.; Kolar, P.; Lasi, H. Fields of Interest and Demands for a Digital Proving Ground Twin. *Transp. Res. Interdiscip. Perspect.* **2023**, *18*, 100782. [CrossRef]
25. Zhang, J.; Ellwein, C.; Heithoff, M.; Michael, J.; Wortmann, A. Digital Twin and the Asset Administration Shell: An Analysis of the Three Types of AASs and Their Feasibility for Digital Twin Engineering. *Softw. Syst. Model.* **2025**, *24*, 771–793. [CrossRef]
26. Sakin, S.A.; Isaacs, K.E. A Literature-Based Visualization Task Taxonomy for Gantt Charts. In Proceedings of the 2024 IEEE Visualization and Visual Analytics (VIS), Tampa Bay, FL, USA, 13–18 October 2024; IEEE: St. Pete Beach, FL, USA, 2024; pp. 236–240.
27. Gai, P.; Urbina, M.; Guidieri, E.; Serano, G.; Serreli, N. AUTOSAR University Package Classic Platform. In Proceedings of the 2022 IEEE 27th International Conference on Emerging Technologies and Factory Automation (ETFA), Stuttgart, Germany, 6–9 September 2022; IEEE: Stuttgart, Germany, 2022; pp. 1–4.
28. Bo, H.; Hui, D.; Dafang, W.; Guifan, Z. Basic Concepts on AUTOSAR Development. In Proceedings of the 2010 International Conference on Intelligent Computation Technology and Automation, Changsha, China, 11–12 May 2010; IEEE: Changsha, China, 2010; pp. 871–873.
29. Park, G.; Ku, D.; Lee, S.; Won, W.-J.; Jung, W. Test Methods of the AUTOSAR Application Software Components. In Proceedings of the 2009 ICCAS-SICE, Fukuoka, Japan, 18–21 August 2009; pp. 2601–2606.
30. Yadav, V.; Bhade, N. Implementation of a Hybrid Hardware-in-the-Loop (HIL) Test System for Automotive Software Validation and Verification. In Proceedings of the SAE Technical Paper Series, New Delhi, India, 11–13 December 2024; SAE International: New Delhi, India, 2024; Volume 1.
31. Kang, H.A.; Lim, J.H. The Integration of Multiple Test Benches for Functional Verification of the Cooperative ADAS. In Proceedings of the 2020 IEEE 92nd Vehicular Technology Conference (VTC2020-Fall), Victoria, BC, Canada, 4–7 October 2020; IEEE: Victoria, BC, Canada, 2020; pp. 1–7.
32. Xie, F.; McEntee, C.; Zhang, M.; Lu, N.; Ke, X.; Vallem, M.R.; Samaan, N. Networked HIL Simulation System for Modeling Large-Scale Power Systems. In Proceedings of the 2020 52nd North American Power Symposium (NAPS), Tempe, AZ, USA, 11–13 April 2021; IEEE: Tempe, AZ, USA, 2021; pp. 1–6.
33. Dobrescu, R.; Chenaru, O.; Florea, G.; Geampalia, G.; Mocanu, S. Hardware-in-Loop Assessment of Control Architectures. In Proceedings of the 2020 24th International Conference on System Theory, Control and Computing (ICSTCC), Sinaia, Romania, 8–10 October 2020; IEEE: Sinaia, Romania, 2020; pp. 880–885.
34. Dawid, A.; Buchwald, P.; Pawlak, B. The Digital Twin to Train a Neural Network Detecting Headlamps Failure of Motor Vehicles. In Proceedings of the Dependable Computer Systems and Networks, Brunów, Poland, 3–7 July 2023; Zamojski, W., Mazurkiewicz, J., Sugier, J., Walkowiak, T., Kacprzyk, J., Eds.; Springer Nature Switzerland: Cham, Switzerland, 2023; pp. 29–38.
35. Stankov, I.; Stefanova-Stoyanova, V. Digital Twin Management Systems—Challenges, Application, Development. In Proceedings of the 2023 31st National Conference with International Participation (^{TEL}ECOM), Sofia, Bulgaria, 16–17 November 2023; IEEE: New York, NY, USA, 2024. [CrossRef]
36. Boschert, S.; Rosen, R. The Industry Use Cases for the Digital Twin Idea. *Adv. Comput.* **2020**, *117*, 79–105.
37. Li, L.F.; Yang, M.J.; Zhang, J.Y. Research on the Control Method of Bending Mode of AFS System Based on Preview Control. *AMM* **2014**, *651–653*, 844–849. [CrossRef]
38. Eddy, C.; Castanier, M.; Wagner, J. Predictive Maintenance of a Ground Vehicle Using Digital Twin Technology. *SAE Int. J. Adv. Curr. Prac. Mobil.* **2025**, *7*, 865–876.
39. Ma, S.; Flanigan, K.A.; Bergés, M. State-of-the-Art Review and Synthesis: A Requirement-Based Roadmap for Standardized Predictive Maintenance Automation Using Digital Twin Technologies. *Adv. Eng. Inform.* **2024**, *62*, 102800. [CrossRef]
40. Jeremiah, S.R.; Azzaoui, A.E.; Xiong, N.N.; Park, J.H. A Comprehensive Survey of Digital Twins: Applications, Technologies and Security Challenges. *J. Syst. Archit.* **2024**, *151*, 103120. [CrossRef]
41. El-Hajj, M.; Itäpelto, T.; Gebremariam, T. Systematic Literature Review: Digital Twins' Role in Enhancing Security for Industry 4.0 Applications. *Secur. Priv.* **2024**, *7*, e396. [CrossRef]

42. University of Jordan; Otoom, S. Risk Auditing for Digital Twins in Cyber Physical Systems: A Systematic Review. *JCSRA* **2025**, *2025*, 22–35. [CrossRef]
43. Nuruzzaman, M. Automotive System Reliability and Technological Convergence: A Review of Smart Powertrain and Mechatronic Diagnostics. *SSRN J.* **2025**, *4*, 175–201. [CrossRef]
44. Ali, W.A.; Fanti, M.P.; Roccotelli, M.; Ranieri, L. A Review of Digital Twin Technology for Electric and Autonomous Vehicles. *Appl. Sci.* **2023**, *13*, 5871. [CrossRef]
45. Kernschmidt, K.E.T. Interdisciplinary Structural Modeling of Mechatronic Production Systems Using SysML4Mechatronics. Ph.D. Thesis, Technische Universität München, Munich, Germany, 2019.
46. Rasheed, A.; San, O.; Kvamsdal, T. Digital Twin: Values, Challenges and Enablers From a Modeling Perspective. *IEEE Access* **2020**, *8*, 21980–22012. [CrossRef]
47. Kołaczek, G. Internet of Things (IoT) Technologies in Cybersecurity: Challenges and Opportunities. *Appl. Sci.* **2025**, *15*, 2935. [CrossRef]
48. Durlik, I.; Miller, T.; Kostecka, E.; Zwierzewicz, Z.; Łobodzińska, A. Cybersecurity in Autonomous Vehicles—Are We Ready for the Challenge? *Electronics* **2024**, *13*, 2654. [CrossRef]
49. Astarita, V.; Guido, G.; Haghshenas, S.S.; Haghshenas, S.S. Risk Reduction in Transportation Systems: The Role of Digital Twins According to a Bibliometric-Based Literature Review. *Sustainability* **2024**, *16*, 3212. [CrossRef]
50. Liu, H.; Zhang, B.; Wu, V.; Yang, X.; Wang, L. Review of Digital Twin in the Automotive Industry on Products, Processes and Systems. *Int. J. Automot. Manuf. Mater.* **2025**, *4*, 6. [CrossRef]
51. *ISO/SAE 21434:2021*; Road Vehicles—Cybersecurity Engineering. International Organization for Standardization (ISO): Geneva, Switzerland; SAE International: Warrendale, PA, USA, 2021.
52. *UN Regulation No. 155*; Cybersecurity and Cybersecurity Management System. United Nations Economic Commission for Europe (UNECE): Geneva, Switzerland, 2021.
53. *ISO 31010*; Risk Management—Risk Assessment Techniques. ISO: Geneva, Switzerland, 2019.
54. Lu, Y.; Liu, C.; Wang, K.I.-K.; Huang, H.; Xu, X. Digital Twin-Driven Smart Manufacturing: Connotation, Reference Model, Applications and Research Issues. *Robot. Comput. -Integr. Manuf.* **2020**, *61*, 101837. [CrossRef]
55. Boschert, S.; Rosen, R. Digital Twin—The Simulation Aspect. In *Mechatronic Futures: Challenges and Solutions for Mechatronic Systems and their Designers*; Hehenberger, P., Bradley, D., Eds.; Springer International Publishing: Cham, Switzerland, 2016; pp. 59–74, ISBN 978-3-319-32156-1.
56. Sridhar, S.; Hahn, A.; Govindarasu, M. Cyber–Physical System Security for the Electric Power Grid. *Proc. IEEE* **2012**, *100*, 210–224. [CrossRef]
57. AUTOSAR. AUTOSAR Adaptive Platform Specifications, Release 24-11. 2024. Available online: https://www.autosar.org/fileadmin/standards/R24-11/AP/AUTOSAR_AP_EXP_SWArchitecture.pdf (accessed on 25 June 2025).
58. ASAM—Association for Standardization of Automation and Measuring Systems XIL API Standard 2020. Available online: https://www.asam.net/standards/detail/xil/ (accessed on 25 June 2025).
59. Fuller, A.; Fan, Z.; Day, C.; Barlow, C. Digital Twin: Enabling Technologies, Challenges and Open Research. *IEEE Access* **2020**, *8*, 108952–108971. [CrossRef]
60. Lenhart, P.; Arndt, P.; von Wedel, J.; Beul, C.; Weldert, J. *Challenges in Integrating Cybersecurity into Existing Development Processes*; SAE Technical Paper 2020-01-0144; SAE International: Warrendale, PA, USA, 2020. [CrossRef]
61. Schluse, M.; Rossmann, J. From Simulation to Experimentable Digital Twins: Simulation-Based Development and Operation of Complex Technical Systems. In Proceedings of the 2016 IEEE International Symposium on Systems Engineering (ISSE), Edinburgh, Scotland, 3–5 October 2016; IEEE: Edinburgh, UK, 2016.
62. Liu, R.; Kothuru, A.; Zhang, S. Calibration-Based Tool Condition Monitoring for Repetitive Machining Operations. *J. Manuf. Syst.* **2020**, *54*, 285–293. [CrossRef]
63. Keysight Technologies. EP1150A PathWave Lab Operations for Battery Test. 2025. Available online: https://www.keysight.com/us/en/assets/3120-1059/data-sheets/PathWave-Lab-Operations-for-Battery-Test.pdf (accessed on 25 July 2025).
64. MarketResearch.com. The Digital Twin Market: Shaping the Future of Industry 4.0. 2024. Available online: https://blog.marketresearch.com/the-digital-twin-market-shaping-the-future-of-industry-4.0 (accessed on 25 July 2025).
65. Zhang, Y. Digital Twins: The Ultimate Virtual Proving Ground. 2025. Available online: https://www.volvoautonomoussolutions.com/en-en/news-and-insights/insights/articles/2025/jun/digital-twins{-}{-}the-ultimate-virtual-proving-ground.html (accessed on 25 July 2025).

energies

Article

Factors Influencing the Energy Consumption in a Building: Comparative Study between Two Different Climates

Abdoul-Razak Ali-Tagba [1,2], Mazabalo Baneto [1,2,*] and Dumitru Dorin Lucache [3]

1 Centre d'Excellence Régional pour la Maîtrise de l'Electricité (CERME), Université de Lomé, 01BP1515 Lome, Togo; razahkalitagba@gmail.com
2 Département de Physique, Laboratoire sur l'Energie Solaire, Université de Lomé, 01BP1515 Lome, Togo
3 Faculty of Electrical Engineering, "Gheorghe Asachi" Technical University of Iaşi, 700050 Iasi, Romania; dumitru-dorin.lucache@academic.tuiasi.ro
* Correspondence: banetopaul@gmail.com; Tel.: +228-90-31-58-37

Abstract: The design of a high energy performance building requires an assessment of the various design options. Energy simulation offers interesting possibilities for clarifying the architect's decisions at this level, especially in the initial design phases where the greatest opportunities for optimization lie. The aim of this work is to develop an approach for the evaluation and optimal use of energy simulation in the building design phases. To do this, EnergyPlus building simulation software was used to simulate the energy consumption of the Faculty of Electrical Engineering building at "Gheorghe Asachi" Technical University in Iasi, in order to identify the factors influencing energy consumption in buildings. The results of this study show that an increase in the cooling setpoint temperature from 22 °C to 28 °C in the roof construction can reduce operating temperatures by 14.2% and 20.0%, respectively. This optimization could significantly reduce the hours of thermal discomfort, in a ratio of 6.0 and 3.25, respectively. Consequently, optimizing parameters linked to design and the heating and cooling systems within the building makes it possible to achieve energy savings and ensure thermal comfort in buildings.

Keywords: energy simulation; building design; influence factors; passive strategies; energy performance

Citation: Ali-Tagba, A.-R.; Baneto, M.; Lucache, D.D. Factors Influencing the Energy Consumption in a Building: Comparative Study between Two Different Climates. *Energies* **2024**, *17*, 4041. https://doi.org/10.3390/en17164041

Academic Editor: Christian Inard

Received: 16 May 2024
Revised: 16 July 2024
Accepted: 22 July 2024
Published: 15 August 2024

1. Introduction

Environmentally friendly building architecture helps to minimize the impact of construction on the environment. This may include using sustainable materials, reducing construction waste, optimizing energy efficiency and minimizing greenhouse gas emissions. Technical and architectural choices impact not only the daily lives of users, but also the future of the planet: the building sector alone currently contributes 37% of greenhouse gas emissions linked to energy and operational processes and accounts for more than a fifth of global emissions [1].

In recent decades, mitigation measures have been gradually put in place to encourage the design of more eco-sensitive buildings, among other things in terms of energy efficiency. These measures have resulted in numerical objectives, marking the evolution of more ecological construction materials and more efficient systems. However, these have not yet been of much help in the search for an efficient architecture, which, according to studies by [2,3], is relative to the methods by which the building is designed.

Building with performance in mind requires a holistic approach, for which the energy question is important in this study. However, this approach is not always obvious if the design process is linear. The literature also mentions that it is possible to achieve substantial energy savings if the architect relies on passive strategies in his concept. Consideration of this aspect, according to studies by Optis et al. [4], is important, since a large part of energy consumption (nearly 65%) is in the operating phase. It is worth mentioning that, in mechanics, ASHRAE (American Society of Heating, Refrigerating and Air- Conditioning

Engineers) constitutes a good database for engineers. However, ASHRAE needs to be improved concerning electrical and architectural design.

With this in mind, energy simulation offers interesting possibilities for clarifying the architect's decisions and thus achieving performance objectives in terms of energy efficiency in buildings. Thus, in this work, the energy simulation software for buildings EnergyPlus was used to simulate the energy consumption of the Faculty of Electrical Engineering building at the "Gheorghe Asachi" Technical University of Iasi, in order to identify factors influencing energy consumption in buildings.

This study aims to identify the parameters influencing energy consumption and to develop a methodological approach to the problem of integrating energy simulation at the start of the process of design and then the use of the building, within the framework of an architecture targeting a passive strategy to achieve energy performance objectives. This will involve evaluating and maximizing the energy performance of a building by opting for passive approaches.

2. Materials and Methods

The objective of this work is to analyze the performance of a building of "Gheorghe Asachi" Technical University simulated through a space of complete parameters, by estimating the energy consumption of the space based on its design. Particular attention was paid to occupancy rate, electrical equipment and lighting, as these are the loads most controllable by residents. Below, the overall approach to the modeling process is described: the occupancy estimation tool, including data; ASHRAE standards [5]; the prototype-building model; and standards compliance using OpenStudio Standards.

2.1. Theoretical Approach

Figure 1 illustrates the energy optimization technique in the traditional mode presented in this work. This corresponds to the approach described in the literature [6,7], and to current practices deduced from case studies [8].

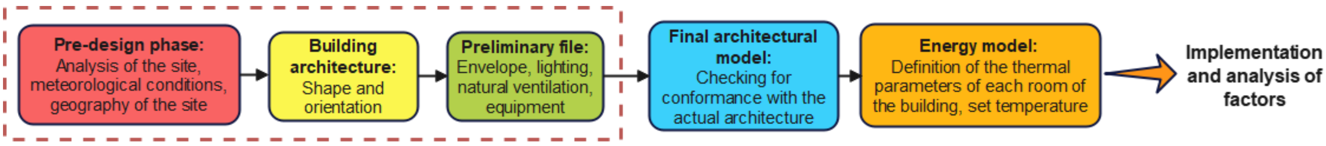

Figure 1. Analysis of the design process.

According to the architect's code of practice, this process is divided into four main stages:

- The site analysis study, which involves seeking the most economical option over the entire life cycle of the building;
- The architectural model: This phase of the process addresses the architectural aspects, the identification of the key performance parameters which were considered in the energy simulation and the analysis of the barriers for which the simulation is still limited in the traditional design framework, in order to achieve performance;
- The design of the architectural model: This phase consists of identifying the parameters which influence the performance of the building, such as the envelope, lighting, natural ventilation, heating and cooling equipment;
- The development of the energy model, which concerns the definition of the thermal parameters of the building spaces, the setting of temperature and finally the evaluation of the energy performance of the HVAC equipment.

The first stages of the process (stages 1, 2 and 3) provide the framework for the study, as they offer the greatest potential for taking advantage of the site's passive energies.

For each of these aspects, the relevant analysis methods and tools are used. Table 1 presents best practices from the literature, which are detailed in Sections 2.1.1–2.1.4.

Table 1. Analysis framework for energy simulation according to the literature. Adapted from [9].

	Miscellaneous					**Energy**				**Thermal**				**Lighting**			
Aspects to Study	**Mask Effect of Peripheral Buildings**	**Psychometric Chart**	**Sun Position**	**Wind Speed**	**Direct and Indirect Solar Radiation**	**Heating Savings**	**Cooling Savings**	**Savings in Artificial Lighting**	**Overall Energy Consumption**	**Thermal Conductivity**	**Heat Phase Shift**	**Thermal Loads**	**Thermal Gains by Daylight**	**Glare Analysis**	**Daylight Factor/Lighting Autonomy**	**Illuminance Estimation**	**Architectural Settings**
Analysis of site	√	√	√	√	√												
Shape	√		√	√		√	√	√	√								Volumetry, Geometry
Orientation	√	√	√	√		√	√	√	√								Optimal orientation
Envelope						√	√		√	√	√	√	√				Thermal conductivity, Thickness, Thermal storage capacity, Fenestration (WWR, U, FS, TL)
Lighting natural	√		√			√	√	√	√				√	√	√	√	WWR, DF optimum, Glare control

√: The checkmark corresponds to the validation of the options by the different parameters addressed in the table.

2.1.1. Site Analysis Phase

The analysis of the site, particularly its climatic conditions, allows the architect to modulate their concept according to the environment. Otherwise, this study aims to estimate the potential of the site in free energy and evaluate the comfort levels of the spaces according to the psychometric diagram [9].

Site Analysis Phase

This study includes a basic evaluation:

- Air temperature and humidity using the psychometric diagram;
- Solar gains and sky clearance levels for a rough estimate of daylight and solar heat gains;
- Wind (speed and direction angles) for a natural ventilation analysis.

The Tools

In choosing the climate file, one that has approximately the same latitude and height as the site was selected. Also, climate files that cover only one year (test meteorological data for a reference year) were avoided, because they cannot represent the long-term meteorological situation [10,11]. The climate analysis was carried out using the Meteonorm tool presented in Table 2.

Table 2. Climate analysis tool features.

Features	Tool	
	Meteonorm	**Ecotect**
Psychometric chart	√	√
Degrees—heating and cooling days	√	√
Sun position	√	√
Direct solar radiation	√	√
Diffuse solar radiation	√	√
Cloud cover	√	√
Wind (speed and direction)	√	√
Temperature, humidity	√	√
Limitations	Only accepts the file in Energy Plus Weather format	Limited functionality for studying natural ventilation effects

2.1.2. Form and Orientation Phase

Studying building options is an important step early in the design process. Architectural decisions at this level will influence the heating and cooling loads, daylighting and natural ventilation [12,13].

Figure 2 shows the building that was evaluated and which is located on the campus of "Gheorghe Asachi" Technical University. It was built in the early 80s and renovated very recently. The building studied in Figure 3 has a total surface area of 1795 m^2 and is made up of a set of two buildings joined by corridors, one called Corp A (P + 2E) and the other called Corp B (P + 3E). The main facades of the two buildings face southwest. The building is a reinforced concrete frame structure, with lightweight concrete masonry walls. The upper slab is made of reinforced concrete and thermally insulated by a layer of stacked granulite 25 cm thick. The exterior walls are made of 110 mm double bricks with 50 mm cavities and 10 mm cement mortar on each side with a U-value of 1.46 W/m^2·K. Figure 4 represents the architectural model that was created in SketchUp.

Figure 2. The Faculty of Electrical Engineering of Iasi.

Figure 3. Architectural model of blocks A and B of the university building.

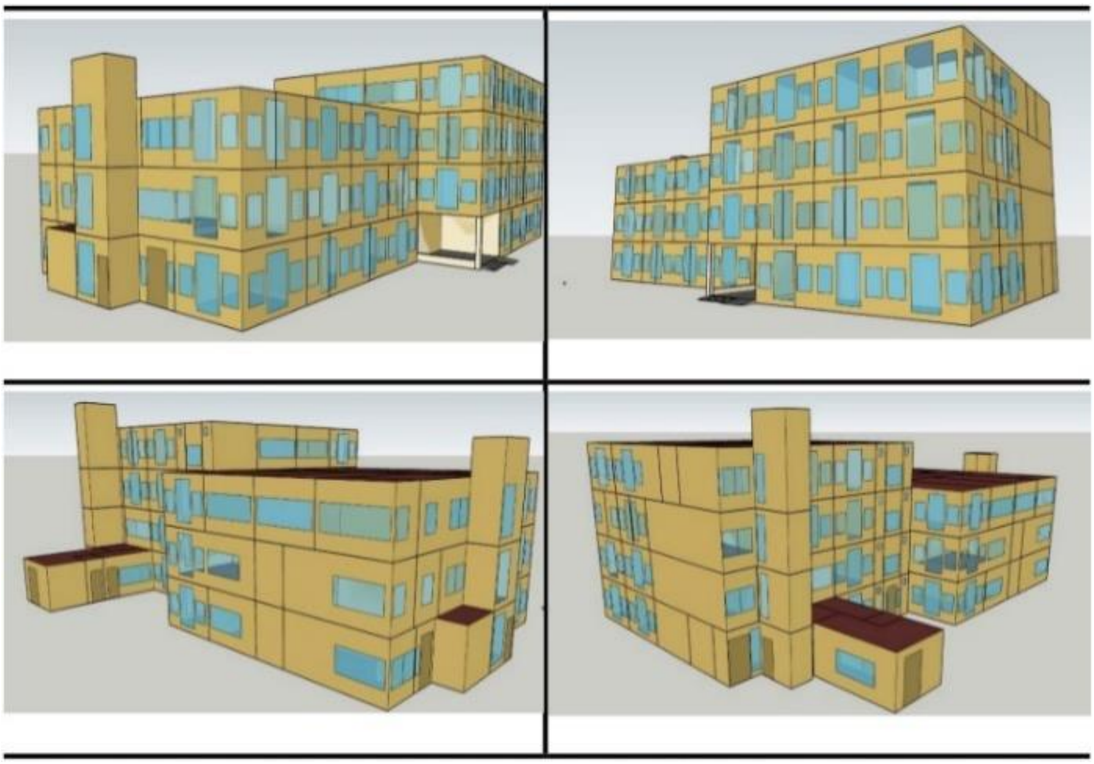

Figure 4. SketchUp modeling of blocks A and B of the Faculty of Electrical Engineering (profile view).

Study Parameters

Various parameters that affect the building's consumption were studied to improve its design and increase its efficiency. Studies on the impact of certain architectural parameters, such as the shape of the building [14,15], the percentage of opening of the facades, colors and shading devices [16], as well as occupancy [17], showed that overall consumption and energy costs fluctuate significantly depending on these parameters.

At this phase of the process, the energy model will be based on approximations of the site's climatic conditions and a limited amount of data such as geometries, building typology, total floor space and floor height, etc. HVAC systems and building materials are defined by default in the simulation tool (Figure 5).

The Tools

The tools presented in Table 3 are those commonly used in firms for the analysis of passive options. SketchUp is used in some architectural firms for orientation studies and mask effects. OpenStudio (SketchUp plug-in) (Figure 6) is a solution which first uses the architectural model of the building designed in SketchUp, then relies on EnergyPlus, which is a calculation engine, to evaluate the energy consumption of the building. Thus, it allows all architectural aspects to be evaluated for this phase. The calculation time is longer, compared to Ecotect. However, it has limits in terms of the analysis of options (volume, shape). The advantage of using the latter is that it allows immediate calculations from limited input data that are suitable criteria for rough sketch calculations.

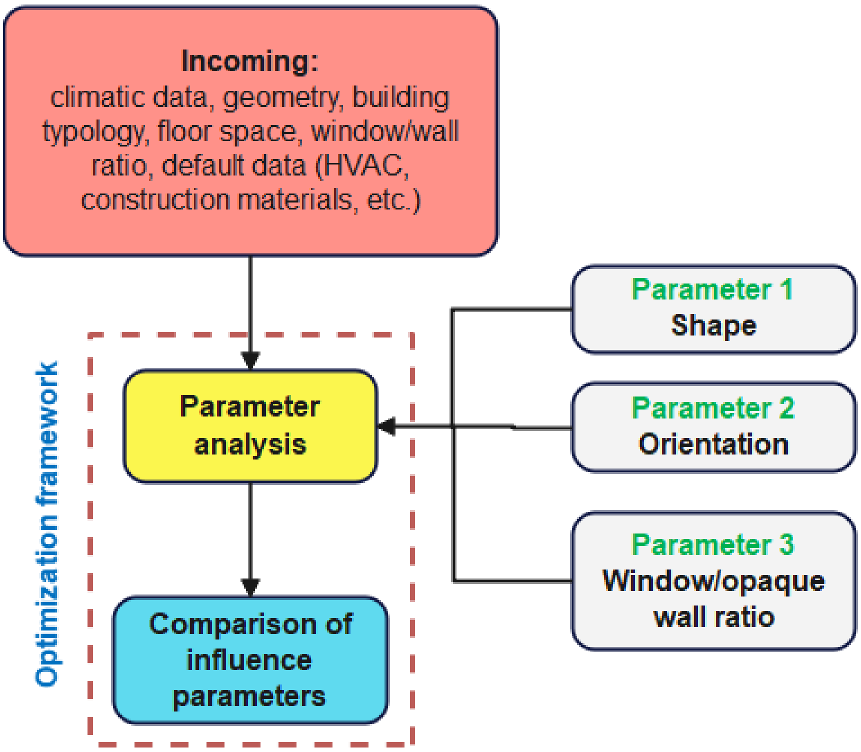

Figure 5. Energy simulation of options during the sketch phase (shape and orientation).

Table 3. Comparison of simulation tool options.

Study Settings	Tools	
	OpenStudio SketchUp Plug-in	**Ecotect**
Building compactness	1	
Shape	1	
Orientation of facades	√	√
Window/wall ratio	√	√
Energy consumption	1	1
Analysis of solar gains		√
Free software	√	
Graphic interface	√	√
Import geometry	2	√

Comments: 1: calculations via EnergyPlus 2: plug-in from SketchUp.

2.1.3. Natural Lighting Phase

A good management of natural light offers the advantage of making substantial energy savings by reducing the need for artificial lighting and associated cooling loads [18,19]. This passive strategy requires a more sophisticated approach than simply purchasing windows with a high light transmittance. The integration of this component involves finding a balance between utilizing daylight, controlling glare and ensuring a uniform light distribution throughout the building.

In the simulation approach, the most adequate lighting performance measures for the climatic conditions of Iasi and Lomé were prioritized. This means that the decision is made to proceed either by the simplified static method, which consists of averaging the daylight factor, or by the dynamic method, which consists of visualizing the daily variations in natural lighting [20]. The first approach is often used by designers by referring to the minimum thresholds indicated by guides and directives. However, this method lacks precision, since it estimates illuminance levels under a single type of sky, while the sky model constantly varies depending on the climate. Therefore, it is advantageous to design this strategy based on dynamic methods to have precise results, predict artificial lighting consumption and have a better design [21].

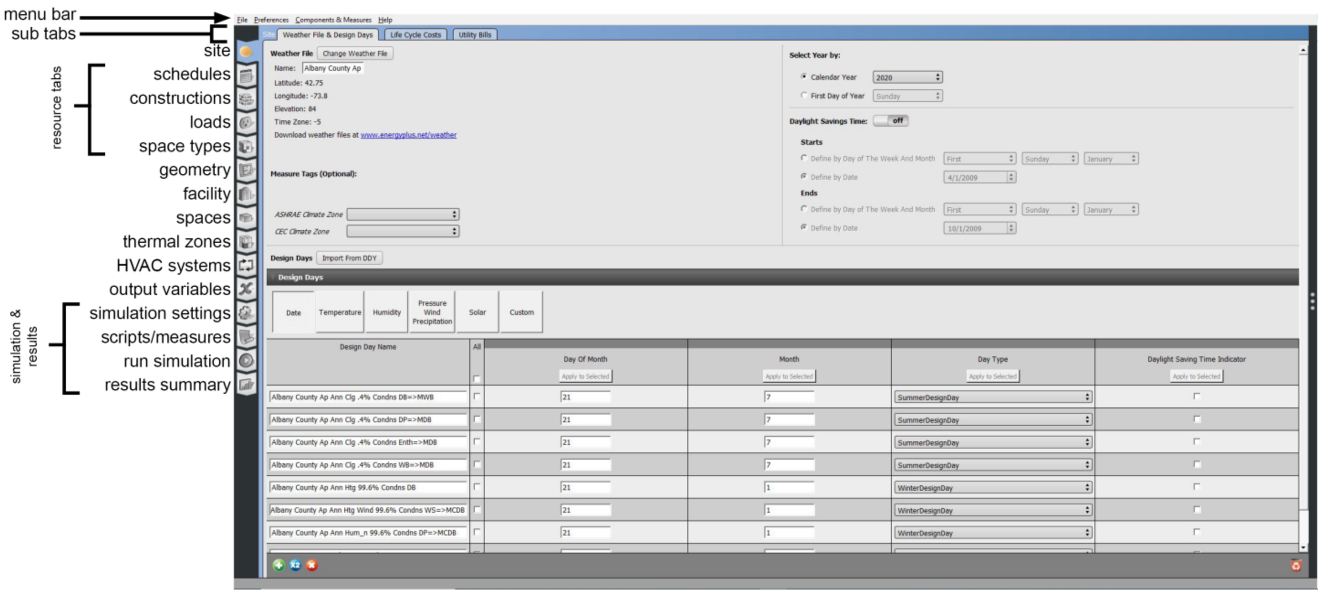

Figure 6. OpenStudio Construction Sets interface.

In the second step, the type of sky most compatible with the meteorological conditions of each site was chosen. Although this step appears simple, it has a considerable impact on the precision of the results, and it is important to control it well. Depending on the performance indicator of the lighting strategy chosen, the type of spaces and lighting thresholds, as well as occupancy times, are also requirements for this study [22]. Based on all these data, a calculation of the lighting and/or luminance of the spaces will be carried out.

2.1.4. Building Envelope Phase

The envelope, including the external walls, roof and openings, often represents the greatest energy loss in the building; hence, depending on its characteristics, the heating and cooling needs will be more or less important.

The way in which the envelope affects the energy needs of the building is a question of playing on well-defined parameters: the level of insulation must be guaranteed at every point of the envelope by carefully avoiding thermal bridges (discontinuity in the insulating layer), because they cause significant thermal losses [23]. Significant thermal inertia avoids the risk of overheating and ensures a delay in heat input. When designing these parameters, the climate, the purpose of the building and the behavior of the occupants were taken into account.

Study Parameters

The energy performance of the envelope was evaluated according to three phenomena: limitation of heat flows, control of solar radiation and limitation of air leaks.

Table 4 presents the main parameters controlling these flows, which are resistance, tightness, quality of fenestration and thermal mass [24]. In the stages of the energy simulation of the building, the strategies associated with the structural parameters in order to improve their performance were considered.

Table 4. Main parameters improving envelope performance.

Thermal Resistance (Opaque Walls, Openings)	Limit heat gains or losses due to conduction by providing an envelope with a low conductivity coefficient. Be very attentive to thermal bridges.
Thermal Mass	Recommend heavy materials, especially for premises with prolonged occupancy presenting significant internal loads and heavily exposed to sunlight.
Glazing Quality	Evaluate the trade-off in glazing using low-e material with other (reflective) coatings.
Waterproofing	Limit infiltration and exfiltration as much as possible to ensure continuity of waterproofing

In the energy model, these parameters are controlled by variables: the thermal mass is defined by a light, medium-heavy or heavy material. The resistance of the walls depends on the thickness, as well as the heat transmission coefficient. To effectively optimize the performance of the envelope, a parametric analysis of all its components was carried out, also considering the geometry and orientation of the building, the surface area of the glazing and the shading devices: These data were necessary so that the model could take into account solar gains and heat losses to predict the performance of the envelope.

This subsection provides an overview of the input ranges and weights that make up the parameter space for building the model and defining the internal environment of the building. To facilitate the energy audit of the building, the building was divided into ten specific zones (Figure 7) according to their utility within the building, while defining a specific thermal zone for each of the ten zones. Then, the indoor environment parameters were set. The indoor temperature is 18 °C and the feedback temperature is 12 °C in winter for the Iasi climate. The indoor temperature is 25 °C and the return temperature is 28 °C in summer for the tropical climate (in Lomé). The humidity control is between 10% and

90%. Then, the parameters associated with occupancy, lighting, schedule and electrical equipment were defined in OpenStudio based on real data from the university building [25]. The population density is 0.04 person/m^2. The personnel coefficient is 0.9. The lighting power is 5 W/m^2–100 lux. The power of the equipment is 3.58 W/m^2. The schedule of the different rooms was defined according to the schedule of the teaching staff and students of the different spaces of the university building. Finally, the building envelope was adjusted to different conditions. The architectural model of the different spaces of the building is illustrated in Figure 7.

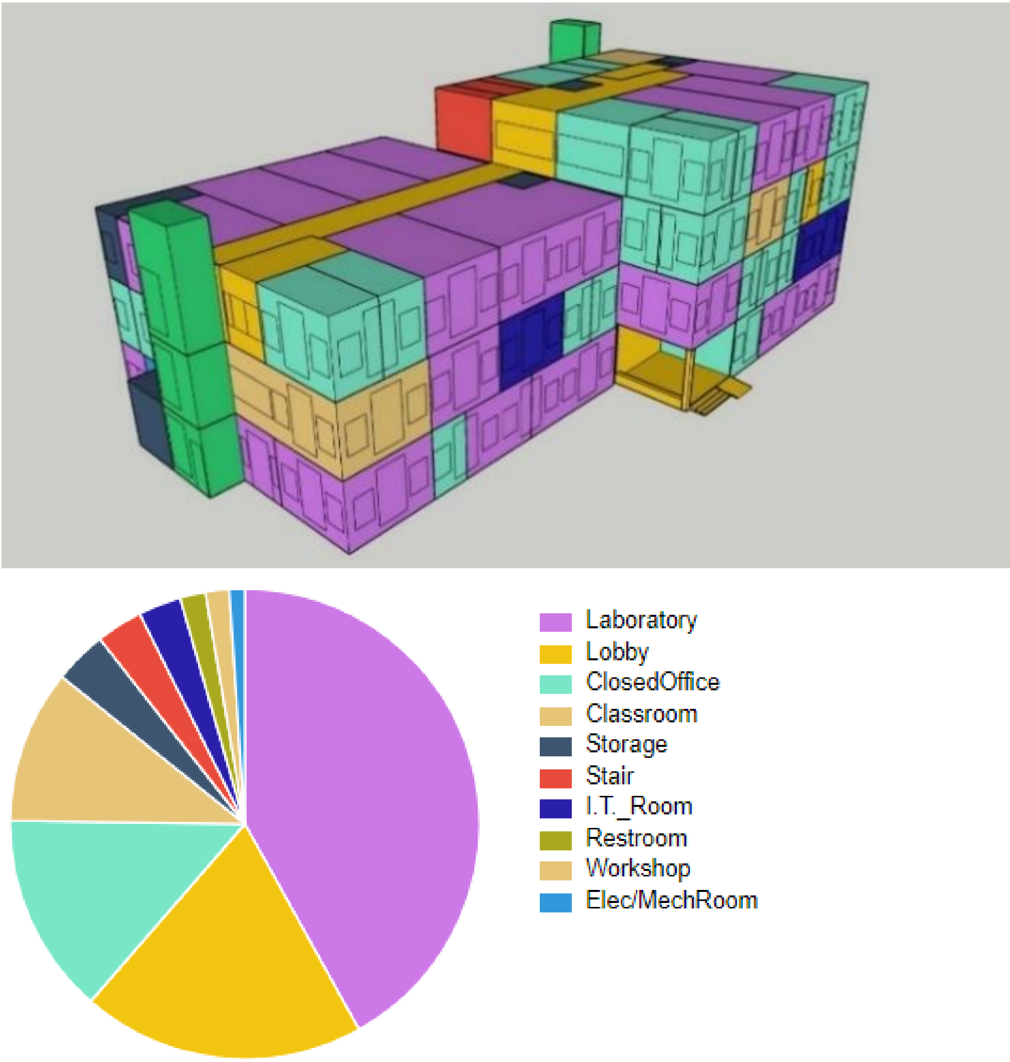

Figure 7. Overview of the different space types.

2.2. Proposed Evaluation Framework

The modeling process comprises three main stages, illustrated in Figure 8. A prototype model of the university building based on ASHRAE standards [5] is developed and adapted to the location, age and size of the building. This prototype model is then customized to represent each space, using data on geometry, envelope properties and internal loads. A series of HVAC system sizing tests are performed to ensure that the HVAC loads are estimated correctly based on the size of the building. An analysis of the HVAC system's sizing and the operation of the internal loads is performed to ensure that the building model operates as intended.

2.2.1. Building Equipment

The data for lighting and equipment are determined from the building data, while assumptions for the equipment and operation of the heating, ventilation and air conditioning systems are derived from the standards.

Internal Loads

Electric lighting and electrical loads are treated separately. The occupancy density, expressed as the number of people per floor area, is calculated for university spaces. Additional controls related to internal loads and schedules have been applied during the analysis. The following checks have been performed on the internal parameters to ensure that the loads are reasonable and function as expected:

- Facilities, lighting and occupancy follow schedules generated by the Create Parametric Schedules command in the OpenStudio software version 3.6.1. For a given number of operating hours per week, the measurement generates internal load schedules typical for an office and university space;
- Equipment, lighting and occupancy programming is carried out for 24 h time slots; they are presented and discussed in the Section 3.

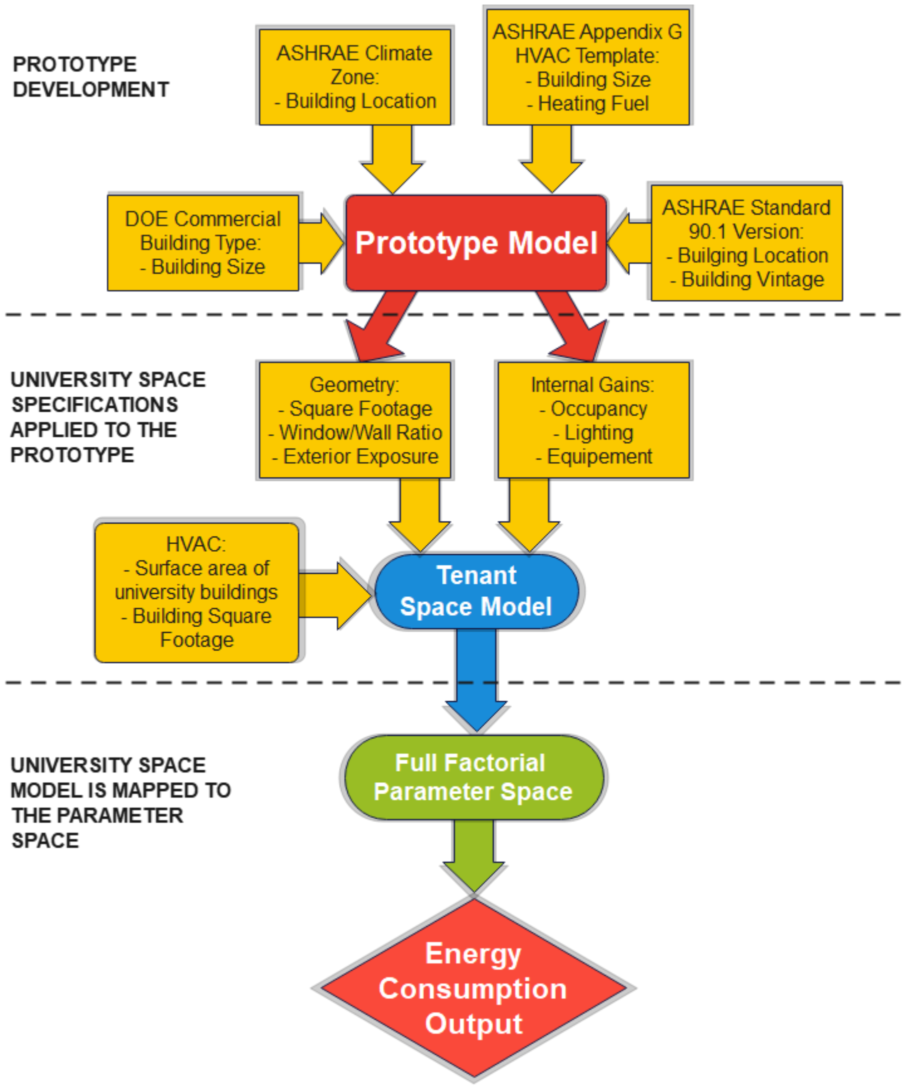

Figure 8. Modeling protocol flowchart.

Plug and Process Loads

To estimate the outlet loads, occupant information was used to determine the power density of the equipment in each room of the building. For each type of space, the number of electrical equipment items set in the space is defined. The power of the equipment is estimated based on the number of residents. Equipment schedules are created based on the number of weekly operating hours.

The Equipment Power Density (EPD) was calculated using Equation (1). The annual energy consumption of the equipment in kBtu can then be calculated using the EPD, floor area and weekly operating hours. The annual site energy consumption can be accurately estimated using Equation (2). Equation (3) provides the annual energy consumption of the source in kBtu/ft^2, which is calculated by multiplying the site energy by a conversion factor of 2.8 and dividing by the building area.

$$EPD\left(\frac{W}{ft^2}\right) = \frac{\sum(peak\ power_{conv}(W) \times quantity_{conv})}{tenant\ floor\ area\ (ft^2)} \tag{1}$$

$$TECE = EPD\left(\frac{W}{ft^2}\right) \times tenant\ floor\ area\ \left(ft^2\right) \times (2.59 + 0.0285 \times hours\ per\ week + (if\ hours\ per\ week > 60\ then\ 0.1,\ else\ 0)) \tag{2}$$

2.2.2. The Hypotheses

The main assumptions relate in particular to the presence of people and electrical equipment. Sizing checks were carried out to determine whether the selected HVAC systems could meet the thermal loads of the building spaces. Several hypotheses concerning the sizing of the systems were made and are summarized below:

- For all models, the assumption of an unoccupied building (zero internal load) was used to size the HVAC systems, as engineers usually do. In practice, there is always a certain base load due to lighting and equipment. Therefore, sizing HVAC systems with a zero base load is a conservative approach and generally results in some oversizing.
- Dimensioning factors of 1.25 for cooling and 1.15 for heating in OpenStudio were utilized. A factor greater than 1 provides an additional margin of safety for extreme weather conditions and unusually high loads.
- A standard sizing routine for non-matching installations was used for all models. This means that sizing decisions for the sized HVAC systems are based on the total distributed loads of the area, regardless of when they occur. Coincidental design is the maximum sum of all loads at a given time, typically represented in design assuming a diversity factor of ~70% on the sum of non-coincidental loads. Inadequate sizing is another conservative approach that contributes to the oversizing of HVAC equipment. A system sizing analysis is performed by considering idle time, partial load factors and several other validation checks.
- Validation: Checking the pressure losses of the fans, the HVAC systems of the building being equipped with a controller for the activation and deactivation of the system were verified, which made it possible to carry out control tests on the economizers installed in the operation heating and cooling loads, and to check the energy consumption of the heating, ventilation and air conditioning systems as a function of temperature and their influences. Thus, the HVAC energy consumption was estimated as a function of temperature: to ensure that the HVAC systems worked as expected and reacted correctly to the outside temperature of the two climate zones (Figures 9 and 10), the energy consumption HVAC versus outdoor air-dry bulb temperature was tracked for each climate zone and HVAC system type. The results obtained after the simulation were compared with the energy balances of the building over the last three years.

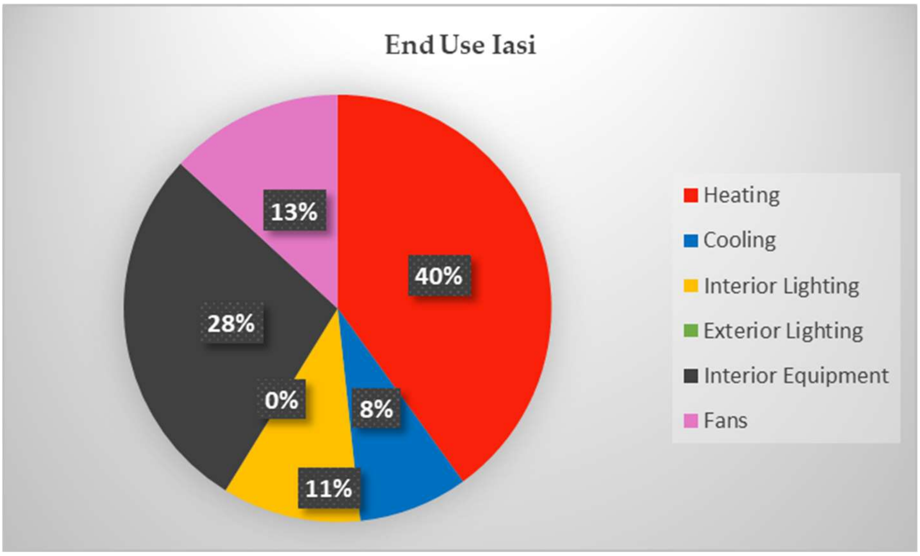

Figure 9. Diagram of energy consumption needs in Iasi.

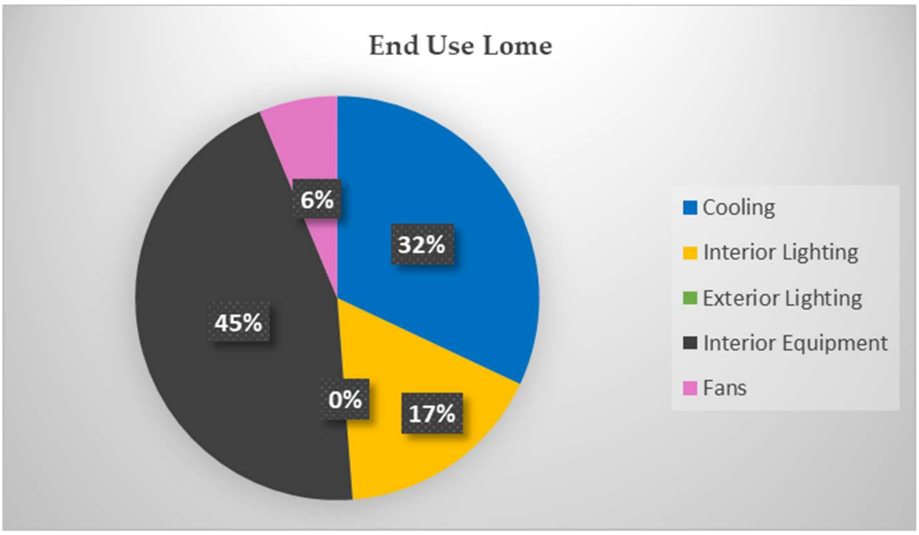

Figure 10. Diagram of energy consumption needs in Lomé.

3. Results and Discussion

An energy consumption analysis was carried out on the building structure. For this model, two energy sources were introduced in the case of the building in Iasi. The structure of the primary energy source is closely related to the type of heating/cooling system in this case. For the Lome city model, the building has only one source for cooling throughout the year. The diagrams shown in Figures 9 and 10 allow you to visualize at a glance the energy consumption data from the primary energy source for both climate zones. These are categorized according to the energy demand and activity of each space in the building.

Thanks to the assumptions on these systems, the HVAC energy consumption was estimated as a function of temperature. Figure 11 shows the building in Iasi, Romania, with a VAV (Variable Air Volume) ventilation system to independently regulate the air flow and ventilation parameters in each room of the building. The heating energy far exceeds cooling in a cold climate like Iasi, which is normal. On the other hand, Figure 12 shows the building in Lomé, Togo, with a PVAV system with PFP boxes (electric cooling, electric heating). The calculations show that the impact of warming on annual HVAC energy (reduction or increase) depends significantly on the climate category. This aligns with the work of Kharseh et al. [26], who demonstrated that the variation in annual HVAC systems energy depends on the climate, varying from cold to hot climates. In mild climates, such as Lome, it has been shown that warming does not significantly impact on the annual energy of HVAC systems. Improving building design parameters can mitigate the impact of warming. The histograms presented in Figures 11 and 12 show the demands of the HVAC systems and the temperature required to achieve thermal comfort.

Tests on the ventilation rate and the infiltration effect of the building were carried out. The results showed that they have a significant impact on the thermal comfort of students and the energy consumption of the building, which is in agreement with the results of previous studies [27,28]. One of the primary causes of infiltration was the difference in atmospheric pressure across the building envelope. This is due to differences in indoor and outdoor air temperatures (stack effect), the operation of the mechanical ventilation system and wind movement [29,30]. Ventilation and infiltration rates affect the heating/cooling load, as well as indoor air temperature and indoor air humidity levels in buildings [31,32]. The infiltration rate is affected by exterior environmental variables, architecture, building age and construction materials. It should be noted that closing air leakage cracks can reduce the energy consumption of the building by reducing the infiltration rate [33].

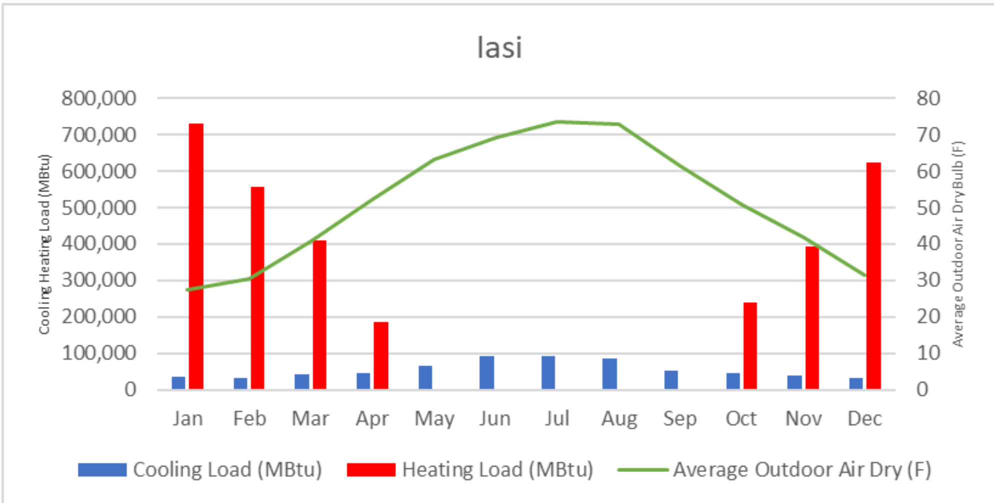

Figure 11. HVAC system energy consumption as a function of building temperature in the continental area.

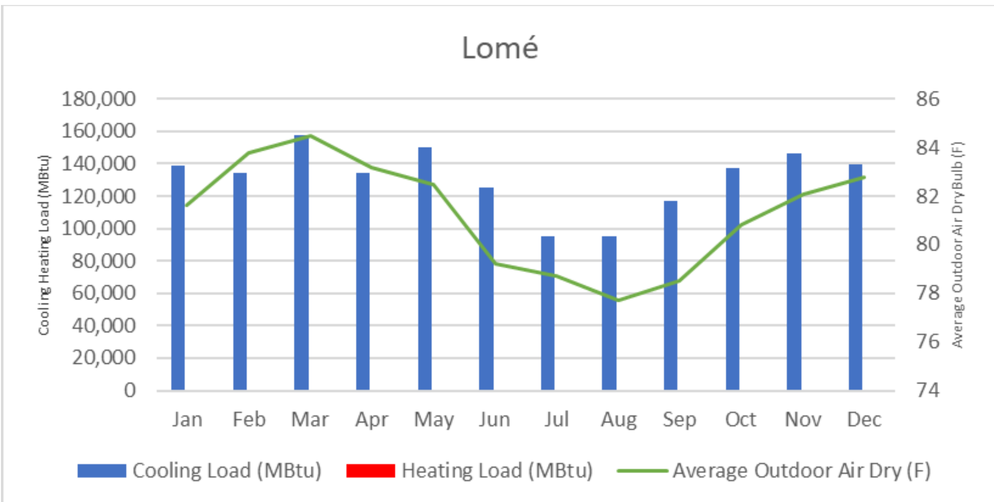

Figure 12. Energy consumption of HVAC system as function of building temperature in tropical zone.

In this study, sensitivity analyses revealed that the mechanical ventilation rate per zone positively influences both the thermal discomfort of students and the building's energy consumption. Increased ventilation rates lead to lower air and operating temperatures, which can contribute to thermal discomfort. The optimal energy consumption was achieved with a zone mechanical ventilation rate of six, while the lowest hours of thermal discomfort were observed with a rate of zero. These results are in agreement with the work of A. Franco et al. and of R. Maddaa-lena et al. [34,35]. Conversely, a study by Scherer et al. [36] highlights that inadequate ventilation rates result in thermal discomfort and excessive energy consumption. Current thermal comfort regulations concerning Indoor Air Quality (IAQ) are not universally defined, leading to varied minimum ventilation rates for similar buildings across different countries [37]. This variation explains the inverse relationship between mechanical ventilation rates and thermal comfort, which subsequently affects the building's energy consumption.

Understanding a building's HVAC system can be complex and often inaccessible to occupants, limiting their detailed knowledge of its operation. Therefore predetermined HVAC systems in OpenStudio are assigned based on building size, following the guidelines in Appendix G of ASHRAE 90.1 [38]. This approach streamlines building modeling and reduces complexity. However, analyzing HVAC energy consumption for individual spaces within a larger building system presents additional challenges due to uncertainties associated with HVAC systems. Due to the uncertainties associated with HVAC systems, the online tool provides a range for annual HVAC energy consumption.

Figures 13 and 14, respectively, show the occupancy schedule and lighting and occupancy programming for 24 h time slots. Reasonable internal loads and time slots operating as expected could be achieved. Figure 13 shows the parametric occupancy schedule for a work week. This schedule assumes shortened work days from Monday to Friday and low occupancy on Saturday and Sunday. Figure 14 outlines the lighting schedule for weekdays, with minimal usage during weekends. Overall, weekend energy consumption remains notably lower than on weekdays.

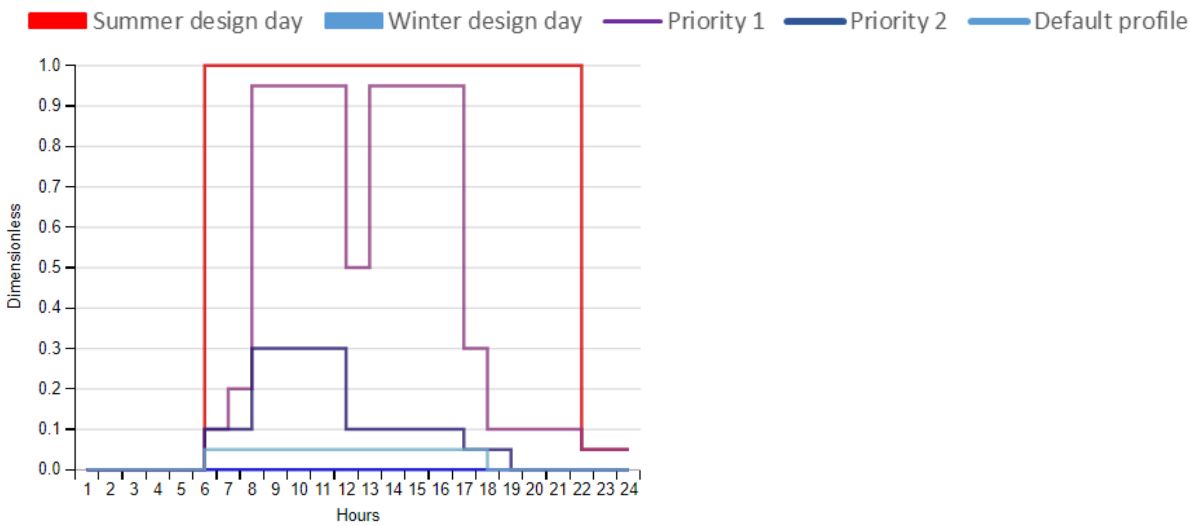

Figure 13. Parametric occupancy calendar with priority days and seasons.

The definition of interior lighting was made by considering the luminous flux received per unit area depending on the type of space in the building, with an estimate of approximately 5 W/m^2. The model has been equipped with standard equipment to ensure the proper functioning of various space types, including electrical equipment offices, laboratories, and classrooms in accordance with their installation.

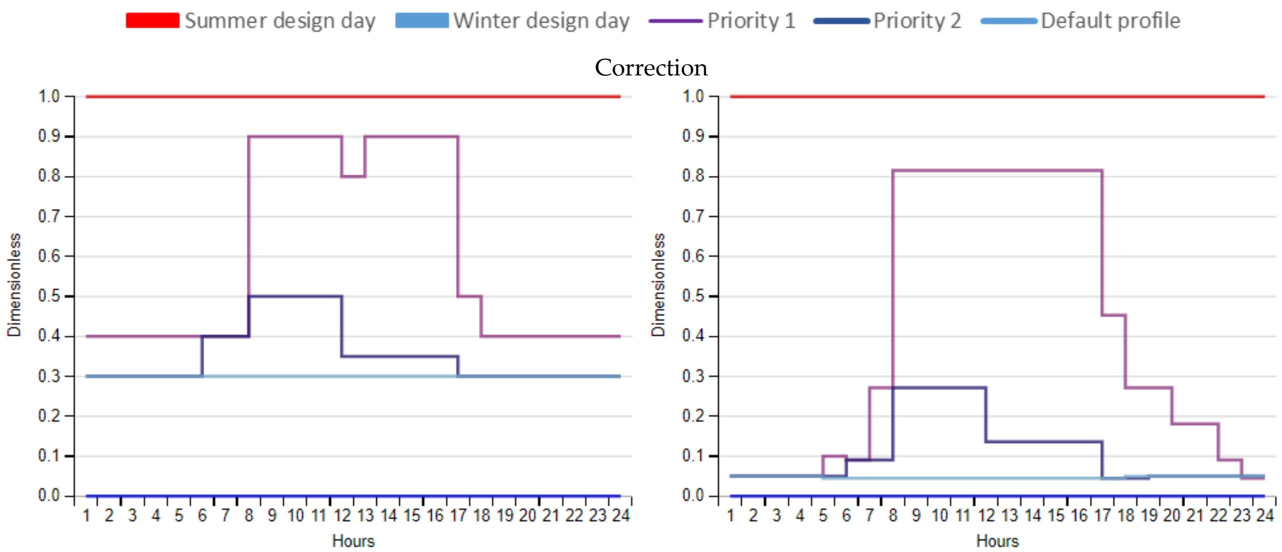

Figure 14. Parametric lighting program and electrical equipment based on space occupancy over 24 h time slot.

Following the hypothesis applied to the model, it was observed that the climatic conditions experienced by the building have a significant impact on heating and cooling needs and on the evolution of the overall electrical consumption of the building (see Figures 11 and 12). As a result, this affects the energy performance of the building. Figure 15 shows that the city of Iasi has a percentage of energy demand and expenditure that fluctuates depending on the winter and summer seasons.

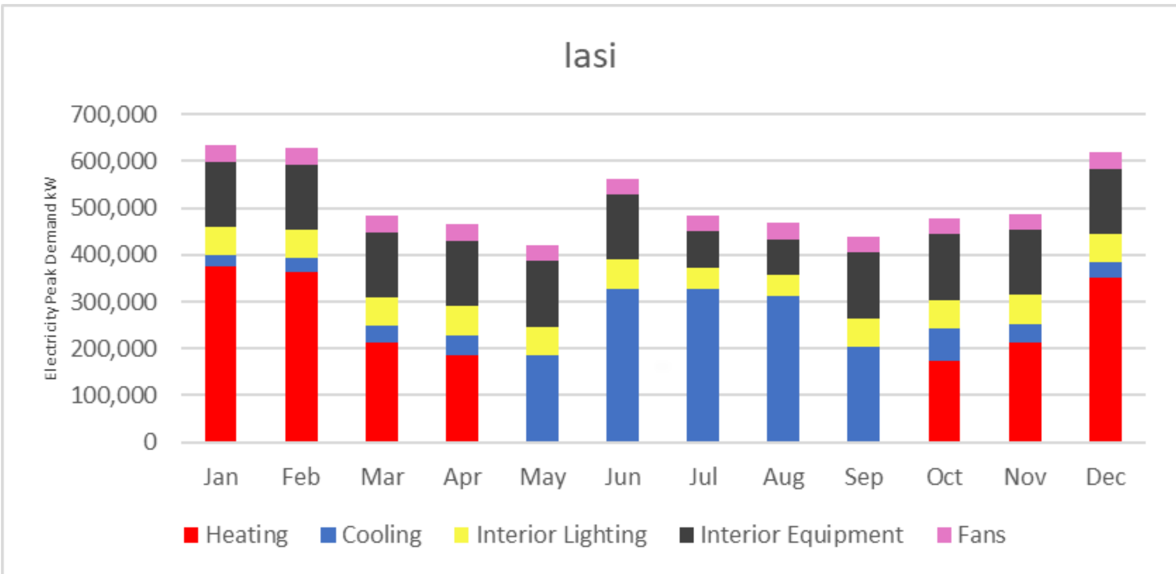

Figure 15. Energy consumption of different building needs in Iasi.

On the other hand, when the model is subject to the climatic constraints of the city of Lomé (Figure 16), a trend reversal of the energy needs of buildings is observed in terms of comfort and the use of electrical equipment. This means that in the case of Lomé, electrical equipment requires much more power to operate optimally than in the case of Iasi. Indeed, in the case of the city of Lomé, electrical appliances are constantly exposed to heat, and thermal conditions are unfavorable for the proper functioning of electrical appliances, which leads to poor performance and the reduced efficiency of the equipment. The energy expenditure linked to HVAC systems is higher in the city of Iasi than that of Lomé, with a difference of 20% for the same electrical equipment used.

Technical and electrical equipment contributes significantly to the overall environmental impacts of the building. These results are in agreement with the work of Hoxha et al. [39], who showed the impact of technical and electrical equipment in a building and recommended including impacts linked to technical and electrical equipment through detailed calculations from the phase of building design.

An analysis of factors influencing energy consumption by region was conducted. In this study, data were collected from meteorological files and design days for each climatic zone. As with Shiker et al. [40], a correlation analysis (Pearson's correlation coefficient) was used to evaluate the degree of correlation between the influencing factors and the intensity of total energy consumption, as well as the intensity of energy consumption of the HVAC system. The Pearson correlation coefficient is the covariance of two variables divided by the product of their standard deviations. The Pearson correlation coefficient is determined by Equation (3):

$$\rho = \frac{Cov(x, y)}{\sqrt{D(x)}\sqrt{D(y)}} \tag{3}$$

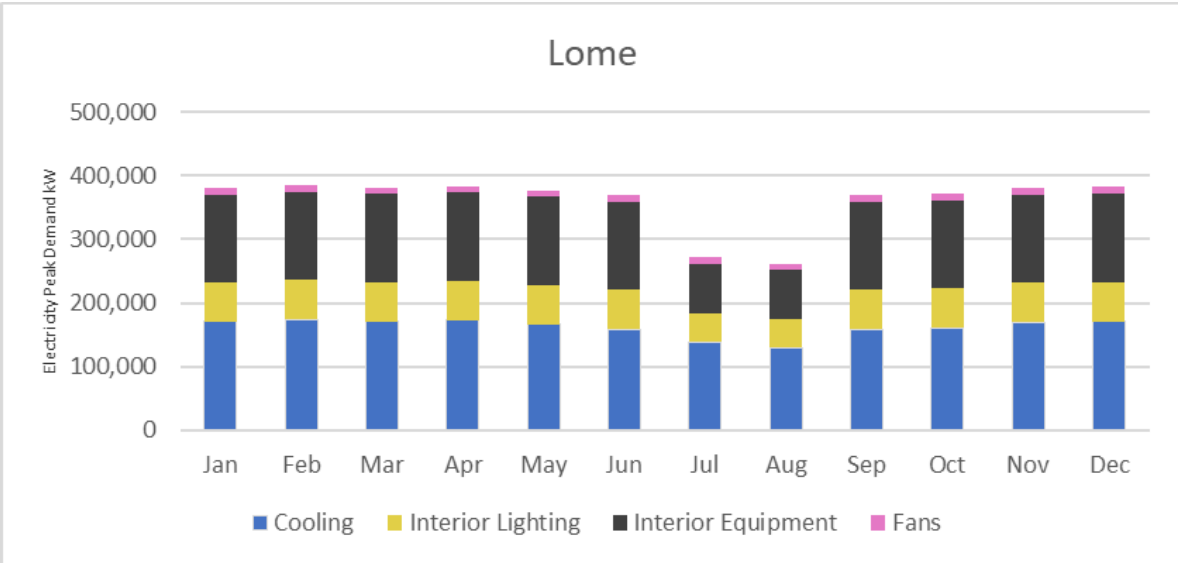

Figure 16. Electricity consumption for different building needs in Lome.

The value of ρ ranges from −1 to 1, where 1 indicates a positive linear correlation, while −1 indicates a negative correlation. A statistical test is then implemented to determine whether the correlation is significant. The relationship between lighting and energy consumption was calculated using Equation (3), resulting in a value of 0.775. This value, being close to 1, indicates a strong influence of the number of openings, the location of windows and shading devices on the interior lighting level of the building. Indeed, all orientations provide natural lighting, but it is, however, preferable to place the openings in such a way that the sun can penetrate inside the room when it is most used. In addition, natural light varies depending on the orientation of the building. This result is in agreement with the work of Piotrowska et al. [41], who reduced the energy consumption of a university building by automatically controlling lighting based on the amount of sunlight entering the rooms.

Furthermore, Figures 11 and 12 show that the power requested by HVAC systems changes with the set temperature. The analysis of the energy consumption intensities of HVAC systems shows that it directly depends on the level of occupancy and the surrounding weather conditions. Hussin et al. [42] studied the correlation coefficient of influencing factors and found that the coefficient of heat sources was higher than those of cooling sources in an academic building. These test results are consistent with the results obtained in the present work. On the other hand, Figures 15 and 16 show that the evolution of energy consumption is mainly explained by the local climatic conditions to which the building is exposed in each zone. Figure 14 outlines the lighting schedule for weekdays, with minimal usage during weekends. Overall, weekend energy consumption remains notably lower than on weekdays. To obtain a more precise estimate of the annual energy consumption of the HVAC, a measurement carrying out a sizing cycle for the entire building was carried out, and the efficiency value of the system was extracted to replace the efficiency in the building space design cycle. However, a limitation of this approach is potential discrepancies in part-load operation between individual spaces and the entire building.

Compared to the relationship between occupancy and electrical energy consumption, following monthly consumption peaks and using equation 4, the strength of the relationship between occupancy and energy consumption is 0.870, which indicates a strong positive correlation for this factor. The influence of this factor is significant regardless of the two climatic zones (see Figure 14). Ambient heat tends to increase the power required by air conditioners to maintain a cool temperature in the space, and vice versa for heating units during winter. However, regardless of the configuration of the HVAC system in the building, when it operates at a constant regime, its energy consumption is reduced. This is in good correlation with the results obtained by Solano et al. [43], where it is found that maintaining a constant mode satisfies over 80% of potential occupants with interior temperatures more than 90% of the time.

In this model, spaces covering a large surface area are those that consume the most energy. Part of this energy expenditure is due to the artificial lighting systems installed. But the vast majority of consumption is due to the use of equipment by the occupants of these spaces. The simulations that were carried out in the two areas show that 75.6% of the overall variation in energy consumption is directly linked to the occupation of the building spaces. Note that for a fixed building, the performance of its envelope structure is fixed, but not the behavior of its occupants. Zhang et al. [44] proposed new parameters to build correlation models between energy consumption and user behavior to predict energy consumption in academic buildings. They were able to predict the evolution of consumption based on the behavior of the occupants. The evolution of energy consumption is directly linked to the behavior of occupants regarding the use and management of this energy.

With the electrical equipment used, the evolution of consumption is fundamentally driven by the commissions and adjustments made by the occupants, which are linked to their behavior. An analysis of the results revealed that 70% of the total variation in energy consumption was due to the equipment used in the building. This is again in line with the value of 68.4% reported by Hussin et al. [42], who used the Pearson correlation coefficient to measure the impact of the use of electrical appliances on the energy consumption of a university building.

In both climatic environments, power demand varies throughout the day and across seasons, with variations of 20% for equipment and almost 30.76% for HVAC systems. A comparative analysis of the results of the two case studies leads to the same conclusion. This means that in most cases, the parameters affecting the building's consumption are more linked to the discomfort felt by the occupants. Alghamdi et al. [45] showed in a study that correctly determining the set temperature of an HVAC system can significantly reduce operating temperatures. These reductions can result in a significant reduction in heat discomfort and improve energy efficiency.

4. Conclusions

In the context of a shortage of fossil resources and high energy needs, buildings constitute potential sources of energy savings, particularly with heating and lighting systems. Hence the importance of identifying them and finding solutions to optimize consumption and reduce bills. This work contributes to the advancement of knowledge by proposing evaluation and optimization methods for integration into the energy simulation of a building. In this work, the study was aimed at university architecture, relying on passive strategies in order to achieve performance objectives.

Thus, an evaluation of HVAC systems, occupancy, thermal comfort and energy consumption was carried out using simulation software, in order to identify the parameters of greatest concern and to show their real impacts in a university building placed in two different climatic conditions. From the analysis, several conclusions emerged: the simulation results identified the parameters that influence consumption and showed significant potential for optimizing these parameters within the building, in order to achieve energy savings and thermal comfort in educational buildings.

Parametric and sensitivity analyses revealed a strong correlation between student occupancy hours and the building's cooling/heating load. Adjustments to cooling and heating setpoint temperatures, along with roof construction details, significantly influenced these design parameters' sensitivity, impacting both energy consumption and student comfort.

Increasing the cooling setpoint temperature from 22 °C to 28 °C in roof construction can reduce operating temperatures by 14.2% and 20.0%, respectively. This optimization could significantly reduce the hours of thermal discomfort, in a ratio of 6.0 and 3.25, respectively.

This study offers actionable insights for architectural design teams, facilitating informed decisions on prioritizing sensitive building parameters based on simulation outcomes.

Author Contributions: Conceptualization, A.-R.A.-T. and M.B.; methodology, A.-R.A.-T. and M.B.; software, A.-R.A.-T.; validation, A.-R.A.-T., M.B. and D.D.L.; formal analysis, A.-R.A.-T.; investigation, A.-R.A.-T.; resources, M.B.; data curation, D.D.L.; writing—original draft preparation, A.-R.A.-T.; writing—review and editing, M.B. and D.D.L.; visualization, A.-R.A.-T.; supervision, M.B. and D.D.L.; project administration, M.B. All authors have read and agreed to the published version of the manuscript.

Funding: This research received no external funding And The APC was funded by Centre d'Excellence Régional pour la Maitrise de l'Electricité (CERME).

Data Availability Statement: The data presented in this study are available on request from the corresponding author. The data are not publicly available due to the fact that these data belong to "Gheorghe Asachi" Technical University.

Acknowledgments: The authors thank the AUF through the "Eugen Ionescu" Mobility Program, which allowed them to carry out a research stay at the "Gheorghe Asachi" Technical University in Iasi (Romania).

Conflicts of Interest: The authors declare no conflict of interest.

References

1. UN Environment. Les Émissions du Secteur Mondial du Bâtiment Restent Élevées et Continuent d'Augmenter. Available online: http://www.unep.org/fr/actualites-et-recits/communique-de-presse/les-emissions-du-secteur-mondial-du-batiment-restent (accessed on 8 June 2024).
2. Bozonnet, E.; Jolas, C.; Le Dréau, J. BIM et conception intégrée—Interopérabilité et optimisation de la performance environnementale. *Tech. Ing.* **2018**. [CrossRef]
3. Reed, B. *The Integrative Design Guide to Green Building: Redefining the Practice of Sustainability*; John Wiley & Sons: Hoboken, NJ, USA, 2009.
4. Optis, M.; Wild, P. Inadequate documentation in published life cycle energy reports on buildings. *Int. J. Life Cycle Assess.* **2010**, *7*, 644–651. [CrossRef]
5. Vaughn, M. ASHRAE Research Report. *ASHRAE J.* **2016**, *58*, 81–91.
6. Imrie, R.; Street, E. *Architectural Design and Regulation*; John Wiley & Sons: Hoboken, NJ, USA, 2011. [CrossRef]
7. Aydemir, A.; Jacoby, S. Architectural design research: Drivers of practice. *Des. J.* **2022**, *25*, 657–674. [CrossRef]
8. Aburamadan, R.; Trillo, C. Applying design science approach to architectural design development. *Front. Archit. Res.* **2020**, *9*, 216–235. [CrossRef]
9. Bambardekar, S.; Poerschke, U. The Architect as Performer of Energy Simulation in The early Design Stage. 2009. Available online: https://www.aivc.org/resource/architect-performer-energy-simulation-early-design-stage (accessed on 8 June 2024).
10. Crawley, D.B. Which weather data should you use for energy simulations of commercial buildings? *Trans.-Am. Soc. Heat. Refrig. Air Cond. Eng.* **1998**, *104*, 498–515.

11. Giama, E.; Chantzis, G.; Kontos, S.; Keppas, S.; Poupkou, A.; Liora, N.; Melas, D. Building Energy Simulations Based on Weather Forecast Meteorological Model: The Case of an Institutional Building in Greece. *Energies* **2023**, *16*, 191. [CrossRef]
12. Alghamdi, S.; Tang, W.; Kanjanabootra, S.; Alterman, D. Optimal configuration of architectural building design parameters for higher educational buildings. *Energy Rep.* **2023**, *10*, 1925–1942. [CrossRef]
13. Latha, H.; Patil, S.; Kini, P.G. Influence of architectural space layout and building perimeter on the energy performance of buildings: A systematic literature review. *Int. J. Energy Environ. Eng.* **2023**, *14*, 431–474. [CrossRef]
14. Yildirim, M.; Gocer, O.; Globa, A.; Brambilla, A. Investigating restorative effects of biophilic design in workplaces: A systematic review. *Intell. Build. Int.* **2023**, *15*, 205–247. [CrossRef]
15. Gassar, A.A.A.; Koo, C.; Kim, T.W.; Cha, S.H. Performance Optimization Studies on Heating, Cooling and Lighting Energy Systems of Buildings during the Design Stage: A Review. *Sustainability* **2021**, *13*, 9815. [CrossRef]
16. Mangkuto, R.A.; Koerniawan, M.D.; Apriliyanthi, S.R.; Lubis, I.H.; Atthaillah; Hensen, J.L.M.; Paramita, B. Design Optimisation of Fixed and Adaptive Shading Devices on Four Façade Orientations of a High-Rise Office Building in the Tropics. *Buildings* **2022**, *12*, 25. [CrossRef]
17. de Meester, T.; Marique, A.-F.; De Herde, A.; Reiter, S. Impacts of occupant behaviours on residential heating consumption for detached houses in a temperate climate in the northern part of Europe. *Energy Build.* **2013**, *57*, 313–323. [CrossRef]
18. Mbadinga, D.; Alibaba, H. Improvement of Thermal Efficiency Through Natural Lighting: Energy Saving. 2019, p. 5. Available online: https://www.researchgate.net/profile/Halil-Alibaba/publication/338188729_Improvement_of_Thermal_Efficiency_Through_Natural_Lighting_Energy_Saving/links/5e05e07f4585159aa49d892c/Improvement-of-Thermal-Efficiency-Through-Natural-Lighting-Energy-Saving.pdf (accessed on 1 January 2019).
19. Bashir, F.M.; Dodo, Y.A.; Mohamed, M.A.S.; Norwawi, N.M.; Shannan, N.M.; Afghan, A.A. Effects of natural light on improving the lighting and energy efficiency of buildings: Toward low energy consumption and CO_2 emission. *Int. J. Low-Carbon Technol.* **2024**, *19*, 296–305. [CrossRef]
20. Ibarra, D.I.; Reinhart, C.F. Daylight Factor Simulations—How Close Do Simulation Beginners 'Really' Get? June 2009. Available online: https://www.aivc.org/resource/daylight-factor-simulations-how-close-do-simulation-beginners-really-get (accessed on 13 May 2024).
21. Lamberts, R.; Hensen, J.L. *Building Performance Simulation for Design and Operation*; Spoon Press: London, UK, 2011.
22. Ezeh, C.I.; Hong, Y.; Deng, W.; Zhao, H. High rise office building makeovers—Exploiting architectural and engineering factors in designing sustainable buildings in different climate zones. *Energy Rep.* **2022**, *8*, 6396–6410. [CrossRef]
23. Stagrum, A.E.; Andenæs, E.; Kvande, T.; Lohne, J. Climate Change Adaptation Measures for Buildings—A Scoping Review. *Sustainability* **2020**, *12*, 1721. [CrossRef]
24. Motawa, I.; Elsheikh, A.; Diab, E. Energy Performance Analysis of Building Envelopes. *J. Eng. Proj. Prod. Manag.* **2021**, *11*, 196–206. [CrossRef]
25. De Dear, R. Recent enhancements to the adaptive comfort standard in ASHRAE 55-2010. In Proceedings of the 45th annual conference of the Architectural Science Association, Sydney, Australia, 14–16 November 2011; Citeseer: University Park, PA, USA, 2011; pp. 16–19.
26. Kharseh, M.; Altorkmany, L.; Al-Khawaj, M.; Hassani, F. Warming impact on energy use of HVAC system in buildings of different thermal qualities and in different climates. *Energy Convers. Manag.* **2014**, *81*, 106–111. [CrossRef]
27. Kükrer, E.; Eskin, N. Effect of design and operational strategies on thermal comfort and productivity in a multipurpose school building. *J. Build. Eng.* **2021**, *44*, 102697. [CrossRef]
28. Moret Rodrigues, A.; Santos, M.; Gomes, M.G.; Duarte, R. Impact of Natural Ventilation on the Thermal and Energy Performance of Buildings in a Mediterranean Climate. *Buildings* **2019**, *9*, 123. [CrossRef]
29. Sfakianaki, A.; Pavlou, K.; Santamouris, M.; Livada, I.; Assimakopoulos, M.-N.; Mantas, P.; Christakopoulos, A. Air tightness measurements of residential houses in Athens, Greece. *Build. Environ.* **2008**, *43*, 398–405. [CrossRef]
30. Caruggi de Faria, L.; Roméro, M.; Porras-Amores, C.; Pirro, L.; Sáez, P. Prediction of the Impact of Air Speed Produced by a Mechanical Fan and Operative Temperature on the Thermal Sensation. *Buildings* **2022**, *12*, 101. [CrossRef]
31. Anand, V.; Kadiri, V.L.; Putcha, C. Passive buildings: A state-of-the-art review. *J. Infrastruct. Preserv. Resil.* **2023**, *4*, 3. [CrossRef] [PubMed]
32. Sadineni, S.B.; Madala, S.; Boehm, R.F. Passive building energy savings: A review of building envelope components. *Renew. Sustain. Energy Rev.* **2011**, *15*, 3617–3631. [CrossRef]
33. Kent, R. *Energy Management in Plastics Processing: Strategies, Targets, Techniques, and Tools*; Elsevier: Amsterdam, The Netherlands, 2018.
34. Franco, A.; Schito, E. Definition of Optimal Ventilation Rates for Balancing Comfort and Energy Use in Indoor Spaces Using CO_2 Concentration Data. *Buildings* **2020**, *10*, 135. [CrossRef]
35. Maddalena, R.; Mendell, M.J.; Eliseeva, K.; Chan, W.R.; Sullivan, D.P.; Russell, M.; Satish, U.; Fisk, W.J. Effects of ventilation rate per person and per floor area on perceived air quality, sick building syndrome symptoms, and decision-making. *Indoor Air* **2015**, *25*, 362–370. [CrossRef] [PubMed]
36. Scherer, P.; de Fauro, D.O.; de Grigoletti, G.C.; Scherer, P.; Fauro, D.d.O.; Grigoletti, G.d.C. Energy Efficiency, Thermal Comfort, and Quality of Natural Ventilation Strategies for Classrooms. In *Cooling Technologies—Technologies and Systems to Guarantee Thermal Comfort in Efficient Buildings*; IntechOpen: Rijeka, Croatia, 2023; ISBN 978-1-83769-582-9.

37. Wouters, P.; Delmotte, C.; Faÿsse, J.-C.; Barles, P.; Bulsing, P.; Filleux, C.; Hardegger, P.; Blomsterberg, Å.; Pennycook, K.; Jackman, P.; et al. Towards improved performances of mechanical ventilation systems. *Tip-Vent Proj. EC Joule* **2001**, 58.
38. Goel, S.; Rosenberg, M.I.; Eley, C. *ANSI/ASHRAE/IES Standard 90.1-2016 Performance Rating Method Reference Manual*; Pacific Northwest National Lab (PNNL): Richland, WA, USA, 2017.
39. Hoxha, E.; Maierhofer, D.; Saade, M.R.M.; Passer, A. Influence of technical and electrical equipment in life cycle assessments of buildings: Case of a laboratory and research building. *Int. J. Life Cycle Assess.* **2021**, *26*, 852–863. [CrossRef]
40. Shiker, M. Multivariate Statistical Analysis. *Br. J. Sci.* **2012**, *6*, 55–66.
41. Piotrowska, E.; Borchert, A. Energy consumption of buildings depends on the daylight. *E3S Web Conf.* **2017**, *14*, 01029. [CrossRef]
42. Hussin, N.H.; Said, R.M.; Ishak, N. Analysis of Influence Factors Affecting The Energy Consumption in Technology Campus, UTEM. *Malays. Constr. Res. J.* **2020**, *32*, 29–36.
43. Solano, J.C.; Caamaño-Martín, E.; Olivieri, L.; Almeida-Galárraga, D. HVAC systems and thermal comfort in buildings climate control: An experimental case study. *Energy Rep.* **2021**, *7*, 269–277. [CrossRef]
44. Zhang, C.; Zhao, T.; Li, K. Quantitative correlation models between electricity consumption and behaviors about lighting, sockets and others for electricity consumption prediction in typical campus buildings. *Energy Build.* **2021**, *253*, 111510. [CrossRef]
45. Alghamdi, S.; Tang, W.; Kanjanabootra, S.; Alterman, D. Effect of Architectural Building Design Parameters on Thermal Comfort and Energy Consumption in Higher Education Buildings. *Buildings* **2022**, *12*, 329. [CrossRef]

Grid support by BESS. Benefits for a Solar Thermal Plant

Dorin Dumitru Lucache
Faculty of Electrical Engineering
„Gheorghe Asachi" Technical University of Iasi
Iasi, Romania
dorin.lucache@tuiasi.ro

Yosef Elia
Electrical And Control Engineering Department
BrightSource Energy
Jerusalem, Israel
yelia@brightsourceenergy.com

Elena Serea (Dănilă)
Faculty of Electrical Engineering
„Gheorghe Asachi" Technical University of Iasi
Iasi, Romania
edanila@tuiasi.ro

Cătălin Daniel Gălățanu
Faculty of Civil Engineering
„Gheorghe Asachi" Technical University of Iasi
Iasi, Romania
catalin.galatanu@tuiasi.ro

2023 10th International Conference on Modern Power Systems (MPS) | 979-8-3503-2682-6/23/$31.00 ©2023 IEEE | DOI: 10.1109/MPS58874.2023.10187444

***Abstract*— During the last decades, battery energy storage systems (BESS) plants have received a growing interest due to appearance of applications supporting the stabilization of the power grid and improving both the performance and revenues for renewable energy sources, such as photovoltaic (PV), concentrated thermal solar (CSP) and wind plants. The integration of the emerging grid disruptive technologies, such as renewable energy sources (RES) and electric vehicles (EVs) destabilize the power grid. Energy storage solutions are now commonly available. For instance, Li-ion manufacturers offer relatively reliable and economic residential battery solutions. BESS technology can support the power grid stabilization through frequency regulation (FR), auto voltage regulation (AVR), peak shaving and other applications, more efficiently and less expensive than the common practice technology used today as capacitors banks and synchronous generators. The paper aims to highlight engineering considerations on BESS technologies design for grid support applications, to more efficient use of renewable energy plants in the context of current and future considerations related to global economy and deep decarbonization of the grids. The work presents a technical-economic analysis based on a project of adding BESS to an existing solar thermal plant, in order to load leveling. The background is related exclusively to the context of the US energy market, as the CSP is subjected to.**

Keywords*— *frequency regulation, battery storage, energy markets, flow batteries

I. Introduction

Energy storage is a critical and growing need in the drive to increase the efficiency and effectiveness of power systems. Energy storage is becoming increasingly important in ground transportation, hybrid and electrical vehicle (EVs). Renewable energy sources as wind and solar require energy storage to buffer power production deficits. Home energy storage can reduce costs by taking grid power during low-demand periods (e.g., at night) and reducing grid power during high-demand periods. High energy costs drive the development of power systems with increased efficiency and effectiveness. One way to increase performance is to store energy that cannot be used concurrent with the production. [1].

The concept of energy storage contains many storage technologies for different applications. The applications that support the power grid are not necessarily energy storage, but they are generally attributed to this category.

Commonly, the BESS uses applications are categorized by services for Behind the meter (BM) and In front of the meter (IFM). The stakeholder for the BM is usually the End User and the services are [2]: Demand charge reduction, Power quality improvement, Renewables generation support (PV & Wind and Storage), Storage for Auxiliary plants (Geothermal, Solar thermal CSP), Backup power (UPS), Microgrid support and Revenues from grid services. The stakeholder for the IFM is usually the Grid Manager and the services are: frequency regulation (FR), energy arbitrage, black start, voltage support (by Auto Voltage Regulation - AVR), spin and non-spin reserve and capacity. There is no clear definition for FR application due to the fact that each network administrator configures this application according to their specific network behavior. Therefore, it is a challenge to design and implement the FR in a unique way for each network.

This article discusses the use of electric storage technology as BESS in the IFM applications to support grid stabilization through FR, AVR and optimize energy utilization for renewable plants. At the end, the economic benefits of using BESS to support a solar power plant are revealed by a feasibility study..

II. Challenges for Introducing Energy Storage into the Energy Market

The concept of energy storage is elaborated, concerning a wide range of technologies, locations, capacities, demands, and costs of investment. [3]. Energy Storage Modelling and Settlements was initiated by Public Utility Commissions (PUC) rule, PUC Project 39917 in the Texas US utility grid. PUCs are responsible for regulating the sale and distribution of electricity at the retail level. Each state in US has a PUC or equivalent organization. PUCs are Rules that were written to consider multiple types of storage technologies such as batteries, flywheels, CAES (Compressed Air Energy Storage), pumped storage, electrochemical capacitors, and thermal energy storage.

It is mandatory to get acquainted of the marketing rules to which the power system is subjected, in the event of connecting to the local utility grid and to be paid for the grid support. Likely particularities will be exemplified with the help of two American energy markets, ERCOT and PJM.

979-8-3503-2682-6/23/$31.00 ©2023 IEEE

A. ERCOT, the Regional Transmission Operator in Texas US Market

To understand the challenge of introducing the energy storage units to the energy market, ERCOT (the regional transmission operator in Texas US) functioning will be presented. Starting from its structure and roles (Fig.1), there were established the energy storage guiding principles as follows [4]:

1. An energy storage resource has the option of receiving wholesale storage load treatment.
2. Wholesale storage load is defined in Nodal Protocol Revision Request (NPRR) 461 as – "Energy that is separately metered from all other Facilities to charge a technology that is capable of storing energy and releasing that energy at a later time to generate electric energy".
3. Load for an energy storage Load Resource must be separately metered to be considered wholesale storage load.
4. Storage facility energy that is re-generated is treated in the same manner as traditional generation. The re-generated energy can self-serve associated Load behind the same point of interface (POI) at the generation site and/or be valued as an injection to the ERCOT system.
5. Storage load is exempt from charges and credits (wholesale on Load Ratio Share or per MWH basis).
6. Wholesale storage load will not be included in the ERCOT 4CP calculations (the average of an individual customer's peaks during the highest grid peak hours for each of the four summer months).
7. Wholesale storage load pricing shall be based on the locational marginal price (LMP) in the electricity market at the electrical bus, not the LMP of the load zone.

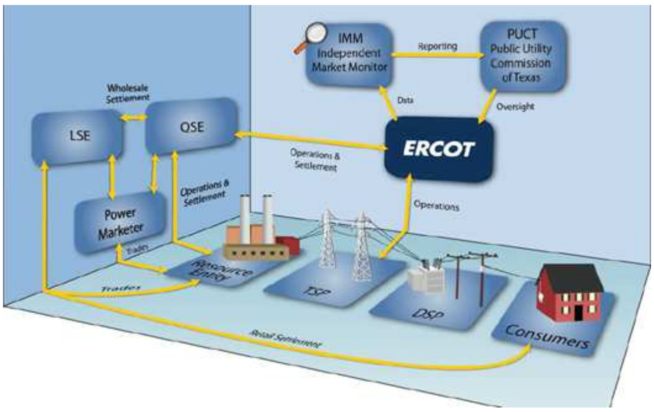

Fig. 1. ERCOT market structure and roles.

Under market environment, LMP based settlement strategy is used to determine the amount of money earned from ISO (International Organization for Standardization) by the energy sellers and paid to ISO by the energy buyers. Thus, the LMP is dependent on different market designs.

B. PJM energy market

The company PJM Interconnection operates several types of competitive wholesale markets through which large volumes of electricity are bought and sold across 13 states and the District of Columbia US. The markets underpin PJM's mission of reliability at the lowest-possible cost by giving financial incentives and encouraging competition to pro-vide electricity when it's needed to the 65 million people that PJM serves. Each market serves a separate function, but they work in tandem.

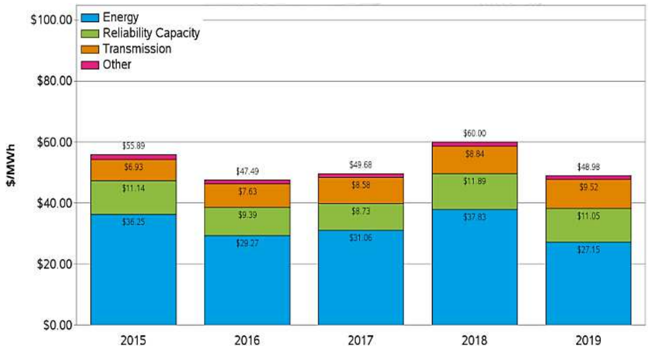

Fig. 2. Size of wholesale cost's components (2020) [5].

The largest of the PJM markets is the Energy Market, making up the majority of wholesale electricity costs (Fig.2). The Energy Market operates much like a stock ex-change. PJM matches the demand for electricity with offers to provide it. As the market operator, PJM's role is to balance the needs of buyers, sellers and other market participants and monitor market activities to ensure open, fair and equitable access. PJM markets are Day-Ahead Market, Real-Time Market, Capacity Market and Ancillary Services Markets. All these markets match offers from power suppliers with bids from power consumers to ensure that suppliers are ready to deliver at the right time and place.

In order to join the PJM energy market, it is necessary to understand the terms of joining in order to design and operate the energy storage units accordingly. It is possible to join all or part of the proposed PJM market conditions, depending on the energy storage capabilities to maximize profits from network support.

C. Market forecast in stationary energy storage

The use of batteries as a network storage system is promoted due to the fact, they are suitable for every stage in electricity supply chain (generation: 1÷50 MW, transmission: 1÷10 MW, distribution: 100 kW÷2 MW, consumption: 1÷10 kWh) [6]. Having a foresight of $82.89 billion growth market in 2021-2025, the global battery market will advance to a compound annual growth rate of 27.77% (with an already 21.56% expansion recorded in September 2021), of which 62% will be Asia-Pacific markets' grow contribution [7]. It is expected that IFM (in front of the meter / grid-scale) market to have an advancement against BM (behind the meter / residential, commercial and industrial) market, due to the larger dimensions of batteries to be installed. The preponderant placing of BESS in IFM sector (except in countries where relief characteristics and grid infrastructure will not allow) might lead to a significant global cost reduction in BM, expected to reach only 57 GWh of deployment, related to 706 GWh forecast in IFM by 2030. In particular, the BEV market (Battery Systems for Electric Vehicles) is expected to register a compound annual growth rate of 13.5% in the next 3 years.

Notwithstanding, concerns regarding a possible material crisis, safety operation, capability for seasonal energy storage without self-discharging or batteries' incompatibility with emerging requirements (railway surges or seasonal storage of solar), open a large market for alternatives. For example, electric train systems would save 15% of their energy if supercapacitors would store braking energy and 95% efficiently boost it into trains leaving; CAES (compressing air energy storage), LAES (liquefied air energy storage), GES (gravitational energy storage) or TES (thermal energy storage) can depot large amounts of electricity seasonally, the periodicity being required as solar is feeble in winter [8]. Segmentation of storage technologies appears as a safety and efficiency measure, preferred where systems require specific techniques for supplying the stored energy. Even if the energy storage market is dominated by Li-ion batteries, it is estimated that in 2041, alternative storage devices to reach 156 GWh: 60% completed by GES, CAES/LAES providing 32%, TES and flywheels 5%, supercapacitors 2%, hydrogen 1%. It reveals that new battery-less stationary storage, capable to operate in any point of the grid, will rise to a $6.5 billion market in 2031[9].

Regarding the source of the energy to be stored with the technologies above, the forecasts confirm the trend in favour of solar, respecting the desideratum of deep de-carbonisation of the grids. The DoE Study [10] shows that by 2035, solar energy has the potential to supply 40% of the US's electricity (with a deployment of 760–1000 GW), compared to 3% at present. As previsioned (Fig.3) the electric grid will deliver twice more energy in 2050, generated almost entirely by solar and other zero-carbon sources.

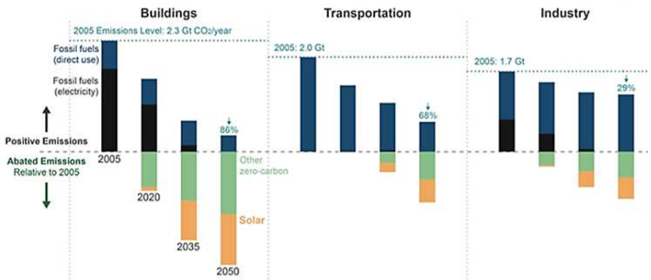

Fig. 3. The expected role of solar in US electric grid, on decarbonisation with electrification scenario

The next challenge for energy storage technologies is to weight a fast response time and the ability to recharge. Various utilities are ongoing to replace worn-out peaking plants that run infrequently with very large BESS systems that can provide power up to 10 hours. This requires energy duration levels beyond those commercially mature today, and a stable and unitary legislation (grid regulations and utility commissions at the federal and state level are still adjusting; in California currently, there is a limitation to 4 hours related to the nature of resource adequacy requirements [11] and in the east area covered by PJM settles that energy storage must have at least a 10-hour duration for its capacity contribution to match rated power capacity [12]). There occurs one favourable emerging technology with the potential to deliver this service: flow battery having the major advantage related to Li-Ion that the power (kW) and energy (kWh) components can be adjusted independently of one another without impacting performance. By increasing the volume of electrolyte, flow batteries can provide a 12 hour or longer duration of rated power capacity. This is a significant distinction from today's stationary Li-Ion products, which typically have duration of rated capacity between 0.5 to 4 hours [13]. Flow batteries can last for more than 20,000 cycles at 100% depth of discharge, are eco-friendly technologies with 67% lower CO2 emissions than Li-Ion, containing no toxic materials and requiring no special permits for disposal even if located underground [14]. That's why though its' market share is 1%, it has a predicted CAGR of more than 12% during 2022-2027 [15].

III. BESS - Various Type of Frequency Regulation (FR) for Grid Support

This paragraph outlines the technical requirements and design considerations for an IFM energy storage system. Several new ancillary services are under consideration within the regional transmission operators [16]. Thus, in addition to current requirements, the BESS should be designed with necessary provisions to provide future services where practical. This paragraph mainly describes the Responsive Reserve Service (RRS) and Fast Responding Regulation Service (FRRS) applications. Power commands are sent every 4 seconds to achieve frequency regulation. In response to the signal, the BESS site, sends back the value of the actual power applied to the batteries. The actual power that is applied to the batteries may be different from the command due to SOC of batteries or due to site policy. In fact, a policy is applied, that limit power at times in order to keep batteries life longer (SOC limit). The purpose of the local controller in BESS projects are:

a) Interface between the local controller at the BESS site and the communication system (SCADA) for the remote market operator;
b) Implement SOC limit for batteries asset in order to extend the batteries pack lifetime;
c) Performs the local frequency response to support the grid;
d) Handle lack of communication situation.

Battery storage plans can consist of one or more BESS units in parallel, producing the total power in the POI and the capacity of the contractual obligation (MW/MWh).

A. BESS units' concept

Each unit comprises of bidirectional inverter, battery banks, battery enclosure (HVAC, fire suppression) and transformer to fit the grid voltage. The complete system interfaces with the grid through switchgear and metering equipment. The local controller interfaces with a site controller which controls and monitors all units.

The application is defined by local utility, in this case study, as follow:

Primary Frequency Response – PFR (Fig.4):

- ±0.017 Hz dead band with drop of 1%.
- Required response time - within 16 seconds.

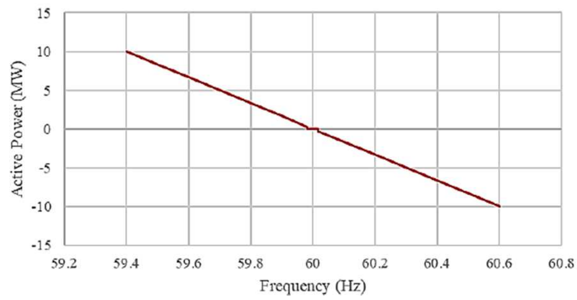

Fig. 4. Primary Frequency Response (PFR)

Responsive Reserve Service – RRS:

- Participate as a generator resource, discharge only.
- Energy requirements: 1 hour during qualification test.

- When PFR is not active and there is no remote signal (updated desired base point - UDBP) charging is allowed.

Remote signal

- Signal is received from utility systems once frequency drops to 59.91Hz (various regional sensing), as an UDBP for generator. Nominal utility frequency is 60Hz.
- Response time - within 10 minutes.

The graph in Fig.5 describes the grid frequency being supported by the BESS system. The blue area describes the frequency behaviour while the orange area describes the BESS system response to the frequency changes. At a nominal 60 Hz frequency, the BESS system does not respond (0 MW active power). Decreasing the grid frequency causes the BESS system to stabilize the frequency by discharge MW active power to the grid.

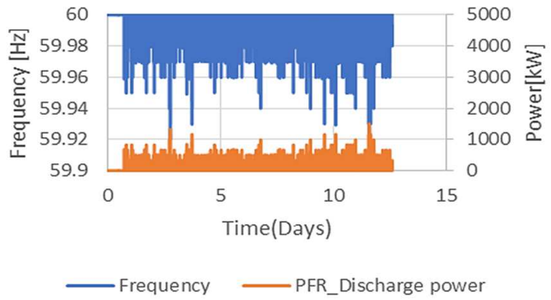

Fig. 5. Grid frequency regulation

Fast-Responding Regulation Service – FRRS

The regional transmission operator FR markets are composed of separate “Up Regulation” (320MW) and “Down Regulation” (300MW) markets. FRRS was implemented in 2014 to facilitate market operation for fast responding resources (like battery energy storage). It clears and operates as a subset of the FR market. Procurement for FRRS is limited to 65MW Regulation Up and 35MW Regulation Down. FRRS requires 8-minute energy duration at qualified offer amount for qualification and participation. FRRS is effectively a combination of frequency regulation and primary frequency response:

a) Frequency regulation response is shown below with both Up and Down deployments (Fig.6) dispatched through regional transmission operator Load Frequency Control (LFC).

b) PFR is required in <1 second when frequency deviations exceed ±0.09 Hz.

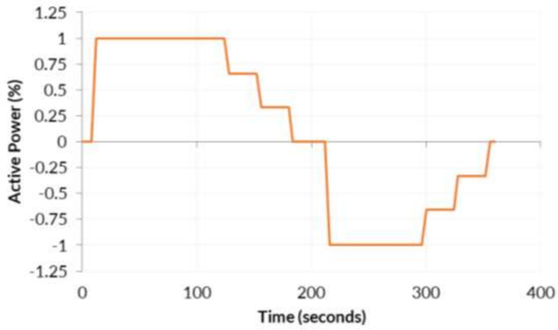

Fig. 6. FRRS up and down deployments

IV. Case Study: Benefits Adding BESS to an Existing Thermal Solar Plant

Cost projections of the energy storage value chain (feasibility, testing, development, construction and operation) are critical in achieving effectively the clean energy goal. Deployment and insertion of utility-scale technologies in order to achieve the decarbonization scenarios should involve costs that underbalance the benefits. Thus, a key reference element in Decarb+E scenarios is the levelized cost of energy or storage (LCOE / LCOS), defined as long term offtake price on a MWh-basis to recoup all project costs over the life time of a project and achieve a required equity hurdle rate on investment. For example, analyses are performed to evaluate storage systems on a levelized basis to derive cost metrics based on nameplate capacity – Fig.7 [17]. The capital structure consists of 20% debt at an 8% interest rate and 80% equity at a 12% cost of equity. Capital costs are compound of the energy storage system (storage module, balance of system and power conversion equipment), solar equipment and engineering, procurement and construction. Augmentation costs are included as part of operating and manufacturing expenses and vary across use cases due to usage profiles and lifespans.

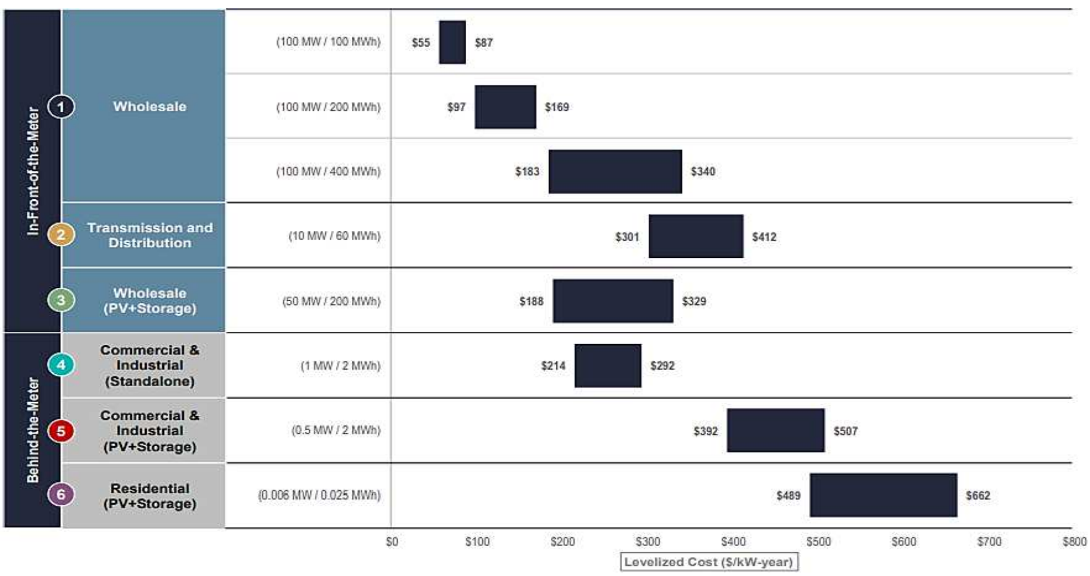

Fig. 7. The levelized cost of storage comparison on storage capacity ($/kW-year)

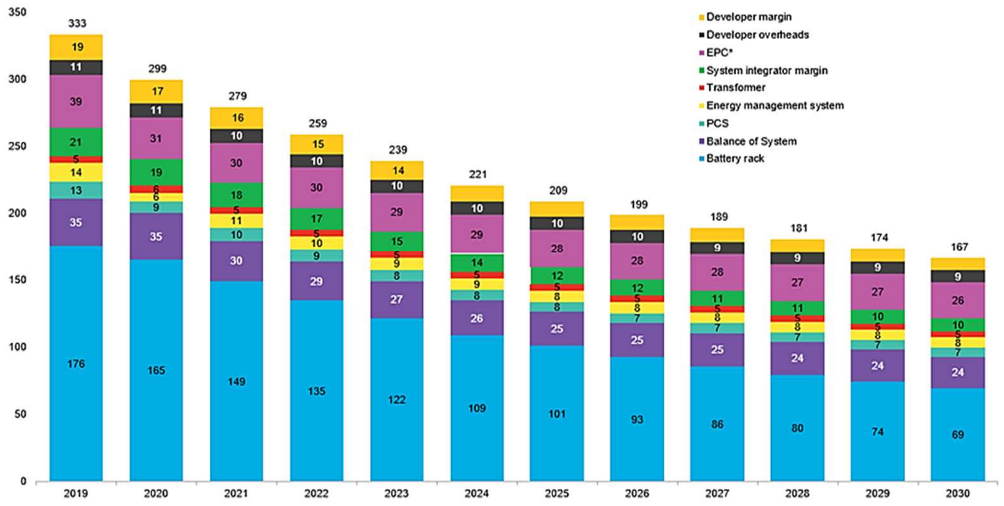

Fig. 8. ESS annual cost projections

As annual projections by 2030, the costs of an energy storage system are distributed decreasingly – Fig. 8. Estimating these investments serve to improve project's profitability as follows:

- Optimize sizing of energy storage assets at inception;
- Optimize augmentation scenario and budget;
- Optimize operational revenue vs. degradation (i.e. cycling);
- Factor the cost of degradation to determine when it is worth running the asset;
- Factor the cost charging the battery;
- Optimize choice of storage technology in function of degradation curve and round trip efficiency;
- Rely on predictive maintenance at subsystem and component level based on the actual hours of operations;
- Calculate Effective Load Carrying Capability (ELCC) - a measurement of BESS's ability to provide energy when the grid is most likely to experience power shortages, typically expressed as a percentage of the resource's capacity.

This section describes an economic feasibility study, adding a BESS system to an existing thermal solar plant in order to time shifting (load leveling) and increase the plant profits. Time shifting (load leveling) involves storing power during periods of light loading on the system and delivering it during periods of high price.

Main Data:

- 140MW existing CSP power plant;
- PPA (Power Purchas Agreement) rate: 110MW;
- Actual production power: 130MW;
- Estimate storage request: 4MW, 4 Hours;
- Estimate annual over capacity: 6000MWh;
- The contractual energy payment for 30 years of the thermal solar plant is 0.25 $/kWh.

Because the PPA contract is rated for 110 MW, any power above this value is not paid or receives a minimal payment. The idea is to store the annual over capacity by the BESS and to discharge during the morning and afternoon were the thermal solar power plant produce low energy.

Feasibility study requests for an estimate budget for one pilot unit: 1MW/4MWh, 10 years lifetime and a year later to add additional 3 units, to have in total 4MW/16MWh energy storage.

Starting from the annual income obtained from the energy supply (Table 1), were calculated the project's capital expenditures (CAPEX) for 1 unit (Table 2) and the internal rate of return (Table 3). CAPEX is calculated as the sum of the effective change in property, plant, and equipment (for the period under analysis) plus the current period depreciation expense. The results show that completing the existing thermal solar plant with BESS is a feasible measure, with the amortization of the investment in 5 years.

TABLE 1. THE VALUE OF THE REVENUE [$/KWH PER YEAR]

	Pilot unit 1MW/4MWh	4 units total 4MW/16MWh
Revenue $/kWh per Year	375000.00	1500000.00

TABLE 2. PROJECT'S CAPEX CALCULATION (CONSTRUCTION NOT INCLUDED)

Element	Notes	Subtotal cost
DC system	Includes: Batteries, Racks, BMS, Cabling and protections.	1,094,800.00
Inverter		100,000.00
Unit Transformer		35,000.00
4 bays MV SWGR		89,000.00
MV Cables		15,000.00
Meter and protection relays		12,000.00
Battery Container	Including HVAC & Fire system	150,000.00
UPS		
400/230Vac aux. panel		3,000.00
24Vdc aux. panel		16,000.00
IMD/RCM (GFP)	Bender	3,500.00
LV cables		14,500.00
Accessories		10,000.00
Unit JB		15,000.00
Manufacturing		60,000.00
Engineering & Project		70,000.00
Shipping equipment's to site	Batteries, Enclosures, Inverter, Taxes.	50,000.00

	Total cost	**1,737,800.00**
	Cost $ per kWh	**434.45 $/kWh**
	Margin	**15%**
	Price	**1,998,470.00**

TABLE 3. PROJECT'S CAPEX CALCULATION FOR FOUR IDENTICAL UNITS (CONSTRUCTION NOT INCLUDED)

Year	**CAPEX for 4 units**	**Revenue**	**Total**	**IRR**
0	-7,993,880		-7,993,880	
1		1,500,000	1,500,000	-81%
2		1,500,000	1,500,000	-46%
3		1,500,000	1,500,000	-24%
4		1,500,000	1,500,000	-11%
5		1,500,000	1,500,000	-2%
6		1,500,000	1,500,000	3%
7		1,500,000	1,500,000	7%
8		1,500,000	1,500,000	10%
9		1,500,000	1,500,000	12%
10		1,500,000	1,500,000	13%

The estimated budget is analysed further from the perspective of the risk whether the project will be delivered respecting exactly the proposed amounts from Table 2 and whether any contingency (extra budget) should be included so that this budget level to be achieved with a certain degree of confidence. As each element has a price within a min/max range, Pert distribution (which assumes that the predominance of the results occurs in the most probable range) can be applied to establish their possible cost. The distributions are assumed to be skewed, and the parameters have been chosen so that costs are more likely to overshoot than undershoot the base case. Results from Table 4 show that most likely the total budget will be of 1744413$, as the probability of meeting the base case value is only of 44.3%. In this case, a contingency of 76894$ is required, to achieve a 95% confidence degree for the required budget, which amounts to 1,814,694$.

The histogram (probability density of meeting the costs base case value), obtained from a simulation of 5000 iterations, is fitted for comparison with Gauss, triangular and Pareto distributions, in case other analyses are to be performed for the project's budget. The comparison graph from Fig.9 displays four curves — the input distribution (Pert), and the distributions created for the best fit analysis, along with summary statistics for each distribution.

TABLE 4. BUDGET COMPLIANCE RISK ANALYSIS

Cost elements	**Base Case**	**Min.**	**Most likely**	**Max.**	**Min.**	**Most likely**	**Max.**	**PERT estimation**
DC system	1094800	90%	100%	110%	985320	1094800	1204280	1094800
Inverter	100000	90%	100%	110%	90000	100000	110000	100000
Unit transformer	35000	90%	100%	110%	31500	35000	38500	35000
4 bays MV SWGR	89000	90%	100%	110%	80100	89000	97900	89000
MV, LV cables	29500	90%	100%	110%	26550	29500	32450	29500
Metering and protection	12000	90%	100%	125%	10800	12000	15000	12300
Battery container	150000	90%	100%	110%	135000	150000	165000	150000
Auxiliary panels (400/230V ac, 24V dc)	19000	90%	100%	125%	17100	19000	23750	19475
IMD/ RCM (GFP)	3500	90%	100%	125%	3150	3500	4375	3588
Accessories	10000	90%	100%	125%	9000	10000	12500	10250
Unit JB	15000	90%	100%	110%	13500	15000	16500	15000
Manufacturing / workforce	60000	80%	100%	130%	48000	60000	78000	61000
Engineering and project	70000	80%	100%	130%	56000	70000	91000	71167
Shipping to site	50000	100%	100%	140%	50000	50000	70000	53333
Output								
Totals	1737800							**1744413**

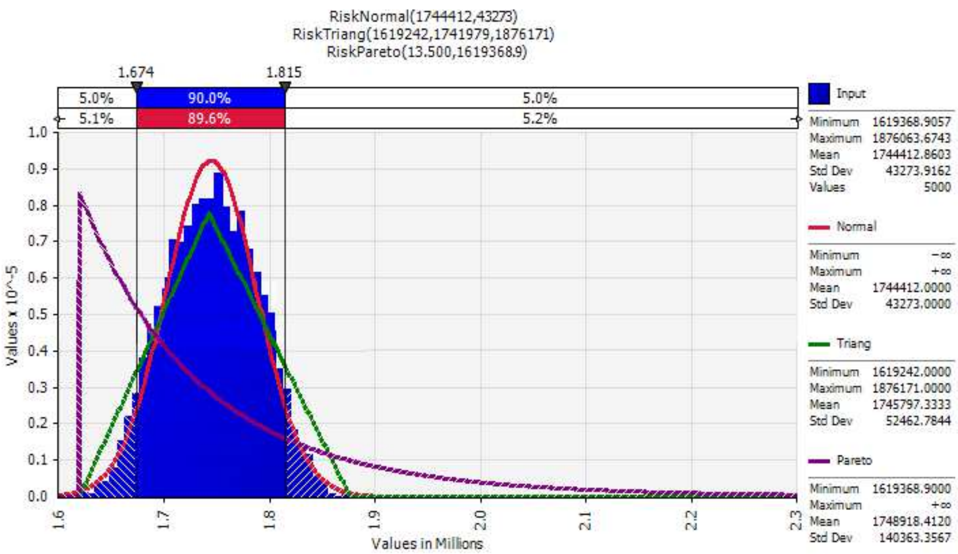

Fig. 9. Fit comparison for total project cost.

Regarding the BESS units, an analysis can be performed to state in term of performance and reliability which of Li-Ion and flow battery is more suitable for long duration storage. For a 1MW flow battery BESS, calculations yield a continuous auxiliary load of 11.125 kW when idle, up to 25.125 kW when discharging, and 72.125 kW when charging.

By comparison, based on [13] multiple leading Li-Ion BESS providers give the range of auxiliary loads for a similarly sized 1 MW system between 1 kW to 5 kW. This shows that flow auxiliary loads are up to 15 times higher than Li-Ion systems.

Related to the requirements of above case study, with the specifications from table 5, Li-Ion and flow batteries storage technologies were compared in terms of net annual cost of electricity, with results in Fig. 10. It is observed that the differences are insignificant for the analysed period of time.

TABLE 5. BESS CHARACTERISTICS TO SUIT THE POWER PLANT

Storage technology	Li-Ion	Flow battery
No. of units	4	4
BESS power capacity (kW)	2000	2000
BESS energy capacity (kWh)	4000	12000
Round trip charge/ discharge efficiency	85%	76%
Annual energy capacity degradation	2-4%	0-0.5%
Initial BESS purchase ($)	1086800	3580720
5-year future pricing reduction	28%	38%
Selected use case stack: DCM (demand change management)		

Because of the higher price and operation costs, flow battery BESS is not yet a preferable technology solution to Li-Ion. More, being an emerging technology, it hasn't valued the large cost reductions due to economy of scale that Li-Ion has purchased. If flow batteries' costs decrease in the future, there may very likely be conditions where this BESS would provide a more attractive solution than Li-Ion. The potential for flow battery technology is to provide, besides higher energy capacity, important benefits by reducing long term replacement requirements.

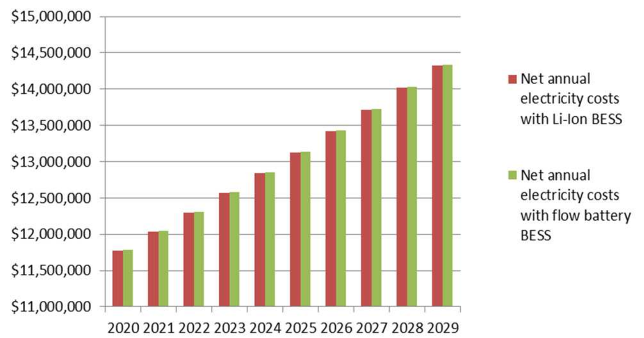

Fig. 10. Economic comparison between 2 BESS technologies suited for CSP.

V. CONCLUSIONS

Using BESS as a grid support brings both operational and economic benefits through frequency regulation, auto voltage regulation, peak shaving and other applications, more efficiently and less expensive than the common practice technology used today as capacitors banks and synchronous generators.

The case study shows that adding a BESS to an existing solar thermal power plant is economically viable. According to IRR calculations, an investment in BESS units will be covered in 5 years. By design an augmentation process in the tenth year, the units will be able to continue working for 20 years. This is a plus in the context in which long-duration energy storage will be needed to decarbonize the global energy system.

In addition to the direct economic advantage, there is another important one. Thermal solar plants are sensitive to the entry of clouds which causes a decrease in power and grid instability. The BESS unit can help with grid stability during clouds.

REFERENCES

[1] C. Rahn, C-Y. Wang. Battery Systems Engineering, John Wiley & Sons, 2013; pp.9-11.

[2] F. Garrett, J. Mandel, J. Morris, H. Touati. The Economics of Battery Energy Storage: How multi-use, customer-sited batteries deliver the most services and value to customers and the grid. Rocky Mountain Institute, 2015; pp.25-26.

[3] H. Abdi, B. Mohammadi, S. Javadi, A. Khodaei, E. Dehnavi. Energy Storage Systems, Butterworth-Heinemann, 2017, Chapter 7, pp. 333-368.

[4] A. Rosel. ERCOT Reports, https://www.pjm.com/-/media/committees-groups/committees /mc/2020/20200121-webinar/20200121-item-07a-markets-report.ashx.

[5] P. Du, N. Mago, W. Li, S. Sharma, Q. Hu, T. Ding. New Ancillary Service Market for ERCOT. IEEE-Access 2020, volume 8, pp. 178391-178401.

[6] Y. Zhao, O. Pohl, A. Bhatt, G.E. Collis, P.J. Mahon, T. Rüther, A.F. Hollenkamp. A Review on Battery Market Trends, Second-Life Reuse, and Recycling. Sustainable Chemistry 2(1), 167-205 (2021).

[7] Technavio. Battery Market by Application and Geography - Forecast and Analysis 2021-2025, sept.2021.

[8] N. Soni, D. Sharma, M.M. Rahman, P.R. Hanmaiahgari, V.M. Reddy. Mathematical Modeling of Solar Energy based Thermal Energy Storage for House Heating in Winter. Journal of Energy Storage 34, Volume 34, 102203 (2021).

[9] P. Harrop. Stationary Energy Storage Without Batteries: Grid, Microgrid, UPS, Trackside 2021-2041. IDTechEx Research Report, April 2021.

[10] U.S. Department of Energy. Solar Futures Study. September 2021, pp.39. https://www.energy.gov/sites/default/files/2021-09/Solar%20Futures%20Study.pdf.

[11] P. Denholm, R. Margolis. The Potential for Energy Storage to Provide Peaking Capacity in California under In-creased Penetration of Solar Photovoltaics, Technical Report NREL/TP-6A20-70905, pp.6.

[12] Electric Storage Participation in Markets Operated by Regional Transmission Organizations and Independent System Operators, Order No. 841, FERC Stats. & Regs. 31,398 (2018).

[13] B. Lavoie. Demonstrating the Benefits of Long-Duration, Low-Cost Flow Battery Storage in a Renewable Microgrid. ESTCP Project EW19-5312 Report, dec.2019.

[14] Long Duration Energy Storage Systems for a Cleaner Future, ESS 2021 https://s28.q4cdn.com/365128779/files/doc_presentations/2021/ESS_Analyst-Day-Presentation-8-30-21.pdf

[15] Flow battery market - growth, trends, covid-19 impact, and forecasts (2022 - 2027) report, https://www.researchandmarkets.com/reports/5552639/flow-battery-market-growth-trends-covid-19.

[16] H.T. Kim, Y.G. Jin, Y.T. Yoon. An Economic Analysis of Load Leveling with Battery Energy Storage Systems (BESS) in an Electricity Market Environment: The Korean Case. Energies 12, 1608 (2019).

[17] Lazard's levelized cost of storage analysis ver.6.0, 2020, pp.5. https://www.lazard.com/media/451418/lazards-levelized-cost-of-storage-version-60.pdf.

applied sciences

MDPI

Article

Electric Bus Indoor Heat Balance in Cold Weather

Gabriel Chiriac [1], Dumitru Dorin Lucache [1], Costică Nițucă [1], Alin Dragomir [2,*] and Seeram Ramakrishna [3]

[1] Department of Energy Utilisation, Electrical Drives and Industrial Automation, Faculty of Electrical Engineering, "Gheorghe Asachi" Technical University of Iasi, Bd. Dimitrie Mangeron, 21-23, 700050 Iasi, Romania; gchiriac@tuiasi.ro (G.C.); dorin.lucache@tuiasi.ro (D.D.L.); costica.nituca@tuiasi.ro (C.N.)

[2] Department of Power Engineering, Faculty of Electrical Engineering, "Gheorghe Asachi" Technical University of Iasi, Bd. Dimitrie Mangeron, 21-23, 700050 Iasi, Romania

[3] Department of Mechanical Engineering, College of Design and Engineering, National University of Singapore, 21 Lower Kent Ridge Road, Singapore 119077, Singapore; seeram@nus.edu.sg

* Correspondence: alin.dragomir@tuiasi.ro

Abstract: The use of electric buses is increasing all over the world; this is due to the aim of limiting pollution in heavily urbanized areas. Using electric buses is one element of the desire to drop local pollution to zero emissions. The necessary electricity can be generated through centralized production, and in the case of electric buses, the pollution level is directly proportional to the amount of electricity produced. Their limited onboard power needs optimization, both in terms of traction and in auxiliary energy consumption. Heating in electric buses consumes the most energy from the auxiliaries, which can reduce the range of the vehicle up to a half, or more in the coldest days of the winter months. In this context, a precise estimation of heat loss and of the energy necessary for heating electric buses is crucial. Using the heat transfer theory, the heat balance method, and the U-value estimation, this article estimates the heat loss for a typical 12 m electric bus for a harsh winter day. Thermal simulations were made in order to estimate the heat flux through the structure of the bus (windows, walls, roof, and floor). Heat loss components were calculated in order to determine the most affected zones of the bus. The calculated data for the energy necessary to heat the bus were compared with the heating system data from an electric bus. By optimizing the necessary auxiliary energy consumption, the emissions at the source of electricity production will be significantly reduced.

Keywords: electric buses heating; heat loss; heat balance method; U-value; thermal modeling

Citation: Chiriac, G.; Lucache, D.D.; Nițucă, C.; Dragomir, A.; Ramakrishna, S. Electric Bus Indoor Heat Balance in Cold Weather. *Appl. Sci.* **2021**, *11*, 11761. https://doi.org/10.3390/app112411761

Academic Editor: Luis Hernández-Callejo

Received: 5 November 2021
Accepted: 8 December 2021
Published: 10 December 2021

1. Introduction

With the accelerated evolution of the development and utilization of electric vehicles, and with many constraints related to energy consumption and environmental pollution, there is more and more research being published related to electric vehicles, giving attention to various goals, such as: reducing energy consumption, improving efficiency for the electric motors, optimizing the auxiliary systems, improving the energy storage capacity, and developing charging system capabilities for the electric vehicles.

Along with these aspects, the thermal comfort of the passengers and drivers, even in extreme conditions, are being studied worldwide, from small electric cars to large electric vehicles, such as electric buses.

Electric buses have many benefits compared with their thermal engine counterparts: they have no emissions and do not pollute the air, they are low noise vehicles and have fewer vibrations, offering superior comfort for the passengers and, importantly, they can use locally produced (and renewable) electric energy.

To make the transition from the conventional engine buses to the electrical ones, authorities and public transport operators have to invest not only in the establishment and development of electric bus fleets but also in new infrastructure. Some countries are planning to ban vehicles with thermal engines, while in some cities there are areas considered to be low or zero emission zones. Some cities are part of the C40 Fossil Fuel Free Street Declaration, which promotes the use of only zero emission buses by 2025, asserting that most of the participating cities will use emission-free vehicles by 2030 [1].

More than 1 million buses are used in Europe and around 690,000 buses are in use in the European Union, with the average age of the buses being about 12 years. Thermal engine buses account for more than 94% of the EU fleet, and less than 2% are battery electric or hybrid electric buses [2].

Some limitations are still obstructing the expanding use of electric buses, as follows:

- The limited range and power, as compared with conventional thermal buses.
- The necessity of new infrastructures, such as the power grid and systems for battery charging.
- The availability of personnel qualified in technologies different from conventional vehicles, for the maintenance of the electric buses.

There are various types of electric buses, which vary depending on whether electrical energy is generated or stored onboard. Hybrid electric, fuel cell electric, and full battery electric buses are currently being used around the world [3].

Hybrid electric buses use both an internal combustion engine and an electric motor to power the vehicle. Because they have partially a similar technology as traditional engine buses, they are a convenient transition to electric vehicles; however, they raise the same issues as classical vehicles (air pollution and dependence on conventional fuel).

Fuel cells are based on a chemical reaction between stored hydrogen and ambient oxygen to generate electricity. They assure long range and low emissions but are expensive and require a special infrastructure to store the hydrogen and to refuel the vehicles.

Full battery electric buses store all the necessary energy in an onboard rechargeable battery pack. They have no emissions and are energy efficient but have limited distance range and require a charging infrastructure [3].

Moreover, there are various charging systems, such as overnight charging (large size batteries are charged statically from the grid at the depot, mainly during the night, for up to 5–8 h); opportunity charging (medium size batteries are recharged at passenger stopping points or at the bus terminals); or a combination of depot charging and opportunity charging.

Irrespective of the types of electric bus and charging system, the energy from the power source is used for the traction needs and for the auxiliary systems on the vehicle (ventilation, heating, cooling, interior and exterior lights, passenger information devices, ticket vending machines, and others).

The energy required by the auxiliaries could reach up to 35% of the total energy consumption of the electric vehicle, and, depending on the environment conditions—especially the external temperature—the non-traction needs could consume up to 50% of the total energy on vehicles [4], or even up to 70% in very cold days in winter, when the heating system is used at full power [4,5]. Thus, the reduction in energy used for non-traction needs is a main challenge in order to reduce the total energy demand on the electric buses. It is particularly important for battery vehicles, because the batteries—as the energy source—have a limited capacity and limited range [4].

From all the auxiliaries, the heating and cooling consume the most energy—up to 35% [6]. Moreover, the temperature inside the vehicles depends on the cabin volume: at the same driving conditions, a large vehicle has a different temperature than a small class one. The class of the vehicle, reflected in the quality of the equipment and materials, will also influence the warming and cooling of the vehicle [7].

Conventional vehicles use internal combustion engines, which produce enough waste heat to heat up the vehicle, through the engine cooling circuit via a heat exchanger. Nevertheless, modern thermal engines are more efficient and produce less waste heat; therefore, supplementary electric heaters are necessary to heat the cabin in cold conditions [8].

Electric vehicles use electric motors which generate low amount of waste heat [8]. Even the heat released from the main battery pack is not enough to heat the interior of an electric bus, being needed for other heat sources. Therefore, the energy for the heating system is supplied by the power source, the battery pack, which is mainly used for driving and has limited capacity.

The heating has a significant influence over the range of the electric vehicle, reducing the range of the electric vehicle by half, or even more with an external air temperature of 0 °C [5].

In order to decrease the energy consumption for the HVAC systems on electric buses, several solutions have been proposed, as follows [8–11]: using recovery heat from the traction batteries; an integrated air conditioning and heating system; improved control systems for the heating system; door air curtains/air screened doors to reduce the heat exchange between the inside and outside of the bus [12]; heat pumps; thermal pre-conditioning; complex additional heating equipment. Infrared radiation heating in the vehicle cabin has also been studied for electric vehicles [13,14]. Solid media high-temperature thermal energy storage systems are also being researched for battery electric vehicles [15].

However, many of the above solutions are based on well-known methods, combined with improved strategies for control and optimization.

Therefore, research aiming to improve the heating are in demand for electric vehicles, in order to consume less energy while maintaining passengers' thermal comfort. Thus, new HVAC systems structures and advanced control will bring the best benefits, rather than using advanced cabin materials or increasing thermal isolation [8].

Urban road transportation usually uses technologies adapted from the car industry. In public transportation, where the doors open frequently, allowing passengers to exit and enter the vehicle, it is difficult to ensure a high comfort level. The most common solution for the heating system involves the use of engine cooling water, along with electrical resistance heating [12].

A combined heating configuration composed of zonal air flow and heated surfaces—driver seat, steering wheel, and floor mat—can reduce the heating energy by up to about 28%, while maintaining an equivalent thermal sensation. By simulation, [16] found that the combination of zonal air and surface heating can lead to a 7–19% improvement of the bus range.

Cabin preheating could also increase an electric vehicle range from 4% to 10% for 20 min of pre-conditioning [8]. There are basically two ways of reducing the power consumption for heating the electric vehicles, as follows: (1) reduction in heating loads and (2) improvement of the thermal system efficiency [8].

The heated load for an electric vehicle includes ventilation load and ambient load. The ventilation load is necessary for two reasons, as follows: the first is to assure the air quality inside the cabin (to keep a low concentration of CO_2) and the second is to prevent fogging on the windshield and on the other windows [9]. Using recirculated air is a method of reducing the ventilation load, along with using a low thermal conductivity glass for the windshield and windows.

The ambient load is a product of the temperature difference between the cabin air and the external environment, because the heat flows through the vehicle body structure. Some studies on using thermal isolation materials for vehicles showed up to 18% less heating load. On the other hand, thermal isolation does not always solve the issues, because it can lead to a strong greenhouse effect during the warm days in summer [9].

Zonal heating and inner surface heating (heated seats) are also methods of reducing the heating loads requirements.

In this article, the main goal was to calculate the heat loss for a typical 12 m electric bus, considering the conditions of a harsh winter day in Romania. Heat loss components were calculated in order to determine the most affected zones of the bus. The analyzed vehicle was actually a trolley bus (supplied from the contact lines), which has been adapted to also operate independently on traction batteries during its route. Due to the limited onboard battery, the distance to be covered as an autonomous vehicle is quite limited, especially in cold weather in winter, when the heating system is in use and the necessary power for the heating system is very high (up to 30 kW). The goal of our work was to calculate the heat loads inside this specific electric vehicle, with the aim to find the possibilities for optimizing the energy consumption for this type of vehicle.

Thermal simulations were carried out in order to estimate the heat flux through the structure of the bus (windows, walls, roof, floor, and doors). The calculated data for the necessary energy to heat the bus were compared with the heating system data from a real electric bus.

2. Heat Balance for an Electric Bus

Optimal energy consumption and interior thermal comfort for the passengers can be calculated and modeled by using heat transfer theory, the heat balance method, and the U-value (thermal transmittance) [17]. Based on the heat transfer theory, there are three mechanisms for transferring heat: conduction, convection, and radiation. Heat transfer into the electric bus is a complicated process, due to the complexity of the vehicle (windows, walls of various layers, floor, roof, and doors) and because all three of the heat transfer mechanisms are present.

2.1. Heat Conduction

Conduction appears inside a solid material or between two solid materials and follows Fourier's law for one-dimension, with a temperature gradient inside the material being required for heat transfer. Thus, considering the one dimension as x direction, a solid material, for which k is the thermal conductivity, and for a local thermal gradient of $\frac{dT}{dx}$, the conduction heat flux (q_{cond}) through the material can be calculated with the following equation:

$$q_{cond} = -k\frac{dT}{dx}, \quad (1)$$

The heat transfer by conduction in electric buses presents in areas such as the windows, the walls, the roof, the floor, the doors, and any other object inside the vehicle (the seats, for example).

2.2. Heat Convection

Convection is an important method of heat transfer for fluids, both inside the fluid and for fluids in contact with solids, and it can be natural or forced convection. Considering the temperature of the fluid T_{fluid} and the temperature of the body T_{body}, the heat flux resulting from convection can be calculated as shown in Equation (2), where the constant, h, is the heat transfer coefficient, as follows:

$$q_{conv} = h\left(T_{fluid} - T_{body}\right), \quad (2)$$

Convection in electric buses takes place at the contact between the surfaces of the walls and the fluids such as air (inside the bus) and the air or rainwater (outside the bus). While in the interior the convection has a low variation, on the outside it is amplified with the increase of the bus speed.

2.3. Heat by Radiation

Radiation is the only energy transfer mechanism that does not need a material support and depends on the source's temperature and the source's surface properties. For cold bodies, the heat transfer is negligible compared with convection and conduction. Based on the Stefan–Boltzmann law for a black body, this energy emission can be calculated as follows:

$$q_{rad}(T) = \epsilon \cdot \sigma \cdot T^4, \quad (3)$$

where ε is the emissivity of the body, σ is the Stefan–Boltzmann constant, and T is the temperature of the body [K].

The main radiation heat load for a bus is caused by the Sun, and, depending on the weather conditions and the seasons, it can have an important contribution to the heat load balance (during a sunny day at midday) or it may have low impact in heating a bus (during a cloudy and cold winter day).

2.4. Heat Balance Method for Vehicles

The heat balance method is a common method for calculating heating and cooling loads in a given space or zone [17]. Based on this theory, all heating loads can be written in a comprehensive equation. Four distinct processes can be assumed for the heat balance into an electric bus, as follows:

1. Outdoor surface heat balance.
2. Indoor surface heat balance.
3. Wall conduction.
4. Inside zone air heat balance.

For an optimal design of the heating system inside the bus, it is crucial to accurately determine the heating loads, because underestimating them may lead to thermal comfort problems, while an overdesign may increase the manufacturing and operating costs for the vehicle [18].

Various heat loads must be considered, but there are eight main heat components to estimate in the modeling and calculation of a vehicle cabin's thermal balance [8,18–20], as follows (Figure 1):

1. Metabolic heat load generated by the passengers—$\dot{Q}_{met}$.
2. Solar heat loads (caused by the Sun's radiation) with three components—$\dot{Q}_{sun}$, as follows:
    - Direct radiation from the Sun;
    - Diffused radiation due to the dispersion in the atmosphere;
    - Reflected radiation from the ground and other surrounding surfaces.
3. Heat load due to the electric motors—$\dot{Q}_{mot}$.
4. Heat load generated by the traction battery—$\dot{Q}_{bat}$.
5. Heat load due to the fresh air supplied by ventilation, which is necessary for passengers' needs—$\dot{Q}_{ven}$.
6. Heat flow changed with the ambient load, due to the temperature gradient between the bus structure (windows, walls, floor, roof, and doors) and the exterior environment—$\dot{Q}_{amb}$.
7. Heat flow changed with the ambient load, due to the doors opening during stops in stations—$\dot{Q}_{door}$.
8. Heat load generated by the heating system from the vehicle in order to assure the thermal comfort for passengers—$\dot{Q}_{hsyst}$.

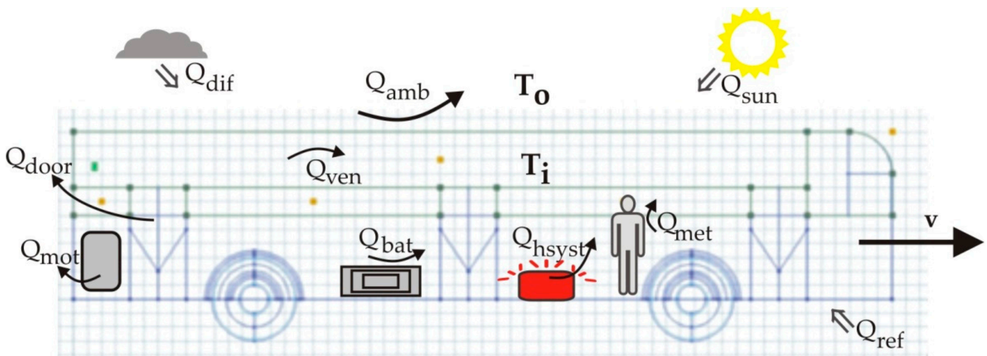

Figure 1. Schematic representation of heat loads: a model for a typical electric bus.

Thus, considering the above heat components, the heat load model for an electric bus is given by Equation (4):

$$\dot{Q}_{total} = \dot{Q}_{met} + \dot{Q}_{sun} + \dot{Q}_{mot} + \dot{Q}_{bat} + \dot{Q}_{ven} + \dot{Q}_{amb} + \dot{Q}_{doors} + \dot{Q}_{hsyst}. \quad (4)$$

3. Heat Load Estimation for an Electric Bus

The necessary power for heating the cabin of the electric buses is estimated in some studies, including [4,6,21,22]. According to [6], the energy consumption for heating a bus can reach up to 35% of the main battery's energy. In [4], data is presented for 12 m electric buses, with the necessary heating power varying from 5 kW up to 25 kW in absolute value, depending on the weather conditions and the time of the day.

In case of resistance heating, the energy demand can, in a worst-case scenario, double or even almost triple the vehicle's energy consumption. From measurements on a 12 m electric bus, it was estimated that the average electric power necessary to keep the cabin's temperature at 17 °C on a cold winter day with a −10 °C environment temperature was about 24 kW [21].

Another calculation estimates a heat loss of about 17.4 kW for a 12 m length bus, depending on the materials of the vehicle and considering only the thermal conduction through the structure of the bus and the heat loss through the open doors [22].

In this article, for the heat loss estimation, a typical low floor electric bus, with the following characteristics, is considered [23]: 12 m length, 100 passengers capacity, 150 kW electric motor, 3 doors, maximum speed 60km/h. The heating system of the bus has an installed power of 33 kW and is composed from 4 heaters of 6 kW each, used to heat the passengers' cabin, and a 9 kW heater for the driver's area. The vehicle is operating mainly as a trolley bus (supplied form the contact lines), and it is adapted to operate also independently on traction batteries during its route.

The estimation of the heating loads assumes difficult case conditions of a cold day in winter with a −10 °C temperature of the outside environment. Heat loads are calculated for continuous working conditions and the heat load required at first start of the bus was neglected at this stage.

The aim was to estimate the rate of heat to be added inside the vehicle by the heating system in order to maintain the desired conditions for thermal comfort, with a temperature of 20 °C being considered for the interior of the vehicle. Additionally, the heat loss by its component is to be determined in order to estimate the area consuming the most energy.

3.1. Metabolic Heat Load Generated by the Passengers, $\dot{Q}_{met}$

Because passengers of a bus sit and stand, the heat load can be estimated separately, as in [18], with the metabolic heat production rates of 60 W/m^2 and 70 W/m^2, respectively, and with 120 W/m^2 for the driver of the bus. These values are related to the surface area of a person, of about 1.80 m^2 [18]. Other authors [24] consider, for the sitting passenger, 55 W/m^2 and 85 W/m^2 for the driver.

Taking into consideration that, during the cold days in winter, the heat released by the human body into the surroundings is limited because the people are dressed in thicker clothes—these thermal values are to be considered for their lower values. Thus, for the calculation, a medium value of 60 W/m^2 is accepted, which, for a person, results in 60×1.8 m^2 = 108 W.

Buses are rarely at their full capacity, the average occupancy of a city bus being less than 40%, or even about 30% [25]; therefore, for the heat load generated by 40 passengers, a 4.32 kW value is estimated.

3.2. Solar Heat Loads—$\dot{Q}_{sun}$

3.2.1. Direct Radiation from the Sun

Heat gain, due to direct radiation, depends on the direct normal irradiance—the incident angle of the radiation—on the area and the transmissivity of the surface. The heat gain due to the direct radiation can be estimated as follows [18]:

$$\dot{Q}_{sunDir} = A \cdot \tau \cdot I_{Dir} \cdot cos(\theta) \quad [\mathrm{W}], \tag{5}$$

where A is the surface area [m^2], τ is the transmissivity of the material, I_{Dir} is the direct normal solar radiation [W/m^2], and θ is the incident angle of the solar radiation.

3.2.2. Diffused Radiation Due to the Dispersion in the Atmosphere

This is a heat gain due to the dispersion of the solar radiation on the atmosphere and has specific calculation formula [18], as follows:

$$\dot{Q}_{sunDif} = A \cdot \tau \cdot I_{Dif} \quad [\mathrm{W}], \tag{6}$$

where A is the surface area [m^2], τ is the transmissivity of the material, and I_{Dif} is the diffused solar radiation [W/m^2].

3.2.3. Reflected Radiation Due to the Ground

In this case, the heat gain is due to the radiation reflected by the ground. Taking into account the winter weather, when the roads are cold, this heat gain is to be considered as negligible for our calculation.

3.2.4. Solar Heat Gain Estimation for Romania

Romania is situated in the Central to East European continent area, between 43°37′ and 48°15′ latitude North, and 20°45′ and 29°41′ longitude East, having a temperate continental weather, with about 6 months of cold weather (from October to March). January and December are the coldest months of the year, with average temperatures of about −6 °C at midday, with lower temperatures (down to −10 °C) during mornings and evenings, and with minimum temperatures of down to −24 °C (based on the official data from the National Meteorological Administration from Romania [26]). During this 6-month period, the solar irradiation to be considered is usually between 9.00 and 15.00 h of the day (direct radiation load decreases due to the decrease in the sun elevation angle for the simulation period, which happens after midday [24]), having clear sky for about 40% of the day [27].

The solar heat gain for a bus varies permanently because it depends on a multitude of factors: time of day, clear or covered sky, the angle of incidence of solar radiation, the variable position of the vehicle, the possibility of shading it depending on the route (especially in the urban areas, with boulevards sheltered by high buildings), varying surfaces, and the transparency of the windows, etc. Therefore, the estimation of heat gain from solar radiation can only be carried out roughly, considering several simplifying hypotheses.

Existent data about the solar irradiation in Bucharest, the Romanian capital, during December and January are summarized in Table 1—global irradiation includes measurements for both direct and diffused solar radiation.

Table 1. Global irradiation includes measurements for both direct and diffused solar radiation.

	Hourly Average of Sun's Brightness, around 12 O'Clock	Hour	9	12	15	Daily Irradiation Average, [W/m^2]
			Global Solar Irradiation, [W/m^2]			
December	0.36	Clear sky	89	145	85	106.3
		Overcast sky	25	68	24	39.0
January	0.39	Clear sky	130	280	132	180.7
		Overcast sky	65	145	68	92.7

If HA_{12} is the "Hourly average of Sun's brightness, around 12 o'clock", and I_{glC} and I_{glO} are the global solar irradiation for the clear sky, respectively, for the overcast sky, then the maximum solar irradiation of the bus happens at noon and can be calculated with the following relation:

$$I_{Max} = HA_{12} \cdot I_{glC} + (1 - HA_{12}) \cdot I_{glO} \quad [\mathrm{W/m^2}], \tag{7}$$

With the data in Table 1, the above relation shows I_{Max} = 197.7 W/m^2. However, the solar irradiation of the bus during these two winter months manifests for maximum of 6 h per day and not all is transformed into the heat. Factors that reduce solar heat inputs, such as the transmissivity of windows, exterior shading, and reflective surfaces, etc., must be taken into account.

The 12 m bus has a transparent window area of 29 m^2, and for a double pane window the transmissivity is τ = 0.75 [18]. Keeping the same hourly average of Sun's brightness and applying Relation (7) for the daily average of solar irradiations, the average heat gain is given in Table 2 for both of the winter months considered.

Table 2. Average heat gain for both direct and diffused solar radiation.

	HA_{12}	Average Solar Irradiation, [W/m^2]	Bus Windows Area, [m^2]	τ	Average Heat Gain [kW]	Daily Average Heat Input, [W/m^2]
December	0.36	63.24	29	0.75	1.38	8.25
January	0.39	126.99			2.76	16.57

The presented calculation is a rough estimation of the heat gain and daily heat input. Contributions of the shading factor or reflected radiation, due to the ground, are neglected. Results showed that the most demanding month for the heating installation is December.

3.3. Heat Flow Due to the Fresh Air Supplied by Ventilation, Which Is Necessary for Passengers' Needs—$\dot{Q}_{ven}$

Ventilation and ambient loads are functions of the temperature difference between the cabin and the ambient load. The air flow rate for the buses depends on the operating of the air conditioning system, with values between the 0.05 m^3/s and 0.3 m^3/s [28]. For the city buses with frequently stops, the fresh air supplied by ventilation is dominated by the air flow through the open doors, and the ventilation can be used for the lower value, which is 0.05 m^3/s [28]. Heat transfer due to the ventilation can be estimated with Formula (8) and depends on the temperature difference (ΔT), the specific heat, the air density (ρ_{air}) and the air flow rate ($\dot{V}$) [29], as follows:

$$\dot{Q}_{ven} = \dot{V} \cdot \rho_{air} \cdot c \cdot \Delta T \quad [\mathrm{W}], \tag{8}$$

For an air flow rate of 0.05 m^3/s, an air density of 1.27 kg/m^3, a specific heat of 1009 J/kg*K, and a gradient of temperature of 30 °C, the heat transfer due to the ventilation is $\dot{Q}_{ven}$ = 1.922 kW.

3.4. Heat Flow Changes with the Ambient Load Due to the Temperature Gradient between the Bus Structure and the Exterior Environment (Ambient Heat Load)—$\dot{Q}_{amb}$

Heat transfer takes place from warm bodies (areas) to colder bodies (areas). So, in the winter cold days, the heat transfer takes place from the heated bus cab to the cold outside environment Thus, a large amount of heat is loss into the atmosphere through the windows, walls, roof, floor, and doors. This heat loss depends on the area of the surfaces, on the heat transfer coefficient (for each material or an overall estimated coefficient), and on the inside and outside temperatures. The heat transfer is estimated considering the conduction through solid materials, the convection between the interior air in the bus and the inner surfaces, and the convection between the exterior air and the outer surfaces of the bus (Figure 2).

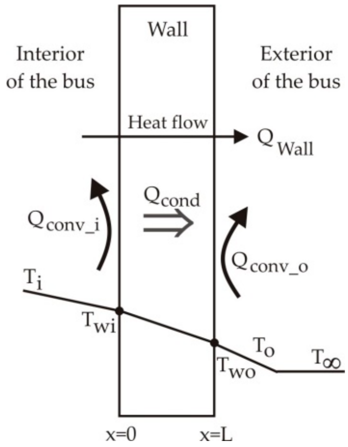

Figure 2. Heat loss through a wall of an electric bus.

For a wall composed by a single layer, the heat transfer is calculated with the following equation:

$$\dot{Q} = A \cdot U \cdot (T_i - T_o) \quad [\mathrm{W}], \tag{9}$$

where A is the cross-sectional area [m^2], U is the heat transfer coefficient [W/m^2 K], T_i is the inside temperature [°C], and T_o is the outside temperature [°C],

The heat transfer coefficient is calculated as a combination of conductive and convective heat transfer, which is given by [18]:

$$\frac{1}{U} = \frac{1}{h_i} + \frac{L}{k} + \frac{1}{h_o}, \tag{10}$$

where h_i is convective heat transfer coefficient between the interior air and the inner surfaces of the wall [W/m^2 K], h_o is the convective heat transfer coefficient between the exterior air and the outer surfaces of the wall [W/m^2 K], L is the thickness of the wall [m], and k is the conductive heat transfer coefficient of the wall [W/mK].

For the vehicles, the convection coefficients of the outer surfaces depend on the vehicle speed, and for the inner space, the coefficient depends on the air speed inside, relative to the inner surfaces [18], as follows:

$$h = 9 + 3.5v^{0.66} \quad [\mathrm{W/m^2\,K}], \tag{11}$$

with v as the relative air speed to the surface [m/s].

In order to estimate the heat loss as accurately as possible, for the walls composed by multiple layers, the thermal contact resistance between the layers of the bus structure will be considered also. Thus, knowing the heat loss on its components will be possible to estimate the possibilities to improve the bus structure to reduce the heat loss.

With limited information on the roughness profile, the density, and the radii of the contact spots, the estimation of the thermal contact resistance brings uncertainty into the calculation. Considering [30–32], the thermal contact resistance of the interface between two layers is given by the ratio between the difference of temperatures along the interface and the heat, $\dot{Q}$ [W], as follows:

$$R_c = \frac{\Delta T_{interface}}{\dot{Q}} \quad [\mathrm{K/W}], \tag{12}$$

where $\Delta T_{interface}$ is the difference of temperature along the layers' interfaces.

Based on heat flux, $q = \dot{Q}/A$ [W/m^2], related to the surface area, the resistance can be considered as follows:

$$r_c = \frac{\Delta T_{interface}}{q \cdot A} \quad [\mathrm{K/m^2W}], \tag{13}$$

Thus, for a multiple layered wall (with thicknesses (L_j) and conductive heat transfer coefficient (k_j)), the overall heat transfer coefficient must be calculated, including the thermal contact resistances between the layers, as follows:

$$\frac{1}{U} = \frac{1}{h_i} + \sum \frac{L_j}{k_j} + \frac{1}{h_o} + \sum r_{cj}, \quad [\mathrm{K/m^2W}], \tag{14}$$

where L_j, and k_j are the thickness and conductive heat transfer of the layer j, and r_{cj} is the thermal resistance for the layer interfaces.

3.4.1. Heat Loss through the Windows of the Bus—$\dot{Q}_w$

The heat lost through the windows is estimated as heat loss due to conduction through the windows and due to the convection to the interior and exterior air. There are various types of windows used for the buses, differing by glass thickness, the quality of the glass (clearness), or by the types of the windows (one layer or two layers with inside air isolation). For this calculation, it was assumed that the windows have a single layer of 6 mm glass thickness and the area of the windows of the bus is 29.0 m^2.

Using Formulas (8)–(10) and a vehicle speed of 40 km/h (11.1 m/s) (as the maximum speed for the city movement of the bus), the heat loss calculated for the all window area of the bus is $\dot{Q}_w$ = 5612 W, for U value = 6.45 W/m^2 K.

For the air inside the vehicle, the speed is assumed to be zero, so h_i = 9 [W/m^2 K], and k = 1.05 [W/mK] is the conductivity of the glass.

In order to estimate the real temperature on the surfaces of the windows, a simulation using Comsol Multiphysics software has been performed. The simulations were made for the steady-state regime by modeling the geometry of the bus structure and considering the actual values for the parameters of the materials.

Figure 3 shows the thermal simulation through a window of the bus considering an inside temperature of 20 °C (left side of the image) and an exterior temperature of −10 °C (on the right side of the image). The exterior temperature was chosen assuming a difficult case scenario for the month of December in Romania. As can be seen, the temperature on the external side of the glass is of 13.4 °C.

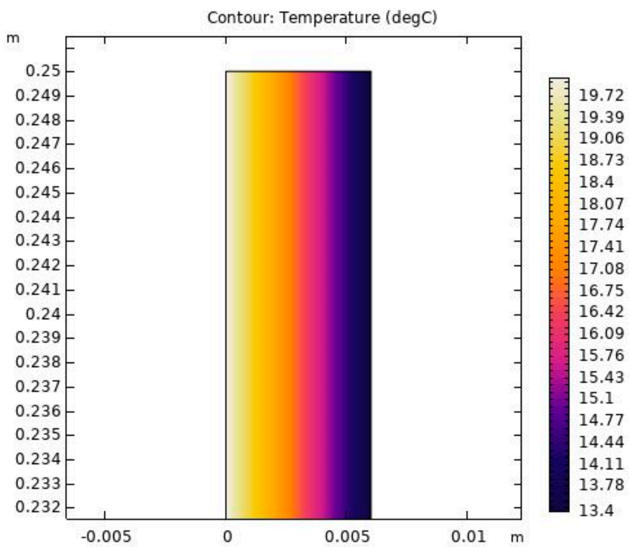

Figure 3. Heat flux variation through the windows of the bus.

3.4.2. Heat Loss through the Walls of the Bus—$\dot{Q}_{wall}$

The walls of the bus are made from three materials, that is (from inside to outside): laminated wood (MDF), polyurethane foam, and a sheet of steel. Their thickness and thermal conductivities are presented in Table 3.

Table 3. Thickness and thermal conductivities for the materials of the wall of the bus.

Material	Thickness [m]	Thermal Conductivity [W/mK]
Iron	0.0008	76.2
Polyurethane foam	0.01	0.04
Laminated wood	0.004	0.107

As for the simulation, in Figure 4a, the model of the three layers of the wall is presented, with a temperature of about −8.1 °C on the exterior wall of the bus, with main thermal loss from the steel and the foam in the wall. The interior side of the vehicle is on the left side of the image (Figure 4a). Vehicle speed is incorporated into the model as the velocity of the fluid (the exterior air).

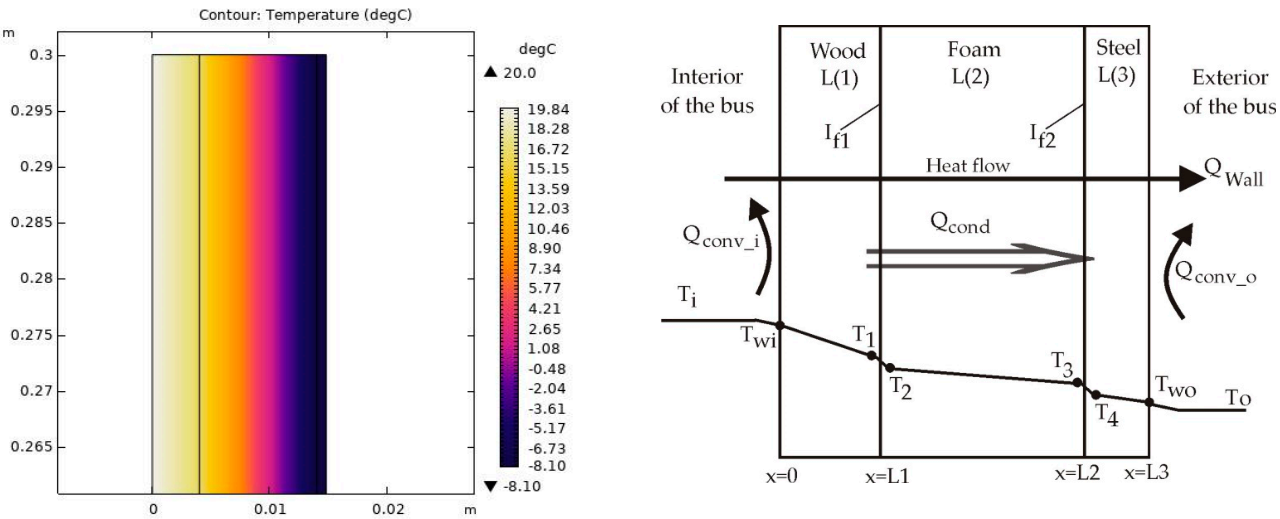

(**a**) (**b**)

Figure 4. (**a**) Heat transfer through the wall. (**b**) Schema of the three layers of the wall of the bus.

For the triple layered wall of the bus (Figure 4b), the overall heat transfer coefficient is calculated as follows:

$$\frac{1}{U_{wall}} = \frac{1}{h_i} + \left(\frac{L_1}{k_2} + \frac{L_1}{k_2} + \frac{L_1}{k_3}\right) + \frac{1}{h_o} + r_{cwall}, \quad [\mathrm{K/m^2W}], \tag{15}$$

The thermal contact resistance for the wall is the sum of the thermal resistance for the two interfaces I_{f1} and I_{f2} (Figure 4b). For the first interface thermal resistance estimation (between the layer of wood, L(1), and foam, L(2)), we assumed that the heat transferred through the surface area of the wall is constant, and we can write the following:

$$\frac{\dot{Q}}{A} = \frac{\Delta T}{\frac{L1}{k1}}, \tag{16}$$

where $\Delta T = T_i - T_1$ [°C] is the difference of temperature along the layer, L(1).

For the interface zone (between the layers L(1) and L(2)):

$$\frac{\dot{Q}}{A} = \frac{\Delta T_{interface}}{r_{c12}}, \quad (17)$$

$\Delta T_{interface} = T_1 - T_2$ [°C], with T_1 and T_2 indicating the temperatures on the interface of the layers L(1) and L(2), between wood and foam layers respectively (Figure 4b).

The interface temperature T_1 and T_2 are estimated from the Comsol simulations (Figure 4a), resulting T_1 = 16.27 °C and T_2 = 16.12 °C.

With these values, and using the Equations (16) and (17), the first interface shows r_{c12} = 0.002 [K/m^2 W]. Similarly, but considering T_3 = −8 °C and T_4 = −8.14 °C, the second interface is calculated, between the second and the third layer, as follows: $r_{c12} = 8{\cdot}10^{-6}$ [K/m^2 W], for the wall of the bus, is r_{cwall} =0.00208 [K/m^2 W].

For the speed of 40 km/h, with 20 °C inside and −10 °C outside temperatures, and for an area of the wall of the bus of A_{wall} = 27 m^2, the U value is determined as U_{wall} = 2.283 W/m^2 K and the heat loss through the wall is $\dot{Q}_{wall}$ = 1849 W.

3.4.3. Heat Loss through the Roof—$\dot{Q}_{roof}$—And the Floor of the Bus—$\dot{Q}_{floor}$

The roof of the bus is composed of a layer of iron sheet, a layer of polyurethane foam (as isolation), and a volume area filled with various equipment (air conditioning, pipes, power supply equipment, and power conductors from the power collecting system). These equipment elements are made mostly from metals and cover about 50% of the roof area. Due to this complex structure of the roof, in order to estimate the U value for the roof, including this complex area (composed of metals materials and air), we consider this area as composed of two parallel layers of metals and air.

The simulation of the heat transfer through the roof is presented in Figure 5a, which shows the differences in temperatures between the metal area of the third layer (on the left) and the air area (on the right of the third layer).

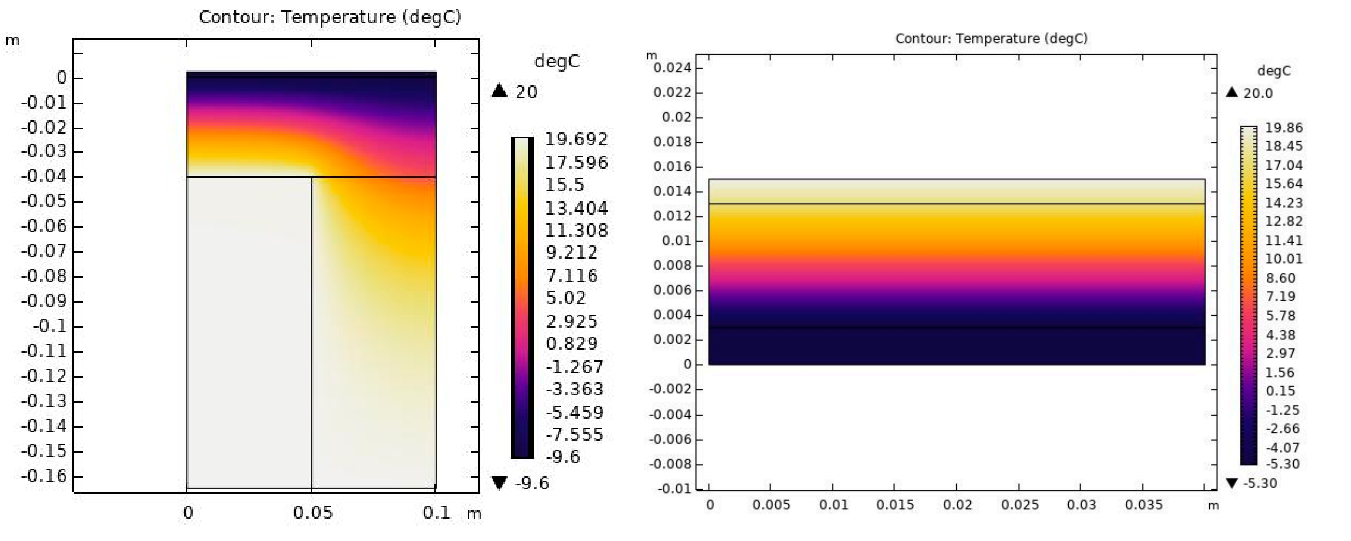

(**a**) (**b**)

Figure 5. (**a**) Heat transfer through the roof of the bus. (**b**) Heat transfer through the floor of the bus.

For the speed of 40 km/h a U value for the roof of 1.87 W/m^2 K, the heat loss is $\dot{Q}_{roof}$ = 1632 W. This calculation include also the thermal resistance of the roof layers (r_{croof} = 0.008 [m^2 K/W]).

The floor is composed of three layers: an iron sheet, a laminated wood layer, and a PVC layer for the intensive transport of people (Table 4). The U value (at 40 km/h) for the floor (including thermal resistance r_{cfloor} = 0.0152 [m^2 K/W]) is 2.747 W/m^2 K and the heat loss is 2425 W.

Table 4. The thicknesses and thermal conductivities for the materials of the floor of the bus.

Material	Thickness [m]	Thermal Conductivity [W/mK]
Iron	0.002	76.2
Laminated wood	0.02	0.107
Polyvinyl/PVC	0.003	0.19

The total heat loss through the windows, walls, roof, and floor of the bus, for a speed of 40 km/h, is determined as $\dot{Q}_{amb}$ = 11,518 W.

The total ambient heat loss (heat loss through the windows, walls, roof, and floor of the bus) is presented in Table 5 for the various speeds of the vehicle (0, 20, 40, and 60 km/h). These values show a significant variation of heat loss between the moment when the bus stops and when it is in motion. It is worth mentioning that the influence of the thermal resistances is less than 3%. Moreover, the differences of heat loss between various speeds are not too high: they are about 3–5%.

Table 5. U values and heat loss through the bus structure into the ambient.

v [km/h]	U Value [W/m^2 K]				$\dot{Q}$Structure [W]				$\dot{Q}amb$ [W]
	Uw	Uwall	Uroof	Ufloor	$\dot{Q}w$	$\dot{Q}wall$	$\dot{Q}roof$	$\dot{Q}floor$	
0	4.4	1.957	1.67	2.272	3832	1585	1458	2004	8879
20	5.988	2.218	1.828	2.66	5209	1797	1595	2346	10,947
40	6.45	2.283	1.87	2.747	5612	1849	1632	2425	11,518
60	6.757	2.32	1.89	2.8	5878	1879	1653	2470	11,880

3.5. Heat Loss Due to the Doors Opening

Estimating the heat loss through the open doors of the bus when it is stopped in stations is quite difficult, due to the air flow complexity between the inside of the bus and the exterior air of the environment, which depends on the random process of the weather conditions and wind speed and direction. The air is assumed to be an ideal gas and is compressible.

When a pressure is applied to the interior air, the volume of the air is modified with a volume equal to the amount of the outside air, which is pressurized into the vehicle cabin, and therefore an air exchange is caused in the process. Some of the income air from outside is mixed with the inside air and is removed through the opening of the doors, due to the airflow direction change and due to the gradient of the temperature and the pressure, this is proportional to the surface area of the opening [33].

The worst-case scenario is when the wind blows directly into the open door, as presented into the cross-section of the bus structure, showing an opened door (Figure 6).

The heat loss through an open door of the bus is estimated with the following formula:

$$\dot{Q}_{door} = \dot{V} \cdot \rho_{air} \cdot c \cdot \Delta T \text{ [W]}, \quad (18)$$

where $\dot{V}$ is the flow rate of the air [m^3/s], ρ_{air} is the air density 1.27 kg/m^3, and c is specific heat of the air 1009 J/kg·K.

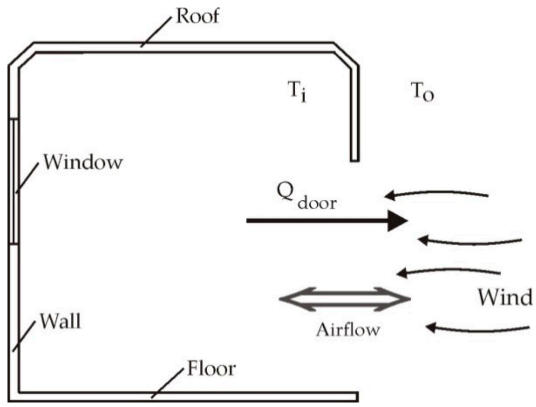

Figure 6. Schema cross-section through the bus structure for an open door.

According to [33], for a single opening enclosure (one open door), for a wind velocity of 10 m/s (a medium wind speed value during a cold day in winter), a flow rate of $\dot{V}$ = 0.4 m^3/s for a surface area of 1.44 m^2 is found. Thus, using Formula (17), heat losses result of $\dot{Q}_{door}$ = 15,377 W for a single open door and, respectively, of $\dot{Q}_{3door}$ = 46,131 W for all the three open doors of the bus,

Obviously, usually the doors do not stay open too frequently. The average stop time for a city bus is about 30 s [21], with an average running time between stops of 4 min, resulting the doors being open for 1/9 h. As consequence, the hourly heat loss from the open doors is 5.125 kW. Depending on the route, the number of stops, and the number of passengers getting on and off the vehicle, this heat loss may have various values.

3.6. Heat Load Due to the Electric Motors and Heat Load Generated by the Traction Battery

The actual electric vehicles use high efficiency electric motors which generate low amount of waste heat [8]. Even the heat released from the main battery pack is not enough to heat the interior of an electric bus, and for the present calculation of the heat inside the bus these heat losses are considered as negligible.

3.7. Heating System Load to Assure the Thermal Comfort for Passengers

Summarizing the heat loads on the bus, a heat gain of 5.72 kW (the sum of $\dot{Q}_{met}$ and $\dot{Q}_{sun}$) and a loss of energy of 18.5 kW (the sum of $\dot{Q}_{ven}$, $\dot{Q}_{amb}$, and $\dot{Q}_{doors}$) is found. As consequence, the necessary load for the heating system of the 12-m long bus is about 12.79 kW. For higher speeds (max. 60 km/h speed of the bus) and for even harsher winter conditions, this value grows up to 14 kW. This load has to be compensated by the heating system, regardless of the technology used to heat the bus [31].

The analysed existent bus is equipped with 4 heaters of 6 kW in the passengers' cabin and 1 heater of 9 kW in the driver's area. This results in 33 kW of power installed for the electric bus heating system, which, compared with our model, is an oversized heating system [34,35]. The oversizing is only useful for more quickly obtaining the ambient comfort parameters in the bus.

4. Discussion

Research on heating in vehicles is of major importance, especially in cold weather zones, but it is not wide spread over all types of vehicles. Most studies are in the area of automobiles, with few on buses, due to the fact that analyzing and simulating a bus (which is significantly larger and has an intricate structure) is a more complex and time-consuming process.

This article aimed to respond to some of the thermal problems related to electric buses. Estimation of the necessary heat to assure thermal comfort during cold winter days is quite important due to the limited power of these types of electric vehicles. Additionally, along with the limits in energy stored onboard and the vehicles complexity, their particular operating regime results in a complex study due to the various numbers of passengers, doors frequently opening, and the necessity to operate throughout the day.

This study estimates the eight main heat load components on electric buses. Two of them were assumed to be negligible for our thermal model. Firstly, the heat load due to the electric traction motor, and secondly that due to the traction battery pack, as the actual elements are highly efficient.

Therefore, six heat loads were considered for our model: metabolic heat load, Sun heat load, ventilation heat load, ambient heat load, heat flow through the open doors, and the heat load generated by the heating system in the bus. These heat loads were calculated for a 12 m electric bus with the following characteristics: 100 passengers, 150 kW electric traction motor, 3 doors, and 33 kW installed power for the heating system. The calculation was estimated for a harsh winter cold day of December in Romania, with a median temperature of −10 °C. The thermal comfort of the passengers was calculated for a 20 °C temperature inside the bus, resulting a gradient of temperature of 30 °C.

The value of the metabolic heat load depends on the passenger numbers in the vehicle, and the Sun heat load depends strongly on the weather conditions. These heat loads are as a contribution (a heat gain) to the inside bus heating (considered as positive in the thermal model of the vehicle), and, for a harsh day in winter, these represent about 22% and less than 15%, respectively, of the necessary heat of the bus. The heat load from ventilation is an energy-consuming heat load (with energy supplied from the onboard storage system) and it represents less than 10% of the necessary heat for the bus. Being a mandatory system in the vehicle, its contribution to the vehicle heating can be considered to be a heat gain. Thus, these three heat loads assure an input of heat of about 23% of the necessary heat inside the bus.

Heat loss on the bus is composed of the ambient heat loss through the bus structure and the heat loss through the open doors at the stops, with an average value of energy demand of 12–14 kWh. Of these, through the bus structure the heat loss is the most significant, with its four components—the windows, the walls, the floor, and the roof—representing about 78% of the total heat loss. The main heat loss is through the windows (about 26%), while the other three heat loss components have almost the same contribution (about 8.1–8.3% each).

Heat loss through the open doors depends on the route of the bus, the number of stops, and the number of passengers getting on and off the vehicle, with an estimation of 22% of the total heat loss.

The heat load balance led to the conclusion that the heating system must supply a minimum heat load of 18.5 kW. This value is useful for more successfully designing the heating system and managing its operation. The thermal model used in this study allows optimization of the process, by using various less frequently studied heating solutions in order reduce the energy consumption for the heating, and implicitly reduce the CO_2 footprint, while preserving the thermal comfort of the passengers and driver.

Author Contributions: Conceptualization, G.C.; methodology, G.C. and D.D.L.; software, G.C.; validation, G.C., D.D.L. and C.N.; formal analysis, D.D.L. and A.D.; writing—original draft preparation, G.C.; writing—review and editing, A.D.; visualization, A.D. and S.R.; supervision, D.D.L. and S.R.; funding acquisition, G.C. and C.N. All authors have read and agreed to the published version of the manuscript.

Funding: This research and the APC were funded by "Gheorghe Asachi" Technical University of Iasi, Romania, grant number GI/P 9_Idei/2021.

Institutional Review Board Statement: Not applicable.

Informed Consent Statement: Not applicable.

Conflicts of Interest: The authors declare no conflict of interest. The funders had no role in the design of the study; in the collection, analyses, or interpretation of data; in the writing of the manuscript, or in the decision to publish the results.

References

1. Transport & Environment. Electric Buses Arrive on Time. Campaigning for Cleaner Transport in Europe. 2018. Available online: https://www.transportenvironment.org/discover/electric-buses-arrive-time/ (accessed on 8 October 2021).
2. ACEA—European Automobile Manufacturers' Association. Report—Vehicles in Use, Europe 2021. 2021. Available online: https://www.acea.auto/publication/report-vehicles-in-use-europe-january-2021/ (accessed on 8 October 2021).
3. MRC_Electric_Bus_Report__28082017—Electric Bus Technology Transport Research Report. 2017. Available online: https://www.coursehero.com/file/48912037/MRC-Electric-Bus-Report-28082017pdf (accessed on 8 October 2021).
4. Bartłomiejczyk, M.; Kołacz, R. The reduction of auxiliaries power demand: The challenge for electromobility in public transportation. *J. Clean. Prod.* **2020**, *252*, 119776. [CrossRef]
5. Oi, H.; Tabata, K.; Naka, Y.; Tochihara, Y. Effects of Regional Heating by Heated Seat in Vehicles on Thermal Sensation at 15 °C. *J. Hum.-Environ. Syst.* **2012**, *14*, 31–39. [CrossRef]
6. Evtimov, I.; Ivanov, R.; Sapundjiev, M. Energy consumption of auxiliary systems of electric cars. *MATEC Web Conf.* **2017**, *133*, 06002. [CrossRef]
7. Simion, M.; Socaciu, L.; Unguresan, P. Factors which influence the thermal comfort inside of vehicles. *Energy Procedia* **2016**, *85*, 472–480. [CrossRef]
8. Lajunen, A.; Yang, Y.; Emadi, A. Review of Cabin Thermal Management for Electrified Passenger Vehicles. *IEEE Trans. Veh. Technol.* **2020**, *69*, 6025–6040. [CrossRef]
9. Zhang, Z.; Wang, D.; Zhang, C.; Chen, J. Electric vehicle range extension strategies based on improved AC system in cold climate–A review. *Int. J. Refrig.* **2018**, *88*, 141–150. [CrossRef]
10. Kang, B.H.; Lee, H.J. A review of recent research on automotive HVAC systems for EVs. *Int. J. Air-Cond. Refrig.* **2017**, *25*, 1730003. [CrossRef]
11. Marshall, G.J.; Mahony, C.P.; Rhodes, M.J.; Daniewicz, S.R.; Tsolas, N.; Thompson, S.M. Thermal management of vehicle cabins, external surfaces, and onboard electronics: An overview. *Engineering* **2019**, *5*, 954–969. [CrossRef]
12. de Lieto Vollaro, R. Indoor climate analysis for urban mobility buses: A CFD model for the evaluation of thermal comfort. *Int. J. Environ. Prot. Policy* **2013**, *1*, 1–8. [CrossRef]
13. Bauml, T.; Dvorak, D.; Frohner, A.; Simic, D. Simulation and measurement of an energy efficient infrared radiation heating of a full electric vehicle. In Proceedings of the 2014 IEEE Vehicle Power and Propulsion Conference (VPPC), Coimbra, Portugal, 27–30 October 2014; pp. 1–6.
14. Collins, D.; Rednic, R.; Thake, C.D. Infrared heating as an adjunct to achieve vehicle occupant thermal comfort. *Extrem. Physiol. Med.* **2015**, *4* (Suppl. S1), A82. [CrossRef]
15. Dreißigacker, V. Solid Media Thermal Energy Storage System for Heating Electric Vehicles: Advanced Concept for Highest Thermal Storage Densities. *Appl. Sci.* **2020**, *10*, 8027. [CrossRef]
16. Jeffers, M.A.; Chaney, L.; Rugh, J.P. Climate control load reduction strategies for electric drive vehicles in cold weather. *SAE Int. J. Passeng. Cars-Mech. Syst.* **2016**, *9*, 75–82. [CrossRef]
17. Sahraei, H. Interior Climate U-Value Calculation and Optimization for Electric Buses at Volvo Buses. Master's Thesis, Department of Mechanics and Maritime Sciences, Chalmers University of Technology Gothenburg, Gothenburg, Sweden, 2020. Available online: https://odr.chalmers.se/bitstream/20.500.12380/300921/1/2020-39%20Hamidreza%20Sahraei.pdf (accessed on 9 December 2021).
18. Tanyeri, N.; Başlamişli, Ç. Prediction of the annual heat load of an articulated electric urban bus. *Isı Bilimi Tek. Derg.* **2020**, *40*, 27–36.
19. Torregrosa-Jaime, B.; Bjurling, F.; Corberan, J.M.; Di Sciullo, F.; Paya, J. Transient thermal model of a vehicle's cabin validated under variable ambient conditions. *Appl. Therm. Eng.* **2015**, *75*, 45–53. [CrossRef]
20. Pedersen, C.O.; Fisher, D.E.; Liesen, R.J. Development of a Heat Balance Procedure for Calculating Cooling Loads. *ASHRAE Trans.* **1997**, *103 Pt 2*, 459–468.
21. Göhlich, D.; Fay, T.-A.; Jefferies, D.; Lauth, E.; Kunith, A.; Zhang, X. Design of urban electric bus systems. *Des. Sci.* **2018**, *4*, e15. [CrossRef]
22. Chiriac, G.; Lucache, D.D.; Nituca, C.; Gabor, G. Aspects regarding the heating of electric buses. In Proceedings of the 13th International Conference on Electromechanical and Energy Systems (SIELMEN), Iasi, Romania, 7–8 October 2021.
23. Nițucă, C.; Chiriac, G.; Gabor, G.; Nucă, I.; Cazac, V.; Burduniuc, M. Geometry Design and Analysis of an Electric Bus for the Interior Thermal Modelling. *J. Energy Technol.* **2021**, in press.
24. Fayazbakhsh, M.A.; Bahrami, M. *Comprehensive Modeling of Vehicle Air Conditioning Loads Using Heat Balance Method*; Technical Paper 2013-01-1507; SAE International: Warrendale, PA, USA, 2013.
25. Yildirim, K.-E.; Finkenrath, M.; Gökoglu, M.; Seidel, F. Monitoring the Fresh-Air Flow Rate for Energy-Efficient Bus Ventilation. In *Energy and Thermal Management, Air Conditioning, Waste Heat Recovery*; Junior, C., Jänsch, D., Dingel, O., Eds.; Springer International Publishing: Cham, Switzerland, 2017; pp. 147–156.

26. National Meteorological Administration of Romania. Available online: https://www.meteoromania.ro/clim/caracterizare-lunara/index.html (accessed on 29 October 2021).
27. Balan, M. Energii Regenerabile. Ed UT PRES. 2007. Available online: http://www.termo.utcluj.ro/regenerabile (accessed on 9 December 2021). (In Romanian).
28. Pirouz, B.; Mazzeo, D.; Palermo, S.A.; Naghib, S.N.; Turco, M.; Piro, P. CFD Investigation of Vehicle's Ventilation Systems and Analysis of ACH in Typical Airplanes, Cars, and Buses. *Sustainability* **2021**, *13*, 6799. [CrossRef]
29. Gis, M.; Wiśniowski, P.; Bednarski, M. Efficiency of electric vehicle interior heating systems at low ambient temperatures. *Open Eng.* **2021**, *11*, 499–507. [CrossRef]
30. Bejan, A.; Kraus, A.D. (Eds.) *Heat Transfer Handbook*; John Wiley & Sons: Hoboken, NJ, USA, 2003; Volume 3.
31. Fang, W.-Z.; Gou, J.-J.; Chen, L.; Tao, W.-Q. A multi-block lattice Boltzmann method for the thermal contact resistance at the interface of two solids. *Appl. Therm. Eng.* **2018**, *138*, 122–132. [CrossRef]
32. Wang, A.; Zhao, J. Review of prediction for thermal contact resistance. *Sci. China Technol. Sci.* **2010**, *53*, 1798–1808. [CrossRef]
33. Haghighat, F.; Rao, J.; Fazio, P. The influence of turbulent wind on air change rates—A modelling approach. *Build. Environ.* **1991**, *26*, 95–109. [CrossRef]
34. Vaswani Reyes, R.H. Optimization of the Heating System of a Bus Cabin: A Numerical Approach through OpenFOAM. Master's Thesis, Politecnico di Torino, Torino, Italy, 2020. Available online: https://webthesis.biblio.polito.it/15401/ (accessed on 8 December 2021).
35. Henning, M.; Smyth, A.; Thomas, A. *An Analysis of the Association between Changes in Ambient Temperature, Fuel Economy, and Vehicle Range for Battery Electric and Fuel Cell Electric Buses*. Technical Report; Urban Publications. 0 1 2 3 1630. 2019. Available online: https://engagedscholarship.csuohio.edu/urban_facpub/1630 (accessed on 9 December 2021).

Original Article

JAAS

Renewable Energy in Algeria: Desire and Possibilities

Journal of Asian and African Studies
1–18

DOI: 10.1177/0021909619900202
journals.sagepub.com/home/jas
SAGE

Mohammed el Amine Boukli Hacene
Laboratory of Condensed Matters and Sustainable Development (LMCDD), University of Sidi Bel Abbes, Algeria

Dorin Lucache
Faculty of Electrical Engineering, "Gheorghe Asachi" Technical University of Iasi, Romania

Habib Rozale
Abbes Chahed
Laboratory of Condensed Matters and Sustainable Development (LMCDD), University of Sidi Bel Abbes, Algeria

Abstract
Algeria, like other developing countries, has been committed to promoting the transition to renewable energy for several years. The national government established several laws and attractive subsidies that encouraged various socio-economic entities to use renewable energies and engage in more sustainable practices. Despite these efforts, industrial and private entities have not responded as hoped. To identify the factors that impede government efforts toward sustainable practices, this paper focuses on the two most energy-consuming sectors: building and transport. The analysis reveals that both financial and socio-cultural issues constitute the two main obstructive elements to energy transition in Algeria. This is the first study to be carried out in Algeria on technico-economic difficulties in the application of energy transition towards renewable sources.

Keywords
Energy, transport, efficiency, renewable, sustainability, building, policy

Introduction

Algeria is once again facing an oil crisis. Oil prices fell from US$115/barrel in June 2014 to nearly US$60/barrel at the end of June 2019. The national energy sector is excessively dependent on

Corresponding author:
Mohammed el Amine Boukli Hacene, Laboratory of Condensed Matters and Sustainable Development (LMCDD), University of Sidi Bel Abbes, 22000, Algeria.
Email: amineboukli@yahoo.fr

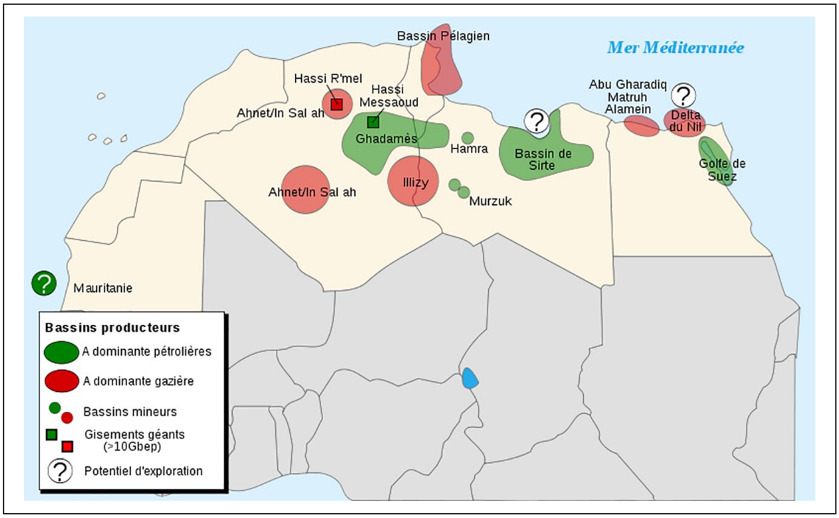

Figure 1. Gas and oil deposits in North Africa (AFP, 2009).

hydrocarbons, which still hold a significant weight in the economy. About 98% of Algeria's export earnings come from oil and conventional gas.

In 2011, a renewable energy and energy efficiency development program was set up with the aim of producing 12,000 MW of renewable electricity per year by 2030. That amount would account for 40% of the national total energy consumption. The production would be 37% solar and 3% wind.

Algeria's energy transition from almost entirely conventional hydrocarbons to a new diverse system will ensure the security of energy, economy, and sustainability of the country.

One ongoing question is how alternative energy sources will combine to meet Algeria's needs. The following analysis shows that renewable energy in Algeria is not profitable. This is the main reason that the renewable energy sector is struggling to develop, and therefore cannot compete with the fossil fuel industry. In particular, the transport and building sectors continue to rely on fossil fuels because renewable energy is not economically feasible. The main reasons for this situation are identified and discussed.

Geographical and economic data of Algeria

Algeria lies in the Maghreb region of North Africa. With an area of 2,381,741 square kilometers (919,595 square miles), Algeria is the tenth-largest country in the world, the world's largest Arab country, and the largest in Africa (CIA, 2014). The southern part, representing 80% of the country's surface, is occupied by Sahara desert.

Algeria's hydrocarbon deposits are among the largest in the world, generally located in the South (Figure 1) (AFP, 2009).

Algeria possesses the fourth-largest economy on the African continent, and the 48th-largest economy in the world. Reduced to purchasing power parity, per capita GDP (PPP) is estimated at US$7600 in 2012.

Algeria is a major producer and exporter of natural gas (fifth-largest producer and fourth-largest exporter (British Petroleum Full Report, 2019)) and oil (13th-largest producer and ninth-largest exporter (British Petroleum Full Report, 2019)). Algeria's trade balance remains highly dependent

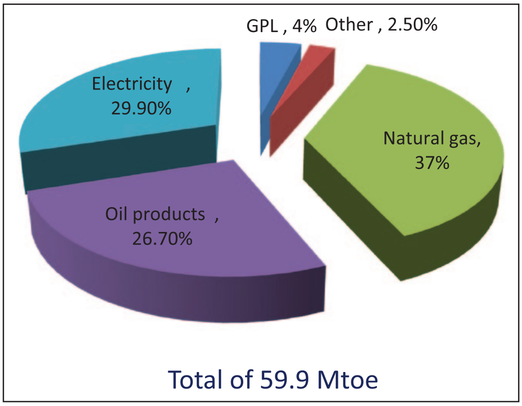

Figure 2. National consumption by energy form (SONELGAZ, 2018).

on the revenues generated by the sale of oil and gas, which alone account for more than 97% of the overall volume of exports in 2017 (Daniel Workman, 2018)

Characterized by a strong dependence on hydrocarbons, Algeria's economic situation seemed favorable, both internally and externally, until 2014. In 2014, the Bank of Algeria predicted that oil and gas revenues would fall by nearly 50% in the first quarter of 2015, from US$15.6 billion in March 2014 to only US$8.7 billion in March 2015, which raised fears that a major financial crisis would occur in the country.

National energy consumption (including losses) reached 59.6 million tons of oil equivalents (Mtoe) in 2017, reflecting a 2.1% increase from 2016. This was driven by a 4.1% increase in final consumption. The structure of national consumption remains dominated by natural gas (37%), followed by electricity (30%) and petroleum products (27%), as illustrated in Figure 2.

The evolution of energy consumption by sector in 2017 can be summarized as follows:

- The transport sector consumption increased to 14.9 Mtoe, driven by higher fuel prices on the domestic market;
- The industrial and public works sector consumption increased by 7.6%, from 9.2 Mtoe to 9.9 Mtoe, driven by the higher consumption of the building materials subsector (+7.5%) and industry (+45.9%);
- The Households and "Other" sector increased consumption by 6.6% from 18.5 Mtoe to 19.8 Mtoe. It was driven by the higher consumption in the residential subsector (+5.7%). In particular, the gas and electricity needs increased with the number of SONELGAZ (Algerian National Society for Electricity and Gas) customers.

The breakdown of consumption by sector is given in Figure 3.

Electricity consumption per capita reached 1363 kWh in 2014, which represents only 45% of the world average (3030 kWh), but 2.4 times the African average (568 kWh) (British Petroleum Full Report, 2016).

The continued growth of domestic energy demand (oil and gas), the risk of depletion of these resources, and the global warming clearly indicate the need to launch an energy transition towards a more sustainable model.

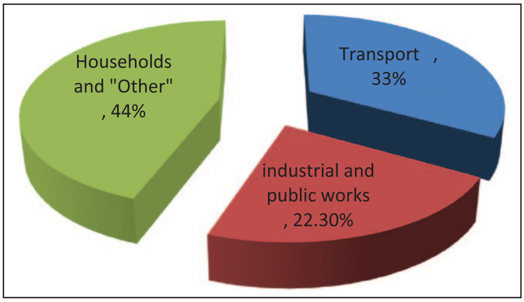

Figure 3. Structure of Algerian final consumption by sector (SONELGAZ, 2018).

Energy transition of Algeria

Achieving the goals of energy security and sustainability, as well as access to clean energy, requires a strong and stable policy framework that imposes the energy efficiency and development of renewable energies as priorities. Energy efficiency, which consists of reducing the need for energy services, is the most important component of a successful energy transition.

Energy efficiency aims both at reducing the costs of energy use and at minimizing greenhouse gas emissions. It represents the most important component of a successful energy transition. Policies of investment in research and encouragement of non-polluting solutions will all be essential to Algeria's energy transition.

The use of fossil fuels made it possible to meet the needs of the Algerian economy. Moreover, dependence on the country's hydrocarbons exports represents a risk for the national economy. So, the challenge of the energy transition is complex: Algeria must respond to higher energy demand and reduce greenhouse gas emissions, while remaining economically competitive.

In this framework, the Algerian government continues to encourage economic sectors to develop the renewable energy sector, whether by circulars, subsidies, or attractive redemption prices.

According to Algeria's 2012 Program for the Development of Renewable Energy and Energy Efficiency (PENREE), the country is aiming at a renewable installed capacity of 22,000 MW by 2030 (Ecofin, 2012). In May 2018, there were 24 photovoltaic power plants, summarizing a total of 344 MWp (HuffPost Maghreb, 2018).

Algeria is the 42nd most "ecologically clean" country in the world, and the first among the Arab countries, particularly because of recent progress made in promoting renewable energies and in view of its energy potential (TSA, 2018). Currently, Algeria is investing in the development of renewable energy by constructing the mixed power plant Hassi R'Mel.

Legal framework and government incentives for the development and use of renewable energies

The Algerian government has encouraged state institutions in the field of energy to develop and promote instruments and mechanisms that encourage investment in renewable energies. The development of renewable energies aims to introduce and promote sectors, including solar energy, geothermal energy (biomass), hydroelectric power, and wind energy.

The adoption of the legal framework, conducive to the promotion of renewable energies and to the construction of infrastructures relating to the production of electricity from renewable energy sources, is defined through the following measures:

- Law No. 04-09 of 14 August 2004 promoted renewable energies in the context of sustainable development (OJ No. 52 of 18 August 2004);
- Law No. 09-09 of 30 December 2009 on the Finance Law for 2010, in particular Article 64 on the creation of the National Fund for Renewable Energies and Cogeneration (FNER) (OJ No. 78 of 31 December 2009);
- Executive Decree No. 13-218 of 18 June 2013 set the conditions for granting bonuses for the costs of diversification of electricity production (OJ No. 33 of 26 June 2013);
- Executive Decree No. 15-319 of 13 December 2015 established operating procedures of Special Account No. 302-131 entitled “National Fund for Energy Efficiency and for Renewable Energies and Cogeneration”;
- Government Order of 2 February 2014 established the guaranteed purchase rates and the conditions of their application for electricity produced from facilities using the wind energy sector (OJ No. 23 of 23 April 2014);
- Government Order of 2 February 2014 established the guaranteed purchase rates and conditions of use for application of electricity produced from installations using the solar photovoltaic sector (OJ No. 23 of 23 April 2014);
- Decree of 1 September 2014 established the guaranteed purchase rates and conditions of use for electricity produced from installations using the cogeneration sector (OJ No. 18 of 8 April 2015) (OJPDRA, 2015).

The Algerian government has set up a National Fund for Energy Management for Renewable Energies and Cogeneration (FNMEERC), which is supplied annually with 1% of the oil royalty and the product of certain taxes. The goals of this fund are:

- To help finance actions and projects included in the promotion of renewable energies and cogeneration;
- To grant non-remunerated loans to energy-efficient investments not included in the national program for the control of energy;
- To guarantee for loans made to banks or financial institutions.

Regulations also provide creative based on guaranteed purchase tariffs. The renewable energy producer thus benefits from purchase prices, which are guaranteed for a period of 20 years for installations in photovoltaic, solar energy, and wind. These purchase tariffs are intended to cover any additional costs resulting from the electricity produced from renewable sources. Electricity produced from renewable sources receives a premium for each kWh produced, marketed, or consumed, as described in Table 1.

In addition to the general framework governing development of investments related to the promotion of renewable energies, the legal framework in force provides direct and indirect support for renewable energies. To encourage industries in this program, the Algerian government also plans to include reduction of import customs duties and VAT for the components, raw materials, and semi-finished products used in the manufacture of equipment necessary for renewable energies and energy efficiency.

Table 1. Guaranteed purchase price per power band and according to the potential in DZD/kWh (AME, 2019).

Regulatory limit of adjustment	Number of hours of operation (kWh/year)	Guaranteed purchase rate (DZD/kWh)	
		Phase I	Phase Ii
– 15%	1275–1349	15.94 DZD	20.08 DZD
	1350–1424		18.83 DZD
	1425–1499		17.45 DZD
Reference potential	1500–1574		15.94 DZD
+ 15 %	1575–1649		14.43 DZD
	1675–1724		13.06 DZD
	>= 1725		11.80 DZD

Notes: The currency in Algeria is the Algerian Dinar (DZD). At time of writing, the exchange rate was 1 Euro = 133.14 DZD.
The reference rate for the fossil-fueled kWh used in buildings is 4.17 DZD.

Problems related to the development of renewable energies in Algeria

Transport and construction are the main two energy-consuming sectors in Algeria (with 41% and 36% respectively of the total energy consumption).

Construction sector (residential and tertiary)

There are two main approaches to improve practically the energy performance of the building sector in Algeria:

- *The improvement of the building envelope*, through the application of bioclimatic architecture, the insulation of walls, windows, and use of a powerful ventilation system (e.g. VMC Double Flow, Canadian Well);
- *Autoproduction of energy by means of PV or thermal panels.*

Seventy percent of Algeria receives an annual insolation more than 1700 kWh/m² (global radiation) (SOLARGIS, 2019) (see Figure 4).

Even though the solar radiations are high, economic validation is needed to adopt this solution. In the following section, a comparative study is presented. For a sample house in Tlemcen, the comparison regards the energy costs of the house using fossil fuels (gas and electricity: real consumption – energy bill), and respectively using photovoltaic panels (dimensioning and simulation).

Description of the sample house. The house in Tlemcen has a total floor area of 100 m² and comprises a ground floor and two upper levels (see Figure 5). The ground level comprises a hall, kitchen, living room, and bathroom. The first level comprises a living room, kitchen, small hall, and small bathroom. The top level has three bedrooms, hall, and bathroom. The architecture and the positioning of the house allow most of its heating needs to be met by solar energy, since the living rooms are facing south-east and south-west. That positioning is a basic principle of bioclimatic architecture. The external walls are 110 mm double brick plus 50 mm cavity, with 10 mm

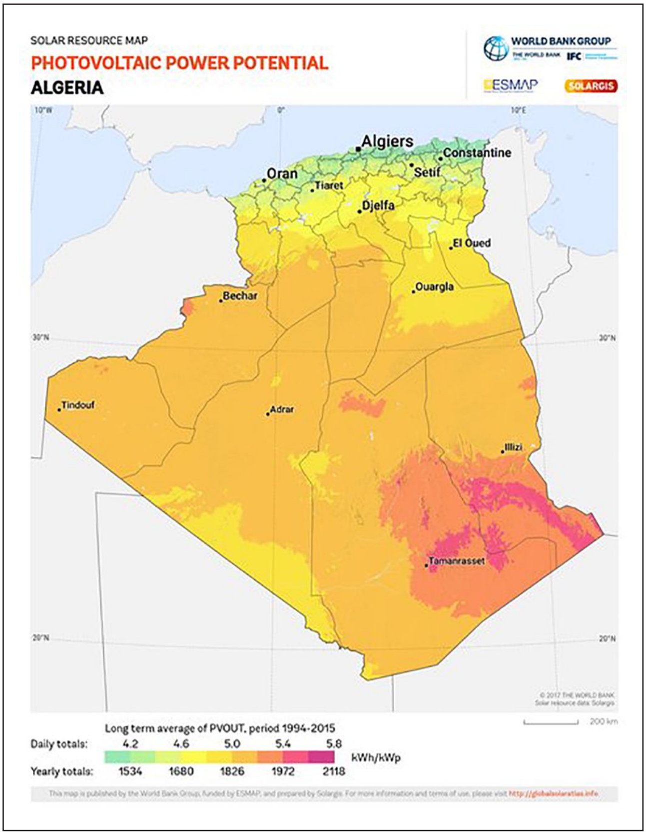

Figure 4. Photovoltaic power potential of Algeria (SOLARGIS, 2019).

cement mortar at each side, U value is 1.46 W/m².K. The single-pane glass windows have a thermal transmittance coefficient U = 5.500 W/m².K. The external metallic solid door has thermal transmittance coefficient U = 5.356 W/m².K. The house is inhabited by four people.

As stated before, Algeria is a major producer and exporter of natural gas and oil. As a natural consequence, 83% of homes are meeting their heating, cooking, and domestic hot water needs entirely through the public natural gas network (AME, 2019). Figure 6 shows the Tlemcen house's use of natural gas and electricity usage throughout the year. Natural gas represents 75% of the overall consumption (Table 2) (Boukli Hacene, 2019).

At a rate of 4.17 DZD for one kWh (~0.030 Euro/kWh), the average annual bill for this house is nearly 40,000 DZD (~281 Euro).

Photovoltaic dimensioning by using PVsyst. Developed by Swiss physicist Andre Mermoud and electrical engineer Michel Villoz, this software is considered a standard for PV system design and simulation worldwide. The developers claim this software is designed to be used by architects, engineers, researchers, and students. It is also a very useful educational tool. It includes a detailed contextual "Help" menu that explains the procedures and models used, and offers a user-friendly approach with a guide to develop a project. PVsyst is able to import meteorological, as well as personal, data from many different sources (see Figure 7).

Figure 5. The sample house used in the case study.

The software offers a quick estimation of energy production from the project planning stage, as well as detailed study, sizing, hourly estimation, and report generation. It represents a handy design tool for PV system design and estimation (see Figure 8). The software simulates most parameters that are required by PV system designers, helps to generate a comprehensive simulation report, and allows high level of control of various factors (PVsystSA, 2018).

The output power P of the PV panels is calculated using the measured maximum voltage and current values as follows:

$$P = V_P \cdot I_P \quad (1)$$

V_P is the maximum voltage of panel and I_P maximum current of panel. The efficiency of a solar cell is determined as the fraction of incident power, which is converted to electricity and is defined as:

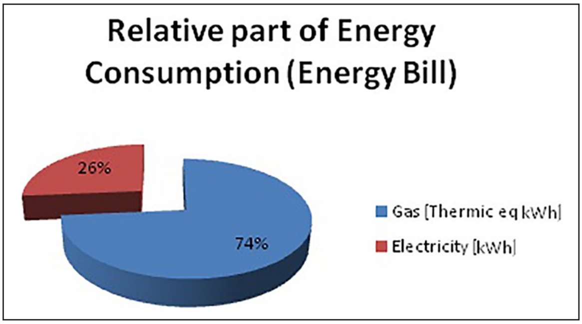

Figure 6. The Tlemcen house's energy consumption from public utilities (Boukli Hacene, 2019).

Table 2. Relative share of the house's real energy consumption (Boukli Hacene, 2019).

	1st quarter	2nd quarter	3rd quarter	4th quarter	Total
Real consumption (energy bill) [kWh]	2918.89	2753.8	1206.79	2702	9581.48
Gas [thermal eq. kWh]	2380.89	2253.8	252.79	2164	7051.48
Electricity [kWh]	538	500	954	538	2530

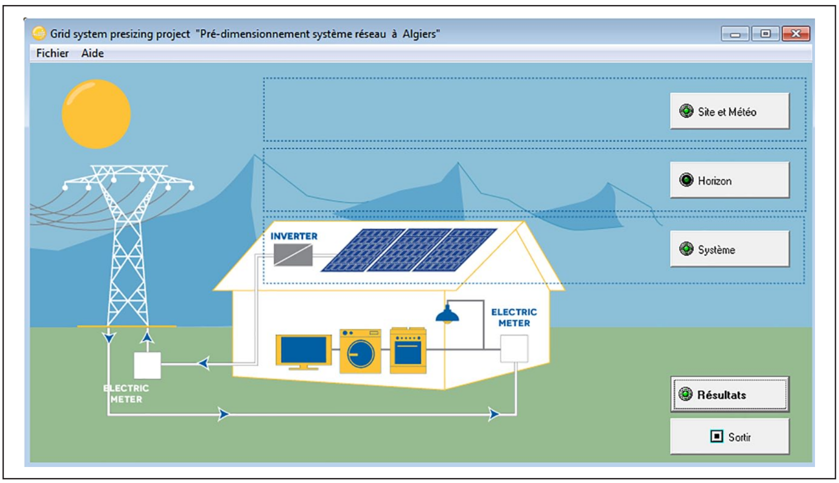

Figure 7. Pre-dimensioning of a photovoltaic system using PVsyst.

$$\eta = \frac{P_{out}}{P_{in}} = \frac{V_{OC} \cdot I_{SC} \cdot FF}{P_{in}} \tag{2}$$

V_{OC} is the open-circuit voltage, I_{SC} is the short-circuit current, FF is the fill factor, while the input power is:

$$P_{in} = A_G \cdot G \tag{3}$$

A_G is the surface area of the solar cell (m²) and G the irradiance (input light) (watt/m²).

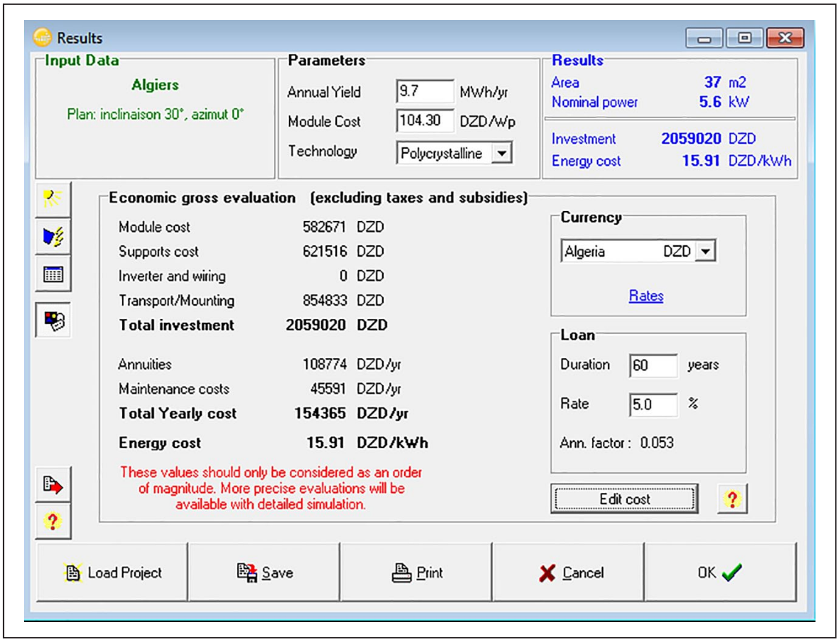

Figure 8. Simulation of the investment in the proposed photovoltaic system by using PVsyst.

Table 3. Comparison between the price of kilowatt hour from fossil fuels and renewable sources.

	Price of kWh	Investment	Annual bill	Investment return time
Electricity from utilities (fossil sources)	4.17 DZD		40,000 DZD (~281 Euro)	
Electricity from the own PV system	15.91 DZD	200,000 DZD (~12,000 Euro)		60 years

Results are presented in Table 3:

The photovoltaic panels (polycrystalline type) will be placed on the roof of the house, facing south, according to the solar mask, with an inclination of 30°. Photovoltaic sizing simulation via PVsyst software gives an investment of around 200,000 DZD (~12,000 Euro) for the installation and maintenance of the photovoltaic panel surface of 37 m², with a nominal output power of 5.6 kWh. The annual output would therefore be around 9700 kWh/year, with a cost of the photovoltaic kWh price estimated at 15.91 DZD/kWh.

The annual energy bill using fossil fuels (gas + electricity) amounts to 40,000 DZD (~281 Euro), which is a kWh price of 4.17 DZD/kWh (state-subsidized cost). As a result, the payback period (PP) is calculated as follows:

$$\text{Payback Period} = \frac{\text{PV Investment}}{\text{Net Cash Flow per Year}}$$

The payback period was found to be about 60 years. The time to recover the investment in the photovoltaic system for the sample house is too long in Algeria—a country that produces cheap

Table 4. Algeria: Evolution of fuel price since 2016.

	Until 31 December 2016	1 January 2017 to 31 December 2017	Since 1 January 2018
	1 Euro = 143 DZD (Algerian Dinar)		
Gasoline price [DZD]/liter	23	35.49	41.97
Gasoline price [Euro]/liter	0.16	0.248	0.29
Gas price [DZD]/liter	13	20.23	23.03
Gas price [Euro]/liter	0.09	0.14	0.16
Average evolution since 2016	/	55.6%	77%

and subsidized natural gas and oil. The other problem is that the Algerian Sahara represents 84% of the national territory, with sunshine of nearly 3,600 hours per year, and temperatures that can exceed 50°C in several regions of the Sahara; therefore, the photovoltaic panel yield would become negligible, and its installation would be better located in the north of the country.

Transport sector

The use of biofuels may improve the energy performance of the transport sector, because the country has a high potential to produce them. It is the world's leading producer of green beans, fifth largest of figs, sixth of dates, eighth of apricots, ninth of artichokes, and tenth of almonds (FAO, 2005). The potential for tree and vine production is close to one million hectares (ha) in 2006. The harvesting area of all combined species is 2,671,140 ha.

The garden areas for market products represent 372,096 ha. Industrial crops, including tomatoes, tobacco, and groundnuts, comprise 10,569 ha. Stone fruit trees cover 280,387 ha, and citrus fruit trees use 57,064 ha. Agriculture is also developing thanks to the planting of several thousand olive trees to make olive oil in Algeria (Algérie-Focus, 2016).

In using biofuels, there are two main practical solutions:

- Integrating biofuels of oleaginous origin into diesel fuel.
- Integrating biofuels from sugar and starch-containing materials into gasoline.

For the lowest fuel prices (petrol and diesel), Algeria is ranked as the fifth in the world, while it is ranked first for LPG (liquefied petroleum gas), according to the 2018 ranking by the specialized site Global Petrol Prices (NAFTAL, 2019).

The price of a liter of petrol in Algeria is estimated at US$0.35 (41.97 DZD), while diesel is estimated at US$0.19 (23.06 DZD), and LPG-c is estimated at US$0.08 (9 DZD). Venezuela is the country with the least expensive gas at US$ 0.01/liter. In second place is Sudan (US$0.13/liter), third place Iran (US$0.29/liter), fourth place Kuwait (US$0.34/liter), and fifth place Nigeria (US$0.41/liter) (NAFTAL, 2019). As for LPG prices, Algeria is followed by Kazakhstan with US$0.21 per liter, and Azerbaijan in third place with US$0.26 per liter (NAFTAL, 2019).

Even though gas prices in Algeria are among the cheapest in the world, Algerians consider the price of 41.97 DZD very high. After 20 years of price stability, the government mandated increases of fuel prices (see Table 4) in both 2017 and 2018. It should also be noted that the price of fuel in Algeria is subsidized by the government.

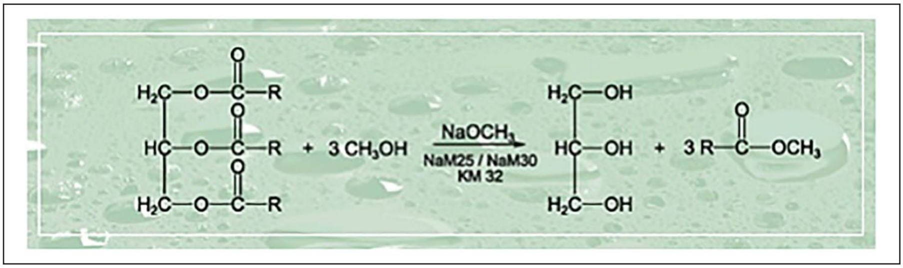

Figure 9. Triglycerides (**1**) are reacted with an alcohol such as ethanol (**2**) to give ethyl esters of fatty acids (**3**) and glycerol (**4**) (The Glycerol Challenge, 2009).

The economic efficiency of introducing biofuels could be a result of comparing the prices of fossil fuels with pure or fossil-mixed biofuels. The last prices can be estimated from the vegetable crops, which can be transformed into biofuels (after refining and chemical treatments).

Biodiesel is a diesel fuel that is made by mixing vegetable oil (cooking oil) with other common chemicals (such as antioxidant additives, alkaline additives, molybdenum disulfide, antiwear additives, etc.). Biodiesel may be used in any diesel automotive engine in its pure form or blended with petroleum-based diesel. The result is a less expensive, renewable, clean-burning fuel. An explanation of how to produce biodiesel from fresh oil follows, but the process can be modified to also use waste cooking oil (e.g. frying oil) by refining and removing residues.

A by-product of the transesterification process is the production of glycerol. For every 1 tonne of manufactured biodiesel, 100 kg of glycerol is produced. Originally, there was a valuable market for glycerol, which helped finance the transesterification process. However, with the increase in global biodiesel production, the market price for this crude glycerol (containing 20% water and catalyst residues) has crashed. Research is now being conducted globally to use this glycerol as a chemical building block. One initiative in the UK is the Glycerol Challenge (Biofuels Wikipedia, 2019).

Biodiesel requires two basic ingredients: oil (sunflower is the most common biofuel) and alcohol (preferably ethanol). When these two products are mixed, a chemical reaction—called transesterification—occurs. Two new elements are obtained during transesterification: the etherification oil, which is biodiesel, and glycerol or glycerin (see Figure 9). The proportions (approximate) are: 10 liters of oils + 1 liter of alcohol –> 10 liters of biodiesel +1 liter of glycerin.

"First-generation" or conventional biofuels have been produced from food crops grown on arable land (see Figure 10). Food crops are thus explicitly grown for fuel production, and nothing else. The sugar, starch, or vegetable oil obtained from the crops is converted into biodiesel or ethanol, using transesterification or yeast fermentation (Biofuels Wikipedia, 2019).

Bioethanol is an alcohol made by fermentation, mostly from the carbohydrates produced in sugar or starch crops, such as corn, sugarcane, or sweet sorghum. Ethanol, an octane enhancer, is blended with gasoline at low- to higher-level blends, or used as a fuel on its own.

The following chemical equations summarize the fermentation of sucrose ($C_{12}H_{22}O_{11}$) into ethanol (C_2H_5OH). Alcoholic fermentation converts one mole of glucose into two moles of ethanol and two moles of carbon dioxide, producing two moles of ATP (adenosine triphosphate) in the process.

The overall chemical formula for alcoholic fermentation is:

$$C_6H_{12}O_6 \rightarrow 2\ C_2H_5OH + 2\ CO_2 \tag{4}$$

Sucrose is a dimer of glucose and fructose molecules. In the first step of alcoholic fermentation, the enzyme invertase cleaves the glycosidic linkage between the glucose and fructose molecules.

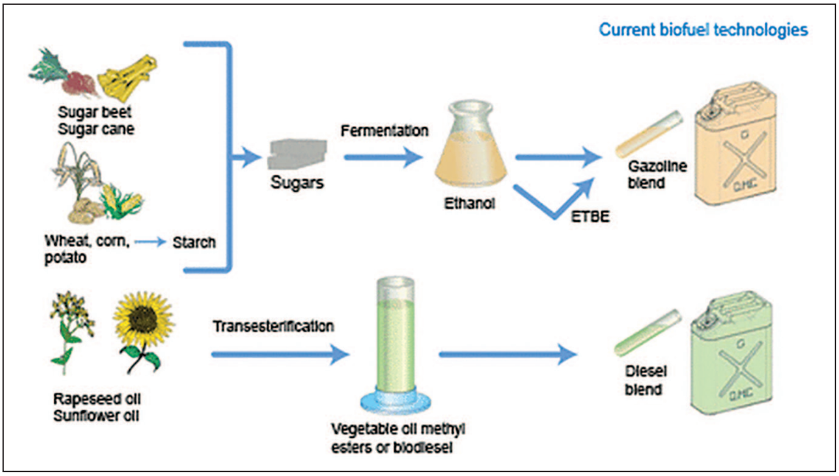

Figure 10. Examples of a first-generation biorefinery (translation from IFP, Panoram 2007, Les nouvelles filières biocarburants) (Biofuels, 2007).

$$C_{12}H_{22}O_{11} + H_2O + \text{invertase} \rightarrow 2\ C_6H_{12}O_6 \tag{5}$$

Next, each glucose molecule is broken down into two pyruvate molecules in a process known as glycolysis (Lubert, 1975). Glycolysis is summarized by the equation:

$$\begin{aligned} &C_6H_{12}O_6 + 2\ ADP + 2\ P_i + 2\ NAD^+ \rightarrow \\ &2\ CH_3COCOO^- + 2\ ATP + 2\ NADH + 2\ H_2O + 2\ H^+ \end{aligned} \tag{6}$$

CH_3COCOO^- is pyruvate, and P_i is inorganic phosphate. Finally, pyruvate is converted to ethanol and CO_2 in two steps, regenerating oxidized NAD+ needed for glycolysis:

$$1.\ CH_3COCOO^- + H^+ \rightarrow CH_3CHO + CO_2 \tag{7}$$

catalyzed by pyruvate decarboxylase

$$2.\ CH_3CHO + NADH + H^+ \rightarrow C_2H_5OH + NAD^+ \tag{8}$$

This reaction is catalyzed by alcohol dehydrogenase (ADH1 in baker's yeast) (Raj et al., 2015).

As shown by the reaction equation, glycolysis causes the reduction of two molecules of NAD^+ (nicotinamide adenine dinucleotide) to NADH. Two ADP (adenosine diphosphate) molecules are also converted to two ATP and two water molecules via substrate-level phosphorylation.

Some features and conversion data:

- One tonne of beet provides about 160 kilos of sugar, compared to 115 kilos for one ton of sugar cane;
- 1 ha of sugar beet yields between 6,000 and 7,000 L of bioethanol;

Table 5. Comparison of the price per liter of gasoline to that of biofuel from sugar and starchy materials.

	1 L of gasoline	Dates	Potatoes	Sugar beet	White sugar
		1 Kg per aliment			
Liter of recovered bioethanol		0.6	0.3	0.5	0.5
Price of 1 liter fuel	41.97	220 DZD	300 DZD	140 DZD	180 DZD

Table 6. Comparison of the price per liter of diesel fuel to that of biodiesel.

	1 L of diesel (fuel oil)	1 L of biodiesel (vegetable oil)
Liter of recovered biodiesel		1
Price of 1 liter diesel fuel	23 DZD	120 DZD

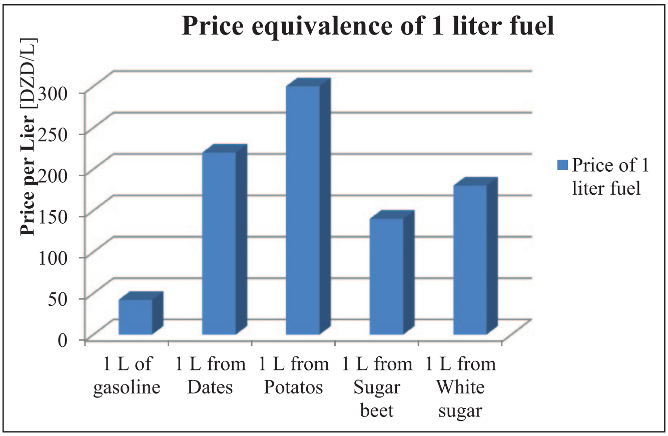

Figure 11. Comparison of the price per liter of gasoline to that of biofuel from sugar and starchy foods.

- Dates are one of the most carbohydrate-rich fruits in the world. 100g of dates comprises 75g of carbohydrates. 100 kg of unpitted dates contain 55% of total weight sugar, from which about 600 liters of vinegar can be obtained;
- 1 ha of wheat or corn can produce 3,000 L of bioethanol;
- 300 ml of wine per kilo of potatoes;
- 100 kg of sugar = 60 L of alcohol;
- Cost of 1 L of bioethanol = 150 DZD (1.66 * 90 DZD).

The calculations are presented in Tables 5 and 6, which compare the price per liter of gasoline to that of biofuel obtained from sugar and starchy foods (see Figure 11), and respectively the price per liter of diesel fuel to that of biodiesel obtained from vegetable oil:

The calorific content of bioethanol compared to gasoline is 66%.

In terms of energy,1.5 liters bioethanol = 1 liter of gasoline.

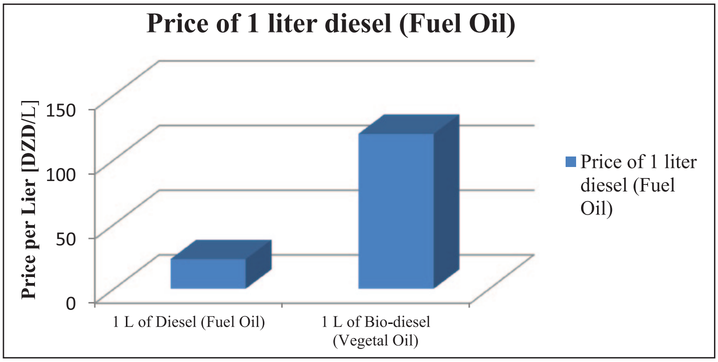

Figure 12. Comparison of the price per liter of diesel fuel to that of biodiesel.

Table 7. Energy equivalence between gasoline and bioethanol.

	Gasoline	Bioethanol
Density (kg/L)	0.755	0.794
Heating value (kJ/L)	32,389	21,283
Heating value/gasoline (equal volume)	1	0.657
Renewable heat value/gasoline (equal volume)	0	0.657

Table 8. Energy equivalence between diesel and vegetable oil.

	Diesel	Vegetable oil
Density (kg/L)	0.84	0.925
Heating value (kJ/L)	37635	36607
Heating value/gasoline (equal volume)	1	0.973

The comparison between prices per liter for fossil fuels and biofuels (Figure 12) shows that it is not enough for a correct economic analysis. In the following, a small comparison between the heating value of fossil fuels and renewable fuels will be presented.

The heating value (or energy value or calorific value) of a substance, usually a fuel or food, is the amount of heat released during the combustion of a specified amount of that substance. The value is calculated for a complete combustion with oxygen under standard conditions. The chemical reaction is typically a hydrocarbon or other organic molecule reacting with oxygen to form carbon dioxide and water and release heat.

The heating value may be expressed with the quantities:

- energy/mole of fuel
- energy/mass of fuel
- energy/volume of the fuel. (Schmidt-Rohr, 2015)

The heating value is different for fossil fuels and renewable biofuels. Thus, the energy level of 1.5 liters of bioethanol equals to 1 liter of gasoline (see Table 7), while 1.03 liter of vegetable oil equals to 1 liter of diesel (see Table 8).

Results and discussion

For the building sector, we found an annual energy bill using fossil fuels (gas + electricity) amounts to 40,000 DZD (~281 Euro), which is a kWh price of 4.17 DZD/kWh (state-subsidized cost). As a result, the payback period (PP) has been found to be about 60 years. The time to recover the investment in the photovoltaic system for the sample house is too long in Algeria, a country that produces cheap and subsidized natural gas and oil.

For the transport sector, we noted from data that despite the increase in fossil fuel prices in Algeria during two successive years, these prices are still far lower than the first-generation biofuel. The results show that the price of bioethanol is between three and four times the price of gasoline in Algeria.

First-generation biodiesel from oleaginous plants is five times more expensive than diesel produced from fossil fuels. That said, despite a heating value almost identical between biodiesel and fossil diesel, the use of diesel is by far the best solution for heat ratio/price.

Conclusion

Alternative energies, even if they prove to be profitable, can only make a very marginal contribution to Algeria's energy needs anticipated by 2030. Therefore, these contributions will not be enough to generate the necessary resources to finance an economy that excludes hydrocarbons.

Under these conditions, only conventional hydrocarbons seem to have the potential to fill the predicted energy deficit and generate the resources needed to finance the economic transition in Algeria. Also, it is essential to focus the bulk of efforts upstream, even if the decline in crude prices persists, to curb—or, even better, reverse—the decline in reserves and production.

This study aims to quantify the use of renewable energies as a substitute for fossil fuels in the energy-intensive building and transport sectors. The results suggest that the main problem blocking the development of renewable energies in Algeria is the low price of fossil fuels compared to renewable energies.

The energy cost in Algeria is already low. Renewable energy therefore cannot compete with the fossil fuels used in the transport and building sectors.

In the building sector, the simulation of PV sizing via the PVsyst software suggests that an investment of around 200,000 DZD (12,000 Euro) would be required for the installation of a photovoltaic panel surface of 37 m^2. The price of photovoltaic kilowatt-hour is estimated at 15.91 DZD/kWh compared to 4.17 DZD/kWh for the fossil kilowatt-hour (state subsidized cost). We found that a return on investment for a PV installation would be about 60 years, which would not be acceptable in a country where the cost of natural gas and oil is very low.

In the transport sector (the second most energy-intensive sector in Algeria), despite the increase in fossil fuel prices in Algeria during two successive years, the prices are still far lower than first-generation biofuel of renewable origin.

The results show that the price of bioethanol is between three and four times the price of gasoline in Algeria. However, the lower calorific supply of bioethanol compared to gasoline is 66%, (1.5 liters bioethanol has the equivalent energy of 1 liter of gasoline). The difference is even greater between first-generation biodiesel from oilseeds and fossil diesel (five-fold increase). That said, despite a nearly identical lower calorific value between biodiesel from oleaginous materials and fossil diesel, the use of diesel is by far the best solution for heat ratio and price.

Funding

The authors received no financial support for the research, authorship, and/or publication of this article.

ORCID iD

Mohammed el Amine Boukli Hacene https://orcid.org/0000-0003-0957-4644

References

AFP (2009) « Nouveaux gisements de gaz en Algérie ». *Journal le FIGARO*, 26 janvier 2009.
Algérie-Focus (2016) « Décryptage/Le Sud, futur eldorado pour l'agriculture algérienne ? », sur *algerie-focus.com*, 31 janvier 2016.
AME (2019) Programmes d'Electrification et de Distribution Publique du Gaz. Algerian Ministry of Energy. Available at: http://www.energy.gov.dz/ (accessed 2 March 2019).
Biofuels Wikipedia (2019) First, second, third and fourth generation biofuels explained (Wikipedia biofuels 15), December 2019. Available at: https://en.wikipedia.org/wiki/Biofuel (accessed 1 September 2019).
Boukli Hacene MA (2019) Energy efficient design optimization of a bioclimatic house. *Indoor and Built Environment*. Epub ahead of print 15 June 2019. DOI: 10.1177/1420326X19856668.
British Petroleum Full Report (2016) Natural gas Production 2019, BP Statistical Review of World Energy 2016. June 2016.
British Petroleum Full Report (2019) Natural gas Production 2019, BP Statistical Review of World Energy 2019.
CIA (2014) "Country Comparison: Area". CIA World Factbook. Archived from the original on 9 February 2014 (accessed 17 January 2013). Available at: https://www.cia.gov/library/publications/the-world-factbook/fields/253rank.html
Daniel Workman (2018) Top World Oil Net Exporters, Crude Oil Exports by Country, Energy Information Administration, 2018.
Ecofin (2012) « L'Algérie vise 22 000 MW d'origine renouvelable dans les 20 prochaines années », Agence Ecofin, 29 novembre 2012.
FAO (2005) « Principaux produits agricoles et alimentaires, et producteurs », sur *FAO*, 2005.
HuffPost Maghreb (2018) « L'Algérie compte 24 centrales photovoltaïques et une ferme éolienne unique », sur *HuffPost Maghreb*, 10 mai 2018 (accessed 2 February 2019).
NAFTAL (2019) Gasoline prices, liter. Available at: https://www.globalpetrolprices.com/gasoline_prices/ (accessed 16 January 2019).
OJPDRA (2015) Official journal of people's democratic republic of Algeria. Available at: https://www.joradp.dz/hen/index.htm (accessed 14 June 2019).
PVsystSA (2018) PVsyst 6.86 - Photovoltaic system study. Available at: http://files.pvsyst.com/help/index.html (accessed 22 December 2018).
Raj SB, Ramaswamy S and Plapp BV (2015) Yeast alcohol dehydrogenase structure and catalysis. *Biochemistry* 53: 5791–5803.
Schmidt-Rohr K (2015) Why combustions are always exothermic, yielding about 418 kJ per Mole of O_2. *Journal of Chemical Education* 92(12): 2094–2099.
SOLARGIS (2019) Solar resource maps of Algeria. Photovoltaic electricity potential. *The World Bank, Solar resource data: Solargis*. Available at: https://solargis.com/maps-and-gis-data/download/algeria (accessed 14 June 2019).
SONELGAZ (2018) Bilan Energétique National pour l'année 2017, Bulletin d'information. Available at: https://www.energy.gov.dz/Media/galerie/benational_2018-edition-2019_5dac85774bce1.pdf
Stryer L (1975) *Biochemistry*. W. H. Freeman and Company. San Francisco, California, p.626.
The Glycerol Challenge (2009) Biofuels and Glycerol. Available at: theglycerolchallenge.org. Archived from the original on 23 May 2008 (accessed 9 July 2008).
TSA (2018) L'Algérie-pays-le-plus-écologiquement-propre, *Tous Sur L'Algérie Journal*. February 2019.

Author biographies

Mohammed el Amine Boukli Hacene is an Associate Professor currently works at the Department of Physics, University of Sidi-Bel-Abbes. Amine does research in Energy Physics, Climate change, Building Energy Efficiency, Sustainability and Energy Policy. Their current project is 'Means of promoting Sustainable

Development in Algeria: Study of the reduction of energy consumption of a state institution' 'Faculty of Exact Sciences - University Sidi Bel Abbes'.

Dorin Lucache is a Professor currently works at the Department Electrical Engineering, Technical University "Gheorghe Asachi" of Iasi . Dorin does research in energy physics Electrical Engineering and Renewable Energy.

Habib Rozale is a Professor currently works at the Department of Physics, University of Sidi-Bel-Abbes. Habib does research in energy physics condensed matter and thermal physics.

Abbes Chahed is a Professor currently works at the Department of Physics, University of Sidi-Bel-Abbes. Abbes does research in energy physics condensed matter and thermal physics.

Journal of Renewable Energies 23 (2020) 318– 330

Journal of Renewable Energies

Revue des Energies Renouvelables

journal home page : https://revue.cder.dz/index.php/rer

Research Paper

Techno-economic assessment of wind energy conversion systems for power generation for the city of N'Djamena in Chad

Marcel Hamda Souloukngа [a*], Dumitru-Dorin Lucache [b],Serge Yamigno Doka [c], Timoleon Crepin Kofane [d]

[a]*Ecole Normale Supérieure de l'Enseignement Technique de Sarh, Tchad*

[b]*Faculty of Electrical Engineering " Gheorghe Asachi " Technical University of Iasi, 21-23 Prof.D. Mangeron Str. IASI-700050 , Romania*

[c]*Department of Physics, Faculty of Science, University of Ngaoundéré, PO Box 454 Ngaoundere, Cameroon*

[d]*Department of Physics, Faculty of Science The University of Yaounde I, P.O. Box. 812, Cameroon*

Centre d'Excellence Africain en Technologie de l'Information et de la Communication, The University of Yaounde I, P.O. Box.812, Cameroon

A R T I C L E I N F O

Article history:

Received 20 July 2020

Accepted 03 December 2020

Keywords:

Wind energy,

N'Djamena,

PVC,

WECS

A B S T R A C T

Around the world, with a significant increase in installed capacity each year, wind power is one of the most profitable forms of renewable energy. In this study, three commercial wind turbines, namely Bonus 300kW/33, Bonus 1MW/54 and Vestas 2MW/80, were selected as large-scale wind power conversion systems (WECS) for the technical evaluation of production electricity for the N'Djamena site in Chad. The economic evaluations of these three WECS for power generation are calculated using the Cost Calculation Technique (PVC). Thus, the results obtained show that the highest capacity factor is 15.29% with Bonus 1MW/54 while the lowest at 11.39% with Bonus 300kW/33. The minimum average cost per kWh is 23 US$ / kWh with the 1 MW/54 Bonus, while the highest cost is 33.8 US$ / kWh with a Bonus of 300 kW / 33.

* *Corresponding author, E-mail address: marcelhamda@yahoo.fr*
Tel : +23563657304

ISSN: 1112-2242 / EISSN: 2716-8247

1. Introduction

Excessive use of fossil fuels can lead to energy and environmental problems. Hence, several countries are obliged to explore the clean sources of energy [1]. In recent decades, wind energy has been used much more in many countries [2]. By making a comparative study of economic resources in view of climatic constraints, reference should be made to the choice of macro-sites to enable the determination of the most favorable sites for wind farms [3]. The choice of macro-sites from the results of the research can provide a crucial basis for wind projects [4-6]. Among the factors to be taken into account for the choice of macro-sites, one can retain the wind energy [7-9]. Wind energy resources can be clearly and efficiently estimated [10, 11]. Wind speed is a disturbing hallmark in the estimation of wind energy [12, 13]. Generally, depending on the observed wind speed data and probabilistic distribution functions, the frequency distribution function can be obtained [14]. In developing countries, it is important to carefully study and understand the energy model to ensure a good standard of living [15]. Wind characteristics such as speed and direction can be developed to determine the wind potential of a site [16]. In many countries around the world, studies and assessments of wind characteristics and the potential of wind energy are being conducted. These countries are the Hong Kong islands whose wind analysis was discussed by Lu et al. [17]. Youm et al. conducted research on the potential of wind power in Senegal using the Weibull probability distribution [18]. For the production of electricity, the wind is an inexhaustible energy resource and appreciable for its non-pollution [19]. Among the renewable energy sources available, wind energy has increased rapidly over the past two decades [20]. Among renewable energy sources such as environmental protection, the security of supply, biodiversity and other socio-economic factors, wind energy is also to be promoted whose growth is the fastest in the world [21]. Due to population growth and industrialization in recent days, in Ethiopia energy production is increasing rapidly. To transform, develop energy resources such as wind, solar, biomass, hydroelectricity, natural gas and geothermal energy can be used within the framework of an optimal economy [22, 23]. Around the world, there are many investigations focused on the assessment of distinctive characteristics of the wind and a study to discern the feasibility of wind projects [24, 25]. In fact, in all regions of Ethiopia, the very limited potential of different sources of renewable energy has been studied [26]. However, the techno-economic evaluation of wind energy conversion systems for power generation for the city of N'Djamena in Chad has never been the subject of a study. It is therefore important to make an economic estimate with a close interest in wind power production in Chad, which will allow investors to secure long-term compensation to improve the profitability of wind power. In addition, wind power generation has been progressing with sustained momentum for some 40 years. In 2018, the commissioning of new wind power plants (onshore and offshore) represented 51.3 GW worldwide. The main objective of this article is to assess the wind resources of the N'Djamena site in the Sahelian zone of Chad. This study focuses on the presentation of the compass rose, the factor of capacity, power and energy as well as the various costs associated with the use of wind energy.

2. Methodology

2.1. Presentation of the data used

Table1. Presentation of the geographical coordinates of the site

Variable	Value
Longitude	15°2 E
Latitude	12 °8 N
Elevation	294 m
Anemometer Height	10 m
Period(year)	20

2.2. Wind potential

The two parameters Weibull probability density function is used to estimate wind speed variations using the following equation:

$$f(v) = \left(\frac{k}{c}\right).\left(\frac{v}{c}\right)^{k-1}.exp\left(-\left(\frac{v}{c}\right)^{k}\right),(k > 0, v > 0, c > 1) \quad (1)$$

To estimate the Weibull parameters, several methods are proposed among which, one can quote: method of the standard deviation, method of the energy form factor, graphical method, method of the maximum of likelihood, method of the density of power and method of the moment. In this study, we used the energy form factor method. It is defined by the following equations [27, 28]. The shape parameter can be estimated as follows [29]. Instead, the scale factor can also be obtained mathematically [30].

2.3. Validation of the wind speed at different heights

The wind speed considered in this study is measured at 10 m altitude at ground level.
For the application of wind energy, it is important to extrapolate the wind speed to the height of the hub .The most commonly used method for this purpose is power law. It is expressed by the following relation [31].

$$v(z_2) = v(z_{10})\left(\frac{z_2}{z_{10}}\right)^{\alpha_1} \quad (2)$$

The exponent α_1 is assumed to be 0.143 (or 1/7). It can be determined as [32]:

$$\alpha_1 = \frac{[0.37-0.088ln(v_{10})]}{\left[1-0.088ln\left(\frac{z_{10}}{10}\right)\right]} \quad (3)$$

The extrapolated Weibull parameters are linked by the expressions below

$$\mathrm{c}(h) = c_0\left(\frac{h}{h_0}\right)^n \quad (4)$$

$$k(h) = k_0\left[1-0.088ln\left(\frac{h_0}{10}\right)\right] / \left[1-0.088ln\left(\frac{h}{10}\right)\right] \quad (5)$$

2.4. Estimated output power for WECS

By considering such a system, for this site, power curves associated with wind turbines, the annual energy output of a selected site can be calculated .WECS cannot exploit its maximum efficiency in general, because of the power rating, and wind shutdown and depending on the wind characteristics of the site, cut-off speeds must be defined. One of the important performance parameters of wind turbines is the capacity factor (C_f) which is a proportion of the average power (Pe, ave) up to the rated electrical power (Per) and is estimated at using the following mathematical equations[33]:

$$P_{e,ave} = P_{eR}\left\{\frac{e^{-\left(\frac{v_c}{c}\right)^k} - e^{-\left(\frac{v_r}{c}\right)^k}}{\left(\frac{v_r}{c}\right)^k - \left(\frac{v_c}{c}\right)^k} - e^{-\left(\frac{v_f}{c}\right)^k}\right\} \quad (6)$$

and the capacity factor C_f of a wind turbine is given by [34]:

$$C_f = \frac{P_{e,ave}}{P_{eR}} \tag{7}$$

$$E_{out} = 8760 * t * P_R * A * C_f \tag{8}$$

2.5. Analysis of the cost of wind energy

The ability to produce energy at a minimum operating cost depends on the feasibility of a wind power plant. The key parameters governing wind energy economics include capital cost, power generation, power generation, operating and maintenance costs, turbine life and fuel efficiency discount.

From one region or country to another, these factors vary. Thus, among all the parameters listed, the generation of electricity using WECS and their investment costs are the most important factors. Moreover, in addition to the cost of the wind turbine set by the manufacturers, the specific cost of a wind turbine changes from one manufacturer to another. Therefore, the specific cost of a wind turbine can be taken (minimum and maximum values) given the band interval [35].

The present value of costs (PVC) is determined using relationship [36]:

$$PVC = I + C_{omr} \times \left[\frac{1+i}{r-i}\right] \times \left[1 - \left(\frac{1+i}{1+r}\right)^t\right] - S \times \left(\frac{1+i}{1+r}\right)^t \tag{9}$$

where, r represents the interest rate, i the inflation rate, t the useful lifetime of turbine, *S* is the scrap value.

To estimate PVC, the following quantities and assumptions are retained:

- *r* and *i* are respectively 11.97% and 3.60%.
- The service life (t) of the machine is 20 years.
- O & M costs: A significant portion of the total annual operating costs of a wind turbine, but their value is not fixed. Operating costs vary each year with changes in inflation and interest rates.

In this study, we admit that the annual Com costs are of the order of 7.5% of the investment cost of the studied wind system (system price /lifetime).

- The factor (S) is an additional cost for most wind farms, located near rural areas of the country. Therefore, installation costs (including the cost of civil works, turbine transportation, and road construction) are still high, compared to the costs that would be incurred if the wind turbines were installed in an urban area. It is admitted here that (S) is equal to 10% of the price of the wind turbine.
- As most projects are carried out in rural areas, the cost of land and civil works are not high. They can therefore be estimated at 20% of the price of the wind turbine.
- The Cost of Electricity (COE) per unit kWh using the PVC method is then expressed by the following expression:
-

$$COE\ (\$/kWh) = PVC / E_{out} \tag{10}$$

3. Results and discussion

3.1. Wind rose

The wind rose plays a very important role in locating sites suitable for the installation of a wind turbine. Figure 1 shows the wind rose for the N'Djamena site. The predominant sectors are South (S), North-West (NW), South-West (SW), South-South-West (SSW) and the dominant sectors are North (N), North-North-East (NNE) and North-North-West (NNW).

We also note, the more the color tends to dark green, the more direction is important for the wind turbine installation. The more the color tends towards the light green, the more the direction is less important.

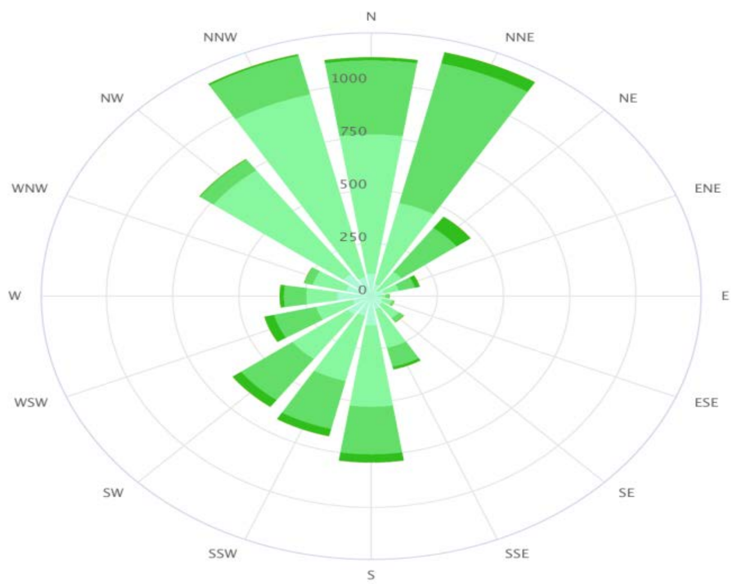

Fig 1. The wind rose

3.2. Extrapolation of wind speed to 30.50 and 67 m altitude

Figure 2 presents the monthly variations of extrapolation of wind speed at 30 m, 50 m and 67 m for the N'Djamena site. This table shows the variation from 3.311 m / s to 5.49 m/s to 30 m; from 3.846 to 6.217 m/s at 50 m and 4.19 at 6.677m/s at 67m. In addition, it is observed that at 30 m altitude, the average annual speed is 4.35 m/s; at 50 m it increases to 4.98 m/s and at 67 m it is 5.38 m/s. This allows us to conclude that the wind speed increases with altitude.

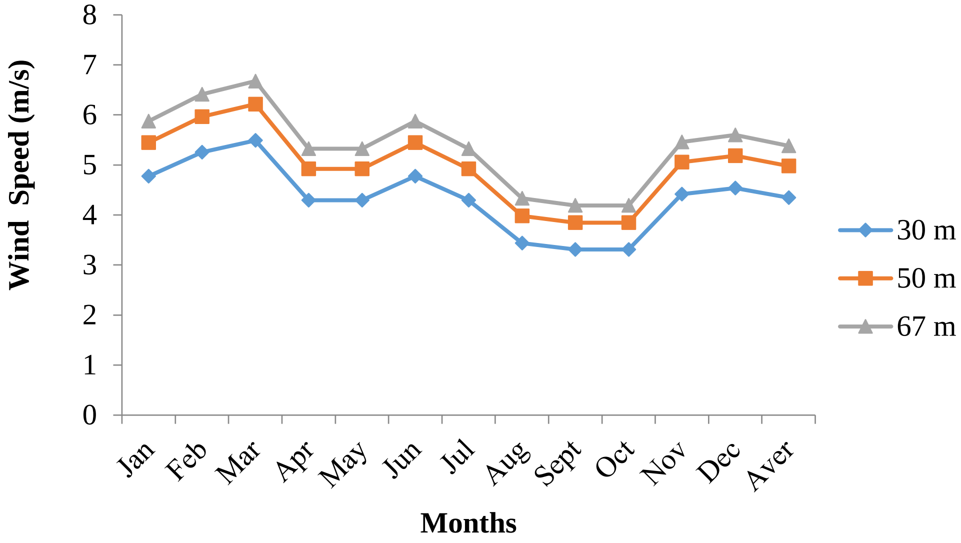

Fig.2 Extrapolation of wind speed to 30.50 and 67 m altitude

3.3. Extrapolation of the Weibull k parameter

Figure 3 presents the monthly variations of the extrapolation of the shape parameter at 30 m, 50 m and 67 m for the N'Djamena site. This table shows the variation from 3.563 to 4.729 at 30 m; from 3.579 to 4.75 to 50m and 3.588 to 4.763 to 67m. On the other hand, at 30 m altitude, the annual value of the Weibull form parameter is 4.27; at 50 m it is 4.293 and at 67 m it goes to 4.30. This allows us to conclude that the shape parameter increases with altitude.

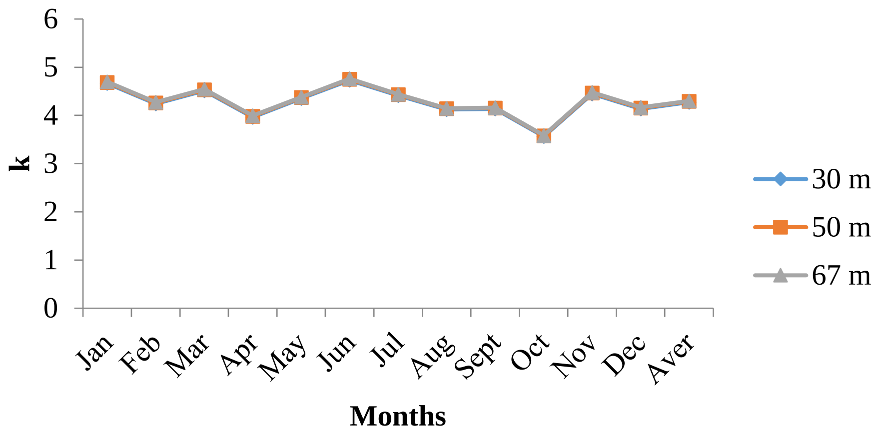

Fig 3. Extrapolation of the shape parameter (k)

3.4. Estimation of the electric power supplied by wind turbines

Three wind turbines are chosen to evaluate wind energy. It's about: Bonus 1 MW/54, Bonus 300 kW/33 and Vestas 2 MW/V80. Their rated power (P_R) is 1000, 300 and 2000 kW, respectively.

Table 2. Choice of selected wind turbines and their characteristics

Characteristics	Bonus 300 kW/33	AN Bonus 1MW/54	Vestas 2MW/80
Rated power P_R *(kW)*	300	1000	2000
Hub height *h (m)*	30	50	67
Rotor diameter *(m)*	33.4	54.2	80
Rated wind speed *Vr (m/s)*	14	15	16
Cut-in wind speed *Vc (m/s)*	3	3	4
Cut-off wind speed V_f *(m/s)*	25	25	25

Table 3. Different values of the cost of wind turbines [38]

Size of wind turbines (kW)	Specific cost ($/kW)	Average cost ($/kW)
<20	2200-3000	2600
20-200	1250-2300	1775
>200	700-1600	1150

3.5. Present value of Cost of wind electricity

Figures 4 and 5 present the monthly values of the cost of wind energy in US$ per kWh and XAF per kWh respectively.

Thus, figure 4 shows that the costs vary from 0.67 to 4.66 $/kWh (Bonus 1MW/54); 0.70 to 6.11 $/kWh (Vestas 2MW/V80) and 0.85 to 7.69 $/kWh (Bonus 300kW/33).

As for figure 5, the costs vary from 364.83 to 2530.63 XAF/kWh (Bonus 1MW/54); 380.08 to 3318.28 XAF/kWh (Vestas 2MW/V80) and 462.22 to 4178.73 XAF/kWh (Bonus 300kW/33). We see that the amount is higher in XAF.

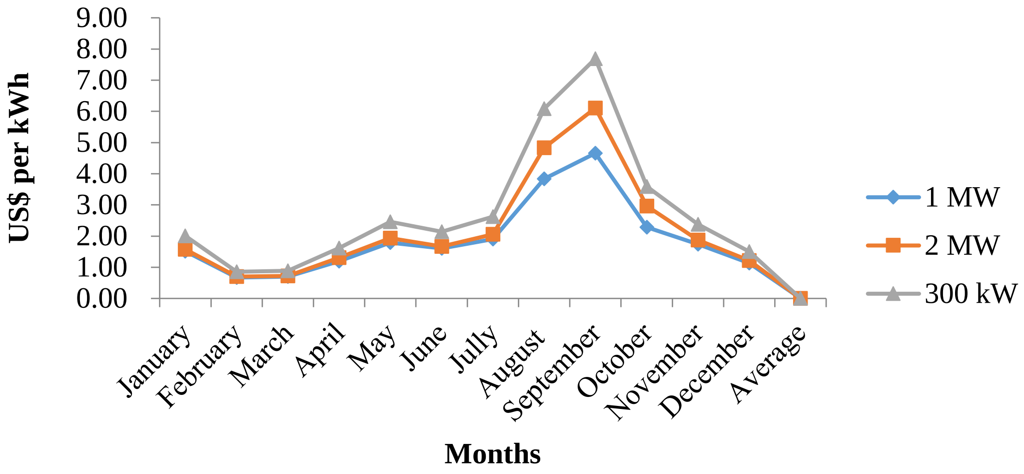

Fig 4.Cost of Energy (US$ per kWh)

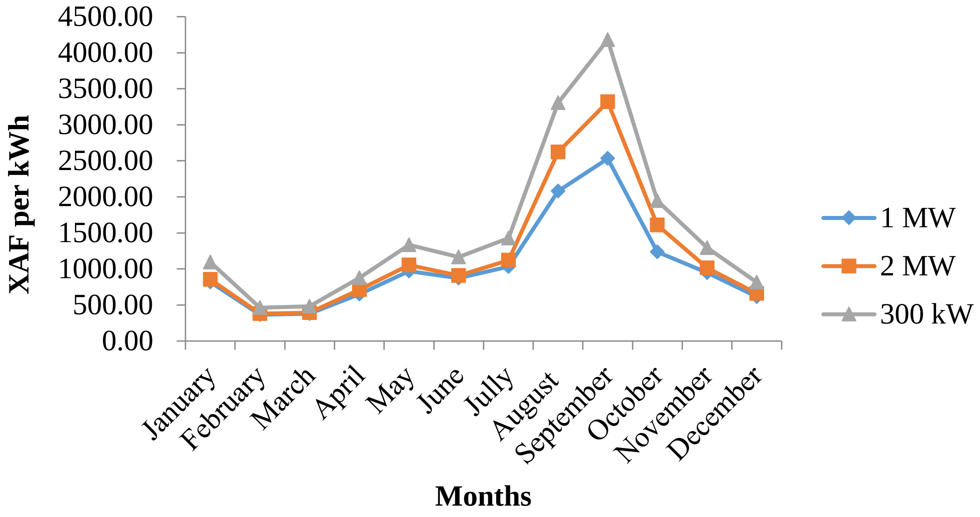

Fig 5. Cost of Energy (XAF per kWh)

Table 4 presents the different annual values of the characteristics for the three wind turbines. Thus, the value of the average annual power varies from 34.18 to 283.31 kW/year. The capacity factor varies from 11.39% to 14.17%. Finally, the annual production varies from 24609 to 203984 MWh / year.

Table 4. Calculated annual energy estimate for selected wind turbines for selected sites

	Bonus 300 kW/33	Bonus 1MW/54	Vestas 2MW/V80
Pe,m (kW/Year)	34.18	152.89	283.31
Cf (%)	11.39%	15.29%	14.17%
Eout (MWh/Year)	24 609	110 080	203 984

Where Cf (%) is the capacity factor of the wind turbine, E_{out} (MWh / year) is the annual production of accumulated energy, $P_{e,\,m}$ (kW / year) is the annual power produced by the wind turbine.

Table 5 also presents the different annual values of the characteristics for the wind turbines in question. Thus, the nominal electric power varies from 300 to 2000kW. The cost in \$ is \$ 23 to \$ 33.8. In the CFA franc, this cost varies from 12495.5 to 18377.7 XAF.

Table 5. Presentation of the annual values of the capacity factor, power averages, energy produced and the cost of energy produced at different hub heights.

	Bonus 300kW/33	Bonus 1MW/54	Vestas 2MW/V80
P_{out}	34.18	152.89	283.31
P_{er}	300	1000	2000
Cf (%)	11.39%	15.29%	14.17%
E_{out}	374250.2	1674101.7	3 102 266
$C_{US\$}$	33.8	23.0	27.0
C_{XAF}	18377.7	12495.5	14647.0

4. Conclusions

This work makes a techno-economic assessment of wind power conversion systems for power generation for the city of N'Djamena in Chad. Thus, it is presented the rose of the wind for the city of N'Djamena. The capacity factor, power and energy are respectively 15.29%, 152.89 kW/year and 110.080 MWh/year using the Bonus 1MW/54 wind turbine. The various costs related to the use of wind energy have been evaluated, with the average minimum cost per kWh of \$ 23.0/kWh. It also emerges in this study that in view of the prices of the wind turbines considered, the price is high. It is therefore desirable in the future to use other characteristics of wind turbines whose prices could be affordable to the population.

5. Acknowledgment

We would like to thank the national meteorological authorities of Chad to make available to us the different data collected, for having made available to us the data that were used in our work.

Nomenclature

$\boldsymbol{k_0}$ and $\boldsymbol{c_0}$ are the shape and scale parameters at the measured height h_0 and the height of the hub h.

k and c are the Weibull form factor and the scale factor

PVC, Present Value of Cost

COE, Cost of Energy

WECS, Wind Energy Conversion System

C_f, Capacity factors (%)

V_f, cut-off wind speed (m/s)

V_r , rated wind speed (m/s)

V_c , cut-in wind speed (m/s)

A, availability of the wind power resource for generating electricity

t, use full life time of turbine in years (20 years)

P_R, Rated power (kW)

C_{om}, is the operation and maintenance cost(7,5% of the investment cost)

6. References

[1] B V. Ermolenko, G V. Ermolenko, YA Fetisova, LN Proskuryakova ,Wind and solar PV technical potentials: Measurement methodology and assessments for Russia, Energy 137 (2017)1001–12.

[2] J.Yang, C. Zhang, Q. Sun & G. Wang, A survey on wind farm sitting. Acta Energiae Solaris Sinica (2012).

[3] J. Schallenberg-Rodríguez, N. García Montesdeoca, Spatial planning to estimate the offshore wind energy potential in coastal regions and islands. Practical case: The Canary Islands, Energy 143(2018) 91–103.

[4] YC Deng, Z. Yu, Methodology of wind resource assessment in wind farm Macrositing based on reference wind turbine, Energiae Solaris Sinica 11(2010)1516–20.

[5] M. H. Soulouknga, S. O. Oyedepo, S. Y. Doka, T.C. Kofane, Assessment of Wind Energy Potential in the Sudanese Zone in Chad, Energy and Power Engineering 9(2017)386-402

[6] J. Dong, T T. Feng, Y S Yang, Macro-site selection of wind/solar hybrid power station based on ELECTRE – II, Renewable & Sustainable Energy Reviews,35(2014)194-204.

[7] Li QW. Micro-setting and wind power research of Da Tang Ji Lin xiang yang. Jilin University (2011).

[8] Shaahid SM, Al-Hadhrami LM, Rahman MK., Economic feasibility of development of wind power plants in coastal locations in Saudi Arabia, Renew Sustain Energy Rev19(2013)589–97.

[9] Na Wang, Research of Wind Energy Resource Assessment in Wind Farm Macro—siting, Hunan University (2015)

[10] C.Mattar, MC. Guzmán-Ibarra, A techno-economic assessment of offshore wind energy in Chile, Energy 133(2017)191–205.

[11] B N. Miranda-Blanco, E. Díaz-Dorado, C. Carrillo, State estimation for wind farms including the wind turbine generator models, Renewable Energy71(2014)453-465.

[12] C. Herrero-Novoa, IA. Pérez, ML. Sánchez, MÁ. García, N. Pardo, B. Fernández-Duque ,Wind speed description and power density in northern Spain, Energy 138(2017)967–76.

[13] S. Muhammad Lawan, WA. Wan Zainal Abidin,Wind energy assessment and mapping using terrain nonlinear autoregressive neural network (TNARX) and wind station data,Cogent Eng (2018).

[14] M. Gökçek, A. Bayülken, Ş. Bekdemir, Investigation of wind characteristics and wind energy potential in Kirklareli, Turkey, Renew Energy 32(2007)1739–52.

[15] A. Ucar, F. Balo, A seasonal analysis of wind turbine characteristics and wind power potential in Manisa, Turkey, Int J Green Energy 5(6) (2008) 466–79.

[16] B. Yaniktepe, T. Koroglu, MM. Savrun, Investigation of wind characteristics and wind energy potential in Osmaniye, Turkey, Renew Sustain Energy Rev 21(2013)703–11.

[17] L. Lu, H. Yang, J. Burnett, Investigation on wind power potential on Hong Kongislands: an analysis of wind power and wind turbine characteristics, Renew Energy 27(2002)12.

[18] I. Youm, J. Sarr, M. Sall, A. Ndiaye, MM. Kane, Analysis of wind data and wind energy potential along the northern coast of Senegal, Renew Sustain Energy Rev 8(2005)95–108.

[19] A. Ucar, F.Balo, Evaluation of wind energy potential and electricity generation at six locations in Turkey, Applied Energy 86(2009) 1864–1872.

[20] G. Murat, G. Mustafa Seedar, Evaluation of electricity generation and energy cost of wind energy conversion systems (WECSs) in Central Turkey, Applied Energy 86(2009)2731–2739.

[21] S.A. Akdag, O. Guler, Evaluation of wind energy investment interest and electricity generation cost analysis for Turkey, Applied Energy 87(2010)2574–2580.

[22] S. A. Akdag, & A. Dinler, A new method to estimate Weibull parameters for wind energy applications, Energy Conversion and Management 50(2009) 1761–1766.

[23] Ch. Breyer, A. Gerlach, M. Hlusiak, C. Peters, P. Adelmann, J. Winiecki, Electrifying the poor: Highly economic of-grid PV systems in Ethiopia a basis for sustainable development (2009).

[24] T. L. Acker, S. K. Williams, E. P. N. Duque, G. Brummels, J. Buechler, Wind resource assessment in the state of Arizona: Inventory, capacity factor, and cost, Renewable Energy 32(2007) 1453–1466.

[25] H. S. Bagiorgas, M. N. Assimakopoulos, D. Theoharopoulos, D. Matthopoulos, G. K. Mihalakakou, Electricity generation using wind energy conversion systems in the area of Western Greece, Energy Conversion and Management 48(2007) 1640–1655.

[26] K. Shiva Prashanth, G. Satyanarayana, Statistical scrutiny of Weibull parameters for wind energy potential appraisal in the area of northern Ethiopia, Renewables:Wind, Water and Solar 14(2) (2015) 1–15.

[27] M.H. Soulouknga, D.K. Kaoga, N. Djongyang, S.D. Yamigno, Comparaison du potentiel énergétique éolien des trois zones climatiques du Tchad, Revue des Energies Renouvelables 19 (2016) 49 – 58.

[28] A. K. Azad, M.G. Rasul, R. Islam, I.R. Shishir, Analysis of wind energy prospect for power generation by three Weibull distribution methods, Energy Procedia 75 (2015)722 – 727.

[29] P. A. C. Rocha, R. C. de Sousa, C. F. de Andrade, da Silva, M. E. V. , Comparison of seven numerical methods for determining Weibull parameters for wind energy generation in the northeast region of Brazil, Applied Energy 89(2012)395–400.

[30] A. Balouktsis, D. Chassapis, T. D. Karapantsios, A nomogram method for estimating the energy produced by wind turbine generators, Solar Energy 72 (2002) 251–259.

[31] E. K. Akpinar, S. Akpinar, An assessment on seasonal analysis of wind energy characteristics and wind turbine characteristics, Energy Conversion and Management 46(2005) 1848–1867.

[32] C.G. Justus, A.Mikhail, Height variation of wind speed and wind distributions statistics, Geophys.Res.Lett 3(1976) 261-264.

[33] M.H. Soulouknga, S. O. Oyedepo, S.Y. Doka, T. C. Kofane, Evaluation of the cost of producing wind‐generated electricity in Chad, International Journal of Energy and Environmental Engineering (2020).

[34] D. K. Kidmo, K. Deli, D. Raidandi, S. D.Yamigno, Wind energy for electricity generation in the far north region of Cameroon, Africa-EU Renewable Energy Research and Innovation Symposium, RERIS 2016, 8-10 March 2016.

[35] M. S. Adaramola, S. S. Paul, S. O. Oyedepo, Assessment of electricity generation and energy cost of wind energy conversion systems in north-central Nigeria, Energy Conversion and Management 52(2011) 3363–3368.

[36] A.S. Ahmed Shata, R. Hanitsch, Evaluation of Wind Energy Potential and Electricity Generation on the Coast of Mediterranean Sea in Egypt, Renewable Energy 31(2006)1183 – 1202.

13th International Conference on DEVELOPMENT AND APPLICATION SYSTEMS, Suceava, Romania, May 19-21, 2016

Wider Generality Relation in the Road Lighting Calculation

Dorin D. Lucache, Gabriel Chiriac, Dan Ioachim
Faculty of Electrical Engineering
"Gheorghe Asachi" Technical University of Iasi
Iasi, Romania
lukake@tuiasi.ro

Radu Dumitru Pentiuc
Faculty of Electrical Engineering and Computer Science
"Stefan cel Mare" University of Suceava
Suceava, Romania
radup@eed.usv.ro

***Abstract*— The design of the outdoor lighting is based on the point-by-point method to estimate the direct component of the illuminance and it has a high complexity. This complexity is higher as the spatial repartition of the luminous intensities is more asymmetrical and as the more random is the position between the luminaire and the visual task. At the present, the lighting-domain specific software helps for quick and precise calculus, using some complex formulas with different degrees of generality. The present paper proposes a new way in applying the point-by-point method, by a different estimation of the zenith (α) and azimuth (β) angles. It uses an orthogonal reference system placed in an arbitrary point, which is transformed by successive rotations into a more convenient one. Using this new method, the resulted relations have a higher generality and the calculus time is shorter, especially in the very complex systems. Even seem apparent complicated, the obtained formulas are a result of the calculus with rotation matrices and can be easy implemented into the software. Moreover, they can be easily customized for any specific conditions.**

Keywords*—road lighting; light intensity; zenith angle; azimuth angle

I. INTRODUCTION

Lighting installations have the role to assure a comfortable illuminating microclimate in the necessary areas when the natural illumination becomes insufficient. The estimation of the visual comfort is made both from the quantitative and the qualitative point of view [1-4]. The quantitative estimation refers usually to the value of the medium illuminance to be assured on the task surface. These values of the illumination are standardized and represent the basic element in the photometric design that leads to the following results: the necessary lamp, the luminaire, the geometry of the lighting installation, the uniformity of the illumination, the installed power, the investments and the maintenance costs and so on.

The qualitative assessment refers usually to the estimation of the luminance (or brightness) and brightness contrast from the visual field (in a normal plan at the view direction) or from the objects on the task surface. In fact, the qualitative estimations are check-ups of the designed lighting installation using the well-known quantitative methods. For the exterior lighting systems, including the road lighting systems, the most used method is the point by point method. Literature mentions also situations when, especially in the case of the streetlight design, the utilisation coefficients method can be applied.

The basic purpose of lighting for road traffic is to enhance the motorist's visual performance, visual comfort and alertness. To maintain a high level of visual performance, the road user must feel comfortable in the visual environment and keep the level of fatigue low. Improving road lighting can enhance visual comfort and may contribute in keeping drivers alert due to its neurological influence [5].

Considering new lamps and technologies as LEDs [6] or metal halide lamps [7], different methods and methodologies for street lighting design have been proposed. The road lighting calculations doubled by measurements proved that, depending on the calculation method, the same road lighting installation may result in different road-lighting quality-parameter values. The higher differences between methods were found when calculating the overall luminance uniformities and longitudinal luminance uniformities, than in the case of the average road surface luminance [8]. Many studies have shown that road lighting can help to reduce the number of night-time accidents by more than 30% and for the pedestrian, easy of recognition of faces during encounters between people in the street may also increase the sense of security and reduces the accidents, injuries and crime attacks [5].

The medium illuminance to a point from the task surface contains two components which are summed [1-3]:

- Direct component of the luminous flux of the light source, meaning the component that reaches directly the surface.
- Reflected component, resulted from the luminous flux that arrives on the task surface after several reflexions on the adjacent surfaces.

These two components have different weights in the illumination final value in the case of interior lighting. On the opposite, in the exterior lighting, the reflected flux (from road, buildings, or vegetation) is negligible, the direct component giving the illumination final value. This is why this paper will focus only on the calculus of the illumination direct component in the case of roads, highways, crossroads, squares or zebra

978-1-5090-1993-9/16/$31.00 ©2016 IEEE

crossing.

The luminaires used for the street lighting [2, 4] are divided, accordingly to their spatial distribution of luminous intensity, in two main categories:

- Symmetrical luminaires, which has a spatial distribution of luminous intensity similar to a revolution body, so having an axis of symmetry.
- Asymmetrical luminaires where the spatial distribution of luminous intensity has one or two symmetry plans (denoted by „C"), as follows:
  - Longitudinal plan of symmetry ($C_{90}C_{270}$), determined by the optical axis, Ω, and the longitudinal axis of symmetry, Λ, of the luminaire.
  - Transversal plan of symmetry (C_0C_{180}), normal to the first one, the intersection line being the optical axis of the luminaire (Fig. 1).

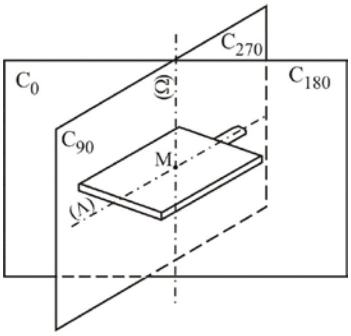

Fig. 1. The symmetry plans of on asymmetric luminaire.

The half-plan (C_0) belongs to the transversal plan of symmetry (C_0C_{180}), being placed to the left when the luminaire is viewed from the front. The polar curves of the light distribution (Fig. 2) are given for a single plan (C) in the case of symmetrical luminaires, in two (if the maximum of the luminous intensity I_{max} belongs to the cross symmetry plan $I_{max} \in (C_0C_{180})$) or three (if I_{max} belongs to any another plan, $I_{max} \in (C_\beta)$ with $\beta = 0...90^0$) symmetry plans, in the case of asymmetrical ones.

The polar curves refer to the situation when the optical axis (Ω) is normal to a horizontal plan and the light source is the standard lamp of 1000 lm. The luminaires can be equipped/fitted with different types of light sources, as inert gas discharge lamps (at low or high pressure), metal vapour lamps, xenon lamps, or lately, with the LEDs. These light sources, regardless the operating principle, generate usual a light spatial distribution with axial symmetry. Inside the luminaire, a mirror-based optical system can preserve or not this symmetry, but in every cases it will modify the solid angle of the emitted luminous flux. Thus, the redistribution of the luminous flux of the source accordingly to the necessities it is assured.

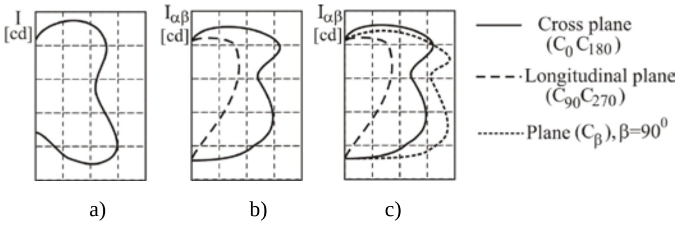

Fig. 2. Polar curves: a) symmetrical b) asymmetrical and $I_{max} \in (C_0C_{180})$, c) asymmetrical and $I_{max} \in (C_{20})$.

In the case of asymmetrical luminaires, the polar curve into the longitudinal plan ($C_{90}C_{270}$) is a co-sinusoidal one, due to the light source dimensions and optical system geometry and it can be estimated by analytically methods [1-4]. Except this, for other secant meridian plans, this approach is not possible or is very complicated.

II. Calculus Of The Illuminance Direct Component

According to the illuminance laws, an asymmetrical luminaire placed into the point M (Fig. 3), will produce an surface S (surface having an arbitrary shape and orientation) estimated with the relation [1-6, 10]:

$$E_d = k \cdot \frac{I(\alpha,\beta) \cdot \cos\theta}{MP^2} \tag{1}$$

where:

- $I(\alpha,\beta)$ is the luminous intensity on the calculus point direction.
- $\alpha = \angle\overline{MP},(\Omega)$ is the zenith angle, and is measured between the optical axis (Ω) and the direction $\overline{MP}$ of the luminous intensity.
- $\beta = \angle(C),(Q)$ is the azimuth angle, measured between the longitudinal plan of symmetry of the luminaire (C)≡($C_{90}C_{270}$) and the meridian plan (Q), determined by the optical axis (Ω) and the calculus point P.
- $\theta = \angle\overline{N}_{dS}, \overline{PM}$ is the incidence angle of the luminous intensity ray over the infinitesimal area element dS that surround the point P.
- $\overline{N}_{dS} = \lambda\bar{i} + \mu\bar{j} + \nu\bar{k}$ is the normal to the area element d*S*, where λ, μ and ν are the cosines directories.
- $MP = |\overline{MP}| = |\overline{PM}|$ is the geometrical distance between the light source and the calculus point.
- k is the lamp's lumen depreciation factor.

For a given luminaire, the light distribution polar curves are usually known:

$$I(\alpha,\beta) = f(\alpha)_{\beta=ct} \tag{2}$$

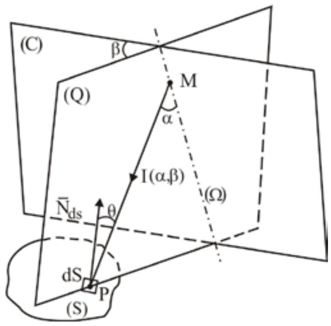

Fig. 3. Direct component of the illuminance.

So, to calculate the illuminance into a specific point at a given distance, firstly must be determined the α and β angles, as well the incidence angle θ. Literature [3, 4] usually offers the necessary relations (mainly based on plan geometry) but only for special particular cases.

Some examples of such particular cases are: the optical axis belongs to a plan normal on a flat task surface, the luminaire is placed along with one axis of the triorthogonal reference system, the origin of the coordinate system is placed in the calculus point etc.

The above particular cases don't cover all the practical situations and this paper proposes a more general method to estimate the zenith and azimuth angles, no matter how the luminaire is positioned or how the shape and the orientation of the task surface is. To estimate the necessary relations one considers a triorthogonal reference system Oxyz (Fig. 4) fixed in space and an asymmetric luminaire, having the optical centre placed into the point $M(x_0,y_0,z_0)$. Its symmetry longitudinal plan (C) makes an angle φ with the horizontal plan xOy

$$\varphi = \angle(\overline{N}_C),(\overline{N}_{xOy}) \tag{3}$$

This is equal with the angle between the normal vectors $\overline{N}$ of the two plans. The angle of incidence θ of the luminous intensity in the Oxyz system is:

$$\cos\theta = \frac{\overline{N}_{ds}\cdot\overline{PM}}{N_{ds}\cdot PM} = \frac{\lambda(x^*-x_0)+\mu(y^*-y_0)+\nu(z^*-z_0)}{\sqrt{(x^*-x_0)^2+(y^*-y_0)^2+(z^*-z_0)^2}} \tag{4}$$

The estimation of the α and β angles could be simple if the triorthogonal reference system should be placed so that the optical axis of the luminaire would be normal to one of its plans. Let us keeping the origin O and consider a system denoted OXYZ (Fig. 5) with

$$(\Omega)\perp(XOY),\ (C)\perp(XOY)\ \text{and}\ (Q)\perp(XOY) \tag{5}$$

In this new coordinate system, the points M and P can be written $M(X_0,Y_0,Z_0)$ and $P(X^*,Y^*,Z^*)$, and the orthogonal projection of the point M on the plan XOY has the coordinates $M'(X_0,Y_0,0)$.Thus, the angles α and β can be estimated as [10]:

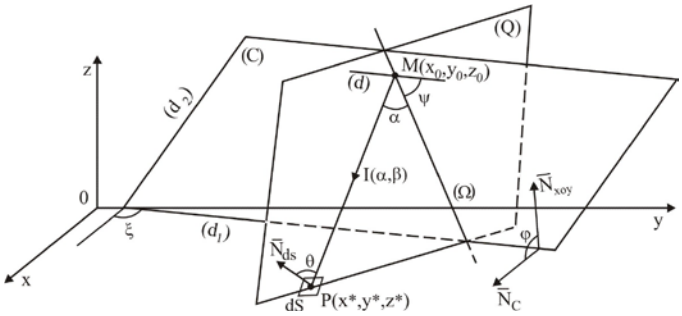

Fig. 4. The luminaire position into a triorthogonal reference system Oxyz, as follows: (d1)=(C)∩(xOy) and (d2)=(C)∩(yOz) , $\xi = \angle(d_1),(Ox)$ and the optical axis (Ω) is inclined toward the line (d1) with the angle $\psi = \angle(d_1),(\Omega) = \angle(d),(\Omega)$ because (d) ∥ (d1), (d) ∈(C), M ∈ (d)

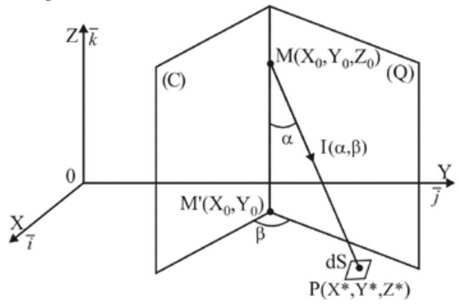

Fig. 5. System OXYZ.

$$\begin{cases} \cos\alpha = \dfrac{\overline{MP}\cdot\overline{MM'}}{MP\cdot MM'} \\ \cos\beta = \overline{N}_Q\cdot\overline{N}_C \end{cases} \tag{6}$$

where the vectors

$$\begin{cases} \overline{MP} = (X^*-X_0)\cdot\overline{i} + (Y^*-Y_0)\cdot\overline{j} + (Z^*-Z_0)\cdot\overline{k} = -\overline{PM} \\ \overline{MM'} = -Z_0\overline{k} \end{cases} \tag{7}$$

have the absolute values:

$$\begin{cases} MP = PM = \sqrt{(X^*-X_0)^2+(Y^*-Y_0)^2+(Z^*-Z_0)^2} \\ MM' = Z_0 \end{cases} \tag{8}$$

and $\overline{N}_Q,\overline{N}_C$ are the unit vectors of the normal vectors to the plans (Q) and (C):

$$\begin{cases} \overline{N}_Q = \dfrac{F\cdot\overline{i}+G\cdot\overline{j}+H\cdot\overline{k}}{\sqrt{F^2+G^2+H^2}} \\ \overline{N}_C = -\overline{j} \end{cases} \tag{9}$$

The director parameters F, G and H of the plan (Q) with the general equation:

$$(Q) \equiv F\cdot X + G\cdot Y + H\cdot Z + L = 0 \tag{10}$$

can be estimated from the condition that the points P, M and M' belong to this plan. Using the equation of a plan passing through three points:

$$(Q) \equiv \begin{vmatrix} X & Y & Z & 1 \\ X^* & Y^* & Z^* & 1 \\ X_0 & Y_0 & Z_0 & 1 \\ X_0 & Y_0 & 0 & 1 \end{vmatrix} = 0 \qquad (11)$$

it results:

$$\begin{cases} F = Z_0\left(Y^* - Y_0\right) \\ G = -Z_0\left(X^* - X_0\right) \\ H = 0 \end{cases} \qquad (12)$$

and:

$$\begin{cases} \cos\alpha = \dfrac{Z_0 - Z^*}{\sqrt{\left(X^* - X_0\right)^2 + \left(Y^* - Y_0\right)^2 + \left(Z^* - Z_0\right)^2}} \\ \cos\beta = \dfrac{X^* - X_0}{\sqrt{\left(X^* - X_0\right)^2 + \left(Y^* - Y_0\right)^2}} \end{cases} \qquad (13)$$

The change from an initial certain plan Oxyz to a more convenient system OXYZ can be done by maximum three rotations around the origin O (to mention that the transformation by rotation doesn't modify the length of the segments and the angles between them. For example, let's consider the successive transformations presented in Fig. 6:

$$\text{Oxyz} \xrightarrow{\xi,\,\text{Oz}} \text{OX}_1\text{Y}_1\text{Z}_1 \xrightarrow{\varphi,\,\text{OX}_1} \text{OX}_2\text{Y}_2\text{Z}_2 \xrightarrow{90-\psi,\,\text{OY}_2} \text{OXYZ} \qquad (14)$$

So, the coordinates in the OXYZ system can be obtained according to the ones in the initial reference system Oxyz by using:

$$\begin{pmatrix} X \\ Y \\ Z \end{pmatrix} = R_3 \cdot R_2 \cdot R_1 \cdot \begin{pmatrix} x \\ y \\ z \end{pmatrix} \qquad (15)$$

where

$$R_1 = \begin{pmatrix} \cos\xi & \sin\xi & 0 \\ -\sin\xi & \cos\xi & 0 \\ 0 & 0 & 1 \end{pmatrix} \quad R_2 = \begin{pmatrix} 1 & 0 & 0 \\ 0 & \cos\varphi & \sin\varphi \\ 0 & -\sin\varphi & \cos\varphi \end{pmatrix} \quad R_3 = \begin{pmatrix} \sin\psi & 0 & \cos\psi \\ 0 & 1 & 0 \\ -\cos\psi & 0 & \sin\psi \end{pmatrix}$$

and

$$R_3 \cdot R_2 \cdot R_1 = \begin{pmatrix} \sin\psi\cos\xi + \cos\psi\sin\varphi\sin\xi & \sin\psi\sin\xi - \cos\psi\sin\varphi\cos\xi & \cos\psi\cos\varphi \\ -\cos\varphi\sin\xi & \cos\varphi\cos\xi & \sin\varphi \\ -\cos\psi\cos\xi + \sin\psi\sin\varphi\sin\xi & -\cos\psi\sin\xi - \sin\psi\sin\varphi\cos\xi & \sin\psi\cos\varphi \end{pmatrix}$$

This relation, apparently complicated, has the advantage to be applied in any particular calculation situations, but also simplifies the specific algorithms used in the specialized software for lighting design.

III. ROAD LIGHTING APPLICATIONS

In practice, the most frequent cases are characterised by a special shape of the task surface and/or by its special orientation, respectively by the position of the plan of symmetry into the reference system considered. Literature usual analyses just these special cases and, for each one, establishes a special relation for the illuminance calculus. These can be deduced from the more general relation (13), as follows.

A. *The shape of the task surface is flat*

It is recommended to choose the reference system Oxyz in such a way so the area (S) to be included or to be parallel with the one of its plans. For the road lighting, the axis of the street will be considered parallel to the plan (yOz).

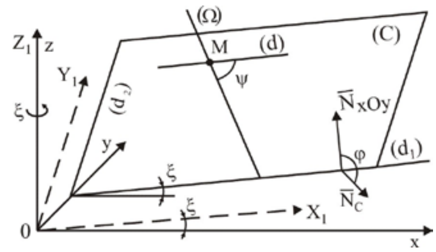

a. Rotation with the angle ξ around the axis Oz and Oxyz → $OX_1Y_1Z_1$.

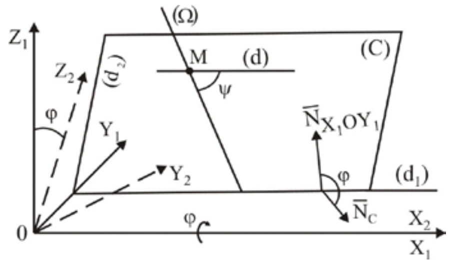

b. Rotation with the angle φ around the axis OX_1 and $OX_1Y_1Z_1 \rightarrow OX_2Y_2Z_2$.

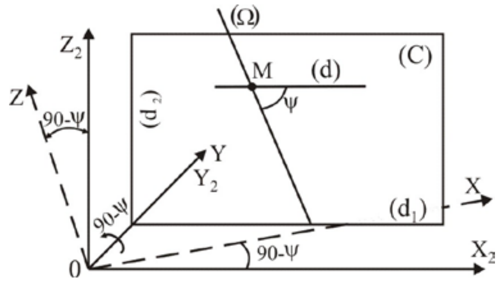

c. Rotation with 90-ψ around the axis OY_2 and $OX_2Y_2Z_2 \rightarrow OXYZ$.

Fig. 6. The transformation of the coordinates using the rotation.

Let us consider (S) ∥ (xOy) ⇒ λ=μ=0, ν=1 ⇒ $\overline{N}_{ds} = \overline{k}$ and then:

$$\cos\theta = \frac{z_0 - z^*}{MP} \qquad (16)$$

which is a customization of the relation (15).

B. The position of the luminaire plan of symmetry (C) relative to the lighten task area

- The plan of symmetry is normal to the axis of the street (Fig.7.a)

$$(C) \parallel (xOz) \Rightarrow (d1) \parallel (Ox),\ (d2) \parallel (Oz) \Rightarrow \xi = \varphi = 0,\ \psi \neq 0 \quad (17)$$

which gives:

$$\begin{pmatrix} X \\ Y \\ Z \end{pmatrix} = \begin{pmatrix} \sin\psi & 0 & \cos\psi \\ 0 & 1 & 0 \\ -\cos\psi & 0 & \sin\psi \end{pmatrix} \cdot \begin{pmatrix} x \\ y \\ z \end{pmatrix} \quad (18)$$

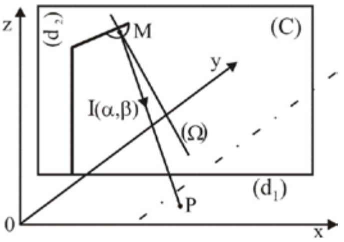

Fig. 7.a.

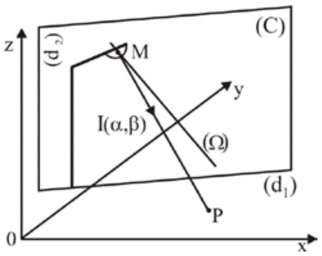

Fig. 7.b.

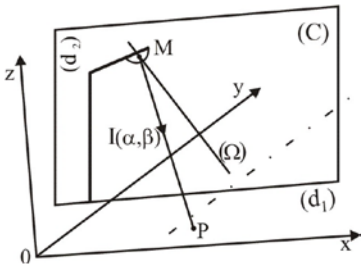

Fig. 7.c.

Fig. 7. Particular cases depending on the position of the task surface and the luminaire's longitudinal plan of symmetry.

- The plan of symmetry is normal to the task area (Fig.7.b)

$$(C) \perp (xOy) \Rightarrow (d2) \parallel (Oz) \Rightarrow \xi \neq 0,\ \varphi = 0,\ \psi \neq 0 \quad (19)$$

which gives:

$$\begin{pmatrix} X \\ Y \\ Z \end{pmatrix} = \begin{pmatrix} \sin\psi\cos\xi & \sin\psi\sin\xi & \cos\psi \\ -\sin\xi & \cos\xi & 0 \\ -\cos\psi\cos\xi & -\cos\psi\sin\xi & \sin\psi \end{pmatrix} \cdot \begin{pmatrix} x \\ y \\ z \end{pmatrix} \quad (20)$$

Such a situation is to be found at the lighting of the crossroads, squares or esplanades, where the poles for the lighting system have two or more luminaires mounted on distinct holders or brackets.

- The plan of symmetry is normal to the axis of the street (Fig.7.c) whose roadway is inclined comparing to the horizontal plan:

$$(C) \perp (yOz),\ (d1) \parallel (Ox) \Rightarrow \xi = 0,\ \varphi \neq 0 \quad (21)$$

which gives:

$$\begin{pmatrix} X \\ Y \\ Z \end{pmatrix} = \begin{pmatrix} \sin\psi & -\cos\psi\sin\varphi & \cos\psi\cos\varphi \\ 0 & \cos\varphi & \sin\varphi \\ -\cos\psi & -\sin\psi\sin\varphi & \sin\psi\cos\varphi \end{pmatrix} \cdot \begin{pmatrix} x \\ y \\ z \end{pmatrix} \quad (22)$$

- The optical axis is normal to the task surface

$$(C) \perp (xOy), \psi = \pi/2 \Rightarrow (d2) \parallel (Oz), \varphi = 0 \text{ with } \xi = 0 \text{ or } \xi \neq 0 \quad (23)$$

If one considers $\xi \neq 0$ it results:

$$\begin{pmatrix} X \\ Y \\ Z \end{pmatrix} = \begin{pmatrix} \cos\xi & \sin\xi & 0 \\ -\sin\xi & \cos\xi & 0 \\ 0 & 0 & 1 \end{pmatrix} \cdot \begin{pmatrix} x \\ y \\ z \end{pmatrix} \quad (24)$$

and for $\xi = 0$ it results a simpler case:

$$\begin{pmatrix} X \\ Y \\ Z \end{pmatrix} = \begin{pmatrix} 1 & 0 & 0 \\ 0 & 1 & 0 \\ 0 & 0 & 1 \end{pmatrix} \cdot \begin{pmatrix} x \\ y \\ z \end{pmatrix} \quad (25)$$

and

$$\begin{cases} \cos\alpha = \cos\theta = \dfrac{z_0 - z^*}{MP} \\ \cos\beta = \dfrac{x^* - x_0}{\sqrt{(x^* - x_0)^2 + (y^* - y_0)^2}} \end{cases} \quad (26)$$

As can be observed, the formulas resulted for the particular cases are in consonance with the ones recommended by literature. Since the proposed calculation method starts based on an arbitrary reference system, not linked to a particular position of the luminaire or task surface, the character of generality is assured.

IV. Experimental Validation

For the experimental validation it was considered an exterior asymmetric luminaire PBT-150 equipped with a high pressure mercury lamp (HPL 125 W/542 Philips, Fig.8). The light source has the standard flux of ϕ_n = 6200 lm and, for the conventional lamp with a flux of ϕ_c = 1000 lm, the luminous intensity into the same direction will be:

$$I(\alpha)_{1000,\beta=ct} = h^2 \cdot E_H \cdot (\phi_c / \phi_n) \cong 0.168 E_H \ \text{[cd]} \quad (27)$$

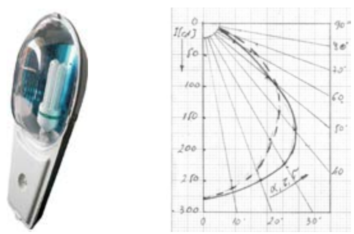

Fig. 8. The luminaire and the polar curves.

The tests and validation calculus followed three steps:

- The luminaire was fixed onto a fixture inside of a dark room; the fixture allows prescribing the zenith and azimuth angles.
- The level of the illuminance was recorded with a luxmeter MAVOLUX 5032 C-USB; its photocell was placed into a fixed position, at the intersection between the normal of the floor and the luminaire's optical axis.
- The luminous intensity was calculated for a preset meridian plan (β=constant) and for different direction (α=variable).

Fig. 8.b shows the polar curves in the plans of symmetry of the luminaire, whose values can be found in Table I that gives the measurement results for the variation of 10 degrees of both angles α and β.

TABLE I. POLAR CURVES I(α, β) FOR THE LUMINAIRE PBT-150.

$\beta[^0]$ \ $\alpha[^0]$	0	10	20	30	40	50	60	70	80	90
0	273.6	265.3	247.7	215.4	186.2	148.5	90.1	41.9	8.8	0
10	273.6	265.1	245.9	216.0	186.7	151.0	95.5	45.9	9.4	0
20	273.6	265.1	246.9	219.7	191.5	158.4	101.1	49.4	9.8	0
30	273.6	265.3	248.6	223.7	197.4	167.7	109.0	52.8	9.1	0
40	273.6	266.1	253.0	231.7	208.2	174.1	110.6	50.9	9.0	0
50	273.6	266.2	256.0	240.6	217.6	171.2	104.0	46.7	8.8	0
60	273.6	267.0	259.2	248.8	224.2	162.2	85.3	40.3	7.5	0
70	273.6	266.7	262.7	255.5	228.6	149.8	69.9	33.0	6.6	0
80	273.6	268.2	265.8	259.8	226.9	139.7	61.8	29.3	6.6	0
90	273.6	266.7	264.6	257.4	225.1	134.7	59.7	28.5	6.2	0

The calculation formulas established previously have been used to get the light intensity when the luminaire was placed in the point M(x_0=1.5 m, y_0 = 5m, z_0 = 8m) and the calculus point is P(x*=4.5 m, y* = 12.5m, z* = 0m), which correspond to the values MP $\cong$ 11.4 m and cosθ = 0.704, common values in the road lighting.

TABLE II. RESULTS FOR THE TWO ANGLES α AND β.

No	φ [0]	ξ [0]	ψ [0]	α [0]	β [0]	I(α,β) [cd]	
						Calculated	Dialux
1	0	0	15	64	133	66.3	66.9
2	0	25	15	47	128	184.7	183.8
3	10	0	15	63	148	110.2	111.3
4	0	25	0	45	38	192.4	193.6
5	0	0	0	45	68	189.8	188.6
6	10	25	15	45	154	179.2	179.7

The values of the angles α and β have been calculated for the particular situation highlighted in chapter III (see the lines 1 to 5 in Table II) but also for an arbitrary situation (see the line 6 in Table II). Finally, the resulted light intensity values have been compared with the ones obtained by means Dialux 4.12 software. The similarity of the results is obvious.

V. CONCLUSIONS

The photometric design of the exterior lighting installations, including the road ones, are realised usually using the point-by-point method. The illuminance of an area from the task surface is directly proportional with the luminous intensity *I*(α,β) for the considered direction and calculus needs the identification of the zenith and azimuth angles, α and β. The paper proposes a new method to determine the zenith and azimuth angles, different and more general and effective than the ones given in literature.

The mathematical basis of the proposed method consists in the rotational transformation of a certain triorthogonal reference system Oxyz into another one, OXYZ. In this new coordinate system, the luminaire optical axis (Ω) have to be normal to the plan XOY.

In summary, the method requires a low initial data that are:

- The spatial position of the optical center M of the luminaire and of the point of calculus P.
- The angle between the symmetry longitudinal plan (C)$\equiv$($C_{90}C_{270}$) of the luminaire and the plan XOY.

and follows the following steps:

- The adaptation of the angle between the joint line of the plan (C) from XOY and the directions (Ox) and (Ω).
- The values I(α, β) are taking from the polar curves of the luminaire provided by the manufacturer.

This method can be applied in any particular situation, not only in the most common cases covered by literature, having a wider character of generality. In future work, this method will be implemented in specific software and the gain in calculus time will be estimated.

REFERENCES

[1] CIE, Lighting of roads for motor and pedestrian traffic. In International commission on illumination, CIE Public Vol.115, Vienna, Austria, 2010.

[2] C. Bianchi, O. Centea, and M. Duminicatu, Proiectarea instalaţiilor de iluminat electric, Ed. Tehnică Bucureşti, 1981.

[3] C. Bianchi, Luminotehnica: Aspecte fundamentale şi aplicative, vol. 2: Iluminatul exterior şi anexe, Ed. Tehnică Bucureşti, 1990.

[4] N. Gheorghiu and P. Militaru, Teoria şi practica iluminatului electric, Ed. Tehnică Bucureşti, 1970.

[5] B. van Wout, Road lighting. Fundamentals, Technology and Application, Springer International Publishing Switzerland, 2015.

[6] V.C. Bender, F.B. Mendes, T. Maggi, M.A. Dalla Costa, and T.B. Marchesan, "Design methodology for street lighting luminaires based on a photometrical analysis", Power Electronics Conference (COBEP), 2013 Brazilian, 27-31 October 2013, pp. 1160 – 1165.

[7] N. Bisketzis, G. Polymeropoulos, and F.V. Topalis, „A mesopic vision approach for a better design of road lighting", WSEAS Transactions on Circuits and Systems, vol. 3, No. 5, pp. 1380–1385, 2004.

[8] A. Ekrias, M. Eloholma, and L. Halonen, An advanced approach to road lighting design, measurements and calculations.: Helsinki University of Technology, Department of Electronics, Lighting Unit, Report 53, 2008.

[9] R.D. Pentiuc, D. Lucache, V. Valentin, and S. Pavel, "Street lighting power quality," Int. Conf. on Electrical and Power Engineering, EPE, Iași, Romania, pp. 1107-1112, 16-18 October 2014.

[10] V. Chilinghir and A. Ilie, "Calculating the illuminance produced by point light sorces with plan symmetry", Buletin of Transilvania University Brasov, vol. 9, no. 44, 2002.

[11] R. D. Pentiuc, C.D. Popa, A. Dascălu and P. Atănăsoae, "The influence of LED street lighting upon network quality in electrical networks," Int. Conf. on Electrical and Power Engineering, EPE, Iași, România, 16-18 October 2014.

Economic Apraisal of Optimal Location and Sizing of Capacitors in Radial Distribution Systems Using PSO

Dorin D. Lucache, Cristina Moisa
Faculty of Electrical Engineering
"Gheorghe Asachi" Technical University of Iasi
Iasi, Romania
lukake@tuiasi.ro, cristina.m.moisa@gmail.com

Jacques Lobry
Electrical Engineering Department, Polytechnic Faculty
University of Mons
Mons, Belgium
Jacques.Lobry@umons.ac.be

Abstract— **The principal roles of capacitors in power systems are to supply reactive power to minimize loss and to improve the voltage profile. The optimization problem has to find the appropriate placement of capacitors that lead both to minimal system power losses and minimal total capacitor costs. This problem is largely presented in literature and is commonly solved using heuristic optimization techniques. However, the project profitability depends on prices and economical context. In this paper, a project economical appraisal was combined with the particle swarm optimization (PSO) technique in order to assess the profitability of the optimal capacitor installation in a 33-bus distribution network. A comparison between two objective functions and different locations numbers to install capacitor banks has been done.**

Keywords-capacitors, distribution system, particle swarm optimization, economic profitability

I. Introduction (Heading 1)

Studies have indicated that approximately 13% of generated power is consumed as loss at the distribution level [1]. Reactive compensation in distribution networks is a typical optimization problem of great technical and economic importance which has been faced over five decades. It consists in determining installation points and operation control program of a certain number of capacitor banks in order to maximize the profits obtained from system losses reduction. The extent of the benefits from capacitor banks installation depends on electrical network configuration and its load states. The net profit corresponds to the amount that is saved by reducing losses after discounting the investment in equipment acquisition and its installation.

Power system optimization problems including reactive power optimization have complex and non-linear characteristics with large number of inequality constraints. The capacitor installation techniques can be classified in four different categories: the analytical methods which are easy to understand and gives detailed mathematical models, the numerical methods (Gauss-Seidel, Newton-Raphson etc.) which are iterative and with or without constraints, the heuristic methods (genetic algorithms, particle swarm optimization, etc.) developed through intuition and experience and artificial intelligence based (annealing technique, artificial neural networks, fuzzy logic) .

The non-traditional techniques called heuristic have been successfully used and are considered practical and powerful ways to obtain the global or quasi-global optimum solution to engineering optimization problems.

This paper proposes a combination of a project economical appraisal with a computationally very efficient methodology for an optimal location and sizing of static and switched shunt capacitors in radial distribution networks. The optimization problem has been cost-formulated as the maximization of the project net present value, the difference between total savings produced by the reduction in energy losses and the total investment costs in procurement and installation of the capacitor banks, over a considered period. Two analyses have been done: the results of the proposed cost objective function have been compared with the ones get with the simple power losses minimization objective-function and secondly, different locations numbers to install capacitor banks have been evaluated.

II. Capacitor Placement Problem

In the reactive compensation problem, the objective function, to be maximized, represents the economic savings obtained due to capacitor banks installation in the distribution network. The capacitor banks usually have nominal capacities that are multiple integers of a standard unit (5, 25, 50, 150 or 300 kVAr, for example). On the other hand, the points of possible installation form a finite group, being the feeder buses, so finally it ends to a combinatorial optimization problem.

A. Model assumptions

The optimal location and sizing of shunt capacitors in the electric distribution network is a non-linear problem. However, as it will be seen next, this problem can be (under certain approximations) linearized and solved by using mixed-integer linear programming [2].

Before starting with the development of the mathematical framework, the main assumptions to be considered are listed below [2]

- Three-phase balanced systems.
- Low polluted network
- The phase shift between the system bus voltage angles is close to zero.

978-1-4799-4161-2/14/$31.00 ©2014 IEEE

- The bus voltage magnitudes are set equal to 1.0 p.u. in the first iteration of the power flow.
- The nodes allowed to be compensated are known according to the all constrains as well as the type of bank capacity that would be installed.

B. Power and energy losses

The expression that gives the electric power losses because of the Joule effect in a line is:

$$\Delta P_i = R_i\left(I_{Ri}^2 + I_{Xi}^2\right) = R_i\frac{P_i^2 + Q_i^2}{|V_i|^2} \qquad (1)$$

and, as consequence, for the annual utilization time T the energy losses become

$$\Delta E_i = \Delta P_i \cdot T \qquad (2)$$

The calculation of T is done with

$$T = 8760 \cdot LLF \qquad (3)$$

Loss load factor LLF is defined as ratio of energy loss in the system during a given time period to the energy loss that could result if the system peak loss had persisted throughout that period. It depends on the load factor LF according an empirical formula

$$LLF = a \cdot LF + (1-a)\cdot LF^2 \qquad (4)$$

in that a - constant having the values 0.1, 0.2 (for medium voltage feeders and distribution substations) or 0.3 (sub transmission systems) [3].

If c_{en} is the cost of one kWh of electric energy, then the annual total cost due to the energy losses in a distribution network with n buses (and n-1 branches) results

$$CEL = c_{en} \cdot \sum_{i=1}^{n-1}\Delta E_i \qquad (5)$$

C. Capacitor investment costs

The investment in capacitive compensators have two components: the first one related to the installation costs IC that are quite the same for one capacitor bank, independently on its capacity, and the second one that is variable because depends on Q_{ck} (the rating of capacitor bank on bus-k, in kVAr). Thus, if C_c is the total investment cost per unit of kVAr, the investment cost for installing a capacitor bank on bus-k yields

$$Inv_k = IC + C_c\left(Q_{ck}\right)\cdot Q_{ck} \qquad (6)$$

Notating with d the number of buses where the capacitor banks will be placed and considering IC a constant, the total capacitor investment cost results

$$Inv = \sum_{k=1}^{d} Inv_k \approx IC \cdot d + \sum_{k=1}^{d} C_c\left(Q_{ck}\right)\cdot Q_{ck} \qquad (7)$$

D. Project cost savings

The annual cost savings S_{an} due to the capacitor banks installation results as the difference between the cost of the energy losses before CEL_0 and after the installation CEL_C:

$$S_{an} = CEL_0 - CEL_C = c_{en}\left(\sum_{i=1}^{n-1}\Delta E_i^0 - \sum_{i=1}^{n-1}\Delta E_i^C\right) \qquad (8)$$

The total project savings in the total project duration (lifetime) D [years], taking into account the annual discount rate r, are

$$S = \sum_{j=1}^{D} S_{an.j}\cdot(1+r)^{-j} \qquad (9)$$

The discount (capital recovery) rate has high significance in the economical appraisals and attempts to reflect how future benefits and cost should be valued against present ones. Its value is established trough governmental politics or by the capital market action (in the countries where the market economy is operational). The World Bank and, more recently, the EBRD (European Bank for Reconstruction and Development) have adopted a required economic rate of return of 10% [4]. This is usually regarded as a quite high cut-of-rate. Usually national governments set the social discount rate for public projects at a lower level than international financial institutions (in the UK 6%, in Italy 5%, in Spain depending on the sector 6% in real terms for transport and 4% for water resource projects and in France 8%. However, the usual yearly discount rates are [5]:

- 10-15% in the emergent countries
- 8-10% in the developed countries.

In the hypothesis that S_{an} is a constant (the variations of the energy costs and load factor are neglected), then

$$S = S_{an}\cdot\sum_{j=1}^{D}(1+r)^{-j} = S_{an}\cdot\frac{(1+r)^D - 1}{r\cdot(1+r)^D} = \frac{S_{an}}{CRF} \qquad (10)$$

where CRF represents the capital return factor, given by

$$CRF = \frac{r\cdot(1+r)^D}{(1+r)^D - 1} \qquad (11)$$

E. Project profitability. Problem formulation

The project profitability can be assessed by the net present value *NPV*, defined as the difference between the savings and investments reflected at the present moment. The condition of the project profitability is

$$NPV = S - Inv > 0 \tag{12}$$

This is equivalent with

$$\frac{S_{an}}{CRF} - Inv > 0 \tag{13}$$

or

$$\frac{c_{en}}{CRF}\sum_{i=1}^{n-1}\Delta E_i^0 - \left(\frac{c_{en}}{CRF}\sum_{i=1}^{n-1}\Delta E_i^C + Inv\right) > 0 \tag{14}$$

Because the first term in (14) represent costs of the energy looses before the capacitor bank installation that are independent to that one, the objective function can be defined as

$$\min\left(\frac{c_{en}}{CRF}\sum_{i=1}^{n-1}\Delta E_i^C + Inv\right) \tag{15}$$

In addition to the objective function, the constraints of the optimization model must be defined. In real applications, limits are placed usual on the choice of control variables.

i. Bus Voltage Limits: The bus voltage magnitudes must be kept within acceptable operating limits throughout the optimization process,

$$V_{\min} \le |V_i| \le V_{\max} \tag{16}$$

where V_{min} is the lower bound of the bus voltage limits, V_{max} is the upper bound of the bus voltage limits, and V_i is the rms value of the bus voltage. Voltage stability problem has a close relationship with the reactive power of the system, and the voltage stability margin is inevitably affected in optimal reactive power flow. Hence, the maximal voltage stability margin should be one of the objectives in optimal reactive power flow problems [6].

ii. Number and Sizes of Shunt Capacitors: Shunt capacitors have constraints. Commercially available capacitors come in discrete sizes, i.e., the shunt capacitors are multiple integers of the smallest capacitor size available:

$$Q_{ck} = L \cdot q_0 \tag{17}$$

where q_0 is the smallest capacitor size available and L an integer. It is worth mentioning that the total reactive power injection is not to exceed the total reactive power demand in the radial distribution system

$$\sum_{k=1}^{d} Q_{ck} \le Q_T \tag{18}$$

where Q_T is the total reactive power demand.

F. Loss sensitivity factor and candidate bus selection

The basic idea is to find the locations for capacitor placement which has maximum contribution towards loss reduction as all locations may not have identical effect. To identify the location for capacitor placement in distribution system Loss Sensitivity Factors have been used [7]. The buses having higher sensitivities would be candidate locations and their knowledge help in reducing the search space for the optimization. As only few buses can be candidate buses for compensation, the installation cost on capacitors can also be reduced.

If P_i and Q_i represents the total active and reactive powers supplied beyond the bus "*i*" and R_i is the electric resistance of the branch supplying the bus "*i*", by derivation of (1) one gets

$$\frac{\partial(\Delta P_i)}{\partial Q_i} = \frac{2R_iQ_i}{|V_i|^2} \tag{19}$$

The Loss Sensitivity Factor $\partial(\Delta P_i)/\ \partial Q_i$ as given by (19) will be calculated from the base case load flows. The values of loss sensitivity factors have been arranged in descending order and, correspondingly, the bus numbers are stored in bus position *BP* vector. The descending order of $\partial(\Delta P_i)/\partial Q_i$ elements of *BP* vector will decide the sequence in which the buses have to be considered for compensation. At these buses of *BP* vector, normalized voltage magnitudes are calculated by considering the base case voltage magnitudes given as below:

$$Vnorm_i = |V_i|/0.95 \tag{20}$$

Then $Vnorm_i$ decides whether the buses need reactive compensation or not. The buses whose $Vnorm_i$ value is less than 1.01 can be selected as the candidate buses for capacitor placement.

III. Capacitor Allocation Using PSO Particle Swarm Optimization Technique

Particle Swarm Optimization Technique (PSO) is a non-conventional population-based iterative optimization technique used for searching nonlinear multidimensional search spaces. It is inspired by social behavior of bird flocking or fish schooling.

PSO is an algorithm for finding optimal regions of complex search-spaces through the interaction of individuals in a population of particles. The particles in PSO change their positions in every iteration based on individual best, global best and a random velocity.

In PSO, a swarm of particles are represented as potential solutions, and each particle i is associated with two vectors, i.e., the velocity vector $V_i = [v^1_i, v^2_i, \dots, v^D_i]$ and the position vector $X_i = [x^1_i, x^2_i, \dots, x^D_i]$, where D stands for the dimensions of the solution space. The velocity and the position of each particle are initialized by random vectors within the corresponding ranges. During the evolutionary process, the velocity and position of particle i on dimension d are updated as [8]

$$\begin{aligned} x_i^d &= x_i^d + v_i^d \\ v_i^d &= \omega v_i^d + c_1 rand_1^d \left(pBest_i^d - x_i^d\right) + c_2 rand_2^d \left(gBest_i^d - x_i^d\right) \end{aligned} \quad (21)$$

where ω is the inertia weigh, c_1 and c_2 are the acceleration coefficients, and $rand^d_1$ and $rand^d_2$ are two uniformly distributed random numbers independently generated within [0, 1] for the d^{th} dimension, *pBest* is the position with the best fitness found so far for the i^{th} particle, and *gBest* is the global best position in the search space.

It should be noted that the PSO parameters should be selected carefully for efficient performance in the afore-mentioned applications. The new position of the particle is also dependent on the weights attached with these quantities. These weights can be static or dynamic. The static weights are determined by repeated execution of the algorithm and set before execution of the program. The dynamic weights change for each iteration of PSO [9]. Any run of an evolutionary algorithm is an intrinsically dynamic and adaptive process [10].

PSO has the advantages of parallel computation, stochastic search (which makes it suitable for searching vast unknown solution spaces) and robustness, and it can find the global optimal solution with a higher probability and efficiency than traditional methods. The main advantages of PSO are that it is easy to realize, fast converging, and intelligent (including multiple particles will reduce the chances of getting trapped in local minima).

PSO has been successfully applied in both scientific research and engineering fields [11], as several power system problems (reactive power and voltage control, optimal power flow [6–13]), as well in dynamic security border identification, state estimation etc.

Although PSO techniques are widely used for solving the optimal capacitor placement problem, it still has disadvantages, such as difficulty in finding the optimal design parameters and properly selecting the initial conditions and parameters for an accurate solution (if the particles initialized, are located in a local space, then the chances of getting trapped in local minima is increased). The two most important and appealing goals in PSO research are: accelerating convergence speed and avoiding the local optima. Starting from the standard PSO, a number of variant PSO algorithms have, hence, been proposed to achieve these two goals: GPSO (global version of PSO), BPSO (binary PSO), EPSO (evolutionary PSO), HPSO (hybrid PSO) [11], APSO (adaptive PSO) and CLPSO (comprehensive learning PSO) [12].

IV. SIMULATION RESULTS

Results obtained by simulation done in Matlab environment are provided in this section. The proposed algorithm and economical appraisal have been applied on an IEEE 33-bus test system.

The set of allowable standard capacitor size to choose from is taken as: 5 and 50 kVAr. Different necessary parameters like energy price, installation costs, load factor etc have been taken as the average values in the Romanian market, and are given in Table I.

TABLE I. VALUES USED FOR THE CASE STUDY

Parameter	Symbol	Value
Nominal voltage (V)	V	400
Load factor	LF	0.8
Load loss factor	LLF	0.52
Energy price (€/kWh)	c_{en}	0.14
Installation costs (€)	IC	500
Discount rate (%)	r	8
Project duration (years)	D	15

A special attention has been paid to get the correlation between the total investment cost per unit of kVAr, C_c, and the rating of capacitor bank Q_c. Prices for similar characteristics banks get from 5 Romanian companies have been averaged. In order to simplify the optimization algorithm, an exponential regression algorithm have been used to obtain the following expression of a fitting function

$$C_c(Q_c) = -292.9 \cdot e^{-1/Q_c} + 296.5 \quad (22)$$

A very good correlation of 0.982 between the real averaged costs per kVAr and the ones get by using the fitting function has been obtained. This correlation is graphically represented in Fig.1.

Another issue to be solved was condition (17). The optimization algorithm gives non-integer values of the capacitors to be installed in different network buses. At the end

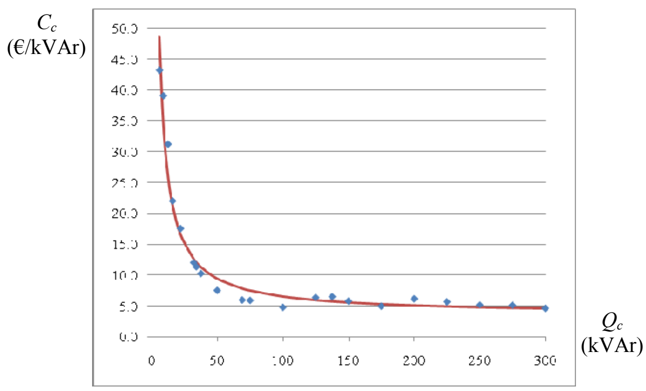

Figure 1. Exponential fitting function for Romanian medium market prices per kVAr

of the optimization algorithm, these non-integer values have been converted in multiples of q_0 by using

$$Q_{ck}' = Q_{ck} - \mathrm{mod}(Q_{ck}, q_0) \quad (23)$$

The conversion can be made by adding or subtracting up to the narrowest q_0 multiple. However, this conversion will be followed by the constraints verification.

The simulations have been conducted to answer to the following questions: which are the influences on the final results regarding capacitor sizes and voltage balance of the economical approach and of the number of the selected buses for the capacitor bank placement. So, to have a comparison with a pure technical criterion as the minimization of the total active power losses, we consecutive applied the same algorithm replacing (15) with the elementary objective function

$$min\left(\sum_{i=1}^{n-1} \Delta P_i^C\right) \quad (24)$$

Secondly, in order to ascertain the optimal number of locations, the number of locations of capacitors is varied according to descending order of their sensitivities. We used consecutively in simulations a number of 3, 6 and 9 buses selected from the bus position *BP* vector.

The simulation results for different considered situations are given synthetically in the following tables: in Table II the ones get using the maximizing NPV proposed objective function (15) and in Table III the ones get with the minimizing power loss objective function (24).

TABLE II. RESULTS OF THE OPTIMAL CAPACITOR PLACEMENT WITH THE OBJECTIVE FUNCTION (15)

No. of Selected buses for capacitors placement	3 buses	6 buses	9 buses
Minimum Bus Voltage (p.u)	0.9231	0.9321	0.9750
Maximum Bus Voltage (p.u)	0.9975	0.9975	1.0071
Reactive Power Injection (kVAr)	1600	1450	3650
Total investment costs (€)	15944	30887	44473
Real Power Losses (kW)	143.06	147.90	187.07
Cost Function (€/year)	74863	78372	99469
Annual Cost Savings (€/year)	61273	56871	21487
Recovery time (years)	0.26	0.54	2.07
Net Present Value (€)	508520	455900	139440

TABLE III. RESULTS OF THE OPTIMAL CAPACITOR PLACEMENT WITH THE OBJECTIVE FUNCTION (25)

No. of Selected buses for capacitors placement	3 buses	6 buses	9 buses
Minimum Bus Voltage (p.u)	0.93	0.94	0.95
Maximum Bus Voltage (p.u)	0.9976	0.9976	0.9977
Reactive Power Injection (kVAr)	1750.00	1850.00	2050.00
Total investment costs (€)	16487	26575	37118
Real Power Losses (kW)	147.53	147.63	158.06
Cost Function (€/year)	77205	77878	84013
Annual Cost Savings (€/year)	57232	57232	47713
Recovery time (years)	0.29	0.46	0.78
Net Present Value (€)	473390	463300	371280

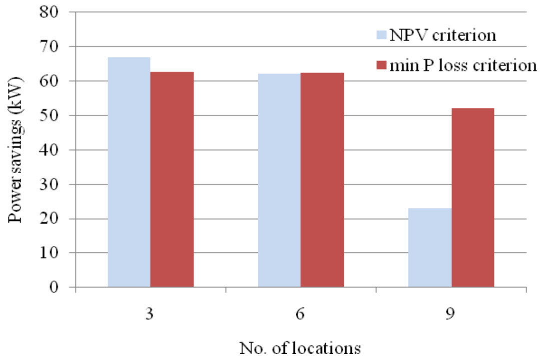

Figure 2. Active power loss versus nnumber of locations

The power savings after capacitor allocation are represented in Fig.2. The system losses without capacitors at the considered load level are 210.08 kW. It is observed from this figure that, surprisingly, the power savings decreases as the selected locations number for capacitors installation increase. It is the opposite of the findings of Singh et al. for a 70-bus network [13]. The better (for only three locations) and the

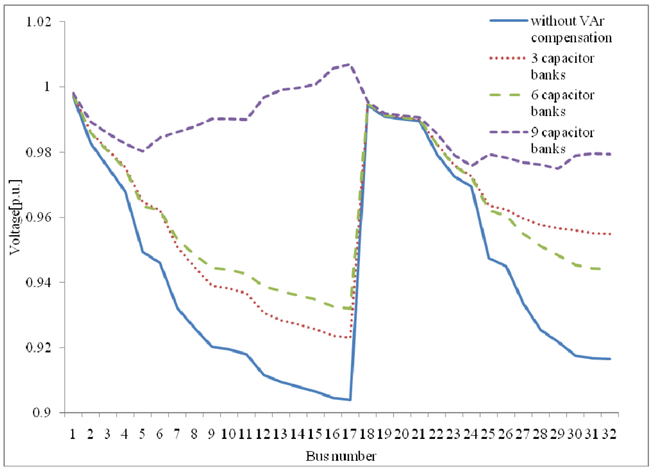

Figure 3. Voltage profile for using the NPV criterium

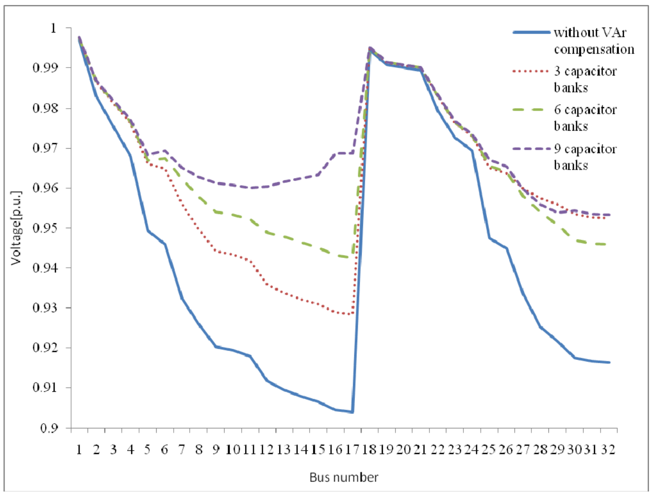

Figure 4. Voltage profile for using the power loss criterium

worst result (for nine locations) are recorded in the case of the NPV criterion application. When 9 locations with the NPV criterion were used for the capacitor banks installations, a difficulty to get the algorithm convergence was noticed. As a consequence, a too severe diminution of the power savings has been obtained.

However, we note the more locations are used to install capacitors, the more total reactive capacity will be installed in these ones. So, the installation cost of these capacitors increases with increase in number of locations causing reduction in money saving. Therefore, the number of locations should be chosen corresponding to maximum saving.

In order to ascertain the long term impact, the savings for 15 years operation (from 10..30 years are recommended as study time in the field of energy projects, as recommended in [14], [15]) with respect to number of locations were obtained. From the values given in Tables II and III it is obvious that the maximum saving is achieved corresponding to only three locations, independent on the used criterion. This procedure is called optimal capacitor allocation using static sensitivity since the effect of capacitors installed at previously decided locations have not been incorporated while deciding the next location [13].

V. CONCLUSIONS

This paper proposes a combination of the PSO algorithm for the optimal sizing and buses allocation in a radial distribution system, with an economical appraisal based on the NPV. This criterion was compared as results with the power losses minimization criterion, for three different numbers of the best suited locations. The results are better for a minimal number of locations for the both criterions, but the NPV one seems to be better.

REFERENCES

[1] Amanifar O., Hamedani Golshan M.E., "Optimal distributed generation placement and sizing for loss and thd reduction and voltage profile improvement in distribution systems using particle swarm optimization and sensitivity analysis", International Journal on "Technical and Physical Problems of Engineering" (IJTPE), Iss. 7, Vol. 3, No. 2, pp.47-53, Jun. 2011

[2] Khodr H.M., Olsina F.G., De Oliveira-De Jesus P.M., Yusta J.M., "Maximum savings approach for location and sizing of capacitors in distribution systems", Elsevier - Electric Power Systems Research 78, pp. 1192–1203, 2008.

[3] Baitch A., "Aurora Energy. Distribution loss factor calculation methodology", Report 4246/3, BES (Aust) Pty Ltd, July 2004.

[4] Stoian A., Gligor L., "Elaborarea analizei de senzitivitate în cadrul analizei cost-beneficiu a proiectelor finanțate din FEDR şi FC. Lucrare clarificatoare nr. 9"(Rom), „Capability development for Cost-Benefit Analysis" project co-financed by FEDR and POAT, 2012

[5] Athanasovici V., Tratat de inginerie termică – Alimentări cu căldură Cogenerare (Rom), Ed. AGIR, Bucureşti, 2010

[6] Dai C., ChenaW., Zhub Y. and Zhang Y., "Reactive power dispatch considering voltage stability with seeker optimization algorithm", Elsevier - Electric Power Systems Research 79, pp. 1462–1471, 2009.

[7] Rao R.S. and Narasimham S.V.L., "Optimal Capacitor Placement in a radial Distribution System using Plant Growth Simulation Algorithm", Proceedings of World Academy of Science, Engineering and Technology, vol. 35, pp. 716-723, 2008.

[8] Eberhart R.C. and Shi Y., "Particle swarm optimization: Developments, Applications and Resources", Proceedings of the IEEE 2001 Congress on Evolutionary Computation, Seoul, Korea, Vol.1, pp. 81 - 86, 2001.

[9] Badar A.Q.H., Umre B.S., Junghare A.S., "Reactive power control using dynamic Particle Swarm Optimization for real power loss minimization", Elsevier - Electrical Power and Energy Systems 41, pp. 133–136, 2012.

[10] Zhang W. and Liu Y., " Multi-objective reactive power and voltage control based on fuzzy optimization strategy and fuzzy adaptive particle swarm", Elsevier - Electrical Power and Energy Systems 30, pp. 525-532, 2008.

[11] Sirjani R., Mohamed A. and Shareef H., " Heuristic Optimization Techniques to Determine Optimal Capacitor Placement and Sizing in Radial Distribution Networks: A Comprehensive Review", Przegląd Elektrotechniczny (Electrical Review), ISSN 0033-2097, R.88, No.7a, pp.1-7, 2012.

[12] Zhan Z-H, Zhang J., Li Y. and Chung H.S-H., "Adaptive Particle Swarm Optimization", IEEE Transactions on Systems, Man, and Cybernetics—Part B: Cybernetics, Vol. 39, No. 6, December 2009, pp. 1362-1381, 2009.

[13] Singh S.P., Rao A.R., "Optimal allocation of capacitors in distribution systems using particle swarm optimization", Elsevier - Electrical Power and Energy Systems 43, pp. 1267–1275, 2012.

[14] ***, "The Economic Appraisal of Investment Projects at the EIB", European Investment Bank, Projects Directorate, March 2013

[15] ***, „Guide to Cost-Benefit Analysis of investment projects", Eurpean Comission, GD of Regional Politics, http://ec.europa.eu/regional_policy/sources/docgener/guides/cost/guide2008_en.pdf, 2008

Environmental Engineering and Management Journal March/April 2009, Vol.8, No.2, 267-271
http://omicron.ch.tuiasi.ro/EEMJ/

"Gheorghe Asachi" Technical University of Iasi, Romania

ON ELECTRO-DEWATERING A CELLULOSIC SLUDGE

Dorin D. Lucache[1*], Adrian Bulgaru[2], Dan Ioachim[1], Elena Dănilă[1]

[1] *"Gheorghe Asachi" Technical University of Iaşi, Faculty of Electrical Engineering, 53 Mangeron Blvd., 700050, Iaşi, Romania*
[2] *S.C. Vrancart S.A., 17 Ecaterina Teodoroiu Str., Adjud, Romania*

Abstract

The paper describes in brief the electro-osmosis process and reviews the possibility to use it in dewatering the pulp and paper waste sludge. The waste sludge main characteristics and dewatering methods from the Vrancart SA factory are revealed. After the experimental method and test bench description, some results from the preliminary laboratory tests on the Vrancart SA sludge are presented and discussed.

Key words: dewatering, electro-osmosis, pulp and paper, residual sludge

1. Introduction

Pulp and paper mill waste sludge and many other types of bio-solids are considered a source of renewable energy, but the conversion of the raw sludge into thermal or electrical energy is not simple. In order to burn, the sludge must have an enough high level of dryness.

Conventionally screw press, rotary press, filter press or centrifuge systems are commonly used to achieve between 25 and 50% solids depending on sludge type and blending of primary, secondary and de-inking sludge (ADI Limited, 2005). Recycled wastepaper accounts for more than 50% of the total raw materials used in the production of pulp for papermaking.

But in most cases, conventional dewatering systems are not effective in achieving low enough moisture content, in order to allow its combustion without blending with other fuels. Electro-osmosis seems to offer one potential cost-effective solution. Its use in the treatment of different kind of soils and wastewaters has given promising results (Banerjee and Law, 1998; Glendinning et al., 2006; Huang and Kim, 2003; Hubbe, 2006).

The paper purpose is to estimate the benefits of applying electro-osmosis for dewatering and sludge-to-energy conversion in the particular case of pulp and paper sludge from Vrancart SA factory.

2. Electro-osmosis

Electrokinetic phenomena can be categorized into four types. Both electro-osmosis and electrophoresis use an applied electric field to induce motion, whereas both the streaming potential and the sedimentation potential have the opposite electrokinetic coupling in that they use motion to produce an electric field.

According to the classical electrokinetic theory, at the interface between a solid and a polar liquid solvent (such as water), the specific adsorption process of some ionic species or electric charging of the liquid by the solid induces a solid double layer.

Fig. 1 shows the case of an electronegative particle immersed in a polar solvent, when the particle is charged negatively and the positive ions come to neutralize the surface charge and form a compact or Stern layer with typically 4 – 10 A° thick. A more mobile diffuse layer surrounds this and when an electric field is applied, the liquid ions in the diffuse layer move to the opposite electrodes. Each ion will carry a number of water molecules with, determining a water flow to one of the electrodes. The net amount of liquid water depends on the relative mobility of the ions of opposite sign. This process that is called electro-osmosis finds wide applications in biochemical analysis, civil engineering etc.

* Author to whom all correspondence should be addressed: e-mail: lukake@tuiasi.ro; Phone: +40-232-278680 int 1235; Fax: +40-232-237627

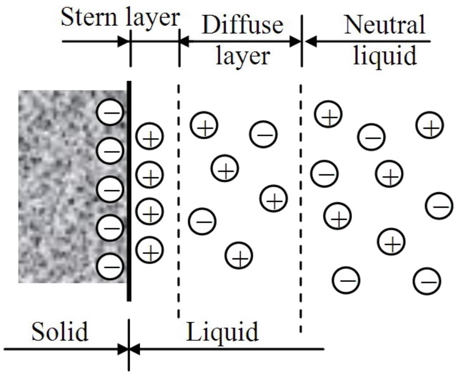

Fig. 1. Electrical double layer and electro-osmotic flow caused by a DC electric field

Since the current is proportional to applied voltage, the flow is also directly proportional to the constant current flowing through the material, in the case of constant electric-current dewatering. The electro-osmotic coefficient (Eq. 1) depends on the permittivity of the liquid, ε , the zeta potential, ζ and the fluid viscosity μ. It is also called *electro-osmotic permeability* and is used as an indicator of materials ability to support electro-osmosis.

$$k_{eo} = \frac{\varepsilon\zeta}{4\pi\mu} \qquad (1)$$

The typical values are included in the range of 10^{-6} ..10^{-4} cm^2/V.s. and compared with the ones of the hydraulic permeability, k_h, which ranges from 10^{-9} to 10^{-5} m/s. The electrokinetik dewatering becomes more efficient as the hydraulic dewatering when the ratio k_{eo}/k_h is high.

It has been showed (Banerjee and Law, 1998) that the expended energy during an electro-osmotic process has a quadratic dependence on time. In the particular case when the bed resistance does not much alter, the quadratic form can be simplified to a linear one, and expended energy can be expressed as (Eq. 2):

$$W = \frac{A}{\sigma_1} J^2 H_1 t \qquad (2)$$

where A is the cross-section of the material bed, σ is the initial electric conductivity, J is the current density and H_1 is the initial height of the bed.

3. Sludge treatment

The sludge dewatering applications are almost entirely dependent on the chemical and physical characteristics of the solids and water that comprise a particular sludge. Pulp and paper wastewater sludge typically contains between 0.5% and 8% dry solids and its consistency must be increased to a minimum of 25% dry solids in order to be land-filled or to a minimum of 40% to 50% dry solids content in order to be used in a fluidized bed combustion system. However, a typical pulp and paper mill sludge contains high concentrations of ash and water, which limit the effective heating value of the sludge and affect the economic viability of sludge to be converted in energy.

The free water is easier to be removed and the mechanical procedures give good results, but the interstitial, capillary mechanically bound water is trapped in the flocs. If the free water (not associated with free particles) is easier to extract, the bounded or vicinal water becomes difficult to remove. Currently only potential gradients produced by thermal methods are sufficiently high to remove interstitial and vicinal waters, involving high capital and operating costs.

Because the flow of water induced by an electrical potential difference is not limited by pore size, electro-osmosis has the potential to remove interstitial water from the sludge flocs, thus greatly improving dewatering efficiency (Glendinning et al., 2006).

There are some factors affecting the electrokinetic potential of cellulosic fibers (Hubbe, 2006): the chemical composition, the mechanical processing, the repeated drying of fibers, the solution PH, the electrolytes nature and multivalent cations presence.

However, for each unique application the various options that are commercially available for sludge dewatering should be evaluated independently.

4. Assessment of the sludge electro-dewatering efficiency at Vrancart S.A.

4.1. Present situation at Vrancart SA

The main characteristic of Vrancart S.A. pulp and paper factory is that uses a raw material with a high content of recycled (secondary) fibers as opposed to virgin wood materials. The moisture content of sludge at the end of production process is about 90%. During years, the cellulosic waste residuals were transported in an open land-filled deposit, operation that now is forbidden by the environmental regulations and the old deposit must be removed or integrated in the natural surroundings. In the last years, the sludge residuals are first collected in two tanks, submitted to a mechanical dewatering process and than burned in a fluidized bed boiler.

There are still unsolved problems: some times the moisture content of the dewatered sludge cakes is not low enough to allow a proper burning in the boiler and the whole process efficiency has to be increased.

Elementary chemical analyses of the residual sludge presented in Table 1 shows the important presence of ash (26.48%) and organic carbon (14%). The presence of heavy metals is reflected in Table 2, for different extraction depth of the sludge probes from the land-field depot.

In order to carry out some efficiency calculations, the relative low heating value of about 1208 kcal/kg (for a sludge with 53% moisture content) is estimated as an weighted average of two experimental heating values for two kind of sludge, different as origin and properties: the one coming from the toilette paper machine (lower heating power) and the other from the fluting paper machine (higher heating power).

Dewatering is performed by two mechanical methods followed by a screw steam dryer that uses the heat recovered from the technological installations. The two steps mechanical dewatering comprises first a filter press that lowered the moisture content from about 90% to about 65% and, second, a screw press that dewaters sludge up to moisture content of about 55%. At the end, the screw steam dryer increase the dryness with only 2-3%.

Table 1. Main chemical content of the sludge from Vrancart SA

Component		*Sludge content*
Hydroscopic humidity	%	38.80
Ash	%	26.48
Combustible sulfur	%	0.10
Nitrogen	%	0.25
Organic carbon	%	14

Table 2. The presence of heavy metals in the sludge extracted from different depths of Vrancart SA depot

Parameter	*Units*	*Extraction depth of sludge probes*		
		10 cm	20 cm	30 cm
Dry content	%	30.5	29.5	27.5
Lead	mg/kg	56	38	38
Cadmium	mg/kg	3.5	0.64	0.06
Chrome	mg/kg	0.9	9.8	11.4
Iron	mg/kg	264	98	284
Zinc	mg/kg	563	289	536
Nickel	mg/kg	3.4	0.84	5.6
Mercury	mg/kg	non detectable		

In average, the electrical energy consumption in the first step was estimated of about 24.8 kWh/ton, and in the second step of about 41.6 kWh/ton. Taking into account the electrical consumption for driving the screw in the screw steam dryer and the one for conveyor, a total specific consumption of 73.7 kWh/ton results for the whole dewatering chain, which produces sludge with 53% moisture contents.

Few problems were noticed and have to be solved. First, this 53% moisture content makes relative difficult the burning of the sludge in the fluidized bed boiler, because the ignition of the sludge cakes on conveyer happens late. Experiments using different other mechanical methods to dry better the sludge have not provided significant results. This is why an electro-mechanical dewatering was taken into account and is the reason for the experiments described in this paper. Second, the energetic efficiency of the screw press is low and alternatives to improve it have to be investigated. Third, the screw dryer uses too weak the residual steam energy and its conception must be reevaluated.

4.2. Experimental method

The laboratory test bench was realized from a PVC cylinder with 190 mm inner diameter, two aluminum electrodes of 2 mm thickness and a rectified and filtered DC source (Fig. 2). Both electrodes were perforated and had 4 mm diameter holes, ranged at 6 mm distance one from other. Supplementary textile gauze covered the electrode's surfaces to improve the wet sludge detainment. The cylinder has a vertically axis and allow a gravitational dewatering trough the lower electrode. An autotransformer allows varying the applied electric voltage between 0 and 80V. A very thin insulating-coated copper-constantan thermocouple was inserted in the middle of the sludge bed and connected to a temperature meter. The both power analyzer and temperature meter allow to continuously record data for power supply voltages, currents and temperature of the bed. These data were then transferred into the computer through a RS232 serial port.

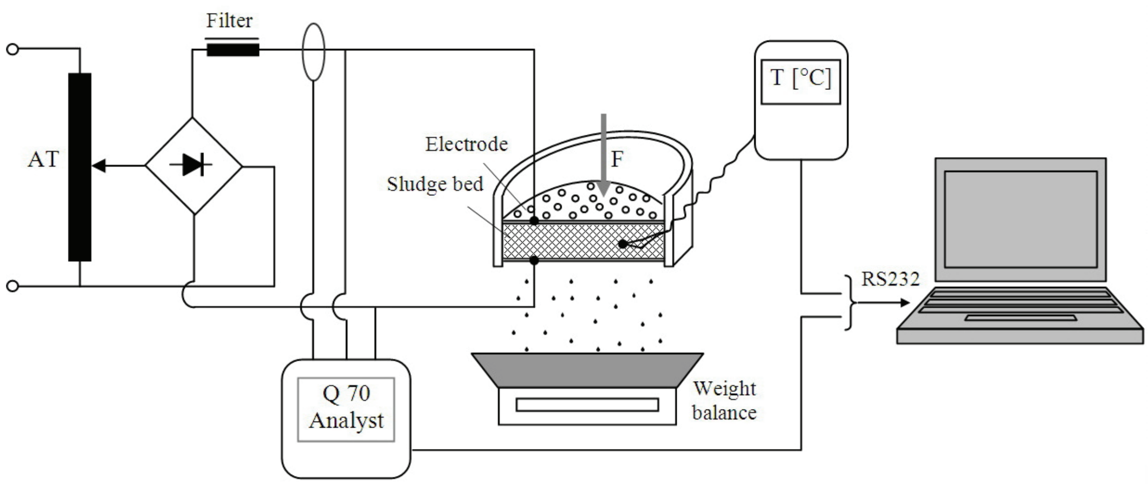

Fig. 2. The experimental test bench

The removed liquid water was collected in a plastic container lying on a weight balance so that the quantity of the removed water was noted every five minutes. The water eliminated by vaporization was calculated as difference between the probe weight decrease and the weight of the collected liquid water.

During the tests a screw press was used in order to keep an approximately constant compression of the bed, compression estimated to 0.5 N/cm^2. This helps to get a better efficiency of the dewatering process than applying only electro-osmosis, because of removing water by pressure and keeping a good electric contact between the electrodes and the treated material.

The performed tests were repeated on three material samples, extracted at different time periods from the sludge tank and treated with a flocculent additive (cationic policrilamide). The sludge sample's initial moisture content was between 90% and 91%.

4.3. Results and discussion

The notation used in the following experimental data tables are: I – constant electric current, m_0 – initial mass of the sample, u_0 – initial moisture content of sample, m_l – liquid water removed in test, m_v – removed water by vaporization, m_w – total mass of the removed water, m_f – final mass of the sample, u_f – final moisture content of the sample, P_m – medium electrical power during the test and g – specific consumption on the removed water.

The results of seven tests on some sludge probes, each of 1110 g weight and 28mm bed thickness, are given in Table 3. The first one was the witness test, in that dewatering was the result only of gravitation and compression forces. Then the tests have been done at constant current for a period of two hours, ones without (tests 2, 4 and 6) and ones with (tests 3, 5 and 7) half-hour water removing by gravitation before applying the electric field.

Table 3. Experimental results for two hours tests (1110 g sludge probes)

Test	*1*	*2*	*3*	*4*	*5*	*6*	*7*
I [A]	0	1.0	1.0	1.5	1.5	3.0	3.0
m_0 [g]	1110	1110	1110	1110	1110	1110	1110
u_0[%]	91	91	91	91	91	91	91
time[min]	120	120	120	120	120	120	120
m_l [g]	454	695	728	709	741	707	712
m_v [g]	-	137	119	144	126	164	166
m_w[g]	454	832	847	853	867	871	878
m_f [g]	646	268	253	257	243	229	222
u_f[%]	84.5	62.7	60.5	57.2	54.7	56.3	55.0

The results of other seven tests on shorter variable periods and new sample material are given in Table 4. The test 8 was a witness test too, namely only mechanical dewatering was applied for one hour to a probe.

As a difference from the previous tests, the used sludge derived from a different material sample, the probe weight was 555 g and, corresponding, the initial bed thicknesses was only of 14mm. The tests 9, 12 and 14 have been performed with a constant current of about 1.5A, the tests 10, 11 and 13 have been performed at constant voltage of about 60V. Before the tests 13 and 14, the material was mixed with 150g of tap water in order to have free water molecules on the surface of particles aiding in initiating the electro-osmotic dewatering process (Banerjee and Law, 1998).

Table 4. Experimental results for variable time tests (555g sludge probes)

Test	*8*	*9*	*10*	*11*	*12*	*13*	*14*
I [A]	0	1.5	var	var	1.5	var	1.5
m_0 [g]	555	555	555	555	555	555	555
u_0 [%]	90	90	90	90	90	90	90
time[min]	60	88	86	45	58	60	60
m_l [g]	176	327	310	180	260	230	240
m_v [g]	-	59	85	95	65	75	115
m_w [g]	176	386	395	275	325	305	355
m_f [g]	379	169	160	280	230	250	200
u_f[%]	85.5	67.5	65.6	80.4	76.1	78.0	72.5
Pm[Wh/h]	0	61.8	87.0	107.2	72.7	67.7	108.3
g [Wh/g]	0	0.23	0.32	0.29	0.22	0.22	0.31

One notices that:

- the dewatering process was different for the three samples of material, the most difficult to dewater was the sample with the higher content of sludge coming from the toilette paper machine;
- comparing with the witness tests, the application of the electric field makes the dewatering process more efficient;
- the moisture content get by electro-dewatering method for the two hours tests is close to the one obtained by two step mechanical drying;
- for the two hours tests, the final sludge cakes are warm, an important quantity of free water is close to the anode (the upper electrode) and so the dewatering can continue easy and relative rapid in a dry environment;
- the dewatering increase with the electric current value, but also the quantity of water removed by vaporization and that affects the whole process efficiency; a current value close to 1.5A seems to be the most proper in terms of efficiency;
- between 60% and 80% of liquid water is removed in the first half hour after applying the electric field and a bubbling effect appears during this interval due to, probably, the internal chemical reactions; the liquid removed by vaporization increase with time and appears even if the temperature in the middle of material bed not outnumbers 70°C;
- during the tests performed at constant voltage, the current first increase and after, when the water is removed and the bed electrical resistance increased,

its value lowers and slows the process; this evolution of current can be seen in Fig. 3 that shows the evolution of current voltage and electrical power for the test 10 (in this case, the voltage was increased continuously after the current becomes to lower under 1.5A in order to get a shorter dewatering process);

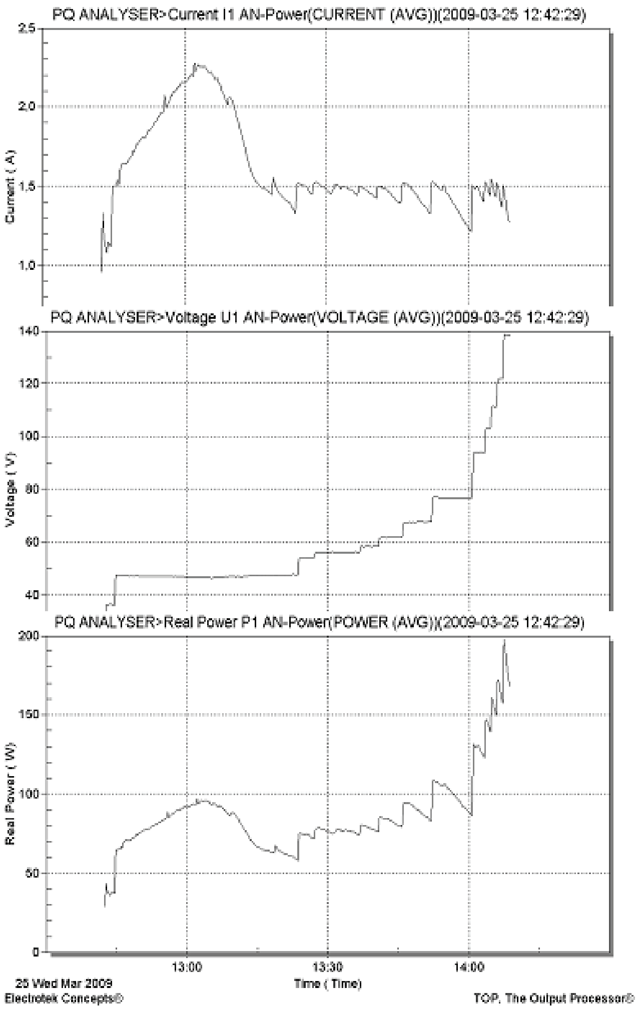

Fig. 3. Experimental data of current, voltage and power for the test 10

- in the tests 13 and 14 was interesting to notice how the removing of the tap water happens very fast, in less than 5 minutes after process starts, but the overall efficiency was not obviously better than in others tests.

5. Conclusions

The experimental tests on dewatering residual cellulosic sludge reveled all over again the difficulty of this process. The difficulty increased with the poorest quality of the secondary residual sludge (when derived from the toilette paper machine).

The electro-dewatering process needs long periods of time to get moisture content of the sludge cakes of about 55%, similar to the one obtained in the factory by mechanical methods. The only advantage could be that cakes seem to be better prepared to be dried in hot air.

The comparison with the dewatering results in the factory is difficult and non-concluding because the difference of the applied mechanical compression forces, in the laboratory tests have been used lower compression strength.

The economic viability of introducing the electro-dewatering process on the existed installation in the analyzed factory depends on a lot of factors and needs a more detailed study.

References

ADI Limited, (2005), *Pulp and paper sludge to energy – Preliminary assessment of technologies*, Report: (34) 0173-479.1.

Banerjee S., Law S.E., (1998), Electroosmotically enhanced drying of biomass, *IEEE Trans. on Ind. Application*, **34**, 992-999.

Glendinning S., Jones C., Philip J.F., (2006), Treatment of sewage sludge using electrokinetic geosynthetics, *Journal of Hazardous Materials*, **139**, 491-499.

Huang S., Kim K.-S., (2003), Improving sludge dewatering by addition of electro-osmosis to belt filter press, *Journal of Environmental Engineering and Science*, 2, 149-153.

Hubbe M.A., (2006), Sensing the electrokinetic potential of cellulosic fiber surfaces, BioResources, **1**, 116-149.

Paillat T., Moreau E., Grimaud P.O., Touchard G., (2000), Electrokinetic phenomena in porous media applied to soil decontamination, *IEEE Transaction on Dielectrics and Electrical Insulation*, **7**, 693-704.

Robust Control Strategy to Parameter Variations for an Interior PM Synchronous Machine

VASILE HORGA, DORIN LUCACHE, MARCEL RĂȚOI,
ALECSANDRU SIMION, MIHAI ALBU
Faculty of Electrical Engineering
"Gh. Asachi" Technical University of Iaşi
53 D. Mangeron Blvd., Iaşi, 700050
ROMANIA
horga@tuiasi.ro, lukake@tuiasi.ro, http://www.ee.tuiasi.ro

Abstract: - The interior permanent magnet (IPM) synchronous machines have several desirable features for automotive, tools machines and residential drive applications. When operating over a wide speed range, the main problem is to assure a proper and automatically set flux weakening. The paper presents a control structure of an IPM synchronous machine proper to be used also in the motoring regime, generating regime or in an integrated starter-generator regime. The control algorithm assures insensitivity to the load parameters variation. Experimental results for both cranking and generation are shown and analyzed.

Key-Words: - synchronous machine**,** interior permanent magnet, flux weakening, vector control

1 Introduction

Due to their high efficiency, the permanent-magnet (PM) synchronous machines with constant rotor flux have been attracting wide attentions and extensively used. A special attention was paid to find the existing electric machines that meet the specifications on cranking torque, driving power and speed range at the same time. The continuous cost reduction of magnetic materials with high energy density and coercitivity led to consider the PM synchronous machines as high attractive candidates both in automotive, tools machines and residential drive applications.

One of the exciting automotive application is the integrated starter generator (ISG) that uses one machine to replace conventional starter and alternator onboard vehicles and provides greater electrical generation capacity and improves the fuel economy and emissions. The ISG is coupled to the combustion engine either directly or by a belt.

Nowadays much of the work was done to get the best substitute of the old Lundell alternator. Unlike the machine in pure electric vehicle, the ISG machine has to enable the charging of the battery and to operate electric loads with nearly constant voltage at the speed range corresponding to the engine speed from idle 600rpm to redline 6000rpm.

The IPM motors due to their saliency develop supplementary reluctance torque and thus present a higher torque capability than the surface-mounted permanent magnet synchronous machine (SPMSM). This is why the IPM synchronous machine (IPMSM) is more suited to play the role of an ISG.

The main requirements of the ISG control are to ensure the necessary high torque as starter and the constant output voltage, irrespective of the input speed and load, as generator.

Because of its geometry, IPMSM has a robust rotor construction, a rotor saliency and the low effective air gap. The IPMSM control is done usual by two kinds of methods: direct torque control [1], [2] and vector control [3].

However, as the speed increases, the back electromotive force also increases, so the IPMSM acting as an ISG must operate well in both the constant torque region and the constant power region. To get this, some various control algorithms for flux weakening have been published mainly in the last two decades [4]..[10]. The constant torque region and constant power region are governed by different equations. In time two types of approaches have been used to control the IPMSM: the ancient one is based on the machine equations [7], which can generate problems at the regime switching, and the newest one that apply different control techniques by continuous adjustment of the reactive current at the condition of bounded voltage and current [8], [9]. Our proposed control strategy belongs to the last one and is based on the voltage error.

The IPMSM was controlled in order to be insensitive to the load parameters variation and the control algorithm was tested in different regimes:

motoring, generating and then playing the role of an ISG. The control algorithm is a combination of some techniques found in the literature and is based on the maximum torque-per-ampere strategy (minimum copper loss). A prototype system was tested in order to confirm the control algorithms and dSPACE based experimental results are presented and discussed.

2 Voltage and current limits

In the *d*-*q* axis synchronous frame, the dynamic equations of the IPMSM can be expressed as:

$$\begin{cases} u_{sd} = R_s i_{sd} + L_d \dfrac{di_{sd}}{dt} - \omega_e L_q i_{sq} \\ u_{sq} = R_s i_{sq} + L_q \dfrac{di_{sq}}{dt} + \omega_e L_d i_{sd} + \omega_e \psi_m \end{cases} \tag{1}$$

Symbols *u* and *i* denote voltage and current, ψ_m the flux linkage of the permanent magnets in the *d*-axis rotor, L_d is the *d*-axis self-inductance, L_q is the *q*-axis self-inductance, ω_e is the electrical speed, respectively, and index *s* denotes parameters and variables associated with stator.

The developed electromagnetic torque t_e in terms of stator currents is expressed as:

$$t_e = p\left[\psi_m i_{sq} + \left(L_q - L_d\right) i_{sd} i_{sq}\right] \tag{2}$$

where *p* denotes the number of pole pairs. This has two components: the alignment torque produced by the flux linkage and the reluctance torque produced by the saliency. It is desirable that the reluctance torque should be properly utilized in order to increase the whole efficiency of the IPMSM drives.

At the low speed, the back-electromotive force is small and so there is enough voltage to control the current to generate the torque. As the rotor speed increases, the marginal voltage to control the current is decreased and the torque becomes highly distorted so the flux weakening method should be applied [4]. The extension range of the speed is solely limited by the structure and the parameters of the motors under the given condition of voltage and current limitation.

The maximum voltage $U_{s\,max}$ that the inverter can supply the machine is limited by DC link voltage and PWM strategy. When the voltage space vector strategy is used, $U_{s\,max} = U_{DC} / \sqrt{3}$. Also the maximum current $I_{s\,max}$ is determined by the inverter current rating and machine thermal rating.

So, the imposed limits for the motor's voltage and current are:

$$\begin{cases} u_{sd}^2 + u_{sq}^2 \le U_{s\,max}^2 \\ i_{sd}^2 + i_{sq}^2 \le I_{s\,max}^2 \end{cases} \tag{3}$$

Neglecting the stator resistance (when speed increases the term ω_e becomes more important), from (1) the steady-state voltage limit equation yields:

$$\left(i_{sd} + \frac{\psi_m}{L_d}\right)^2 \left(\frac{L_d}{L_q}\right)^2 + \left(i_{sq}\right)^2 \le \left(\frac{U_{s\,max}}{\omega_e L_q}\right)^2 \tag{4}$$

From (3) and (4) it can be seen that the current limit equation determines a circle with a radius of $I_{s\,max}$, while the voltage limit equation determines a series of nested ellipses (for the IPMSM, $L_q > L_d$). Fig.1 shows the current-limit circle and the voltage-limit ellipses in the i_{sd}-i_{sq} plane.

The voltage-limit ellipse decreases as the speed increases. At a so-called base speed ω_{base}, the maximum torque point *A* is on the cross point of maximum torque-per-current trajectory and current-limit circle. When the IPMSM is operated from the start up to the base speed in the constant torque region, the voltage-limit ellipse exceeds the maximum current boundary and no voltage limitation needs to be considered in this situation.

But beyond the base speed, the IPMSM cannot be operated without flux-weakening control and so, to extend the speed range, a proper demagnetizing current has to be applied depending on the operating speed. The current vector trajectory will move along the boundary of the current-limit circle (from A to B in Fig.1) as rotor speed increases.

Without a proper flux weakening at higher speed, the current regulators would be saturated and lose their controllability. Since the onset of current regulator saturation varies according to the load conditions and the machine parameters, the beginning point of the flux weakening should be varied. The late starting of the flux weakening may result in undesired torque drop, but the early starting deteriorates the acceleration performance [5].

3 The control algorithm

As opposed to SPMSM, the i_d=0 control method is not suitable for the IPMSM because the reluctance torque is not produced even if this kind of machine has a saliency.

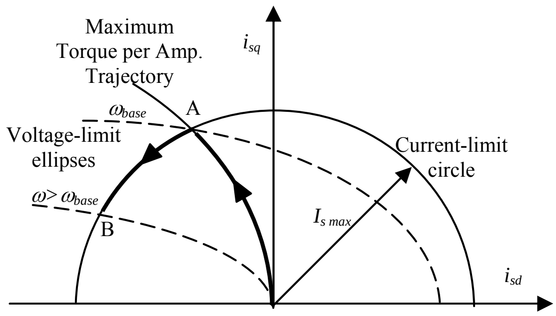

Fig.1 Current-limit circle and voltage-limit ellipses in the i_{sd}-i_{sq} plane

At low speeds, because the absence of voltage limitation, the current vector might be controlled to fully use reluctance torque in order to maximize the machine efficiency. Typically, it is chosen to maximize the torque per amper ratio by controlling the current vector in order to have an optimum inclination versus *q*-axis. To get the maximum torque control, the inclination angle γ of the current vector (Fig.2) depends on the load conditions, taking values between 0 and 45° [6].

The maximum torque-per-ampere (MTPA) strategy seeks to get a certain torque with the smallest possible stator current amplitude (so with minimum copper loss). Because $i_{sd} = -i_s \sin\gamma$ and $i_{sq} = i_s \cos\gamma$, where $i_s = |\underline{i_s}|$, (2) becomes:

$$t_e = p\left[\psi_m i_s \cos\gamma + \frac{1}{2}\left(L_q - L_d\right)i_s^2 \sin 2\gamma\right] \quad (5)$$

and imposing the condition :

$$dt_e / d\gamma = 0 \quad (6)$$

the relation between i_{sd} and i_{sq} for the maximum torque per amper control is derived as

$$i_{sd} = \frac{\psi_m}{2\left(L_q - L_d\right)} - \sqrt{\frac{\psi_m^2}{4\left(L_q - L_d\right)^2} + i_{sq}^2} \quad (7)$$

This relation is shown as the maximum torque-per-ampere trajectory in Fig.1.

Above the base speed, the normal operation is possible only applying the flux weakening and the maximum torque is obtained when the drive operates in the voltage and current limits. The flux weakening control of IPM synchronous machines is conducted by injecting the *d*-axis current i_{sd} negatively, which is different from induction machine where the flux is weakened by decreasing the *d*-axis current.

However, another relation between i_{sd} and i_{sq} could be established and so the control in the constant torque region and constant power region is based on different equations. Some authors, as [6], proposed an algorithm for the control mode transition, but all kind of transitions can lead to instability. The authors of [4] proposed another method by adjusting the *d*-axis current command depending as well as the bounds of the maximum *q*-axis current of the speed controller in the following manner: the *d*-axis current is fixed as a transient which is initiated such that the *q*-axis current bound can be gradually adjusted by a PI controller. The corresponding *q*-axis bound is calculated simultaneously as the PI controller adjusts the *d*-axis current, but it is found that under transient conditions cannot follow the true bounds instantaneously. A field weakening control scheme based on a real-time adjustment is present also in [7], but the used

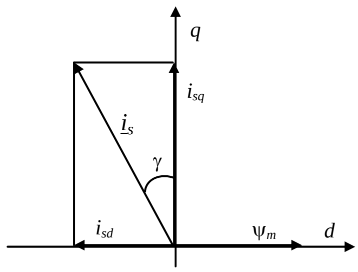

Fig.2 Current phasor diagram in the *d*-*q* frame

maximum torque-per-ampere strategy lead to inadequate torque at high speeds and light loads. In [8] the flux weakening control algorithm takes into account the error between the maximum voltage and the command voltage and the flux weakening could be set to prevent the saturation of the current regulators. Other authors like [9] pointed out that the PI controller should be replaced by an integral (I) controller, to either ensure the drive stability or simplify the controller design. In order to eliminate the gradual adjustment by feedback mechanisms so as to achieve faster response and better stability, [10] proposed o new flux-weakening control method based on a closed-form solution of the available maximum torque.

The proposed control strategy is an improved combination of the previous discussed techniques based on the voltage error. The Fig.3 presents the schemes used in the three operating cases: motoring, generating and ISG, the block components being detailed in the last one.

The *d*–axis and *q*-axis currents cannot be controlled independently by u_{sd} and u_{sq} because of the cross-coupling effects (the terms $\omega_e L_q i_{sq}$ and $\omega_e L_d i_{sd}$ in (1)) that are dominant for IPMSM due to relatively large inductances and increase as the speed increases. The cross-coupling effects are usually canceled by the feedforward compensation [6].

Two PI controllers, implemented in the synchronous reference frame, are used for the current control, followed by a decoupling circuit. In the constant power operation, a closed-loop voltage control is used to ensure an automatically onset of the accurate flux-weakening operation, depending on the load condition and machine parameters. Flux weakening mode is entered when the error

$$\varepsilon = u_{s\,max}^2 - \left(u_{sd}^2 + u_{sq}^2\right) \quad (8)$$

becomes negative. This error, passing through a low-pass filter (LPF) and regulated by an I controller, lead to the *d*-axis current increases toward the negative direction to prevent saturation of the current regulators. The I controller output is limited (to avoid irreversible demagnetization) so that the *d*-axis current to be between 0 and the minimal allowable

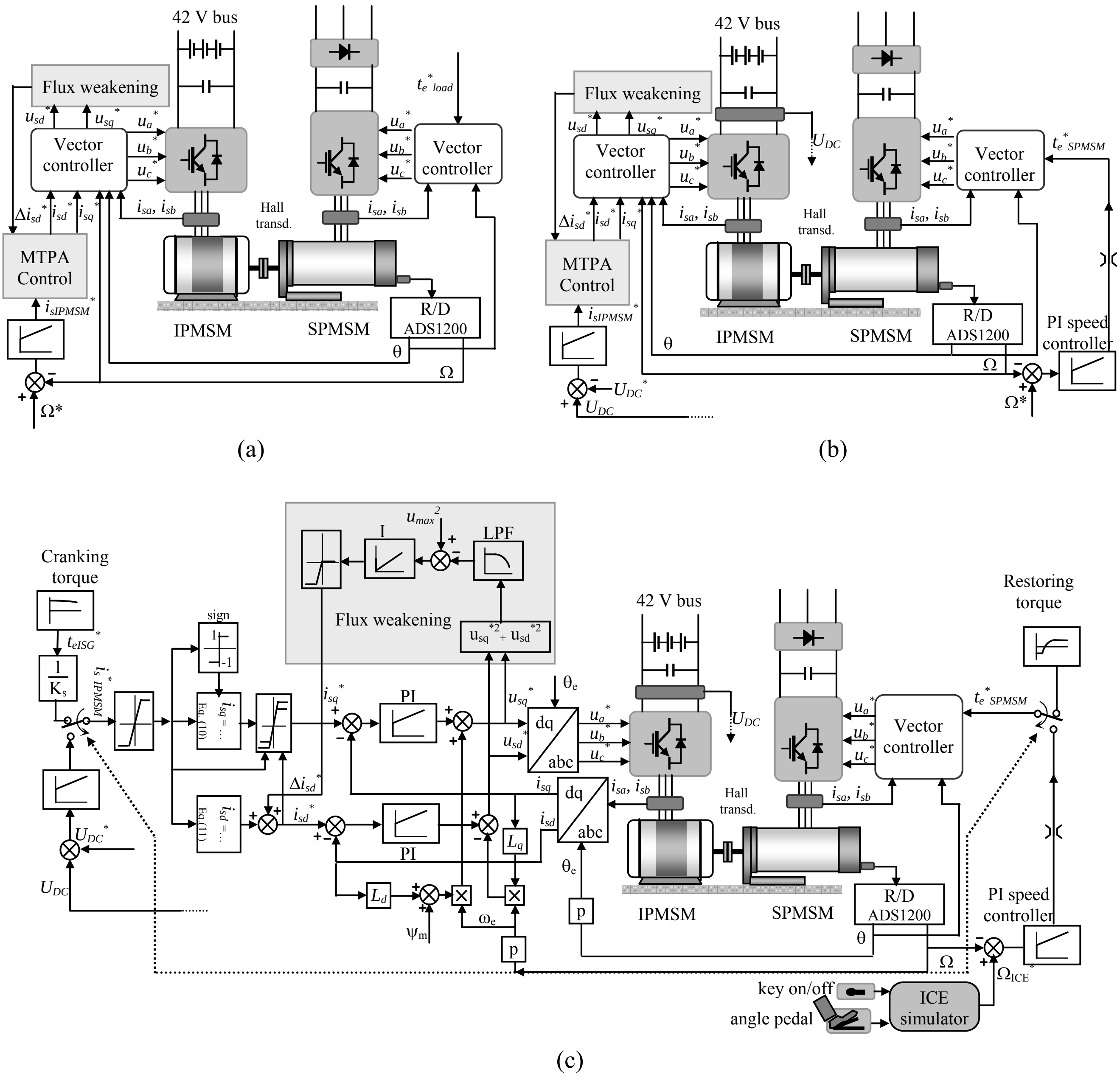

Fig.3 The control schemes: (a) – motoring regime, (b) – generating regime, (c) – ISG regime

$i_{sd}^{*} = -I_{sd\,max}$.

The magnitude of the injected stator current i_s can be expressed as

$$i_s = \sqrt{i_{sd}^2 + i_{sq}^2} \qquad (9)$$

and taking into account (7), the d-q axis components of the current vector that ensures the maximum torque-per-ampere yields

$$i_{sq} = sign(i_s) \cdot \sqrt{i_s^2 - i_{sd}^2} \qquad (10)$$

where

$$i_{sd} = \frac{\Psi_m - \sqrt{\Psi_m^2 + 8\left(L_q - L_d\right)^2 i_s^2}}{4\left(L_q - L_d\right)} \qquad (11)$$

The last equation is equivalent with (7) but expressing the d-axis current as a function of i_s, taking into account (9).

Thus, when the d-axis current is increased with respect to the voltage limit, the q-axis current is depressed in order to ensure the current limit condition. Moreover, a saturation block with adaptive limits take into account the flux weakening command Δi_{sd}^{*} and forces once more the operating point to not exceed the current-limit circle. In this way the current regulators regain the ability of regulating the d-axis and q-axis currents and the maximum torque-per-ampere is produced at the crossing point between the current limit circle and voltage limit ellipse, in the constant power region.

Because this scheme utilizes for flux weakening the output voltage of the PI current regulators and the outer voltage-regulating loop instead of the IPMSM model, it becomes robust and insensitive to load conditions and load parameters.

The external lead-acid battery pack has a double role: provides the energy necessary in the ISG motoring mode and stores the energy produced in the generating mode. A capacitive filter is connected to the DC line.

4 Experimental results

In this paper a commercial IPMSM, designed for playing as automotive generator, operating at low voltage and high currents, was used (rated parameters in Table 1). This is mechanical coupled (Fig.4) to an internal combustion engine simulator that consists in a SPMSM (1.9 kW, 330V, 4.4A and 4000rpm). The speed of the engine simulator can be varied in closed loop by means of its own inverter.

The engine simulator is based on a mean torque predictive engine model, which would take into account the major dynamics (lag and delays) inherent in the spark ignition torque production process [12]. Though the obtained speed characteristics may be different from a real engine, and the power ratio between ISG and engine simulator is not proper, this experimental setup allows testing the validity of the proposed control algorithms successfully.

Table1 IPM synchronous machine characteristics

Rated power [kW]	4
Peak current constraint [A]	160
Number of phases	3
Number of poles	12
R_s [mΩ]	21
L_d [mH]	0.076
L_q [mH]	0.12
ψ_m [Wb]	0.009
Rated speed [rpm]	2000
Rated voltage [V]	11

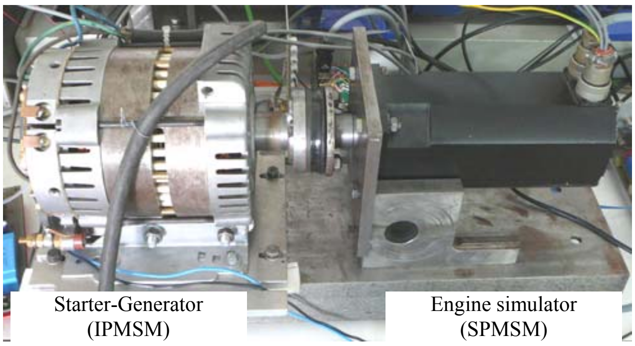

Fig.4 View of the test bench

The PWM converter connected to IPMSM is a standard three-phase bridge that is capable of bi-directional power flow. In the ISG motoring mode this converter acts as an inverter and in the generating mode it acts as a boosting rectifier. A few years ago, the automobile industry agreed to adopt standards for a new 42V voltage for production and use of electrical power. This new standard was not adopted in a rush and various system voltage ranging from 42V to 500V were proposed.

To control the whole experimental system, a dSPACE 1104 board and ControlDesk software is being used. This board contains all the peripherals and resources necessary to control simultaneously both the load machine (engine simulator) and IPMSM. The speed information comes from the resolver included in the SPMSM and is digitalized with an ADS1200 resolver-to-digital converter. For the currents and the voltages measure the Hall transducers are used.

4.1 IPMSM motoring regime

The control scheme corresponds to Fig.3.a and the IPMSM base speed was estimated of about 1200rpm. The Fig.6 catch the moments when the IPMSM starts-up in the motoring regime for a time

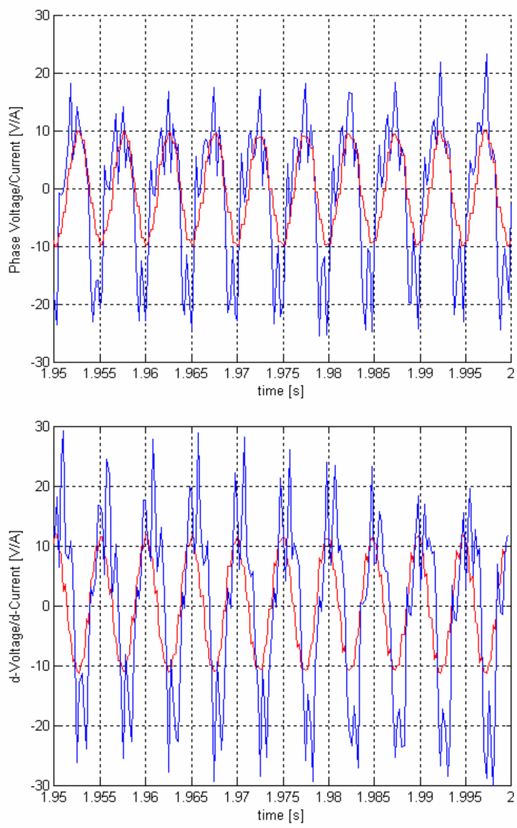

Fig.5 The phase- and *d*-axis voltage and currents

interval of two seconds, both bellow and above the base speed. The high DC current/phase current demand can be noticed up the system stabilizes at the reference speed.

Due to its specific geometry and construction, IPMSM produces non-sinusoidal currents, as seen in Fig.5. These currents are acquired and used to generate the reference voltage commands. The reference and measured currents in the d-q frame are presented in Fig.8. The current and voltage space phasor loci in the stationary reference frame presented in Fig.7 confirm the presence of the fifth harmonic in the phase current of the IPMSM [13]. More, Fig.8 shows how the flux-weakening block acts with Δi_{sd}^* to prevent the regulators saturation when the base speed is surpassed.

4.2 IPMSM generating regime

In the generating regime, the PWM inverter boosts up to about 38V on the DC link, charging the batteries pack with a low current (approx. 1.2A) as seen in Fig.9.b While the battery pack is connected, this will keep the DC voltage approximately constant during non-high load variations.

As in the previous case, the current and voltage space phasor loci in the stationary rotating reference frame presented in Fig.10 confirm the presence of the fifth harmonic in the phase current of the IPMSM, issue that causes many oscillations of the

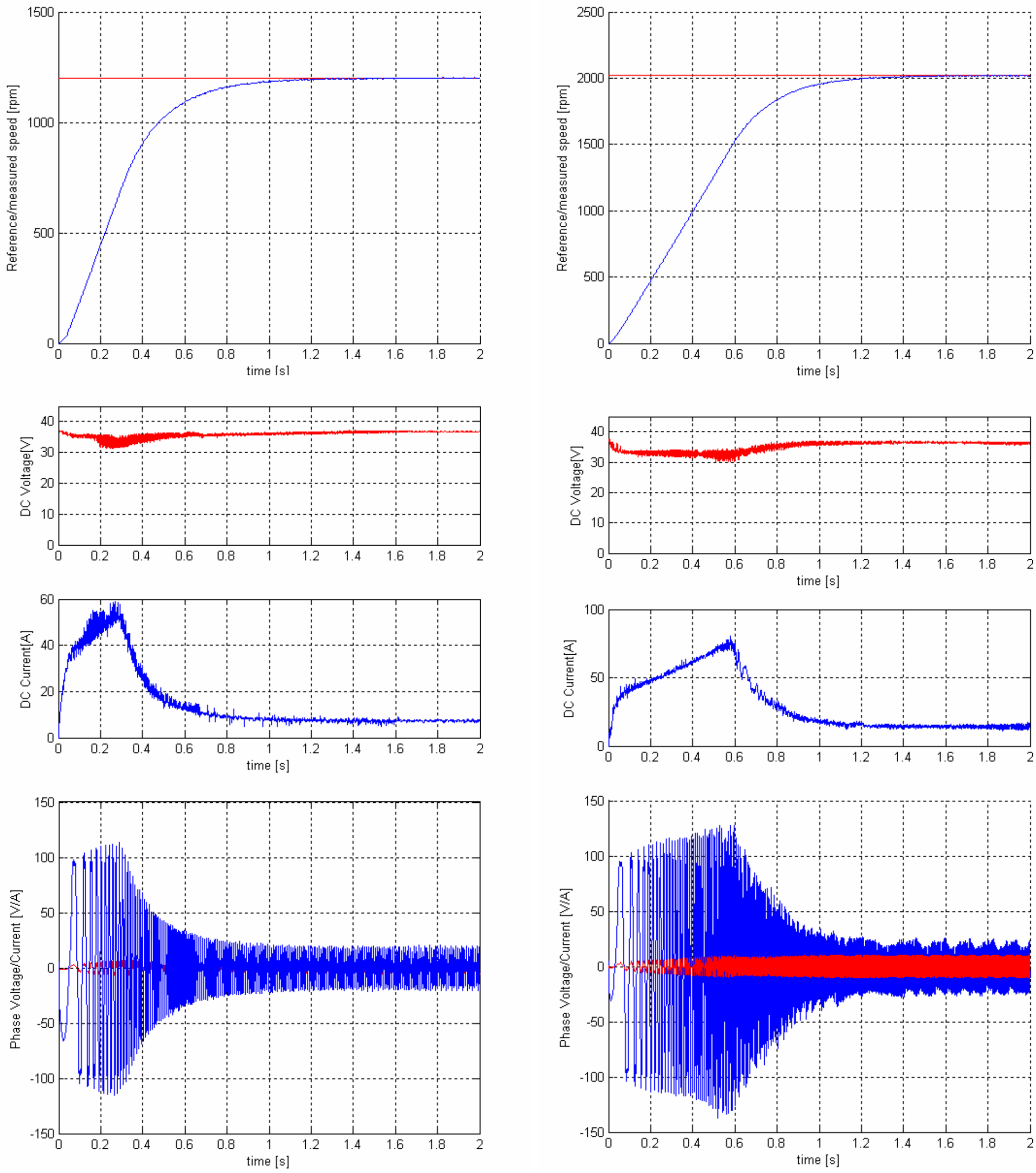

Fig.6 Experimental results bellow (left side) and above (right side) the base speed

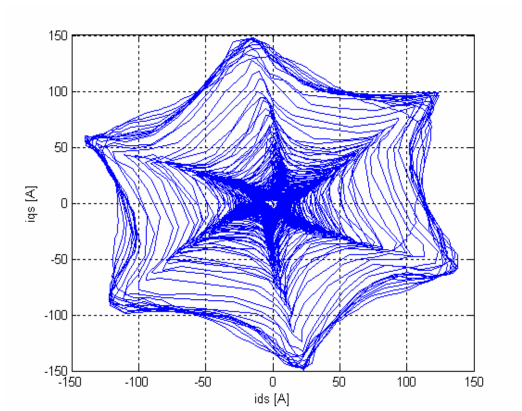

Fig.7 Current space phasor loci in the stationary reference frame bellow the base speed

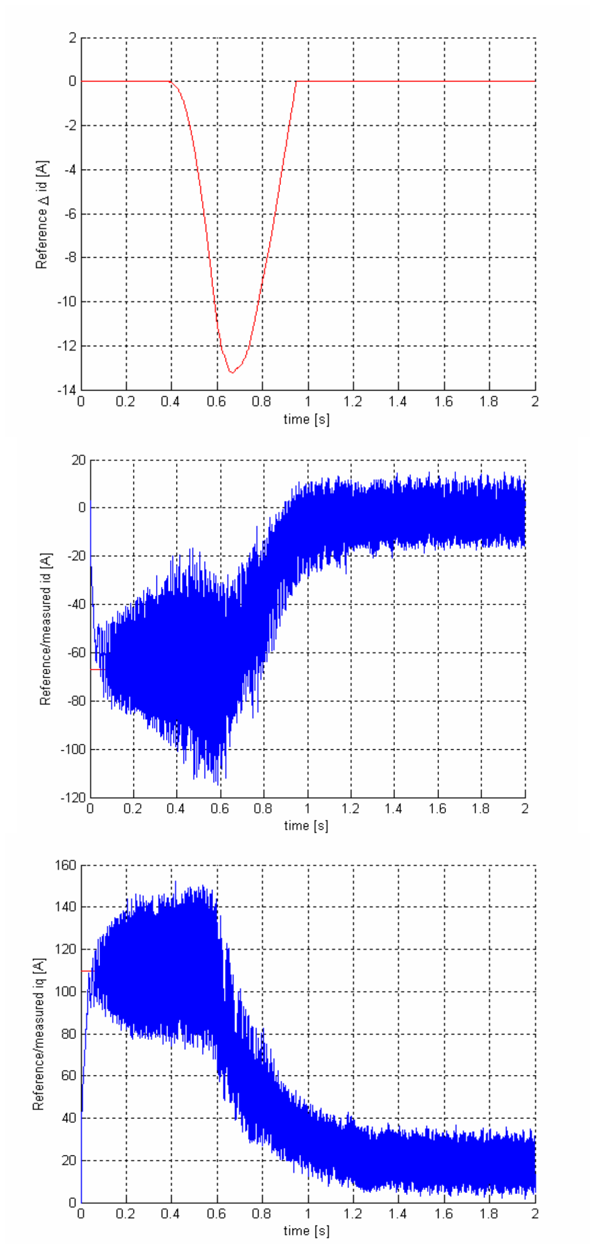

Fig.8 Reference and measured currents in the *d-q* frame

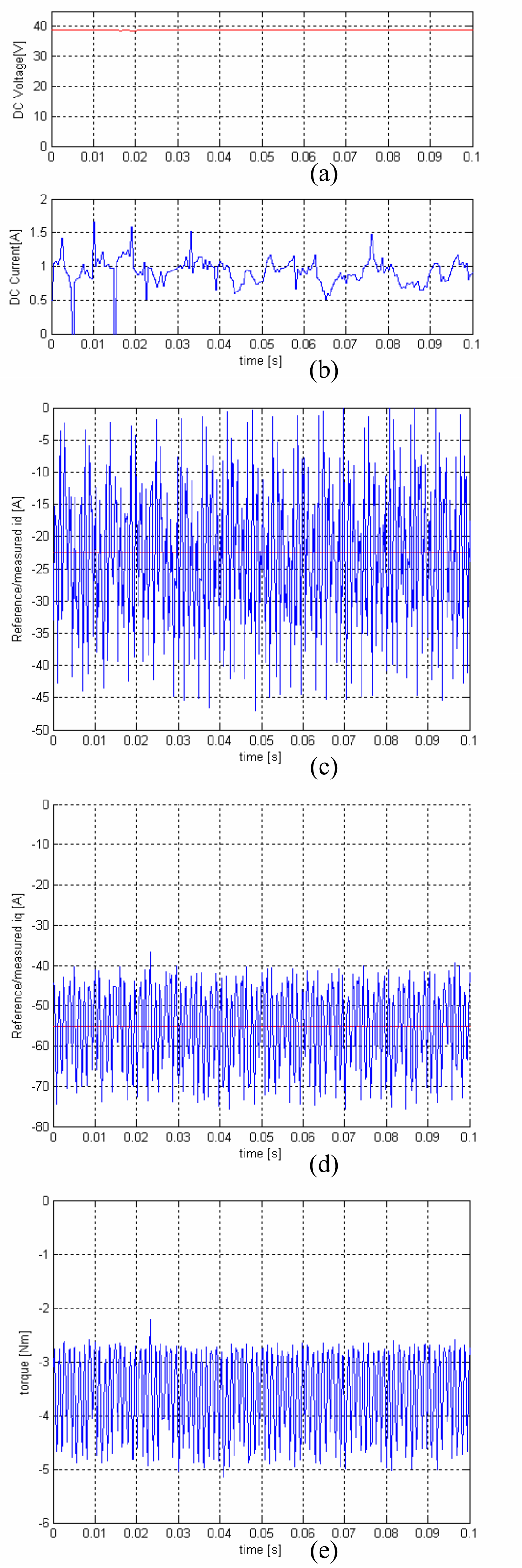

Fig.9 Experimental obtained values for the IPMSM in generating regime

generated i_d and i_q currents as we can see in Fig.9.c and Fig.9.d. In the absence of the corresponding transducer, Fig.9.e shows the estimated electromagnetic torque.

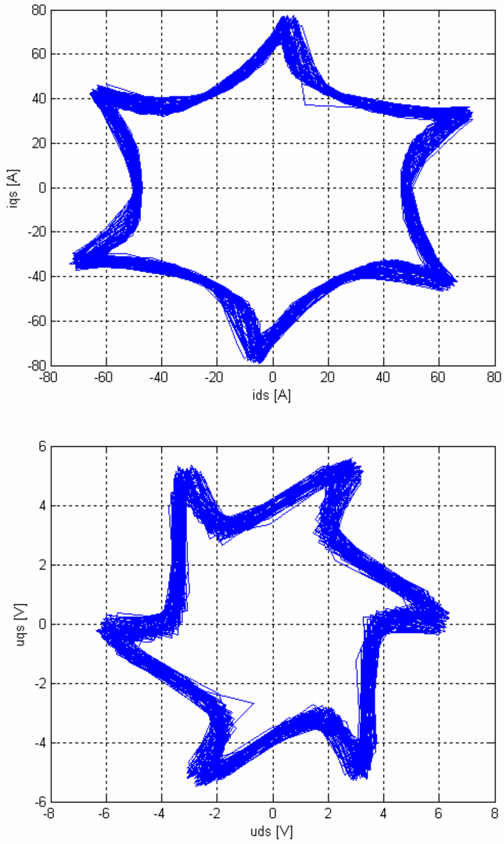

Fig.10 Current and voltage space phasor loci in the stationary reference frame

4.3 IPMSM as integrated starter-generator

The conceived control algorithm was tested as part of an integrated-starter-generator system. The considered time interval was set again at two seconds. In the first moments, during 0.28 sec, the engine is cranked by the ISG from 0 up to 600 rpm. As motor, the ISG takes a large current from batteries to generate the necessary cranking torque. Once the speed gets 600 rpm, the engine control system switches on the speed loop, producing acceleration up to the reference cruise speed (in our case 1200 rpm).

At the same time, the ISG control system changes from the motoring to generating regime. In the generating regime, the PWM inverter boosts up to about 38V on the DC link, charging the batteries pack as previously (Fig.11).

Once the start-up period was surpassed, the system will keep the engine-imposed speed and the same output voltage, the DC voltage being approximately constant because the connected batteries pack.

The experimental results presented in Fig.12 and 13 are, as expected, a mixture of the previously studied regimes and show good system stability to the regime switching from motoring to generating.

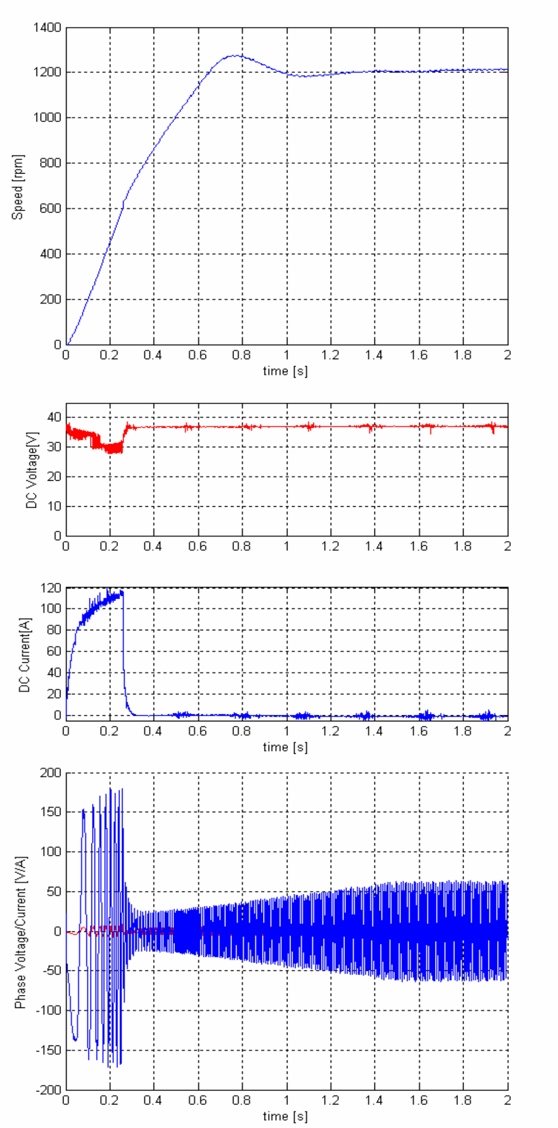

Fig.11 External characteristics of the ISG system

5 Conclusions

This paper has provided a control solution for an IPMSM using the vector control technique in order to get high performances as requested in automotive applications. The proposed system is implemented both as a torque control scheme in motoring mode and as output voltage control scheme in generating regime when the IPMSM is driven by an engine simulator.

A laboratory prototype for the ISG system has been implemented to validate the proposed method. The results of the paper suggest that the controlled IPMSM responds to the specific demands in different operating conditions and offers good dynamic performances.

Two difficulties we have had to surpass in the testing experiments. First, the low design characteristics of the IPMSM that produces a high

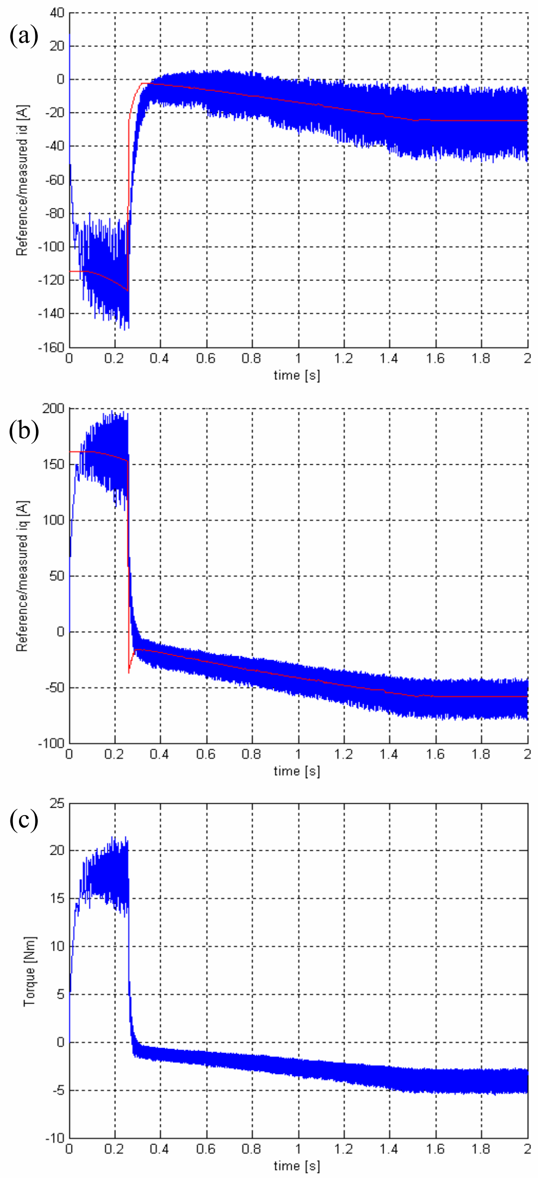

Fig.12 The reference and measured i_d , i_q currents and the estimated electromagnetic torque t_e

fifth-harmonic in its phase currents and so hardly influences the generated reference command-voltages. Second, the PWM converter connected to IPMSM is built with IGBT devices. These ones have a high voltage drop and become difficult to use the converter at low voltages, as requested in many specific automotive applications.

In a future research we intend to apply the conceived control algorithm to a hybrid-excited synchronous machine, taking into account the minimum loss criterion as in [11].

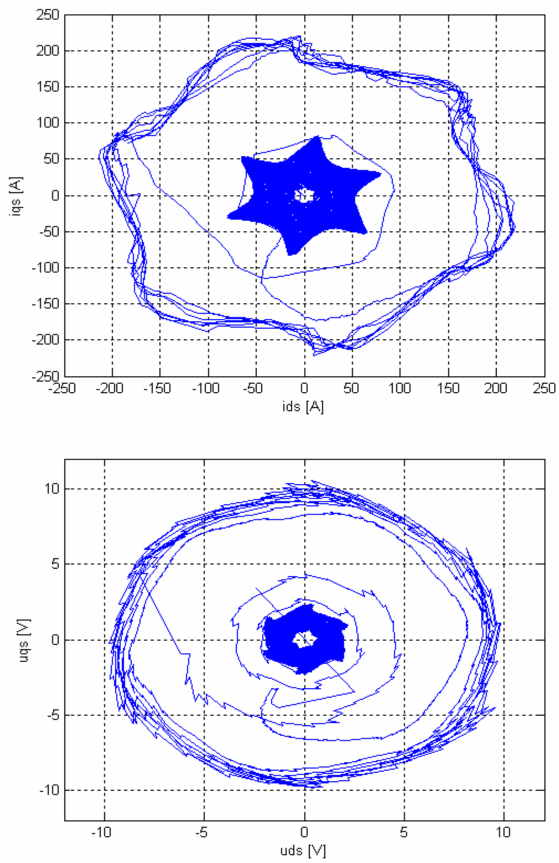

Fig.13 Current and voltage space phasor loci in the stationary reference frame

References:

[1] G. Noriega, M. Strefezza, Direct torque control of a permanent magnet synchronous motor using fuzzy logic, *Proc. of the 7th WSEAS International Conference on Power Systems*, Beijing, China, September 15-17, 2007

[2] S.V. Paturca, M. Covrig, L. Melcescu, A modified direct torque control scheme for permanent magnet synchronous motor drives, *WSEAS Transactions on Systems and Control*, Issue 2, Volume 1, December 2006, ISSN 1991-8763, pp.135-140

[3] P.Vas, *Vector Control of the AC Machines*, U.K.Oxford University Press, 1990

[4] J. H. Song, J. M. Kim, and S. K. Sul, A new robust SPMSM control to parameter variations in flux weakening region, *IEEE IECON*, vol. 2, pp. 1193-1198, 1996.

[5] Y. S. Kim, Y. K. Choi and J. H. Lee, Speed-sensorless vector control for permanent-magnet synchronous motors based on instantaneous reactive power in the wide-speed region, *IEE Proc-Electr. Power Appl.*, vol. 152, No. 5, pp. 1343-1349, Sept. 2005.

[6] S. Morimoto, M. Sanada and K. Takeda, Wide-speed operation of interior permanent magnet synchronous motors with high performance current regulator, *IEEE Trans. Ind. Applicat.*, vol. 30, pp. 920-926, July/Aug. 1994.

[7] J.Wai, T.Jahns, A new technique for achieving

wide constant power speed operation with an interior PM alternator machine, *Proc. of IEEE Ind. Appl. Society Annual Meeting*, Chicago, IL, Oct. 2001

[8] J. M. Kim and S. K. Sul, Speed control of interior permanent magnet synchronous motor drive for the flux weakening operation, *IEEE Trans. Ind. Applicat.*, vol. 33, pp. 43-48, Jan./Feb. 1997.

[9] N.Bianchi, S.Bolognani, High-performance PM synchronous motor drive for an electrical scooter, *IEEE Trans. on Industry Applications*, vol.37, no.5, Sept./Oct.2001, pp.1348-1355

[10] C-T. Pan, S-M. Sue, A linear maximum per ampere control for IPMSM drives over full-speed range, *IEEE Trans. on Energy Conv.,*Vol.20, No.2, June 2005, pp.359-366

[11] S.Shinnaka, T. Sagawa, New optimal control current methods for energy efficient and wide speed-range operation of hybrid-field synchronous motor, *IEEE Int. Conf. on Electric Machines and Drives*, May 2005, pp. 535 – 542

[12] D.Lucache, V.Horga, M.Ratoi, M.Albu, Hardware-in-the-loop testing of an integrated starter alternator, *Proc. Of Joint Conferences ACEMP'07 & Electromotion'07*, September 2007, Bodrum, Turkey, pp.363-368

[13] P. Vas, *Parameter Estimation, Condition Monitoring, and Diagnosis of Electrical Machines*, Clarendon Press, Oxford, 1993

[14] A. Nait Seghir, M.S. Boucherit, Artificial Neural Network to Improve Speed Control of Permanent Magnet Synchronous Motor**,** *Proc. of the 6th WSEAS/IASME Int. Conf. on Electric Power Systems, High Voltages, Electric Machines*, Tenerife, Spain, December 16-18, 2006

[15] M. Rashidi, A Robust and Adaptive RBF Neural Network Based on Sliding Mode Controller for Interior Permanent Magnet Synchronous Motors, *Proc. of the 5th WSEAS/IASME Int. Conf. on Electric Power Systems, High Voltages, Electric Machines*, Tenerife, Spain, December 16-18, 2005, pp.46-51